

Towards Simplified Tools for Analysis of Reinforced Concrete Structures Subjected to Impact and Impulsive Loading: A Preliminary Investigation

by

Heather Trommels

A thesis submitted in conformity with the requirements
for the degree of Master of Applied Science

Civil Engineering
University of Toronto

Towards Simplified Tools for Analysis of Reinforced Concrete Structures Subjected to Impact and Impulsive Loading: A Preliminary Investigation

Heather Trommels

Master of Applied Science

Civil Engineering
University of Toronto

2013

Abstract

The analysis of reinforced concrete structures under blast and impact loads is an area of research that has become increasingly relevant in recent years. Complex hydrocodes are typically used for impact analyses, although single-degree-of-freedom methods have also been developed. There are a number of disadvantages associated with both methods, and the Canadian Nuclear Safety Commission (CNSC) is looking for a tool that can be used in conjunction with hydrocodes to analyze hard and soft missile impacts, with target damage ranging from flexural cracking to perforation.

The VecTor programs, a suite of nonlinear finite element programs developed at the University of Toronto for the analysis of reinforced concrete structures, can potentially be developed into such tools. The analytical work done in this study serves to investigate the current impact and impulse loading analysis capabilities in VecTor2 and VecTor3, and to identify areas where work should be focused in the future.

Acknowledgments

Firstly I'd like to thank Professor Vecchio for his guidance and expertise over the course of my graduate studies. I'd also like to thank Professor Sheikh for his comments while reviewing this thesis.

This work is sponsored by the Canadian Nuclear Safety Commission (CNSC), through Contract 87055-11-0541, "R456.4: Development of Simplified Analytical Tools for Impact and Impulsive Loading Analysis of Reinforced and Pre-stressed and Steel-Plate-Concrete (SC) Concrete Slabs". Their support is gratefully acknowledged.

I would also like to thank Fady ElMohandes for his assistance with VecTor3, and I'd like to thank Trevor Hrynyk, David Carnovale, Ivan Chak, and Vahid Sadeghian for their help throughout the course of my graduate studies.

I would also like to thank my family for their support and encouragement.

Table of Contents

Acknowledgments.....	iii
Table of Contents.....	iv
List of Tables.....	ix
List of Figures.....	xii
List of Appendices.....	xxv
Notation.....	xxvi
1 Introduction.....	1
2 Literature Review.....	6
2.1 Experimental Studies.....	6
2.1.1 Impulsive Loading.....	6
2.1.2 Impact Loading.....	6
2.1.2.1 Scope of Review.....	6
2.1.2.2 Experimental Studies.....	7
2.2 Numerical Modeling of Blast and Impact Loading.....	11
2.2.1 Analysis Types.....	11
2.2.1.1 Riera Method.....	12
2.2.2 Constitutive Models.....	14
2.2.2.1 Strain Rate Effects: Dynamic Increase Factors.....	14
2.2.2.2 Strain Rate Effects: Constitutive Modeling at High Rates of Loading...15	
2.2.2.3 Accounting for Loss of Concrete Material.....	15
2.2.3 Numerical Investigations.....	17
3 VecTor2 Methodology.....	23
3.1 Introduction.....	23
3.2 Stiffness Formulation.....	24

3.3	Dynamic Analysis Formulation in VecTor2.....	26
3.3.1	Rayleigh Damping	26
3.3.2	Newmark Method of Direct Integration	26
3.3.3	Strain Rate Effects in VecTor2.....	28
4	2D Verification Studies.....	35
4.1	Introduction.....	35
4.2	University of Texas Specimens	35
4.2.1	Finite Element Model	36
4.2.2	Pre-Tensioned Specimen Analysis Results.....	39
4.2.2.1	Comparison of Peak and Residual Crack Widths for Pre-tensioned University of Texas Specimen.....	44
4.2.3	Post-Tensioned Specimen Analysis Results	46
4.2.3.1	Comparison of Peak and Residual Crack Widths for Post-tensioned University of Texas Specimen.....	50
4.2.4	Summary.....	52
4.3	University of Ottawa Specimen	53
4.3.1	Finite Element Model	53
4.3.2	Results.....	56
4.3.2.1	Comparison of Peak and Residual Crack Widths for University of Ottawa Specimen.....	61
4.3.3	Summary.....	63
4.4	U.S. Army Doubly-Reinforced Shock Tube Specimens	64
4.4.1	Introduction.....	64
4.4.2	Specimen Details and VecTor2 Modeling.....	65
4.4.3	Displacement Results and Discussion	70
4.4.4	Discussion of Slab Damage	73
4.4.5	Summary of Doubly-Reinforced U.S. Army Slabs	77

4.5	U.S. Army Singly-Reinforced Shock Tube Specimens	78
4.5.1	Introduction.....	78
4.5.2	Specimen Details and VecTor2 Modeling.....	79
4.5.3	Results and Discussion	84
4.6	Summary and Discussion of 2D Verification Studies	91
5	Modeling of IRIS_2012 Specimens.....	93
5.1	Introduction.....	93
5.2	IRSN Triaxial Tests	95
5.2.1	Model Details.....	96
5.2.2	Analysis Results.....	97
5.2.2.1	Material-Level Results	97
5.2.2.2	Summary of Material-Level Triaxial Test Results.....	104
5.2.2.3	Structural-Level Triaxial Results	107
5.3	VTT-B1 Flexural Specimen.....	113
5.3.1	Introduction.....	113
5.3.2	VecTor2 Missile Modeling.....	115
5.3.2.1	Mesh and Simplifying Assumptions	115
5.3.2.2	Effect of b/t Ratio	119
5.3.2.3	Load Profile	120
5.3.2.4	VecTor2 Missile Results	121
5.3.3	Modeling of Impact Using Nodal Forces.....	124
5.3.3.1	VecTor2 Modeling	124
5.3.3.2	VecTor3 Modeling	125
5.3.3.3	Comparison of VTT-B1 Displacement Results.....	127
5.3.3.4	Effect of Concrete Cover and Mesh Size	131
5.3.3.5	VecTor3 Deformed mesh and Crack Patterns	132

5.3.3.6	Comparison of VecTor3 and Experimental Results	135
5.3.4	Summary of VTT-B1 Modeling	138
5.4	VTT-P1 Punching Specimen	140
5.4.1	VecTor2 Modeling.....	142
5.4.1.1	VecTor2 Missile Results	146
5.4.2	VecTor3 Modeling.....	149
5.4.3	VecTor3 Results.....	150
5.4.4	Summary of VTT-P1 Modeling.....	156
5.5	Observations from IRIS_2012 Modeling.....	157
5.6	Missile Modeling in VecTor3	159
5.6.1	P1 Modeling.....	159
5.6.2	P1 Results.....	160
5.6.2.1	Missile Results.....	160
5.6.2.2	Slab Results	163
5.6.3	Summary of P1 VecTor3 Modeling with Missile.....	168
6	Modeling of Prestressed Impact Specimens	169
6.1	Test Series I.....	169
6.1.1	Introduction.....	169
6.1.2	Test Specimens and Modeling Approach	169
6.1.3	Experimental and Modeling Results.....	171
6.2	Test Series II	173
6.2.1	Introduction.....	173
6.2.2	Test Specimens and Modeling.....	173
6.2.3	Experimental and Modeling Results.....	174
6.3	Discussion of Hard Missile Modeling in VecTor3	175
6.3.1	Missile Modeling Using Average Strain for Rupture	178

7	Conclusions and Lessons Learned	181
8	Recommendations	188
	References	190

List of Tables

Table 3-1: Strain Rate Effects Formulations in VecTor2	28
Table 4-1: University of Texas Specimens Blast Pressures and Impulses	39
Table 4-2: Displacement Results for University of Texas Pre-tensioned Specimen	39
Table 4-3: Displacement Results for University of Texas Post-tensioned Specimen	46
Table 4-4: University of Ottawa Specimen Blast Pressures and Impulses	54
Table 4-5: Displacement Results for University of Ottawa Specimen	56
Table 4-6: Experimental Matrix for Doubly Reinforced Shock Tube Tests at ERDC-Vicksburg	64
Table 4-7: US Army Two-Way Specimens Peak Pressure and Impulse	64
Table 4-8: Reinforcement and Concrete Material Properties for Doubly-Reinforced US Army Specimens	67
Table 4-9: Displacement Comparison for U.S. Army Slabs	70
Table 4-10: US Army Singly-Reinforced Specimens Peak Pressure and Impulse	78
Table 4-11: Reinforcement and Concrete Material Properties for Singly-Reinforced U.S. Army Specimens	80
Table 4-12: Peak and Residual Displacements for Singly-Reinforced Reinforced Concrete Shock Tube Tested Slabs	84
Table 5-1: IRSN Triaxial Specimen Data	95
Table 5-2: VecTor2 Triaxial Test Model Data	96
Table 5-3: Material Properties Specified in VecTor2 Triaxial Analyses	96

Table 5-4: Triaxial Experiment Results.....	97
Table 5-5: Stress-Strain Results for All Specimen 4 Material-Level Analyses.....	100
Table 5-6: Stress-Strain Results for All Specimen 7 Material-Level Analyses.....	101
Table 5-7: Stress-Strain Results for All Specimen 8 Material-Level Analyses.....	102
Table 5-8: Stress-Strain Results for All Specimen 9 Material-Level Analyses.....	103
Table 5-9: Results for Montoya/Ottosen Confinement Model with Montoya 2003 Dilatation.	104
Table 5-10: Results for Kupfer/Richart Confinement Model with Montoya 2003	104
Table 5-11: Results for Montoya/Ottosen Confinement Model with Variable-Kupfer Dilatation	105
Table 5-12: Results for Kupfer/Richart Confinement Model with Variable-Kupfer	105
Table 5-13: Results of Structural-Level Triaxial Analyses in VecTor2	108
Table 5-14: Material Properties for VTT-B1 Analyses	117
Table 5-15: VTT-B1 Missile: VecTor2 Missile Properties	119
Table 5-16: Effect of b/t on Peak Displacement.....	120
Table 5-17: Displacement Results for VecTor2 and VecTor3 VTT-B1 Analyses Using Nodal Loads.....	127
Table 5-18: Comparison of Displacements for VecTor3 VTT-B1 Analyses With and Without Strain Rate Effects	128
Table 5-19: Displacement Comparison for VecTor3 Analysis of VTT-B1 With Reinforcement Depths of 15 mm and 30 mm.....	131
Table 5-20: VTT-P1 Missile Properties.....	144
Table 5-21: VTT-P1 Target Properties	145

Table 5-22: Comparison of VecTor3 and Experimental VTT-P1 Displacements.....	151
Table 5-23: Comparison of VecTor3 (With Missile Modeled) and Experimental Displacements for VTT-P1.....	163
Table 6-1: Test Series I: Concrete Strength, Missile Velocity, and Specimen Reinforcement .	171
Table 6-2: Comparison of Experimental and VecTor3 Results for Prestressed Impact Test Series I	172
Table 6-3: Test Series II: Concrete Strength, Missile Velocity, and Specimen Reinforcement	173
Table 6-4: Comparison of Experimental and VecTor3 Results for Prestressed Impact Test Series II	174
Table 6-5: Summary of Hard Missile Modeling Results in VecTor3.....	175
Table 6-6: Comparison of Analytical and Experimental Failure Modes for Hard Missile Impacts on 250 mm Thick Reinforced Concrete Targets.....	177
Table 6-7: Comparison of Analytical and Experimental Results for Hard Missile Impacts with Average Strain Rupture Criterion in VecTor3	179
Table A 1: Displacement sensor locations.....	A-1
Table A 2: Concrete strain gauge locations	A-2
Table A 3: Rebar strain gauge locations	A-3
Table B 1: Displacement sensor locations	B-1
Table B 2: Concrete strain gauge locations	B-2
Table B 3: Reinforcement strain gauge locations	B-3

List of Figures

Figure 1-1: Centre displacement history of VTT-B1 (blind simulation results from IRIS_2010).	3
Figure 1-2: VTT-P1 missile residual velocity (blind simulation results from IRIS_2010).	3
Figure 2-1: Damage to slab (Fiquet and Dacquet, 1977) [front face (left); back face (right)].	7
Figure 2-2: Effect of reinforcement ratio and shear reinforcement on panel damage (Sugano et al., 1993b).	9
Figure 2-3: Impact load for Boeing 720 using Riera method (Riera, 1968).	12
Figure 2-4: Modeling of impacts on plain (left) and reinforced concrete targets (right) (Magnier and Donze, 1998).	18
Figure 2-5: DEM modeling of full-scale GE-J79 engine impact on RC target (Sawamoto et al., 1998).	19
Figure 2-6: Axisymmetric models (Itoh et al., 2000).	20
Figure 2-7: SOFiSTiK model (left) and ADINA model (right) (Zinn et al., 2007).	21
Figure 2-8: Comparison of experimental and analytical impact results (Tai, 2009).	22
Figure 3-1: VecTor2 coordinate reference systems (Vecchio, 1990).	24
Figure 3-2: Flowchart for dynamic analyses in VecTor2 (Saatci, 2007).	27
Figure 3-3: DIFs for concrete in compression: fib MC 2010.	30
Figure 3-4: DIFs for concrete in tension: fib MC 2010.	30
Figure 3-5: DIFs for concrete in compression: fib MC 1990.	32
Figure 3-6: DIFs for concrete in tension: fib MC 1990.	32
Figure 3-7: DIFs for steel: Malvar-Crawford.	33

Figure 3-8: DIFs for steel: CEB-FIP 1988.....	34
Figure 4-1: Finite element mesh for VecTor2 University of Texas (left); pre-tension reinforcement (middle); post-tension reinforcement (right).....	37
Figure 4-2: Experimental (left) and VecTor2 (right) pressure-time history for University of Texas Blast 1.....	38
Figure 4-3: Experimental (left) and VecTor2 (right) pressure-time history for University of Texas Blast 2.....	38
Figure 4-4: Experimental (left) and VecTor2 (right) pressure-time history for University of Texas Blast 3.....	38
Figure 4-5: VecTor2 and experimental results for University of Texas Blast 1 (pre-tensioned panel, VecTor2 model has some fixity, no SRE).....	40
Figure 4-6: VecTor2 and experimental results for University of Texas Blast 2 (pre-tensioned panel, VecTor2 model has some fixity, no SRE).....	40
Figure 4-7: VecTor2 and experimental results for University of Texas Blast 3 (pre-tensioned panel, VecTor2 model has some fixity, no SRE).....	41
Figure 4-8: Crack pattern from VecTor2 for University of Texas Blast 1	43
Figure 4-9: Crack pattern from VecTor2 for University of Texas Blast 2 (pre-tensioned; residual).....	43
Figure 4-10: Crack pattern from VecTor2 for University of Texas Blast 3 (pre-tensioned; residual).....	43
Figure 4-11: VecTor2 calculated residual crack widths after Blast 3 for University of Texas pre-tensioned panel.....	44
Figure 4-12: Crack pattern from VecTor2 for University of Texas Blast 1	45

Figure 4-13: Crack pattern from VecTor2 for University of Texas Blast 2 (pre-tensioned; at peak).....	45
Figure 4-14: Crack pattern from VecTor2 for University of Texas Blast 3 (pre-tensioned; at peak).....	45
Figure 4-15: VecTor2 and experimental results for University of Texas Blast 1 (post-tensioned panel, VecTor2 model has some fixity, no SRE).....	46
Figure 4-16: VecTor2 and experimental results for University of Texas Blast 2 (post-tensioned panel, VecTor2 model has some fixity, no SRE).....	47
Figure 4-17: VecTor2 and experimental results for University of Texas Blast 3 (post-tensioned panel, VecTor2 model has some fixity, no SRE).....	47
Figure 4-18: Crack pattern from VecTor2 for University of Texas Blast 1	49
Figure 4-19: Crack pattern from VecTor2 for University of Texas Blast 2	49
Figure 4-20: Crack pattern from VecTor2 for University of Texas Blast 3	49
Figure 4-21: Crack pattern from VecTor2 for University of Texas Blast 1	51
Figure 4-22: Crack pattern from VecTor2 for University of Texas Blast 2	51
Figure 4-23: Crack pattern from VecTor2 for University of Texas Blast 3	51
Figure 4-24: Finite element model for University of Ottawa specimen.	54
Figure 4-25: VecTor2 pressure-time history for University of Ottawa Blast 1.....	55
Figure 4-26: VecTor2 pressure-time history for University of Ottawa Blast 2.....	55
Figure 4-27: VecTor2 pressure-time history for University of Ottawa Blast 3.....	55
Figure 4-28: Comparison of VecTor2 and experimental response for University of Ottawa Blast 1.....	56

Figure 4-29: Comparison of VecTor2 and experimental response for University of Ottawa Blast 2.....	57
Figure 4-30: Comparison of VecTor2 and experimental responses for University of Ottawa Blast 3.....	57
Figure 4-31: VecTor2 crack pattern for University of Ottawa Blast 1 (residual).....	60
Figure 4-32: VecTor2 crack pattern for University of Ottawa Blast 2 (residual).....	60
Figure 4-33: VecTor2 crack pattern for University of Ottawa Blast 3 (residual).....	60
Figure 4-34: VecTor2 crack pattern for University of Ottawa Blast 1 (at peak).....	62
Figure 4-35: VecTor2 crack pattern for University of Ottawa Blast 2 (at peak).....	62
Figure 4-36: VecTor2 crack pattern for University of Ottawa Blast 3 (at peak).....	62
Figure 4-37: Specimen details for doubly reinforced specimens tested at U.S. Army ERDC (Robert et al., 2009).	66
Figure 4-38: Stress-strain curves for vanadium and conventional reinforcement (Robert et al., 2009).	66
Figure 4-39: VecTor2 model for US Army doubly reinforced specimens; reinforcement (left), supports (right).....	67
Figure 4-40: Slab 3 experimental pressure-time and impulse-time history (Robert et al., 2009).68	
Figure 4-41: Slab 5 experimental pressure-time and impulse-time history (Robert et al., 2009).68	
Figure 4-42: Slab 6 experimental pressure-time and impulse-time history (Robert et al., 2009).69	
Figure 4-43: Slab 9 experimental pressure-time and impulse-time history (Robert et al., 2009).69	
Figure 4-44: US Army Slab 3 results comparison.	71
Figure 4-45: US Army Slab 5 results comparison.	71

Figure 4-46: US Army Slab 6 results comparison.	72
Figure 4-47: US Army Slab 9 results comparison.	72
Figure 4-48: Residual crack pattern predicted by VecTor2 for Slab 3 (left: crack pattern; right: crack widths).	73
Figure 4-49: Experimental damage to front face of Slab 3 (Robert and Johnson, 2009).	73
Figure 4-50: Residual crack pattern predicted by VecTor2 for Slab 5 (left: crack pattern; right: crack widths).	74
Figure 4-51: Experimental damage to front face of Slab 5 (Robert and Johnson, 2009).	74
Figure 4-52: Residual crack pattern predicted by VecTor2 for Slab 6 (left: crack pattern; right: crack widths).	75
Figure 4-53: Experimental damage to front face of Slab 6 (Robert and Johnson, 2009).	75
Figure 4-54: Residual crack pattern predicted by VecTor2 for Slab 9 (left: crack pattern; right: crack widths).	76
Figure 4-55: Experimental damage to front face of Slab 9 (Robert and Johnson, 2009).	76
Figure 4-56: Specimen details for singly-reinforced specimens tested at ERDC-Vicksburg (UMKC, 2012).	79
Figure 4-57: Stress-strain curves for vanadium (high strength) and conventional reinforcement (UMKC, 2012).	80
Figure 4-58: VecTor2 model for US Army singly-reinforced slabs (UMKC, 2012).	80
Figure 4-59: Support conditions for blast side of US Army specimens (UMKC, 2012).	81
Figure 4-60: Support conditions for non-blast side of US Army specimens (UMKC, 2012).	82
Figure 4-61: Experimental pressure-time histories for high strength specimens (UMKC, 2012).	83

Figure 4-62: Experimental pressure-time histories for regular strength specimens (UMKC, 2012).	83
Figure 4-63: Displacement-time histories for singly-reinforced shock-tube tested reinforced concrete panels.	85
Figure 4-64: Crack pattern at peak predicted by VecTor2 for Slab 1 (left: crack pattern; centre: crack widths; right: principal compressive strain).	87
Figure 4-65: Crack pattern at peak predicted by VecTor2 for Slab 2 (left: crack pattern; centre: crack widths; right: principal compressive strain).	88
Figure 4-66: Crack pattern at peak predicted by VecTor2 for Slab 5 (left: crack pattern; right: crack widths).	89
Figure 4-67: Crack pattern at peak predicted by VecTor2 for Slab 6 (left: crack pattern; centre: crack widths; right: principal compressive strain).	90
Figure 5-1: Centre displacement history of VTT-B1 (blind simulation results from IRIS_2010).	93
Figure 5-2: VTT-P1 missile residual velocity (blind simulation results from IRIS_2010).	94
Figure 5-3: VecTor2 triaxial compression test material-level model [a) confinement load; b) nodal loads].	98
Figure 5-4: Triaxial test strain gauge locations (Vu, 2007).	98
Figure 5-5: Specimen 2: comparison of VecTor2 and experimental stress-strain results.	99
Figure 5-6: Specimen 4: comparison of VecTor2 and experimental stress-strain results.	100
Figure 5-7: Specimen 7: comparison of VecTor2 and experimental stress-strain results.	101
Figure 5-8: Specimen 8: comparison of VecTor2 and experimental stress-strain results.	102
Figure 5-9: Specimen 9: comparison of VecTor2 and experimental stress-strain results.	103

Figure 5-10: VecTor2 triaxial compression test structural-level model	107
Figure 5-11: Results from analyses using Montoya/Ottosen & Variable-Kupfer.	109
Figure 5-12: Results from analyses using Montoya/Ottosen & Variable-Kupfer.	109
Figure 5-13: Results from analyses using Montoya/Ottosen & Variable-Kupfer.	110
Figure 5-14: Results from analyses using Montoya/Ottosen & Variable-Kupfer.	110
Figure 5-15: Results from analyses using Montoya/Ottosen & Variable-Kupfer.	111
Figure 5-16: VTT-B1 dimensions and support conditions (Vepsä, 2010a).....	113
Figure 5-17: Horizontal cross section of VTT-B1 (Vepsä, 2010a).	114
Figure 5-18: Vertical cross section of VTT-B1 (Vepsä, 2010a).....	114
Figure 5-19: VTT-B1 missile (Vepsä, 2010a).	115
Figure 5-20: VecTor2 VTT-B1 mesh including missile and target.	116
Figure 5-21: Close-up of VecTor2 VTT-B1 target [a) mesh; b) reinforcement].....	116
Figure 5-22: Effect of b/t on peak displacement of VTT-B1 target.	120
Figure 5-23: Displacement-time history of rear of missile from VecTor2 analysis of VTT-B1.	121
Figure 5-24: Velocity-time history of rear of missile from VecTor2 analysis of VTT-B1.	122
Figure 5-25: Load-time history in compression-only truss bars from VecTor2 analysis of VTT-B1.	122
Figure 5-26: Impulse derived from truss bar forces from VecTor2 analysis of VTT-B1.....	123
Figure 5-27: Stress contours of VTT-B1 missile at t=10.1 ms (half-way through impact).....	123
Figure 5-28: Displaced shape of VTT-B1 missile at t=10.1 ms (half-way through impact).	123

Figure 5-29: Stress contours of VTT-B1 missile at t=20.2 ms (end of impact).	123
Figure 5-30: Displaced shape of VTT-B1 missile at t=20.2 ms (end of impact).	123
Figure 5-31: VecTor2 VTT-B1 target fine mesh.	125
Figure 5-32: VecTor2 VTT-B1 target coarse mesh.	125
Figure 5-33: VecTor2 VTT-B1 target coarse mesh (aspect ratio=1).	125
Figure 5-34: VecTor3 VTT-B1 mesh.	126
Figure 5-35: Load applied to quarter slab and loaded nodes in VecTor3 VTT-B1 (indicated in blue in the lower left corner of the mesh).	126
Figure 5-36: Comparison of VecTor3 and experimental displacement-time response for centre of VTT-B1.	128
Figure 5-37: Comparison of VecTor2 truss forces to Riera load for VTT-B1.	129
Figure 5-38: Displacement-time response for centre of VTT-B1 using Riera load in VecTor3.	130
Figure 5-39: VecTor3 VTT-B1 deformed mesh at t=10.8 ms (front face).	132
Figure 5-40: VecTor3 VTT-B1 deformed mesh at t=10.8 ms (vertical section).	133
Figure 5-41: VecTor3 VTT-B1 deformed mesh at t=10.8 ms (horizontal section).	133
Figure 5-42: Crack pattern on front face of VTT-B1 at t=10.8 ms (centre of slab, point of impact, located in lower left corner).	134
Figure 5-43: Crack pattern on back face of VTT-B1 at t=10.8 ms (centre of slab, point of impact, located in lower left corner).	134
Figure 5-44: Comparison of VecTor3 and experimental displacement responses for centre of VTT-B1.	135

Figure 5-45: Comparison of reinforcement strains at midspan of VTT-B1	136
Figure 5-46: Comparison of support forces for VTT-B1.....	137
Figure 5-47: Comparison of impulse at support for VTT-B1	137
Figure 5-48: VTT-P1 dimensions and support conditions (Vepsä, 2010b).....	140
Figure 5-49: VTT-P1 missile (Vepsä, 2010b).	141
Figure 5-50: Horizontal cross section of VTT-P1 (Vepsä, 2010b).....	141
Figure 5-51: Vertical cross section of VTT-P1 (Vepsä, 2010b).....	142
Figure 5-52: VecTor2 mesh of VTT-P1 missile and target.	143
Figure 5-53: VecTor2 VTT-P1 support and reinforcement locations.	144
Figure 5-54: VecTor2 VTT-P1 crack pattern.	145
Figure 5-55: Load profile from VecTor2 truss forces and VecTor3 VTT-P1 analyses.....	145
Figure 5-56: Stress contours in concrete-filled VTT-P1 missile after impact.	146
Figure 5-57: Displacement-time history of back of missile in VecTor2 VTT-P1 analysis.	146
Figure 5-58: Velocity-time history of back of missile in VecTor2 VTT-P1 analysis.	147
Figure 5-59: Load-time history from truss forces in VecTor2 VTT-P1 analysis.	147
Figure 5-60: Impulse from truss forces in VecTor2 VTT-P1 analysis.....	148
Figure 5-61: VecTor3 VTT-P1 model.	149
Figure 5-62: VTT-P1 loaded nodes and load profile.....	149
Figure 5-63: VTT-P1 experimental damage (Vepsä, 2010b) [left: front; right: back]	150
Figure 5-64: Displacement response, predicted by VecTor3, for centre of VTT-P1.	150

Figure 5-65: Deformed VecTor3 VTT-P1 mesh at time of maximum displacement ($t=7.9$ ms).	152
Figure 5-66: Displacement profile along front of slab for different stages in the VecTor3 VTT-P1 simulation.	152
Figure 5-67: Displacement profile along back of slab for different stages in the VecTor3 VTT-P1 simulation.	153
Figure 5-68: Crack pattern of front face of VTT-P1 at $t=7.9$ ms (centre of slab, and point of impact, located in lower left corner).	154
Figure 5-69: Crack pattern of back face of VTT-P1 at $t=7.9$ ms (centre of slab located in lower left corner).	154
Figure 5-70: Crack pattern of vertical cross section of VTT-P1 at $t=7.9$ ms.	155
Figure 5-71: Crack pattern of horizontal cross section of VTT-P1 at $t=7.9$ ms.	155
Figure 5-72: VecTor3 VTT-P1 model (missile and slab).	159
Figure 5-73: Displacement-time profile for VTT-P1 missile in VecTor3.	161
Figure 5-74: Velocity-time profile for VTT-P1 missile in VecTor3.	161
Figure 5-75: Impact force-time profile for VTT-P1 missile in VecTor3.	162
Figure 5-76: Impulse-time profile for VTT-P1 missile in VecTor3.	162
Figure 5-77: Deformed VTT-P1 mesh at $t=3.09$ ms (with missile modeled).	164
Figure 5-78: Crack pattern on the front of VTT-P1 at $t=3.09$ ms (with missile modeled).	164
Figure 5-79: Crack pattern on the back of VTT-P1 at $t=3.09$ ms (with missile modeled).	165
Figure 5-80: Displacement profile along front edge of VTT-P1 from VecTor3 analysis with missile modeled.	166

Figure 5-81: Displacement profile along back edge of VTT-P1 from VecTor3 analysis with missile modeled.	166
Figure 5-82: Comparison of displacement profiles at max displacement for front of VTT-P1.	167
Figure 5-83: Comparison of displacement profiles at max displacement for back of VTT-P1.	167
Figure 5-84: Comparison of displacements between VecTor3 P1 models.....	168
Figure 6-1: Prestressing and transverse steel reinforcement layout (Orbovic, N. and Blahoianu, A., 2011) [horizontal cross section].....	170
Figure 6-2: Prestressing and transverse steel reinforcement layout (Orbovic, N. and Blahoianu, A., 2011) [vertical cross section].....	170
Figure 6-3: VecTor3 Prestressed Test Series I Results.....	172
Figure 6-4: VecTor3 Prestressed Test Series II Results.	174
Figure 6-5: Comparison of all hard impacts modeled in VecTor3.	176
Figure 6-6: Comparison of hard impact results in from VecTor3 analyses with average strain rupture criterion.	180
Figure A 1: Displacement sensor locations.....	A-1
Figure A 2: Concrete strain gauge locations.....	A-2
Figure A 3: Rebar strain gauge sensor locations	A-3
Figure A 4: Displacement results at sensor location W1 (centre of the slab).....	A-4
Figure A 5: Displacement results at sensor location W2.....	A-4
Figure A 6: Displacement results at sensor location W3.....	A-5
Figure A 7: Displacement results at sensor location W4.....	A-5
Figure A 8: Displacement results at sensor location W5.....	A-6

Figure A 9: Reinforcement strain D3.....	A-6
Figure A 10: Reinforcement strain D4.....	A-7
Figure A 11: Reinforcement strain D5.....	A-7
Figure A 12: Reinforcement strain D6.....	A-8
Figure A 13: Reinforcement strain D7.....	A-8
Figure A 14: Reinforcement strain D8.....	A-9
Figure A 15: Reinforcement strain D10.....	A-9
Figure A 16: Reinforcement strain D15.....	A-10
Figure A 17: Concrete Strains at Sensor R1	A-10
Figure A 18: Concrete Strains at Sensor R2	A-11
Figure A 19: Concrete Strains at Sensor R3	A-11
Figure A 20: Total support force	A-12
Figure A 21: Support impulse.....	A-12
Figure B 1: Displacement Sensor Locations.....	B-1
Figure B 2: Concrete strain gauge locations	B-2
Figure B 3: Reinforcement strain gauge locations.....	B-3
Figure B 4: Displacements at location W2	B-4
Figure B 5: Displacements at location W3	B-4
Figure B 6: Displacements at location W4	B-5
Figure B 7: Displacements at location W5	B-5

Figure B 8: Concrete strains at location R1	B-6
Figure B 9: Concrete strains at location R2	B-6
Figure B 10: Reinforcement strains at location D1	B-7
Figure B 11: Reinforcement strains at location D3	B-7
Figure B 12: Reinforcement strains at location D4	B-8
Figure B 13: Reinforcement strains at location D5	B-8
Figure B 14: Reinforcement strains at location D6	B-9
Figure B 15: Reinforcement strains at location D7	B-9
Figure B 16: Reinforcement strains at location D8	B-10
Figure B 17: Total support force.....	B-10
Figure B 18: Total impulse at support	B-11

List of Appendices

Appendix A: Comparison of VecTor3 VTT_B1 Results to Experimental Results

Appendix B: Comparison of VecTor3 VTT_P1 Results to Experimental Results

Notation

$P(t)$	total reaction force
$P_b(t)$	missile body crushing load
$x(t)$	distance from nose of aircraft
$\mu(t)$	aircraft mass per unit length
$v(t)$	velocity of uncrushed portion of missile
P_m	static buckling resistance of hollow tube missile
H	wall tube thickness (for calculating missile static buckling resistance)
R	tube thickness (for calculating missile static buckling resistance)
σ_0	yield strength of tube material (for calculating missile static buckling resistance)
$[\sigma]$	stress matrix
$[D]$	material matrix
$[\varepsilon]$	strain tensor
$[D_c]'$	concrete material matrix with respect to principal axes
$[D_c]$	concrete material matrix
\overline{E}_{c1}	secant modulus of concrete in principal direction 1
\overline{E}_{c2}	secant modulus of concrete in principal direction 2
\overline{G}_c	secant shear modulus
f_{c1}	concrete stress in principal direction 1
ε_{c1}	concrete strain in principal direction 1
f_{c2}	concrete stress in principal direction 2
ε_{c2}	concrete strain in principal direction 2
$[D_s]'$	steel material matrix with respect to the steel elements' axis
ρ_i	reinforcement ratio
\overline{E}_{si}	secant elastic modulus for steel reinforcement i
f_{si}	stress in reinforcement i
ε_{si}	strain in reinforcement i
$[T]$	transformation matrix
$[B]$	shape function matrix
$[k]$	stiffness matrix

a_1	damping proportionality constant
a_0	damping proportionality constant
ξ_i	damping ratio for mode i
ξ_j	damping ratio for mode j
ω_i	frequency of mode i
ω_j	frequency of mode j
γ	direct integration constant (dynamic analyses)
Δt	time increment
β	direct integration constant
$[m]$	mass matrix
$[k_0]$	initial stiffness matrix
$[u]$	displacement vector
$[\dot{u}]$	velocity vector
$[\ddot{u}]$	acceleration vector
$[p]$	load vector
$\dot{\epsilon}_c$	concrete strain rate (compression)
$\dot{\epsilon}_{ct}$	concrete strain rate (tension)
$f_{c,imp}$	dynamic concrete strength
f_{cm}	static concrete compressive strength
$\dot{\epsilon}_{c0}$	reference concrete strain rate (compression)
$f_{ct,imp}$	dynamic concrete tensile strength
f_{ctm}	static concrete tensile strength
$\dot{\epsilon}_{ct0}$	reference concrete strain rate (tension)
$E_{c,imp}$	dynamic concrete modulus
E_{ct}	static concrete modulus
$\epsilon_{c1,imp}$	dynamic concrete strain at peak stress
ϵ_{c1}	concrete strain at peak stress (static)
α_s	parameter for concrete DIF compression calculation (fib MC 1990)
γ_s	parameter for concrete DIF compression calculation (fib MC 1990)
δ_s	parameter for concrete DIF tension calculation (fib MC 1990)
β_s	parameter for concrete DIF tension calculation (fib MC 1990)

$f_{y,imp}$ dynamic yield stress
 f_y static yield stress
 $f_{u,imp}$ dynamic ultimate stress
 f_u static ultimate stress
 $\dot{\epsilon}_s$ steel strain rate
 $\dot{\epsilon}_{s0}$ reference steel strain rate

1 Introduction

The testing and analysis of structures under blast and impact loading conditions has been studied for decades, but there has been a resurgence in this area of study in the last few years. The renewed attention is due, in part, to the increased concern over potential natural and man-made hazards. The applications of research in blast and impact loading range from protection of infrastructure from deliberate attacks to designing industrial buildings able to withstand accidental explosions. Increasingly, research is being focused on increasing the resistance of critical infrastructure to accidental or deliberate blasts or impacts.

The nuclear power industry is one of the leading sectors driving the research activity. Common nuclear power plant structures contain reinforced concrete, prestressed concrete, and steel-concrete composites. Research is being done on the blast and impact response of these materials, with damage ranging from light flexural damage to penetration of the structure. One of the current focuses is to determine, using finite element analysis, whether critical infrastructure such as nuclear power plants will be able to withstand accidental or deliberate extreme loads. A number of programs currently exist to carry out such analyses, however more simplified analysis procedures are desired.

Currently, both single-degree-of-freedom (SDOF) and finite element methods are available for analyzing structures subjected to blast or impact loads. For design purposes, SDOF methods have been used extensively in the past. Although detailed design guidelines have been developed based on SDOF methods (US DoA, 1990), this analysis technique has a number of inherent drawbacks. Firstly, the geometry of the specimen is simplified to a single degree of freedom; because of this, inertial effects, which can be important under dynamic loading conditions, are ignored. Secondly only the displacement-time response can typically be obtained from a SDOF analysis, while in general it is important to be able to look at crack patterns or damage conditions. For impact loading, empirical formulae are available to predict penetration depth and whether or not perforation will occur. These formulae, however, oversimplify the structures as well as the loading and cannot provide the detailed results that are sometimes required.

For research or highly specialized design, hydrocodes such as LS-DYNA are often used. The use of these types of programs overcomes the limitations of the overly simplistic SDOF methods, and can provide highly detailed results. That being said, hydrocodes are not without disadvantages. Firstly, the modeling process is both time-consuming and complex. Missiles, in the case of impact loading, must be modeled in great detail, as does the target. In addition, the material models used in these programs often require an inordinate number of input properties for concrete, many of which are not typically known. While a great deal of effort and time is required to build the model, the analysis time for these programs can also be quite large. A single slab can be composed of hundreds of thousands of nodes, leading to excessively long analysis times. In addition, modeling the behaviour of reinforced concrete, particularly the shear behaviour, is complex. Although it is well known that shear mechanisms tend to dominate the behaviour of structures under hard missile impacts, many of these programs do not adequately capture them.

The results of the IRIS_2010 workshop highlight the need for improved analysis methods, and the need for simplified analysis tools that can be used to verify the complex codes. IRIS_2010 was a workshop intended to validate evaluation techniques used in the assessment of structures impacted by missiles (NEA, 2011). For IRIS_2010, two impact specimens discussed in this thesis, VTT-B1 and VTT-P1, were analyzed as part of a blind prediction exercise. The spread in the results of the analysis for VTT-B1 and VTT-P1 are shown in Figure 1-1 and Figure 1-2, respectively. Figure 1-1 summarizes the blind simulation displacement-time history predictions for the centre of the flexural specimen, and compares the predictions to the experimental result. Figure 1-2 shows the residual velocity predictions for the punching specimen. For both of these specimens, there was a great deal of scatter in the analytical results.

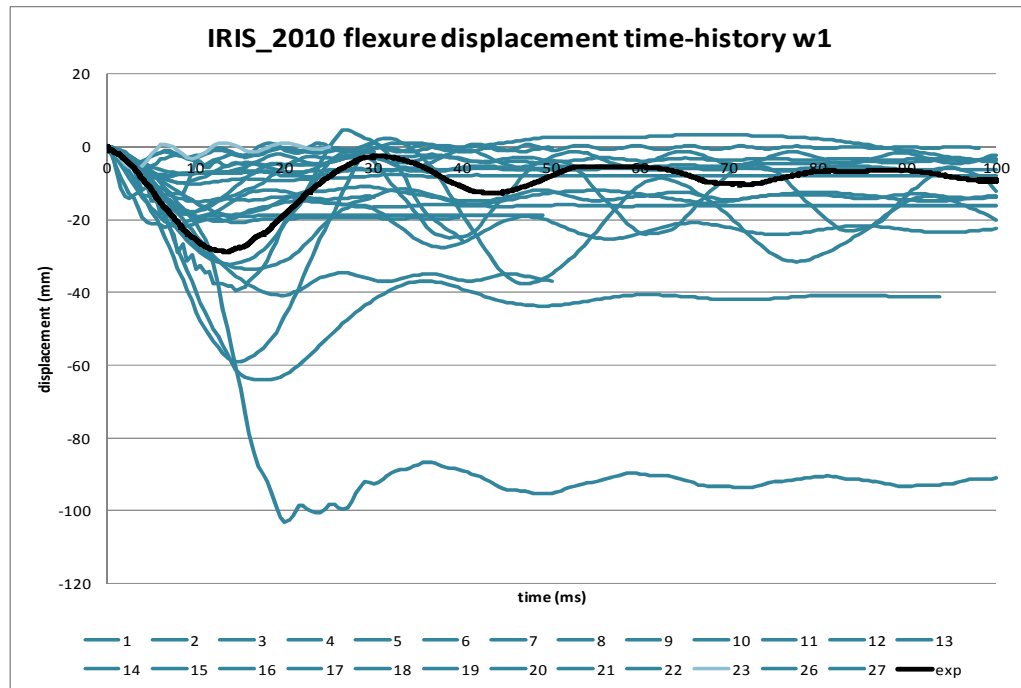


Figure 1-1: Centre displacement history of VTT-B1 (blind simulation results from IRIS_2010).

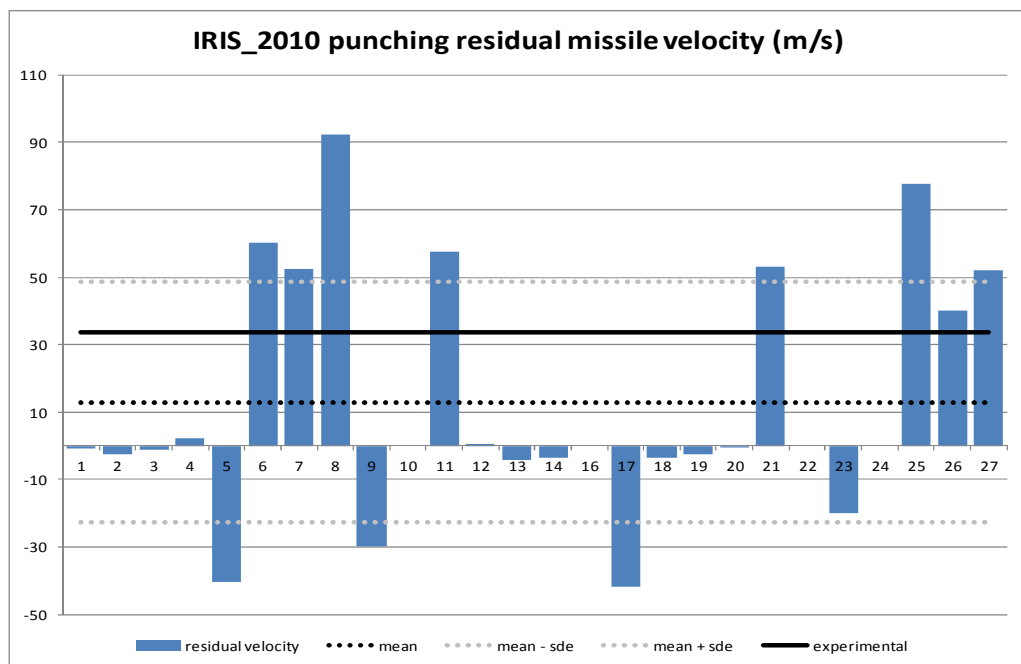


Figure 1-2: VTT-P1 missile residual velocity (blind simulation results from IRIS_2010).

After reviewing the two analysis options discussed above, it is clear that there is a need for an analysis technique that can occupy the middle ground. It would also be useful to have a quick analysis technique more comprehensive than a SDOF analysis that could be used in conjunction with a hydrocode analysis to provide more confidence in the results. In particular, the Canadian Nuclear Safety Commission (CNSC) is interested in developing an analytical tool for nonlinear analysis of concrete structures under impact loading. The VecTor suite of programs may be a good candidate for such a program.

The VecTor programs, developed at the University of Toronto, are a suite of nonlinear finite element analysis programs for reinforced concrete structures. While originally formulated for static and quasi-static loading conditions, they have recently been updated to include dynamic load capabilities. The VecTor programs have demonstrated an ability to accurately model the response of shear-critical structures, while using far fewer degrees of freedom than would be required of a hydrocode. This study is the first step in the possible further development of the VecTor programs as a simplified analysis tool for blast and impact loading. The work done for this study serves to verify the dynamic analysis capabilities of VecTor2 and VecTor3, with respect to blast and impact loading, and to identify areas of deficiency where future research should be focused.

The nuclear power industry is seeking analytical tools that can consider reinforced concrete, prestressed concrete, and steel-concrete composite concrete slabs. As part of this study, both reinforced concrete and prestressed concrete specimens were analyzed; impact loading experiments on steel-concrete composite slabs have not yet been done. In terms of the loading conditions to be considered in the simplified analysis tool, both hard and soft missile impacts, with missile velocities of up to 250 m/s, must be included. The experimental data currently considered in this study had maximum missile velocities of 150 m/s; in future studies, experimental data will need to be taken from the literature to cover the entire impact velocity range. In terms of damage, the simplified program should be able to model damage up to and including perforation of the target. Although perforation cannot be modeled yet in the VecTor programs, the analysis results are discussed in terms of peak displacements and response type.

First, the results of 2D verification studies performed for VecTor2 will be discussed. The specimens considered included shock-tube tested slabs where the applied impulse was fairly well

known. Secondly, the results of modeling impact specimens in VecTor2 and VecTor3 will be discussed. The experimental data used for modeling these specimens were provided by the Canadian Nuclear Safety Commission as part of IRIS_2012, Improving Robustness Assessment Methodologies for Structures Impacted by Missiles, a workshop on the modeling of concrete structures under missile impacts held in Ottawa in October 2012. This workshop was a follow-up to IRIS_2010.

2 Literature Review

2.1 Experimental Studies

2.1.1 Impulsive Loading

Numerous experimental studies have been carried out using shock tubes, where a uniform blast pressure is applied to a specimen at the end of the tube, simulating a far-off blast. At the University of Texas, Williamson recently carried out shock tube tests on prestressed concrete panels. Two prestressed panels, one pre-tensioned and one post-tensioned, were simultaneously tested, and were subjected to three consecutive blasts of increasing intensity. The goal of these tests was to investigate the inelastic deformation of panels under blast loads (Dunkman et al., 2009). Saatcioglu, at the University of Ottawa, examined the performance of FRP sheets on reinforced concrete panels under blast loading conditions in a shock tube. In one particular experimental investigation, thirteen reinforced concrete wall and slab specimens, some retrofitted with FRP sheets, were tested under blast loading conditions. Although there were some issues with debonding failure, results indicated that externally bonded FRP retrofits are an effective way to increase blast resistance (Jacques, 2011). Specimens from these two investigations were used for the verification of VecTor2 impulse loading capabilities. Tests have also been carried out at the U.S. Army Engineer Research and Development Center (ERDC) to investigate the performance of both high strength concrete and vanadium micro-alloyed high strength steel under blast loading conditions (Robert and Johnson, 2009). Tests of both doubly and singly reinforced panels were carried out, and the singly reinforced specimens were included in a blind prediction competition. VecTor2 analyses were performed for both sets of specimens.

2.1.2 Impact Loading

2.1.2.1 Scope of Review

A survey of the literature shows a number of experimental studies have been performed consisting of low-mass high-velocity impacts on reinforced concrete targets. The majority of these tests focused on hard missile impacts, where the damage to the reinforced concrete target was localized and included scabbing, penetration, and perforation. The tests carried out at the Technical Research Centre of Finland (VTT) (Vepsä, 2010a & b), which were used as benchmark tests in IRIS_2010, provide additional hard missile impact data as well as results for

a soft missile impact. In a soft missile impact, there is more of a global flexural response of the target, and the missile typically buckles or is crushed.

The experimental studies summarized in this section include impacts of up to 250 m/s, commonly regarded as the maximum impact velocity that can be modeled with a simplified analytical procedure. For the most part, the studies discussed described damage in terms of scabbing, penetration, and perforation. In some cases, depth of penetration, residual velocity, and maximum target displacement were also reported.

2.1.2.2 Experimental Studies

In 1977, Fiquet and Dacquet (1977) carried out perforation tests on concrete slabs 5 m long by 5 m wide, with thicknesses of 400 mm and 500 mm. Missile weights were within a range of 160 kg to 227 kg, and the heaviest missiles were 305 mm in diameter and 1030 mm long. Five missiles were fired at each slab, with one fired at the centre and the remainder being aimed at the corners of the slab, for a total of 25 shots. The projectiles were shot at the concrete slabs with increasing speed, ranging between 77 m/s and 160 m/s. In terms of experimental results, the impact speeds and penetration depths were reported and photos of damage were also presented. Examples of damage are shown in Figure 2-1.

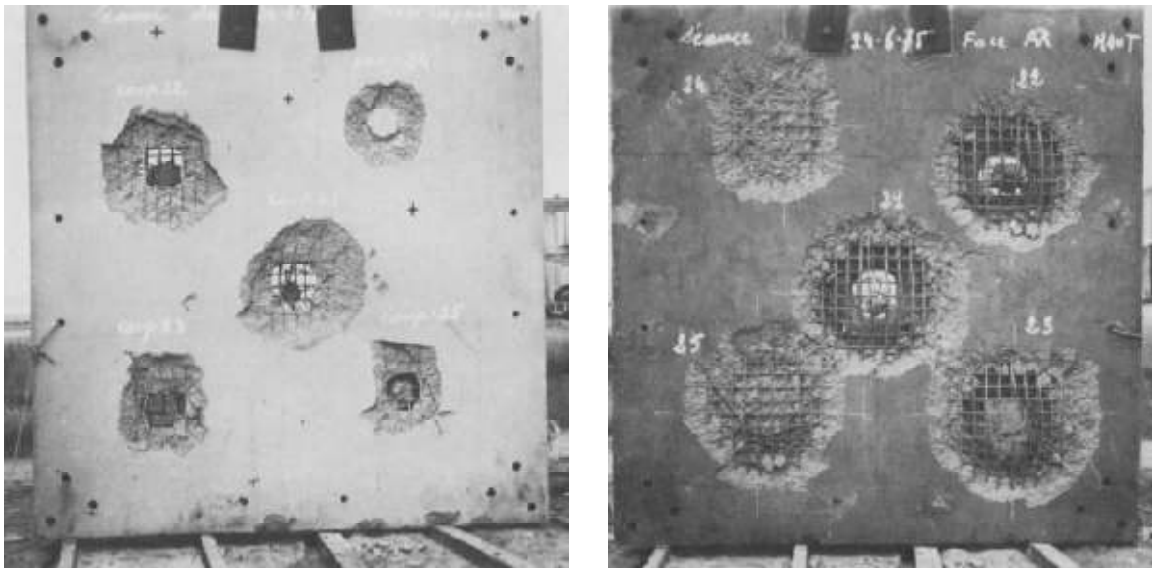


**Figure 2-1: Damage to slab (Fiquet and Dacquet, 1977)
[front face (left); back face (right)].**

Also in 1977, Goldstein et al. (1977) carried out experimental work studying the perforation of reinforced concrete slabs by rigid projectiles. One-fifth scale concrete slabs were subjected to projectile impacts of 100 m/s to 150 m/s, with projectile masses ranging from 30 kg to 120 kg. A total of 18 slabs were tested, and the reported results included impact and residual velocities.

One of the most well-known series of impact tests on reinforced concrete slabs is the Meppen slab test series, carried out in Meppen, Germany from 1979-1982 (Nachtsheim and Stangenberg, 1982). Impacts from this test series have been analysed numerous times, and have been used in verification studies as well. The test series consisted of highly deformable projectiles impacting reinforced concrete slabs. The projectile masses were approximately 1000 kg, and were launched at the reinforced concrete slabs with velocities in the range of 220 m/s to 250 m/s. Three different slab thicknesses were utilized, and many different combinations of longitudinal and shear reinforcement were used.

Another large test series examining local damage of reinforced concrete structures by the impact of deformable missiles was carried out by Muto et al. (1989a). The experimental program consisted of small-, intermediate-, and full-scale impact tests. The impact velocity varied in the small-scale and intermediate-scale tests, and was kept at a constant 215 m/s in the full-scale impact tests. A total of 44 1.5 m square panels, 60 mm to 350 mm thick, were tested in the small-scale tests. The design compressive strength of the concrete was approximately 23.5 MPa, and different reinforcement ratios were used. Impact velocities were 100 m/s, 150 m/s, and 215 m/s, for missiles with a mass of 3.6 kg. The test program and small-scale test results are presented in Muto et al. (1989a). For each test, the extent of damage was reported in terms of perforation, scabbing, and penetration. For the intermediate-scale series, a total of 33 panels were tested. The panels were 2.5 x 2.5 m with thicknesses ranging from 300 mm to 600 mm and different reinforcement ratios were used once again. The missiles in the intermediate scale tests were 100 kg, and were fired at the reinforced concrete panels at velocities of 100 m/s to 250 m/s (Esashi et al., 1989). Perforation and scabbing thicknesses from the impact tests were compared to predictions from empirical equations. Photos of impact damage, see Figure 2-2, were also used to qualitatively compare the influence of the reinforcement ratio and shear reinforcement. The third test series from Muto et al. (1989b) consisted of six reinforced concrete slabs subjected to impacts from aircraft engines at velocities of 215 m/s. The reinforced concrete panels in this full-scale test series were 7 m square, with thicknesses of 900 mm to 1600 mm. The average

missile weight was 1750 kg. A brief summary, and discussion of the results of all three test series, are presented in Muto et al. (1989c). A more thorough summary of the results of this test series is found in Sugano et al. (1993a). For the small-scale tests, the damage mode, dimensions of the damaged region, and missile damage are reported. The evaluation of test results by Sugano et al. (1993b) is generally the same as the discussion presented by Muto et al. (1989c).

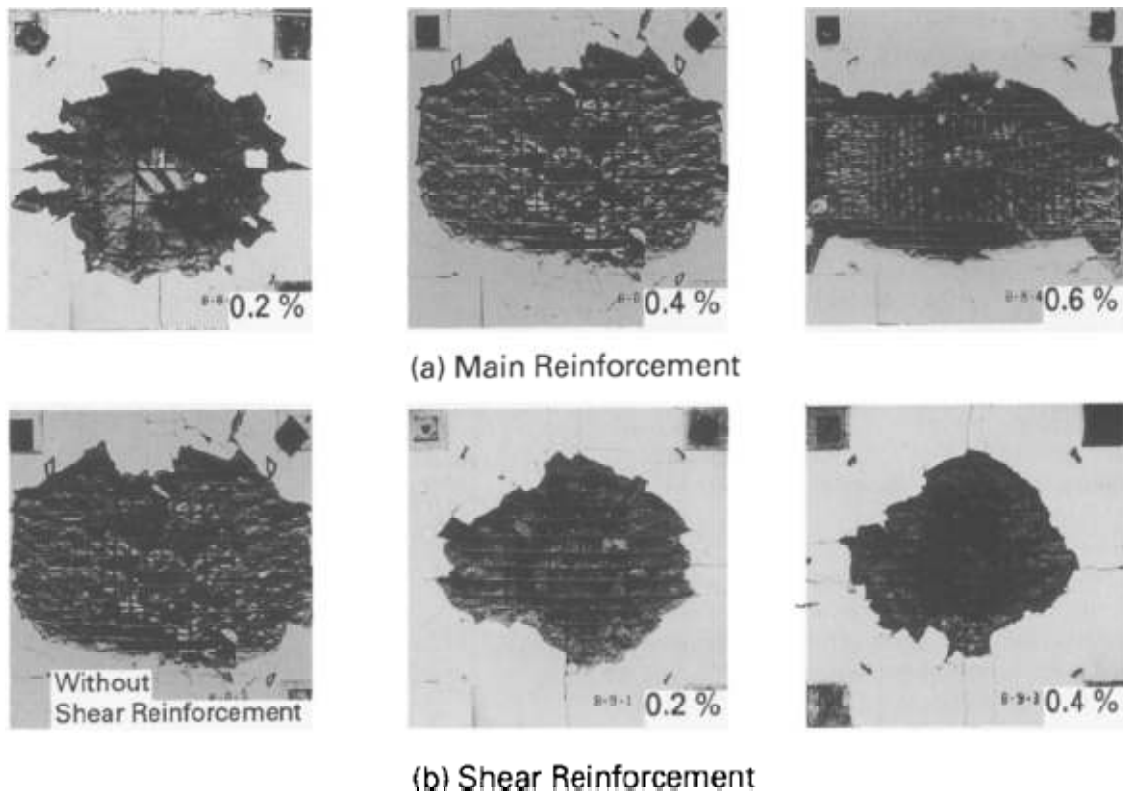


Figure 2-2: Effect of reinforcement ratio and shear reinforcement on panel damage (Sugano et al., 1993b).

Kojima (1991) also carried out an experimental study on the local behaviour of reinforced concrete slabs impacted by missiles, performing 12 impact tests on reinforced concrete targets. Three different reinforced concrete slab types were used in this test series: a singly reinforced concrete slab, a doubly reinforced concrete slab, and a reinforced concrete slab with a steel lining on its rear face. The slabs were 1.2 m square, with thicknesses varying between 60 mm and 240 mm. Both rigid and deformable missiles, each weighing 2 kg and having a design impact velocity of 200 m/s, were used in this series. Results reported include penetration depth, extent of spalling and scabbing, number of rebar ruptured, type of damage sustained, and maximum reaction force.

The investigation carried out by Ohno et al. (1992) is among other experimental studies that have been done examining local damage to reinforced concrete slabs impacted by deformable missiles. Five different types of projectiles were fired with a velocity of 200 m/s at 600 mm square reinforced concrete slabs with thicknesses ranging from 70 mm to 150 mm. One of the focuses of this particular study was the effect of projectile nose shape.

In 1996, Dancygier and Yankelevsky (1996) presented an experimental study looking at the response of high strength concrete to hard projectile impacts. Both normal and high strength concrete plates, reinforced with different types of reinforcement, were subjected to impacts from hard projectiles. The projectile mass was 120 g, and impact velocities were in the range of 85 m/s to 230 m/s. A total of 21 400 x 400 mm concrete plates, 40 mm to 60 mm thick, were tested. The regular strength concrete specimens had an average compressive strength of 35 MPa, while the high strength specimens had an average compressive strength of 100 MPa. Alongside the results of the experimental investigation, comparisons to analytical predictions were also presented for penetration depth, scabbing, and perforation. The effects of concrete strength and reinforcement type were also discussed. It was observed that while high strength concrete contributed to a greater resistance against impacts, it made the response more brittle. It was also observed that steel fibers decreased the brittleness of the high strength concrete, and reduced punching on the impact face of the target. Dancygier (1997) also examined the effect of the reinforcement ratio on the response of reinforced concrete slabs to hard impacts.

In 2007, Dancygier and Yankelevsky published a subsequent study on the response of high performance concrete plates to non-deformable projectile impact (Dancygier et al., 2007). This

test series was a follow-up to the earlier series of small-scale tests (Dancygier and Yankelevsky, 1996) outlined above. In this test series, impact tests were performed on 800 x 800 x 200 mm reinforced concrete plates. Projectiles weighing 1.5 kg were used, with impact velocities reaching 315 m/s. Different high strength concrete mixes were used to determine their effect on concrete impact response, and results were compared to 30 MPa control specimens. Within this test series, there were five tests where the impact velocity was within 250 m/s.

More recently, Tai (2009) carried out an experimental investigation of the resistance of ultra-high strength concrete targets, with and without steel fibers, to high-velocity impacts. The 240 x 240 x 50 mm targets were impacted by flat-ended projectiles weighing 297 g, with impact velocities in the range of 27 m/s to 104 m/s. It was found that the high performance concrete plates were much more brittle than regular reinforced concrete targets, but that the brittleness could be decreased by adding steel fibers (Tai, 2009).

2.2 Numerical Modeling of Blast and Impact Loading

2.2.1 Analysis Types

For the modeling of structures under blast loading conditions, a coupled or uncoupled analysis can be used. An uncoupled analysis consists of determining the loads resulting from a particular blast and then applying them to the structure using nodal loads or a pressure-time history. This can be done in LS-DYNA, AUTODYN, and VecTor2 and VecTor3. The SDOF analysis method is also a common uncoupled technique. A coupled analysis considers blast wave propagation and structural response simultaneously, and can be carried out in ABAQUS, AUTODYN, and LS-DYNA.

For the modeling of impact loading, SDOF analyses are not particularly useful. For hard impacts in particular, damage typically includes scabbing, spalling, penetration, and perforation damage modes which cannot be captured by SDOF models. While there are numerous empirical formulae available to provide estimates of penetration depth or perforation, these have limited accuracy and oversimplify the structure and loading. In general, finite element methods must be used for impact problems. As with impulsive/blast loading, LS-DYNA and ABAQUS are two programs that are often used.

2.2.1.1 Riera Method

In uncoupled analyses, the load function is usually determined in one of two ways. The first approach to determine the load is to carry out an impact analysis of the missile on a hard surface, determine the impact force, and apply it to the model using nodal loads. The second approach is to use the Riera method (1968), originally developed as a simplified procedure to determine the impact force of an aircraft on a nuclear facility. Figure 2-3 illustrates a sample load-time profile.

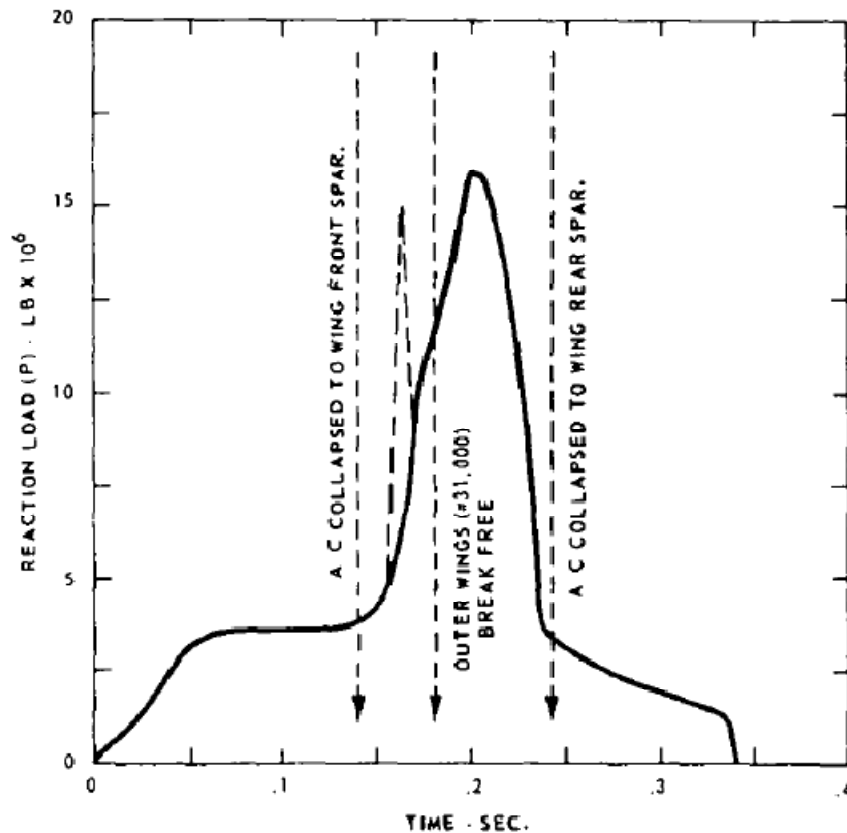


Figure 2-3: Impact load for Boeing 720 using Riera method (Riera, 1968).

The Riera method calculates the force-time relationship for a normal impact of a deformable missile on a hard surface. One of the underlying assumptions of the method is that the deformation of the target is small compared to that of the missile and thus the target can be considered rigid (Riera, 1968).

The total reaction force, $P(t)$, is expressed as:

$$P(t) = P_b[x(t)] + \mu[x(t)]v^2(t) \quad (2-1)$$

where

$x(t) = \int_0^t v(\xi)d\xi$ = the distance from the nose of the aircraft,

$P_b(x)$ = the load required to crush or deform the fuselage (body of the missile),

$\mu(x)$ = the mass of the aircraft/missile per unit length, and

$v(t)$ = the velocity of the uncrushed portion of the aircraft/missile.

For soft cylindrical missiles, the buckling resistance, $P_b(x)$, can be calculated based on the static buckling resistance, P_m , (Jones, 1989):

$$P_b = DIF \cdot P_m \quad (2-2)$$

$$P_m = 2(\pi H)^{3/2} R^{1/2} \sigma_0 (1/3)^{1/4} \quad (2-3)$$

where

DIF = dynamic increase factor,

H = wall tube thickness,

R = tube radius, and

σ_0 = yield strength of tube material.

2.2.2 Constitutive Models

In dynamic analyses there are two additional components of material behavior that must be considered, strain rate effects and local damage. Under high rates of loading, there is an apparent increase in the strength and stiffness of both concrete and steel. In SDOF and other simplified analysis techniques, this strain rate effect is captured using dynamic increase factors (DIFs). In hydrocodes, strain rate effects are typically incorporated into the material constitutive models. The consideration of local damage is also a key part of impact loading analyses. SDOF methods cannot account for local damage. In terms of simplified procedures, empirical formulae are currently the only option. In hydrocodes and finite element procedures, local damage is typically considered through the use of an element erosion criterion. Element erosion is often used to simulate the loss of material that occurs during impact events, but it is also important for being able to continue analyses once an element is severely damaged.

2.2.2.1 Strain Rate Effects: Dynamic Increase Factors

As mentioned above, strain rate effects are accounted for in simplified analysis methods using DIFs. The 1990 CEB formulation (CEB, 1990) for the DIF for concrete is one of the most widely accepted, and captures the following material behaviours: the DIF is higher for lower strength concrete, the DIF is different for tension and compression, and the threshold strain rate is 30 s^{-1} (Malvar and Crawford, 1998). The 2010 *fib* Model Code provides DIF formulations for the concrete modulus of elasticity and strain at maximum stress. However, these formulations are only approximations as little information regarding the effect of high strain rates on the shape of stress-strain diagrams is available (CEB-fib, 2010). For the DIFs for reinforcing steel, provisions are not given in the *fib* Model Code 2010. Formulations can be taken from CEB (1988) or Malvar and Crawford (1998).

In SDOF models, it is important to include DIFs, since the geometry of the specimen is not taken into account and inertial effects are neglected. For finite element analyses, however, it may not be necessary to include the DIF for concrete, as the increase in strength may be accounted for by inertial effects and confinement. The use of a DIF for steel alone may be more appropriate for these types of analyses.

The strain rate formulations included in VecTor2 and VecTor3 are discussed in a later section.

2.2.2.2 Strain Rate Effects: Constitutive Modeling at High Rates of Loading

Incorporating strain rate effects into concrete constitutive models remains a challenge. In complex hydrocodes, some material models have accounted for increases in strength due to dynamic loads through enhancement of the failure surface at higher strain rates. Winnicki et al. (2000) is one of the more recent additions to this area of research, proposing a viscoplastic model for concrete under dynamic loading. State-of-the-art finite element programs also commonly employ the Winfrith model, the cap model by Schwer and Murray, the Riedel-Hiermaier-Thoma (RHT) model, the Johnson-Holmquist-Cook (JHC) model, and the Karagozian and Case (K&C) concrete model (Unosson, 2002). The Winfrith model, employed in LS-DYNA, offers crack formation options with or without accounting for strain rates (Schwer, 2010). The cap model by Schwer and Murray (1994) is a three-invariant smooth cap model which can be fitted to classical failure surfaces or observed experimental results. The RHT model, incorporating hardening, strength loss and stiffness degradation, is strain and stress rate dependent (Riedel et al., 1999). The K&C concrete model was specifically developed to be used in LS-DYNA (DYNA3D) for analyzing structures under blast loading (Malvar et al., 1997).

2.2.2.3 Accounting for Loss of Concrete Material

As mentioned above, finite element programs may account for local damage by using element erosion. A material model has recently been developed for LS-DYNA, Material Model 159, which allows for damage-based softening with erosion and modulus reduction, where damage begins to occur once the peak strain has been reached. Damage values range from 0 to 1, and elements erode when damage exceeds 0.99 and the maximum principal strain exceeds a user-specified value. When an element erodes, it is removed from the calculation from that point onward. A downside to this model is that the erosion strain value affects the computed response; lower erosion values tend to result in a more flexible simulation (FHWA, 2007).

There are also a wide variety of other ways to include element erosion in LS-DYNA and AUTODYN. Luccioni and Aráoz (2011) discuss the various erosion criteria that are available in these programs and that have been used by different researchers. They note that although element erosion is often used to simulate the physical loss of material, it is important to remember that element erosion is actually a numerical technique used to permit computation

extension (Luccioni and Aráoz , 2011). In terms of strain-based criteria, the following criteria are most often used: instantaneous geometric strain, maximum principal strain, and maximum shear strain.

The instantaneous geometric strain (ANSYS, 2009) is calculated as:

$$\varepsilon_{eff} = \frac{2}{3} \sqrt{(\varepsilon_1^2 + \varepsilon_2^2 + \varepsilon_3^2) + 5(\varepsilon_1\varepsilon_2 + \varepsilon_1\varepsilon_3 + \varepsilon_2\varepsilon_3) - 3(\varepsilon_{12}^2 + \varepsilon_{23}^2 + \varepsilon_{13}^2)}$$

Stress-based criteria may also be used. Elements can be eroded based on a maximum/minimum pressure or principal stress.

2.2.3 Numerical Investigations

There have been numerous analytical studies carried out in recent years, many of which were done in conjunction with experimental investigations. Both Dunkman (2009) and Jacques (2011) carried out SDOF analyses to complement their shock tube test programs. The results of those analyses are discussed in comparison to VecTor2 results in Chapter 4.

The numerical investigations discussed below address different analysis techniques, methods for dealing with large displacements, and methods for handling local damage to targets. The basic modeling technique used in each study is summarized, along with the agreement with experimental results.

Schwarzkoopp et al. (1989) were among the first researchers to analyze the Meppen slabs. Schwarzkoopp et al. (1989) presented an algorithm, based on the Finite Difference Method (FDM) and using a layered element approach, for the analysis of missile impacts on concrete structures, including consideration of slab penetration, target stresses, and target and missile deformations. The loading function used in the analysis was derived from an interpolation between a hard and soft impact. The results presented were compared to Meppen results and included missile deformation, maximum target displacement, penetration depth, and load duration. Overall, good agreement was observed.

Magnier and Donze (1998) investigated the response of reinforced concrete beams subjected to impacts from rigid spherical-nose projectiles using the Discrete Element Method (DEM). In the study, normal impacts with rigid missiles were represented with 2D models, and the analyses captured concrete crushing and fracturing, as well as spalling, scabbing, penetration, and perforation. Comparisons were made between the numerical results and experimental data from tests performed by the Commissariat à l'Énergie Atomique and Électricité de France (CEA-EDF), and there was good agreement between the two. Shown in Figure 2-4 are the results of two simulations, both of which consisted of impacts with 50 kg non-deformable missiles at an initial velocity of 300 m/s.

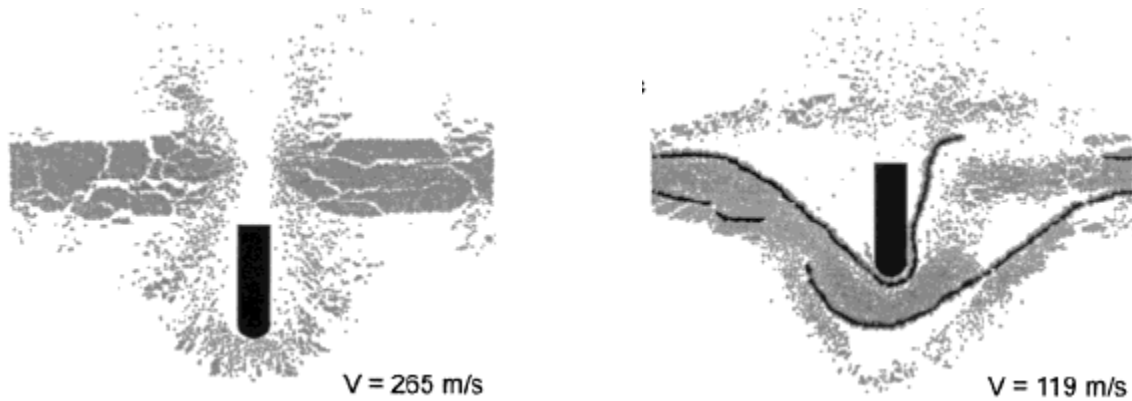


Figure 2-4: Modeling of impacts on plain (left) and reinforced concrete targets (right) (Magnier and Donze, 1998).

Riera and Iturrioz (1998) also applied the Discrete Element Method to the analysis of reinforced concrete plates subjected to impacts and impulsive loading. The method developed allowed for the consideration of larger displacements by updating nodal coordinates at each time integration step. In addition, concrete fracture was assumed to occur when a critical strain value was reached, with the concrete failing in the direction of the principal tensile strain. The model was validated through an analysis of one of the Meppen slabs.

Sawamoto et al. (1998) also carried out an analytical study on the local damage of reinforced concrete structures under impact loading using the Discrete Element Method. The Mohr-Coulomb model with tension cut-off was used for concrete failure, allowing for shear, compressive, and tensile failures to occur. The model was used to simulate the impact tests carried out by Sugano et al. (1993); Figure 2-5 illustrates the results of one of the analyses. Comparison to experimental data confirmed the suitability of the material constants, failure criteria, and dynamic strength increase factors. The comparison to the Sugano experiments also yielded good results. Damage to the reinforced concrete panels was modeled with a satisfactory degree of accuracy.

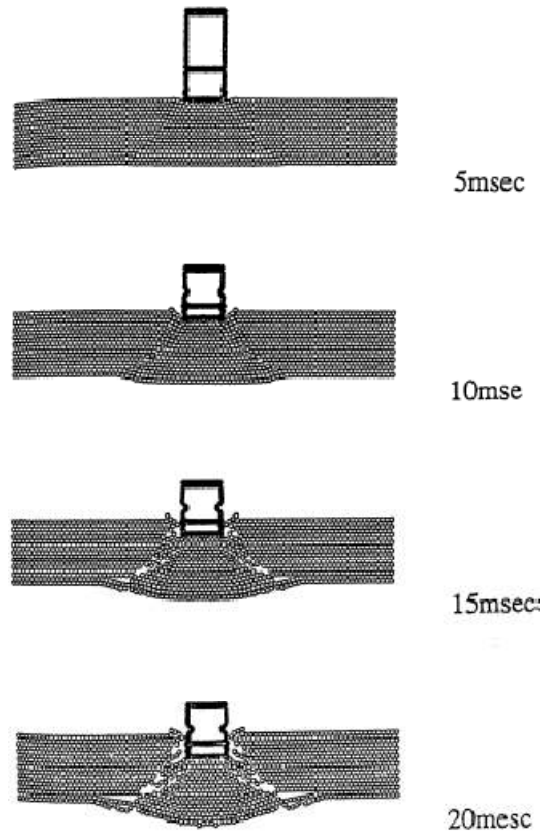


Figure 2-5: DEM modeling of full-scale GE-J79 engine impact on RC target (Sawamoto et al., 1998).

Much of the more recent research has focused on the use of complex hydrocodes in the analysis of reinforced concrete structures under high-velocity impacts. Another analytical study done using the Sugano (1993) experimental data was the work carried out by Itoh et al. (2000) using AUTODYN. Itoh et al. (2000) presented a new constitutive and failure model for concrete, an extension of the Dynamic Drucker-Prager CAP Model in AUTODYN, tailored to impact modeling. The authors incorporated a maximum yield stress in compression, as well as strain rate effects. In the simulations of the Sugano experiments, AUTODYN-2D, a two-dimensional coupled hydrocode based on the explicit finite difference method, was used, and the targets were modeled axisymmetrically. Although the targets were actually square, a circular target with an equivalent area was used in these analyses. The results of the analyses were compared to experimental results, and examples of the models used are illustrated in Figure 2-6; twenty simulations in total were carried out. Reasonable agreement with the experimental results was obtained.

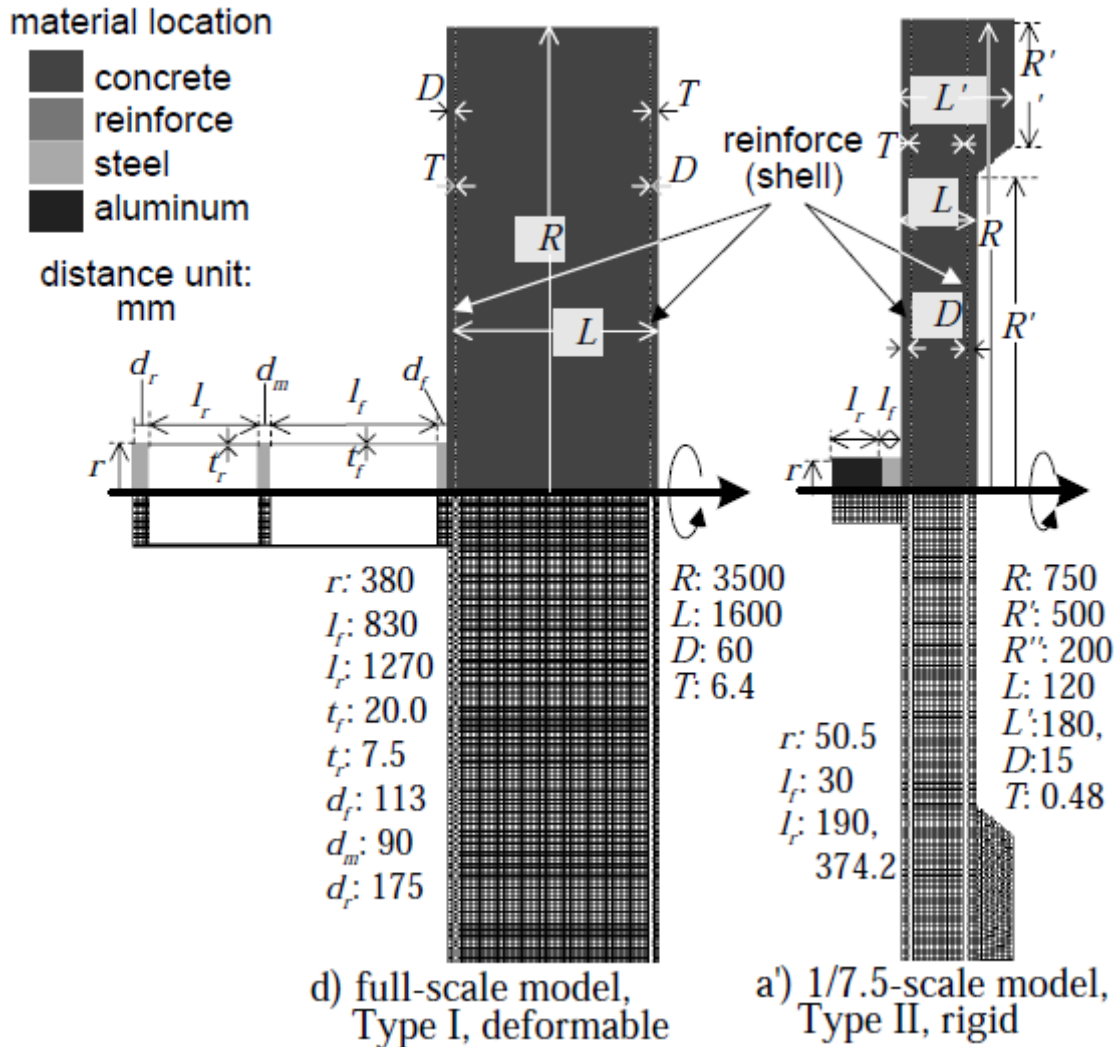


Figure 2-6: Axisymmetric models (Itoh et al., 2000).

Teng et al. (2005) investigated normal and oblique impacts of ogive-nose steel projectiles on reinforced concrete slabs using DYNA-2D. Analytical results were compared to experimental data from Hanchak et al. (1992), and the residual velocities obtained numerically agreed well with the experimental data. After verifying the model, the ballistic limits of reinforced concrete slabs were investigated numerically. Slabs with thicknesses of 600 mm, 700 mm, and 800 mm were analyzed with projectile impacts ranging from 50 m/s to 240 m/s, and the residual velocities were noted. Oblique impacts were also analyzed.

In 2007, Zinn et al. (2007) analysed the Meppen tests (Riech, H and Rüdiger, E., 1984) using two finite element programs, ADINA and SOFiSTiK, achieving good agreement with experimental results. The models used in SOFiSTiK and ADINA are shown in Figure 2-7. SOFiSTiK is based on a layered concrete model using shell elements, while ADINA models concrete using volume elements with reinforcing steel modeled by truss elements. In SOFiSTiK, non-linear effects are calculated through an iterative procedure using a modified Newton method with a constant stiffness matrix, and shear deformations are approximated by including a comparison of element shear stresses to the ultimate shear strength specified by the user. Meppen slabs II/12, II/20, and II/21 were modeled, with the load applied using a load-time function derived from the measured support reaction forces, and the results were compared to the experimental displacements. An acceptable level of accuracy was achieved.

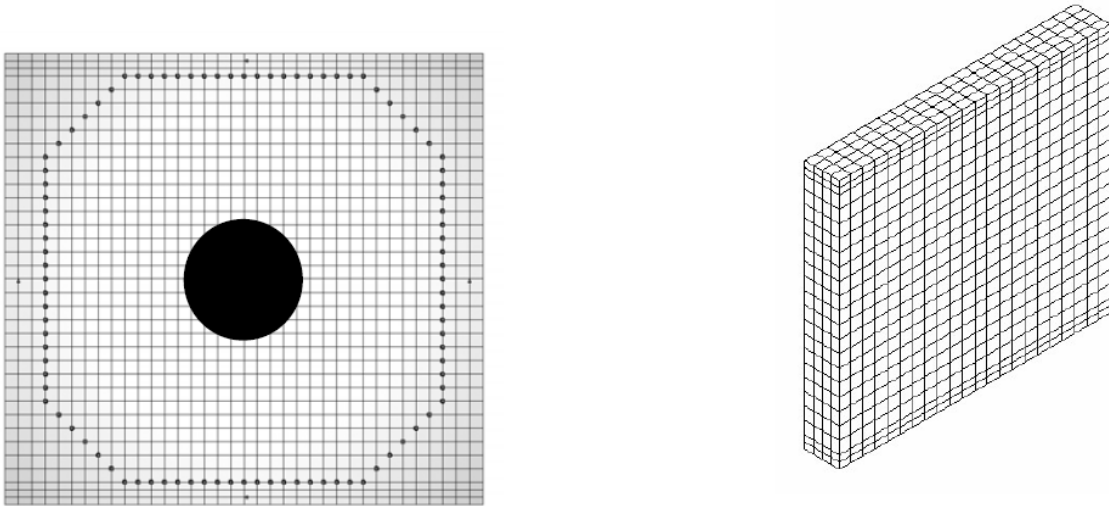


Figure 2-7: SOFiSTiK model (left) and ADINA model (right) (Zinn et al., 2007).

In addition to the experimental study, Tai (2009) performed an analysis of one of the test specimens using LS-DYNA. A quarter of the test specimen was modeled, since the supports and loading were symmetric. In terms of contact modeling, sliding surfaces were used to model the impact of the projectile and concrete target, and the effect of friction was neglected. The dynamic tensile fracture strain was taken as 0.02 for spalling, based on initial parametric analyses. In the analyses, when the principal tensile strain in an element reached 0.02, erosion occurred. Reasonably good agreement with experimental data was obtained in the analyses (Tai, 2009). A comparison of experimental and analytical results is shown in Figure 2-8.

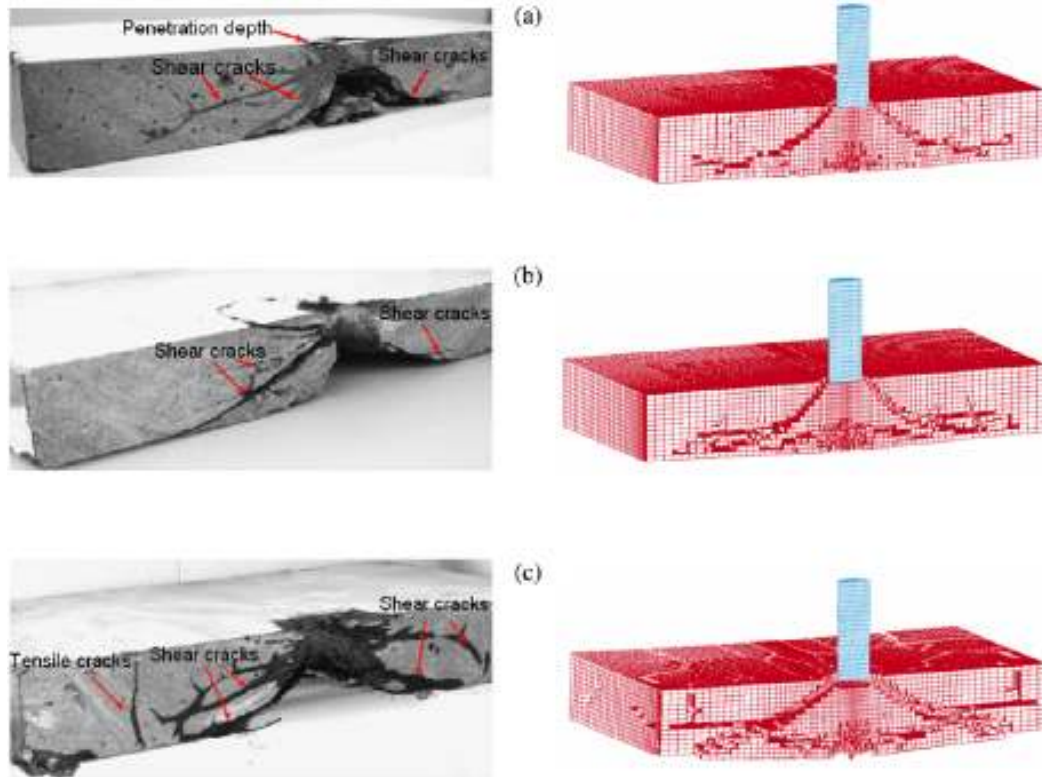


Figure 2-8: Comparison of experimental and analytical impact results (Tai, 2009).

Finally, the two VTT Technical Research Centre of Finland specimens introduced in Section 2.1.2.1 were part of the two IRIS workshops. For the first workshop, IRIS_2010, the specimens were used for a blind prediction exercise, with 28 teams submitting results. The simulation results, and the workshop conclusions and recommendations, can be found in (NEA, 2011). For IRIS_2012, predictions submitted for IRIS_2010 were updated and sensitivity studies were performed. The VecTor modeling of these specimens will be discussed further in Chapter 5.

3 VecTor2 Methodology

3.1 Introduction

VecTor2 is a two-dimensional finite element program for the analysis of reinforced concrete membrane structures under static and dynamic loading, formulated initially based on the Modified Compression Field Theory (MCFT) and later updated to include the Disturbed Stress Field Model (DSFM).

Based on the results of panel tests conducted at the University of Toronto, the MCFT is an analytical model for predicting the load-deformation response of reinforced concrete elements subjected to in-plane shear and normal stresses. The MCFT treats cracked concrete as a unique material, distinct from uncracked concrete, with cracks distributed through the element. Equilibrium, compatibility, and stress-strain equations are formulated in terms of average stresses and average strains. While cracks are smeared through the concrete element, an important feature of the MCFT is the consideration of local stress and strain conditions at crack locations. Details of the MCFT can be found in Vecchio and Collins (1986).

The DSFM was developed to address the deficiencies of the MCFT that have been found to exist under certain loading conditions. For lightly reinforced elements, it was found that the rotation of the principal stress field lagged the principal strain field and that the MCFT overestimates the stiffness of those elements. Conversely, for elements with limited rotation of the stress and strain fields, it has been found that the MCFT underestimates shear strength and stiffness. The DSFM is essentially an extension of the MCFT, which addresses the aforementioned deficiencies. The main development introduced in the DSFM is the decoupling of the orientations of the principal strain and principal stress fields. The DSFM also augments the compatibility relationships of the MCFT to include crack shear slip deformations, eliminating the crack shear check. A detailed description of the DSFM can be found in Vecchio (2000).

3.2 Stiffness Formulation

This section outlines the stiffness matrix formulation used in VecTor2, for the coordinate reference system shown in Figure 3-1.

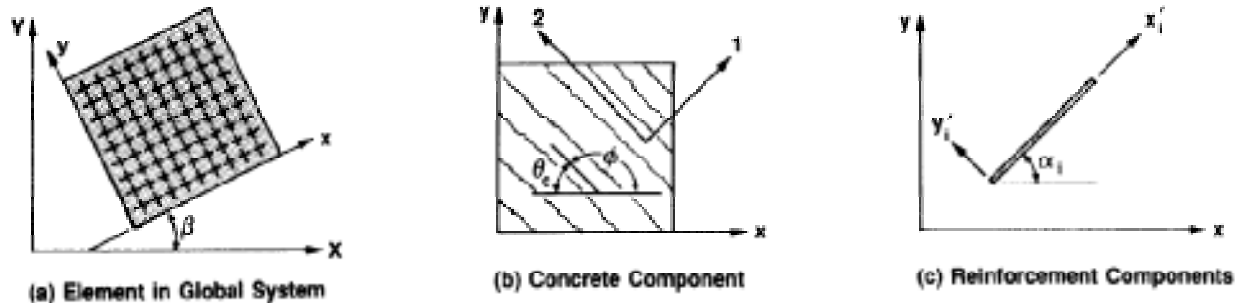


Figure 3-1: VecTor2 coordinate reference systems (Vecchio, 1990).

For any element in the model, the stress state in the element is determined as follows:

$$[\sigma] = [D][\varepsilon] \quad (3-1)$$

where the material stiffness matrix $[D]$ is calculated as:

$$[D] = [D_c] + \sum_{i=1}^n [D_s]_i \quad (3-2)$$

where

$$[D_c]' = \begin{bmatrix} \overline{E_{c1}} & 0 & 0 \\ 0 & \overline{E_{c2}} & 0 \\ 0 & 0 & \overline{G_c} \end{bmatrix} \quad (3-3)$$

$$\overline{E_{c1}} = \frac{f_{c1}}{\varepsilon_{c1}}; \overline{E_{c2}} = \frac{f_{c2}}{\varepsilon_{c2}}; \overline{G_c} = \frac{\overline{E_{c1}} \cdot \overline{E_{c2}}}{\overline{E_{c1}} + \overline{E_{c2}}} \quad (3-4)$$

$$[D_s]'_i = \begin{bmatrix} \rho_i \overline{E_{si}} & 0 & 0 \\ 0 & 0 & 0 \\ 0 & 0 & 0 \end{bmatrix} \quad (3-5)$$

$$\overline{E_{si}} = \frac{f_{si}}{\varepsilon_{si}} \quad (3-6)$$

and

$$[D_c] = [T_c]^T [D_c]' [T_c] \text{ for concrete} \quad (3-7)$$

$$[D_s]_i = [T_s]^T [D_s]'_i [T_s] \text{ for steel} \quad (3-8)$$

$$[T] = \begin{bmatrix} \cos^2 \psi & \sin^2 \psi & \cos \psi \sin \psi \\ \sin^2 \psi & \cos^2 \psi & -\cos \psi \sin \psi \\ -2 \cos \psi \sin \psi & 2 \cos \psi \sin \psi & \cos^2 \psi - \sin^2 \psi \end{bmatrix} \quad (3-9)$$

In the calculation of the transformation matrix [T]:

$$\psi = \phi + \beta = 180 - \theta_c + \beta \text{ for concrete, and}$$

$$\psi = \alpha_i + \beta \text{ for reinforcement.}$$

Once the material stiffness matrix is determined, the element stiffness matrix [k] can be calculated as:

$$[k] = \int_{vol} [B]^T [D] [B] dV \quad (3-10)$$

where [B] changes depending on the assumed element displacement functions. VecTor2 offers triangular, rectangular and quadrilateral elements. Triangular and rectangular elements are most commonly used, and these plane stress elements assume linear displacement functions.

The finer details of the VecTor2 methodology can be found in the FormWorks manual (Wong et al., 2012).

3.3 Dynamic Analysis Formulation in VecTor2

VecTor2 was originally developed for static loading conditions, with additional subroutines added by Saatci (2007) to allow dynamic loading conditions to be considered. For dynamic analyses, Rayleigh Damping and a dynamic analysis algorithm based on Newmark's Method of Direct Integration are used.

3.3.1 Rayleigh Damping

Rayleigh damping is not meant to be the main source of damping in a VecTor2 dynamic analysis. The majority of damping should occur through the material hysteresis, concrete cracking, and other mechanisms. Rayleigh damping is used mainly to ensure the stability of the solution. The two damping coefficients are calculated as follows.

$$a_1 = \frac{2\xi_j\omega_j - 2\xi_i\omega_i}{\omega_j^2 - \omega_i^2} \quad (3-11)$$

$$a_0 = 2\xi_i\omega_i - a_1\omega_i^2 \quad (3-12)$$

3.3.2 Newmark Method of Direct Integration

As mentioned previously, the dynamic analysis formulation in VecTor2 is based on Newmark's Direct Integration method, which was modified to be compatible with the secant stiffness formulations of VecTor2. The following equation is the main equation used in dynamic analyses in VecTor2.

$$\left[k_{i+1} + \frac{1+\gamma\Delta t a_0}{\beta\Delta t^2} m + \frac{\gamma\Delta t a_1}{\beta\Delta t^2} k_0 \right] u_{i+1} = p_0 + p_{i+1} + \left[\frac{1+\gamma\Delta t a_0}{\beta} m + \frac{\gamma\Delta t a_1}{\beta} k_0 \right] \left\{ \frac{u_i}{\Delta t^2} + \frac{\dot{u}_i}{\Delta t} + \frac{\ddot{u}_i}{2} \right\} - [a_0 m + a_1 k_0] \{ \dot{u}_i + \Delta t \ddot{u}_i \} - m \ddot{u}_i \quad (3-13)$$

There are only two unknowns in Equation 3-12, $[k_{i+1}]$ and $[u_{i+1}]$, both of which can be solved through an iterative procedure, summarized in Figure 3-2 below. Details of the dynamic analysis procedure can be found in Saatci (2007).

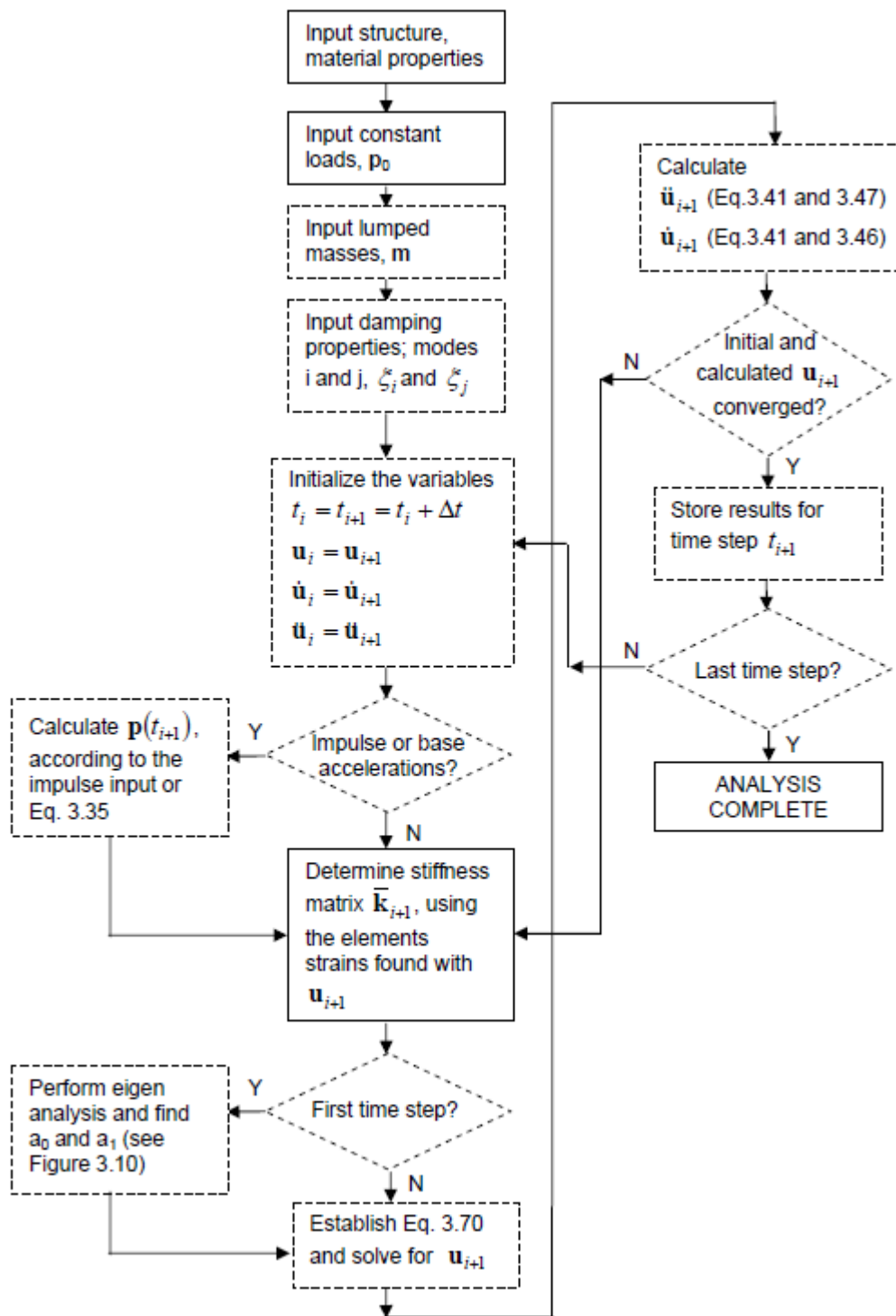


Figure 3-2: Flowchart for dynamic analyses in VecTor2 (Saatci, 2007).

3.3.3 Strain Rate Effects in VecTor2

Strain rate effects are implemented in VecTor2 using dynamic increase factors (DIFs). DIFs are available for the yield and ultimate stresses of steel as well as the compressive strength, tensile strength, strain at peak stress, and modulus of concrete. The initial implementation of strain rate effects had two options, the consideration of strain rate effects for both steel and concrete or for neither material (Ho, 2004). Recently, the strain rate effects formulations have been updated, and the user now has the option of considering strain rate effects for one, both, or neither material. Updated formulations for DIFs have also been added, and are discussed in this section.

For concrete strain rate effects, the two formulations available in VecTor2 are the fib MC 2010 and fib MC 1990 formulations. For steel, the Malvar-Crawford and CEB-FIP 1988 formulations are included. There are nine different strain rate effects options included in VecTor2; Table 3-1 summarizes these options.

Table 3-1: Strain Rate Effects Formulations in VecTor2

Concrete	Steel
Not Considered	Not Considered
Not Considered	Malvar-Crawford
Not Considered	CEB-FIP 1988
fib MC 2010	Not Considered
fib MC 2010	Malvar-Crawford
fib MC 2010	CEB-FIP 1988
fib MC 1990	Not Considered
fib MC 1990	Malvar-Crawford
fib MC 1990	CEB-FIP 1988

When strain rate effects are not considered, DIFs are taken as 1.0 for all material properties.

fib MC 2010

For concrete in compression, the fib MC 2010 formulations (CEB, 2010) are valid for $30 \times 10^{-6} s^{-1} < |\dot{\epsilon}_c| < 3 \times 10^2 s^{-1}$; in tension, the range of strain rate applicability is $1 \times 10^{-6} s^{-1} < \dot{\epsilon}_{ct} < 3 \times 10^2 s^{-1}$. The DIF are plotted in Figure 3-3 and Figure 3-4.

Compressive strength:

$$f_{c,imp}/f_{cm} = (\dot{\epsilon}_c/\dot{\epsilon}_{c0})^{0.014} \text{ for } \dot{\epsilon}_c \leq 30 \text{ s}^{-1} \quad (3-14)$$

$$f_{c,imp}/f_{cm} = 0.012(\dot{\epsilon}_c/\dot{\epsilon}_{c0})^{1/3} \text{ for } \dot{\epsilon}_c > 30 \text{ s}^{-1} \quad (3-15)$$

where $\dot{\epsilon}_{c0} = 30 \times 10^{-6} \text{ s}^{-1}$.

Tensile strength:

$$f_{ct,imp}/f_{ctm} = (\dot{\epsilon}_{ct}/\dot{\epsilon}_{ct0})^{0.018} \text{ for } \dot{\epsilon}_{ct} \leq 10 \text{ s}^{-1} \quad (3-16)$$

$$f_{ct,imp}/f_{ctm} = 0.0062(\dot{\epsilon}_{ct}/\dot{\epsilon}_{ct0})^{1/3} \text{ for } \dot{\epsilon}_{ct} > 10 \text{ s}^{-1} \quad (3-17)$$

where $\dot{\epsilon}_{ct0} = 1 \times 10^{-6} \text{ s}^{-1}$.

Modulus of Elasticity:

$$E_{c,imp}/E_{ct} = (\dot{\epsilon}_c/\dot{\epsilon}_{c0})^{0.026} \quad (3-18)$$

where $\dot{\epsilon}_{c0} = 30 \times 10^{-6} \text{ s}^{-1}$ for concrete in compression, and $\dot{\epsilon}_{ct0} = 1 \times 10^{-6} \text{ s}^{-1}$ in tension.

Peak strain:

$$\epsilon_{c1,imp}/\epsilon_{c1} = (\dot{\epsilon}_c/\dot{\epsilon}_{c0})^{0.02} \quad (3-19)$$

where $\dot{\epsilon}_{c0} = 30 \times 10^{-6} \text{ s}^{-1}$ for concrete in compression, and $\dot{\epsilon}_{ct0} = 1 \times 10^{-6} \text{ s}^{-1}$ in tension.

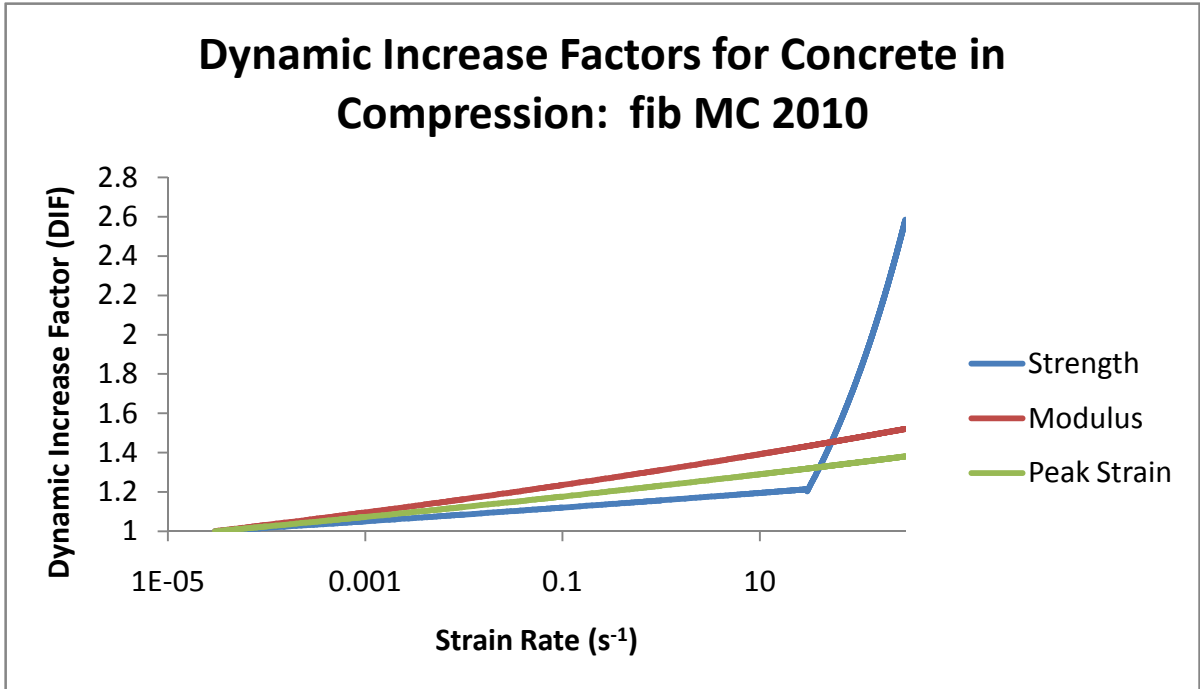


Figure 3-3: DIFs for concrete in compression: fib MC 2010.

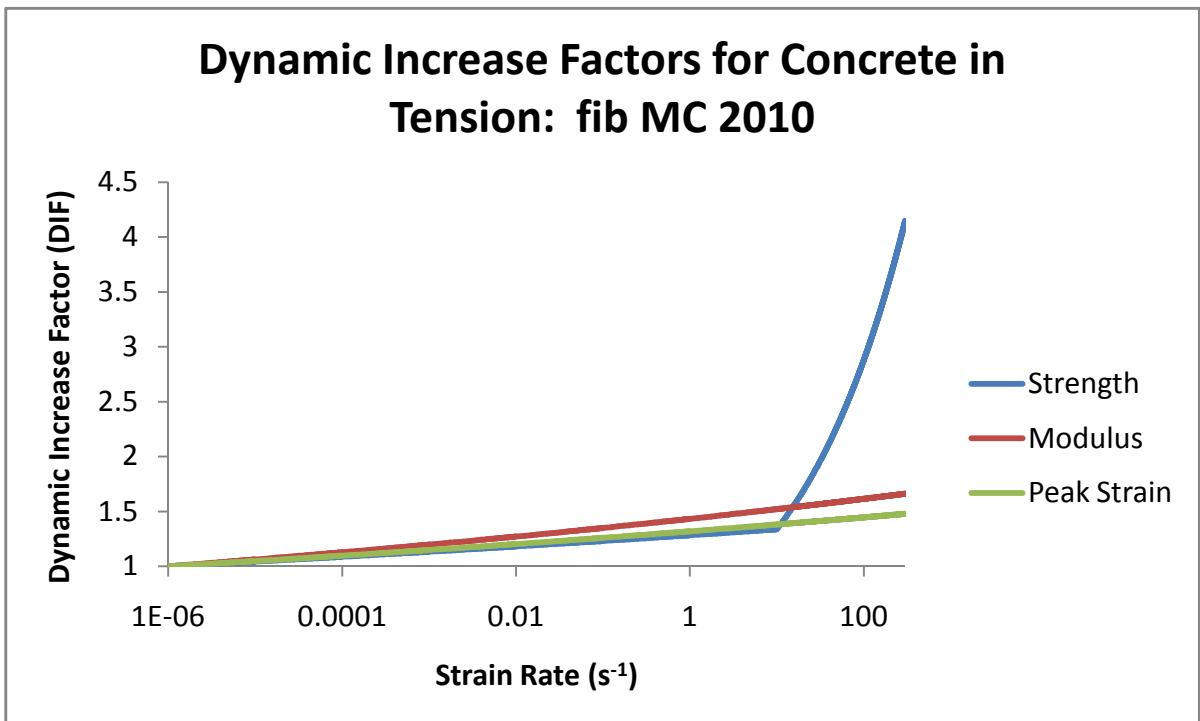


Figure 3-4: DIFs for concrete in tension: fib MC 2010.

fib MC 1990

For concrete in compression, the fib MC 1990 (CEB, 1990) formulations are valid for $30 \times 10^{-6} \text{ s}^{-1} < |\dot{\epsilon}_c| < 3 \times 10^2 \text{ s}^{-1}$; in tension, the strain rate formulations are valid for the strain rate range of $3 \times 10^{-6} \text{ s}^{-1} < \dot{\epsilon}_{ct} < 3 \times 10^2 \text{ s}^{-1}$. The DIFs are illustrated in Figure 3-5 and Figure 3-6.

Compressive strength:

$$f_{c,imp}/f_{cm} = (\dot{\epsilon}_c/\dot{\epsilon}_{c0})^{1.026\alpha_s} \text{ for } |\dot{\epsilon}_c| \leq 30 \text{ s}^{-1} \quad (3-20)$$

$$f_{c,imp}/f_{cm} = \gamma_s(\dot{\epsilon}_c/\dot{\epsilon}_{c0})^{1/3} \text{ for } |\dot{\epsilon}_c| > 30 \text{ s}^{-1} \quad (3-21)$$

$$\alpha_s = \frac{1}{5+9(f_{cm}/f_{cm0})} \quad (3-22)$$

where $f_{cm0} = 10 \text{ MPa}$, $\log \gamma_s = 6.156\alpha_s - 2$, and $\dot{\epsilon}_{c0} = -30 \times 10^{-6} \text{ s}^{-1}$.

Tensile strength:

$$f_{ct,imp}/f_{ctm} = (\dot{\epsilon}_{ct}/\dot{\epsilon}_{ct0})^{1.016\delta_s} \text{ for } \dot{\epsilon}_{ct} \leq 30 \text{ s}^{-1} \quad (3-23)$$

$$f_{ct,imp}/f_{ctm} = \beta_s(\dot{\epsilon}_{ct}/\dot{\epsilon}_{ct0})^{1/3} \text{ for } \dot{\epsilon}_{ct} > 30 \text{ s}^{-1} \quad (3-24)$$

$$\delta_s = \frac{1}{10+6(f_{cm}/f_{cm0})} \quad (3-25)$$

where $f_{cm0} = 10 \text{ MPa}$, $\log \beta_s = 7.112\delta_s - 2.33$, and $\dot{\epsilon}_{ct0} = 3 \times 10^{-6} \text{ s}^{-1}$.

Modulus of Elasticity:

$$E_{c,imp}/E_{ci} = (\dot{\epsilon}_c/\dot{\epsilon}_{c0})^{0.026} \quad (3-26)$$

where $\dot{\epsilon}_{c0} = -30 \times 10^{-6} \text{ s}^{-1}$ for concrete in compression and $\dot{\epsilon}_{ct0} = 3 \times 10^{-6} \text{ s}^{-1}$ in tension.

Peak strain:

$$\epsilon_{c1,imp}/\epsilon_{c1} = (\dot{\epsilon}_c/\dot{\epsilon}_{c0})^{0.02} \quad (3-27)$$

where $\dot{\epsilon}_{c0} = -30 \times 10^{-6} \text{ s}^{-1}$ for concrete in compression and $\dot{\epsilon}_{ct0} = 3 \times 10^{-6} \text{ s}^{-1}$.

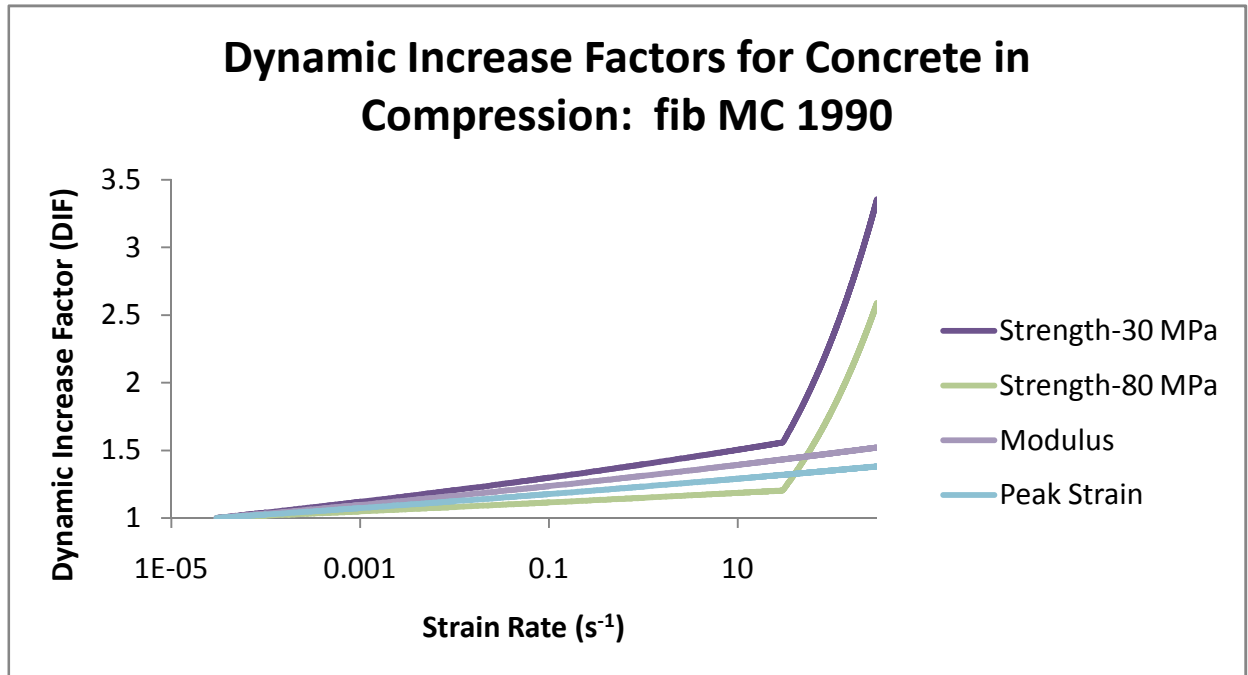


Figure 3-5: DIFs for concrete in compression: fib MC 1990.

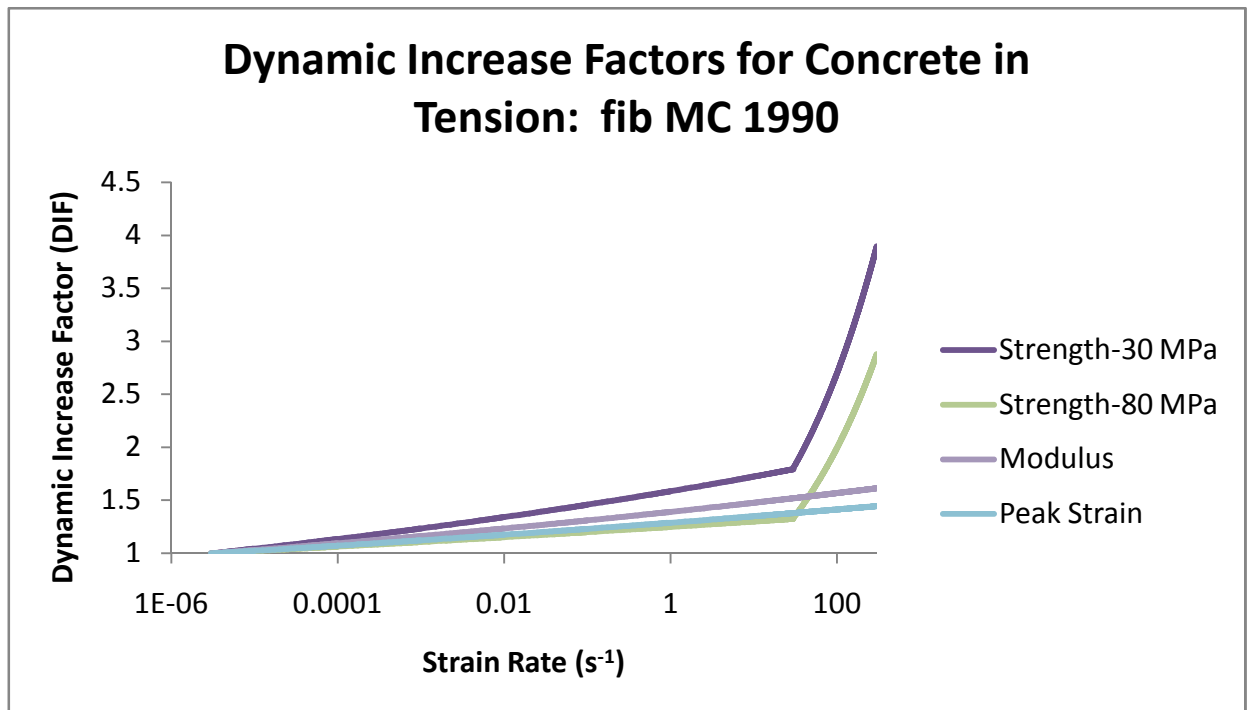


Figure 3-6: DIFs for concrete in tension: fib MC 1990.

Malvar-Crawford

The Malvar-Crawford (1998) strain rate effects formulations for steel are valid for steel bars with yield stresses between 290 MPa and 710 MPa, and for the strain rate range of $10^{-4} \text{ s}^{-1} < \dot{\epsilon}_s < 225 \text{ s}^{-1}$. The DIFs are shown in Figure 3-7.

$$DIF = \left(\frac{\dot{\epsilon}_s}{10^{-4}} \right)^\alpha \quad (3-28)$$

where $\alpha = \alpha_y$ for the yield stress, and $\alpha = \alpha_u$ for ultimate stress.

$$\alpha_y = 0.074 - 0.040 \frac{f_y}{414} \quad (3-29)$$

$$\alpha_u = 0.019 - 0.009 \frac{f_y}{414} \quad (3-30)$$

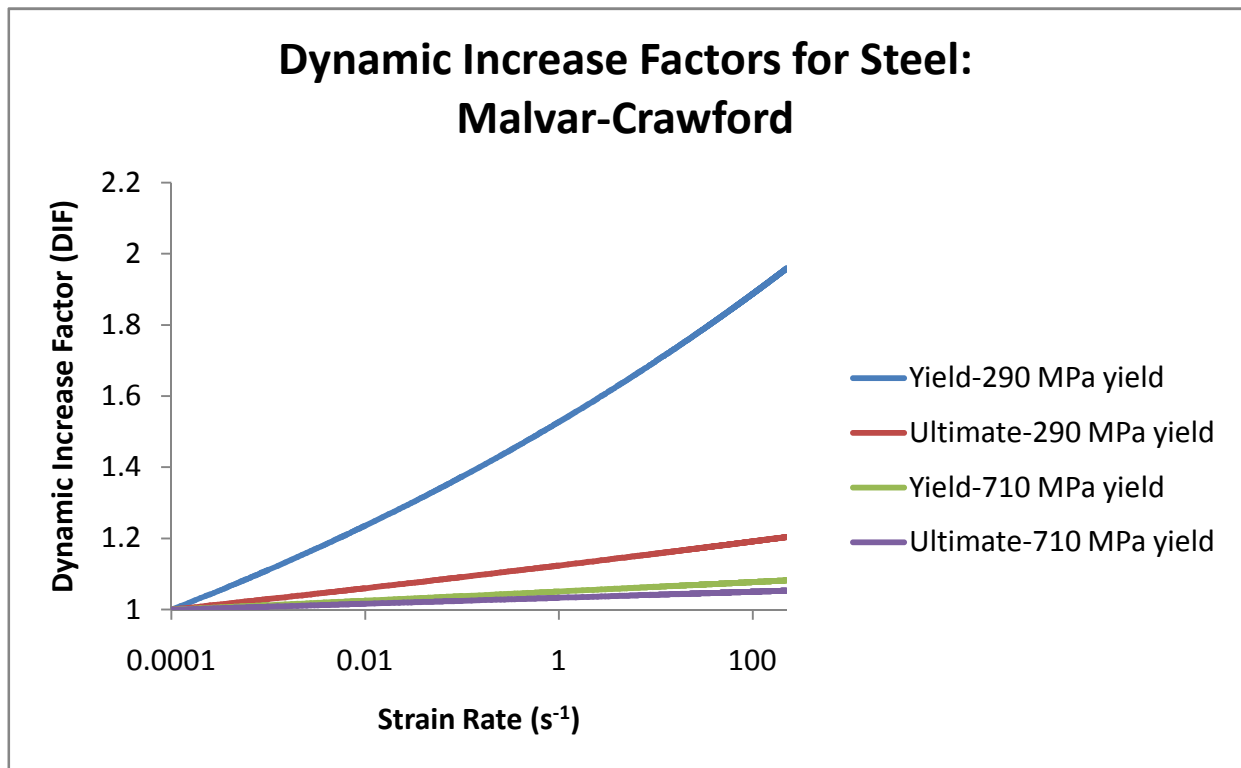


Figure 3-7: DIFs for steel: Malvar-Crawford.

CEB-FIP 1988

The CEB-FIP 1988 (CEB, 1988) formulations for steel are valid for strain rates up to $\dot{\epsilon}_s = 10 \text{ s}^{-1}$. The formulations for yield stress and ultimate stress are shown below, and illustrated in Figure 3-8. For illustration purposes, a sample yield and ultimate stress of 400 MPa and 600 MPa, respectively, were chosen.

$$f_{y,imp}/f_y = 1 + (6/f_y) \cdot \ln(\dot{\epsilon}_s/\dot{\epsilon}_{s0}) \quad (3-31)$$

$$f_{u,imp}/f_u = 1 + (7/f_u) \cdot \ln(\dot{\epsilon}_s/\dot{\epsilon}_{s0}) \quad (3-32)$$

where $\dot{\epsilon}_{s0} = 5 \times 10^{-5} \text{ s}^{-1}$.

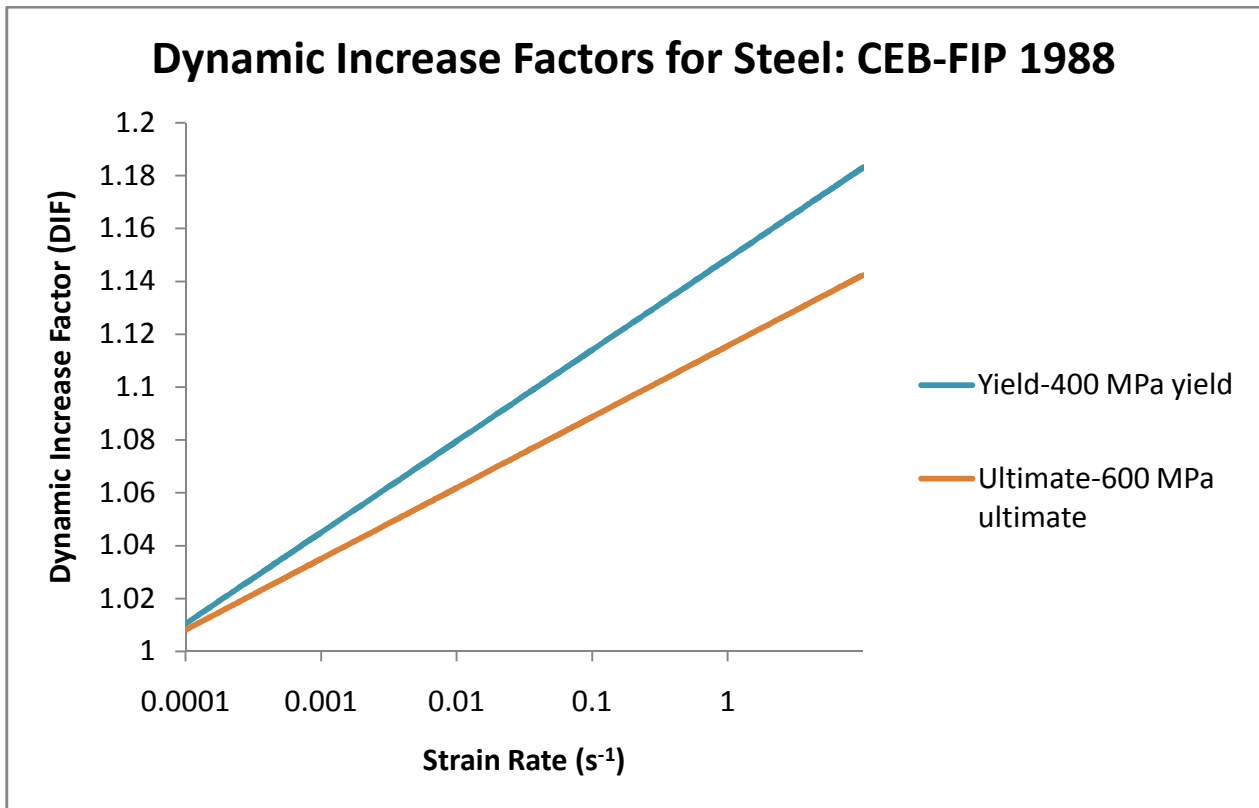


Figure 3-8: DIFs for steel: CEB-FIP 1988.

4 2D Verification Studies

4.1 Introduction

In this chapter, three test series consisting of reinforced concrete panels subjected to blast loading are examined as a verification study for the dynamic loading formulations in VecTor2. Analytical results for another test series are also presented, and were part of a blind simulation competition. In terms of the modeling approach taken for analyzing these panels, half of the specimen was modeled due to the fact that both the loading and the geometry were symmetric. All specimens were simply-supported reinforced concrete slabs, symmetric about the midspan. Restraints to movement in the y-direction along the bottom of the model were used to represent this symmetry. All specimens were loaded in a shock tube, where the pressure is assumed to be applied as a uniformly distributed load on the entire face of the specimen. For this reason, the same force-time history was applied to each node on the blast face. Modeling half of the specimen also has the advantage of faster analysis time. For the supports, compression-only truss bars or nodal restraints were used to represent the simply-supported conditions.

4.2 University of Texas Specimens

The first specimens modeled were reinforced concrete panels tested in a shock tube at the University of Texas. Two reinforced concrete panels, one pre-tensioned and one post-tensioned, were subjected to three blasts of increasing intensity. For this investigation, both the pre-tensioned and post-tensioned panels were considered. The panel dimensions were 2578 x 1029 x 88.9 mm, with a simply-supported span of 2438 mm. The concrete strength was 30.8 MPa, and half-inch diameter Grade 270 low-relaxation strands were used, prestressed to 75% of their ultimate strength. Grade 60 reinforcing bars were also used as additional longitudinal reinforcement as well as for out-of-plane reinforcement (Dunkman et al., 2009). Midspan deflections were measured using with a string potentiometer, while the pressure was recorded by five pressure sensors located just inside the opening of the shock tube. The first cycle of the response was reported, as well as a sketch and qualitative description of crack patterns and damage. Analytical results are compared in terms of peak displacement and displacement-time history. Crack patterns are also discussed. In conjunction with the experiment, a SDOF analysis was carried out to determine the peak displacements, and these results are also compared to the VecTor2 results. In the SDOF analyses, a simplified triangular

impulse was used, and for Blast 3 this had a noticeable effect on the analysis results. For Blasts 1 and 2, the experimentally measured pressure profiles were essentially triangular, and thus the simplification to a triangular load function did not have an overwhelming effect.

4.2.1 Finite Element Model

The slab dimensions, as reported previously, were 2578 x 1029 x 88.9 mm, with a simply-supported span of 2438 mm. In modeling half of the specimen, the midspan was restrained against movement in the y-direction (see Figure 4-1). A compression-only truss bar was placed at the support location. A mesh of 10 x 10 mm rectangular plane stress elements was used. A total of 1360 rectangular elements and 1529 nodes were used, with 119 loaded nodes on the blast face. For the supports, in the experiment the top and bottom of the panel were wedged between steel angles, and were shimmed with wooden blocks. Some fixity was introduced to the supports through the wedging and this was accounted for in the model through the use of an additional compression-only truss bar. The finite element model is shown in Figure 4-1.

A concrete compressive strength of 30.8 MPa was given in the report by Dunkman et al. (2009), in addition to the steel yield strengths. The concrete tensile strength, modulus, and strain at peak stress were calculated based on the compressive strength. All other concrete material properties were kept as the default VecTor2 values. For the prestressing steel, the yield and ultimate strengths were 1640 MPa and 1860 MPa, respectively. The yield and ultimate strength for the regular reinforcing steel was taken as 414 MPa and 600 MPa, respectively.

In terms of time-step, the initial time-step used was 0.1 ms. A time-step of 0.01 ms was also used in order to determine the effect of time-step on the analyses. Lumped masses, which must be assigned to unrestrained degrees of freedom in VecTor2 dynamic analyses, were calculated by dividing the total mass of half of the slab by the number of nodes in the model. Damping was initially specified as 1% and 3% for the first two modes. After determining the support conditions, a sensitivity analysis was performed on the damping ratios. The damping ratios for the first two modes were reduced until the results became unstable.

For concrete, the Hoshikuma (1997) model was used. All other models used were VecTor2 default models. Rayleigh damping was employed, and strain rate effects were not considered in

the base analysis. In a subsequent analysis, strain rate effects were considered by applying the CEB 1988 formulations for concrete and the Malvar/Crawford formulations for steel.

The experimental pressure-time histories and the pressure-time histories used in the VecTor2 analyses for Blast 1, 2 and 3 are shown in Figure 4-2, Figure 4-3, and Figure 4-4, respectively. The peak pressure and impulse for each blast are summarized in Table 4-1.

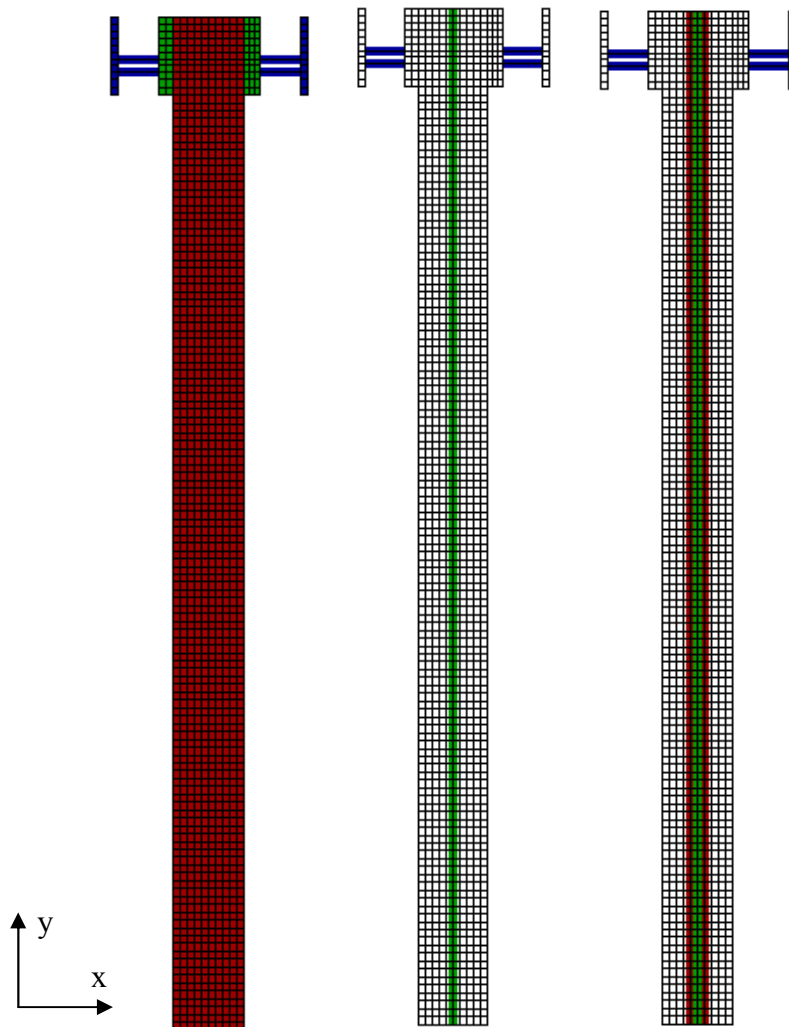


Figure 4-1:
Finite element mesh for VecTor2 University of Texas (left); pre-tension reinforcement (middle); post-tension reinforcement (right).

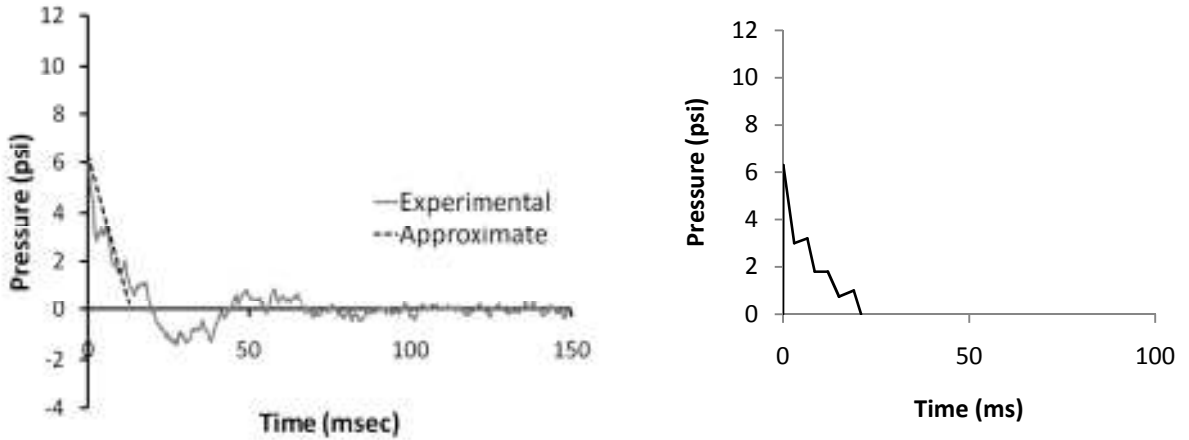


Figure 4-2: Experimental (left) and VecTor2 (right) pressure-time history for University of Texas Blast 1.

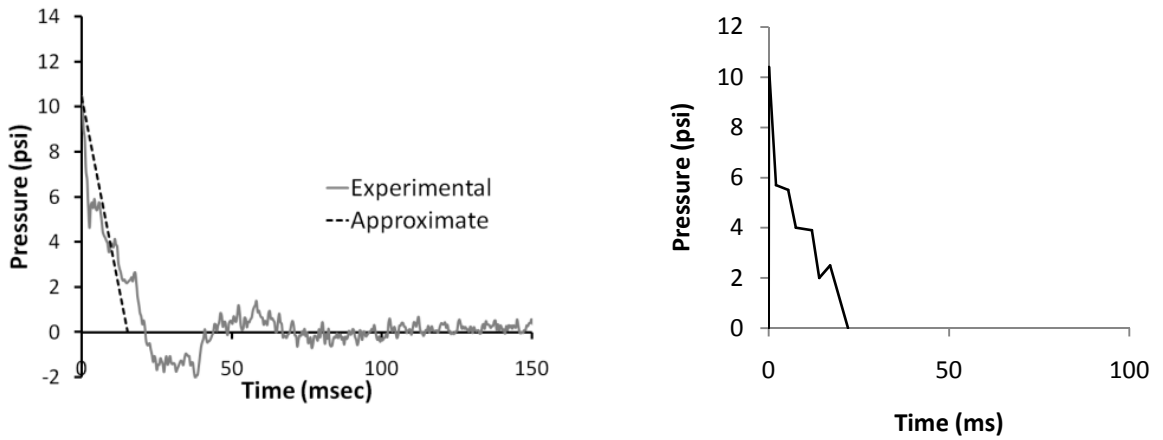


Figure 4-3: Experimental (left) and VecTor2 (right) pressure-time history for University of Texas Blast 2.

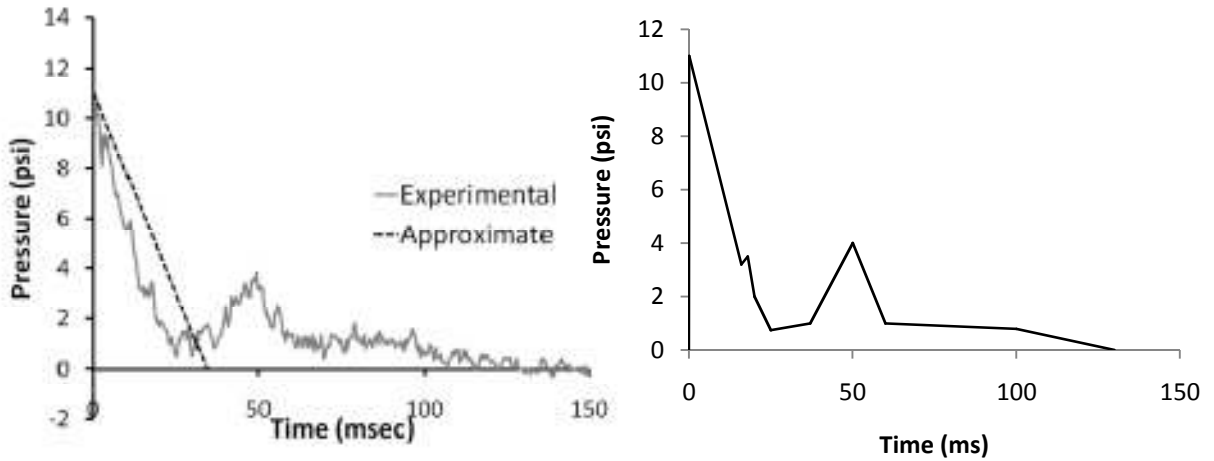


Figure 4-4: Experimental (left) and VecTor2 (right) pressure-time history for University of Texas Blast 3.

Table 4-1: University of Texas Specimens Blast Pressures and Impulses

Blast	Peak Pressure (kPa)	Impulse (kPa-s)
1	43.4	0.290
2	71.7	0.552
3	75.8	1.31

4.2.2 Pre-Tensioned Specimen Analysis Results

In this section, the VecTor2 results are compared to experimental results and to the SDOF analysis carried out by Dunkman et al. (2009). The SDOF analysis carried out in conjunction with the experiment was performed using the approximate triangular impulses shown in the experimental pressure-time histories. VecTor2 results are presented for the purely simply-supported condition with and without strain rate effects, as well as for a model with some fixity added. Displacement results for the pre-tensioned specimen are summarized in Table 4-2. Displacement-time histories, for the model with fixity added and a time-step of 0.1 ms, are shown in Figure 4-5 through Figure 4-7. For the simply-supported case, with 1% and 3% damping specified for the first two modes, the peak displacement for all three blasts was overestimated. Since wooden shims were used to wedge the supports tight, and it was noted by the experimenter that some fixity had been introduced, it was considered justified to introduce some fixity through the use of another compression-only truss bar. As the degree of fixity increased, the peak displacement for Blast 2 approached experimental values, while the peak displacement for Blast 3 was slightly underestimated.

Table 4-2: Displacement Results for University of Texas Pre-tensioned Specimen

Specimen	Time-step (ms)	Blast 1		Blast 2		Blast 3		Blast 3-Triangle	
		Peak Displacement (mm)	% Error	Peak Displacement (mm)	% Error	Peak Displacement (mm)	% Error	Peak Displacement (mm)	
Experimental (Dunkman et al., 2009)	-	5.59	-	24.38	-	66.40	-	-	
SDOF w/ Strain Rate (Dunkman et al., 2009)	0.1	13.46	140.91	28.96	18.77	-	-	101.09	
VecTor2 (Simply-Supported)	No SRE	0.1	12.46	123.00	32.17	31.97	76.07	14.56	122.94
	W/ SRE	0.1	10.72	91.86	28.33	16.19	67.24	1.27	107.82
VecTor2-Some Fixity (No SRE)	0.1	10.65	90.66	25.68	5.34	61.18	-7.87	-	
	0.01	10.63	90.19	25.82	5.89	61.51	-7.37	-	

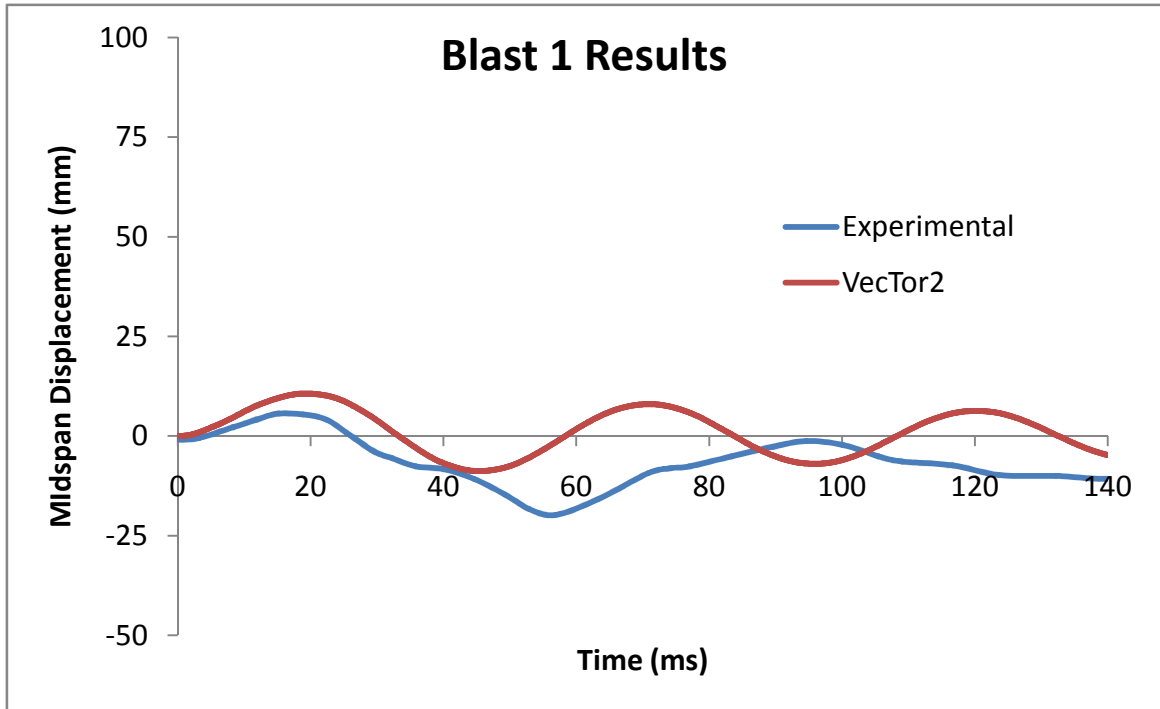


Figure 4-5: VecTor2 and experimental results for University of Texas Blast 1 (pre-tensioned panel, VecTor2 model has some fixity, no SRE).

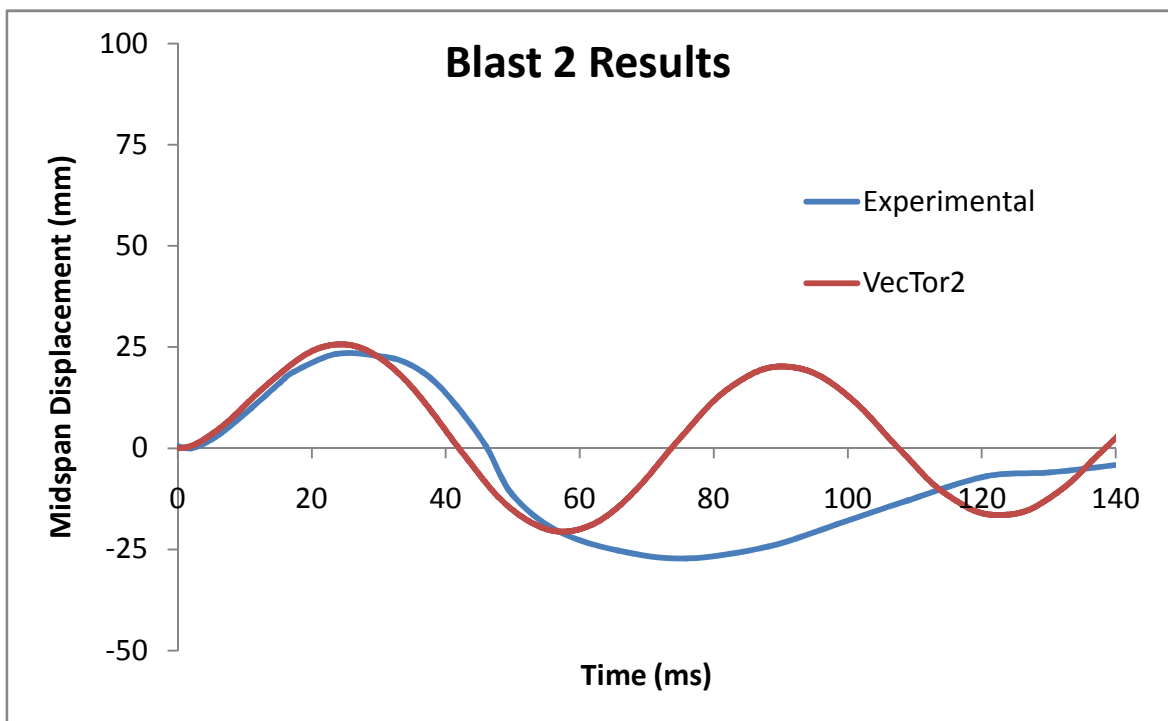


Figure 4-6: VecTor2 and experimental results for University of Texas Blast 2 (pre-tensioned panel, VecTor2 model has some fixity, no SRE).

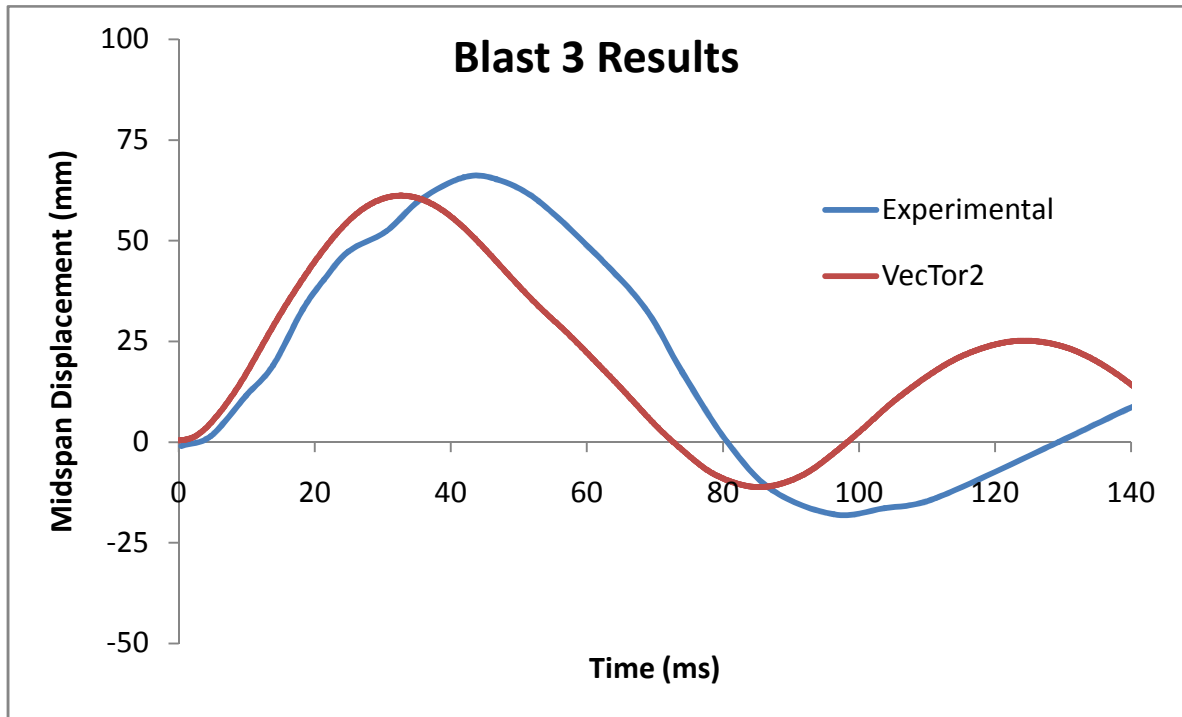


Figure 4-7: VecTor2 and experimental results for University of Texas Blast 3 (pre-tensioned panel, VecTor2 model has some fixity, no SRE).

For Blast 1, both VecTor2 and the SDOF analysis overestimated the peak deflection by a sizeable margin. Firstly, since the blast was so small, the slab was barely damaged, and predictions for behavior barely within the damage region are difficult. In fact, while VecTor2 predicted light cracking (see Figure 4-8), with the majority of cracks being of negligible width, it was reported experimentally that there were no visible cracks. This again indicates that the slab was only slightly damaged, if at all. As well, rigid body movement of the shock tube or issues with the support conditions experimentally could account for part of the difference between experimental and analytical results.

The experimentally observed Blast 1 rebound deflection was four times larger than the positive deflection (Dunkman et al., 2009). This is not something that one could reasonably expect, nor is it predicted by VecTor2, and could again be an indicator that there was an issue with the support conditions.

For Blast 2, while the peak displacement predicted by VecTor2 agrees fairly well with the experimental result, examining Figure 4-6 we can see that the post-peak responses do not match

in terms of both period and amplitude of rebound. It is possible that there were again issues with the supports experimentally which affected the post-peak response of the specimen. However, since the response was not reported beyond the first period, it is difficult to make further comparisons. It is noted, though, that the shape of the response predicted by VecTor2 is the expected response, considering that the intensity of this blast is not particularly high.

The Blast 2 crack pattern from VecTor2 is shown in Figure 4-9. Slight damage was reported experimentally. A few concentrated cracks were reported on the back face at midspan. The cracking reported by VecTor2 is more distributed than was reported experimentally, however there are a number of 0.1 mm cracks concentrated around midspan, which is consistent with experimental observations.

For Blast 3, while the total impulse was larger than that of Blast 2, the peak pressures were similar. The pressure-history for Blast 3 was more elongated, with a substantial secondary peak. For the SDOF analysis, Dunkman et al. (2009) used triangular loads. To compare the peak displacement predicted by VecTor2 for the simply supported case to the SDOF analysis, a triangular load was also used in one analysis. As can be observed in Table 4-2, the difference between using a triangular load and defining the load more precisely is quite large. While both the VecTor2 analysis with one truss bar and the SDOF analysis over-predicted the experimentally observed peak displacement for the pre-tensioned specimen, the error is reduced from 85% to 15% when the pressure-time history is modeled correctly. The VecTor2 displacement-time history is compared to the experimental response in Figure 4-7. VecTor2 predicts a shorter period, indicative of a stiffer response.

Figure 4-10 shows the crack pattern for Blast 3 from VecTor2. More cracks have opened, although the maximum crack width is still fairly small (only 0.1 mm, residual). Experimentally, it was reported only that more cross-panel cracks appeared, and while this is consistent with the results from VecTor2, a comparison in greater detail cannot be made. It was also observed experimentally that after Blast 3 there was some residual deflection, although the amount was not indicated. The residual deflection from VecTor2 is approximately 1.3 mm.

In terms of the effect of time-step, it was observed that decreasing the time-step from 0.1 ms to 0.01 ms had very little effect on the analysis results. The time-step of 0.1 ms was initially chosen so that the experimental pressure history could be modeled with sufficient detail.

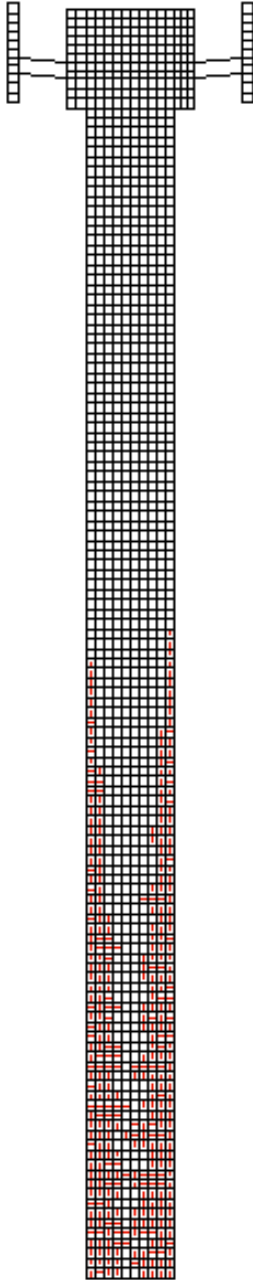


Figure 4-8:
Crack pattern from
VecTor2 for
University of Texas
Blast 1
(pre-tensioned;
residual).

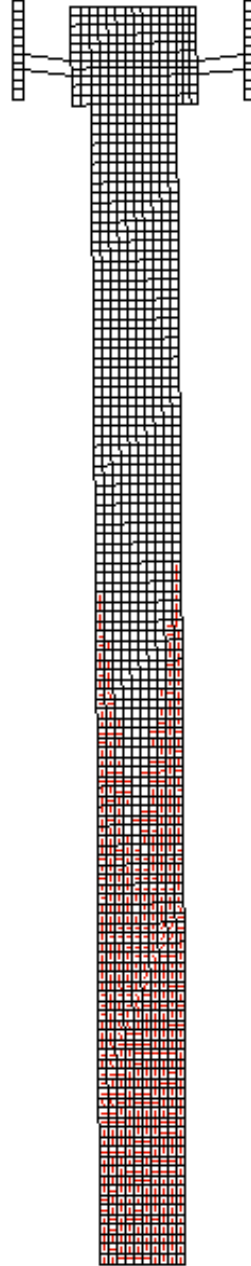


Figure 4-9:
Crack pattern from
VecTor2 for
University of Texas
Blast 2
(pre-tensioned;
residual).

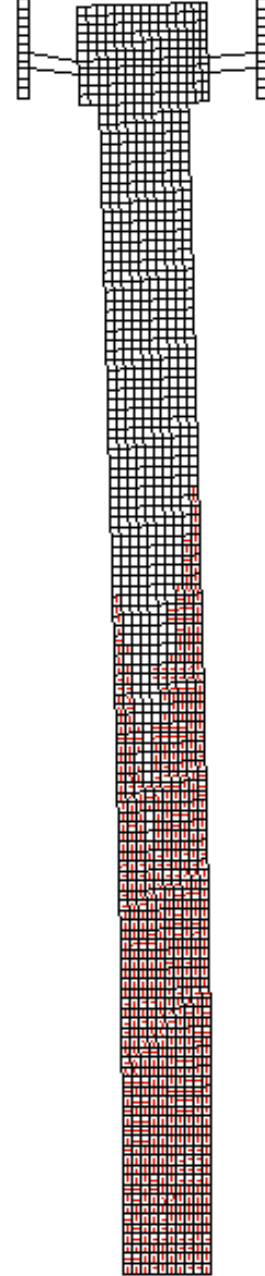


Figure 4-10:
Crack pattern from
VecTor2 for
University of Texas
Blast 3
(pre-tensioned;
residual).

4.2.2.1 Comparison of Peak and Residual Crack Widths for Pre-tensioned University of Texas Specimen

Residual displacement and crack widths were small for all three blasts. As shown in Figure 4-8, after Blast 1, cracking was distributed around the midspan on both the front and back faces of the panel. The majority of cracks were negligible in width, or had closed; the maximum residual crack width calculated for Blast 1 was 0.1 mm. At the time of peak displacement for Blast 1, VecTor2 predicts a number of larger cracks, ranging from 2.0 mm to 4.9 mm. The crack pattern at the time of peak displacement is shown in Figure 4-12.

After Blast 2, light cracking on both sides of the panel was predicted by VecTor2. While more of the panel was cracked, as shown in Figure 4-9, residual crack widths were limited to 0.1 mm or less. At peak, VecTor2 calculated crack widths of 6.0 mm to 26 mm, and the crack pattern is shown in Figure 4-13. In general, the larger cracks were located closer to midspan.

The final crack pattern calculated for Blast 3, shown in Figure 4-10, is similar to the residual crack pattern from Blast 2 in terms of cracked area. On the front and back faces of the panel, the maximum residual crack width was only 0.1 mm. There was, however, cracking near the prestressing, as shown in Figure 4-11. These crack widths ranged from 0.2 mm (red) to 0.4 mm (light green). At peak, VecTor2 calculated crack widths ranging from 7.5 mm to 76 mm. The crack pattern at peak is shown in Figure 4-14.

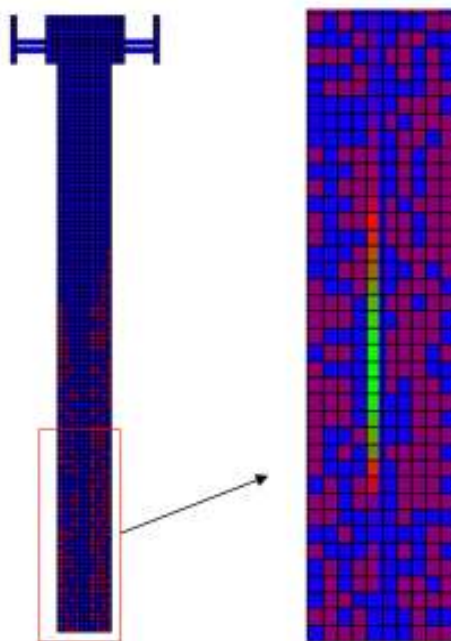


Figure 4-11: VecTor2 calculated residual crack widths after Blast 3 for University of Texas pre-tensioned panel

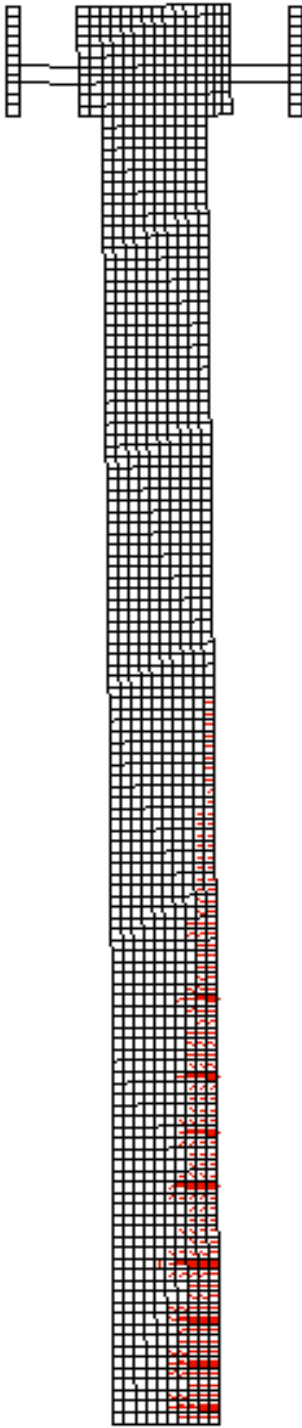


Figure 4-12:
Crack pattern from
VecTor2 for
University of Texas
Blast 1
(pre-tensioned; at
peak).

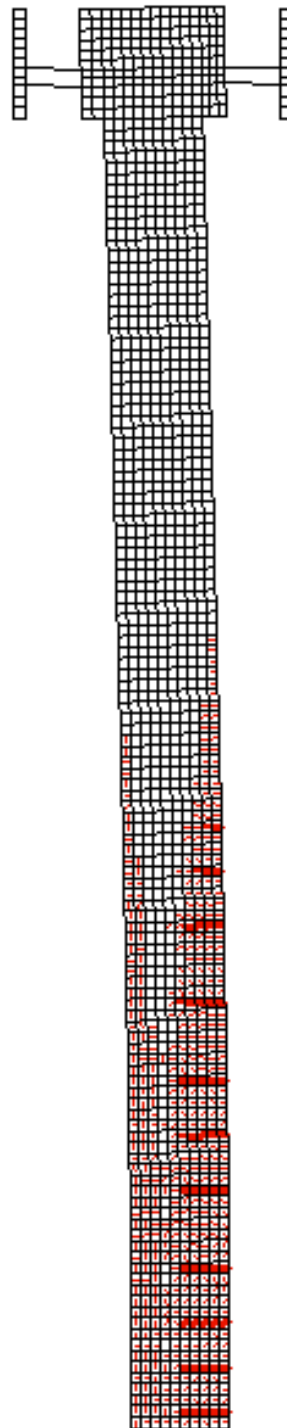


Figure 4-13:
Crack pattern from
VecTor2 for
University of Texas
Blast 2
(pre-tensioned; at
peak).

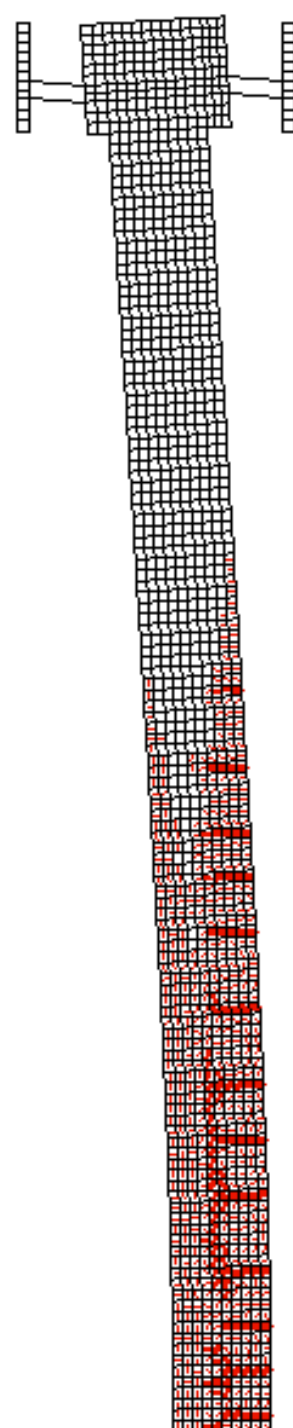


Figure 4-14:
Crack pattern from
VecTor2 for
University of Texas
Blast 3
(pre-tensioned; at
peak).

4.2.3 Post-Tensioned Specimen Analysis Results

In this section, the VecTor2 results are compared to experimental results and to the SDOF analysis carried out by Dunkman et al. (2009). The SDOF results presented are the same as those presented in the previous section, because these were the only analytical results presented in Dunkman et al. (2009), where it was also stated that the SDOF analysis results varied by less than 1% between the pre-tensioned and post-tensioned analyses.

The VecTor2 analysis results presented in Table 4-3 are for an analysis carried out using a time-step of 0.1 ms, and with some fixity introduced at the supports. The fixity used in the post-tensioned analyses was the same amount of fixity used in the pre-tensioned analyses.

Table 4-3: Displacement Results for University of Texas Post-tensioned Specimen

Specimen	Time-step (ms)	Blast 1		Blast 2		Blast 3	
		Peak Displacement (mm)	% Error	Peak Displacement (mm)	% Error	Peak Displacement (mm)	% Error
Experimental (Dunkman et al., 2009)	-	4.32	-	27.18	-	94.49	-
SDOF (Dunkman et al., 2009)	0.1	13.46	211.76	28.96	6.54	101.09	6.99
VecTor2 (With Some Fixity)	0.1	10.56	144.65	25.40	-6.53	61.09	-35.35

The displacement results for the post-tensioned specimen are shown in Figure 4-15 through Figure 4-17.

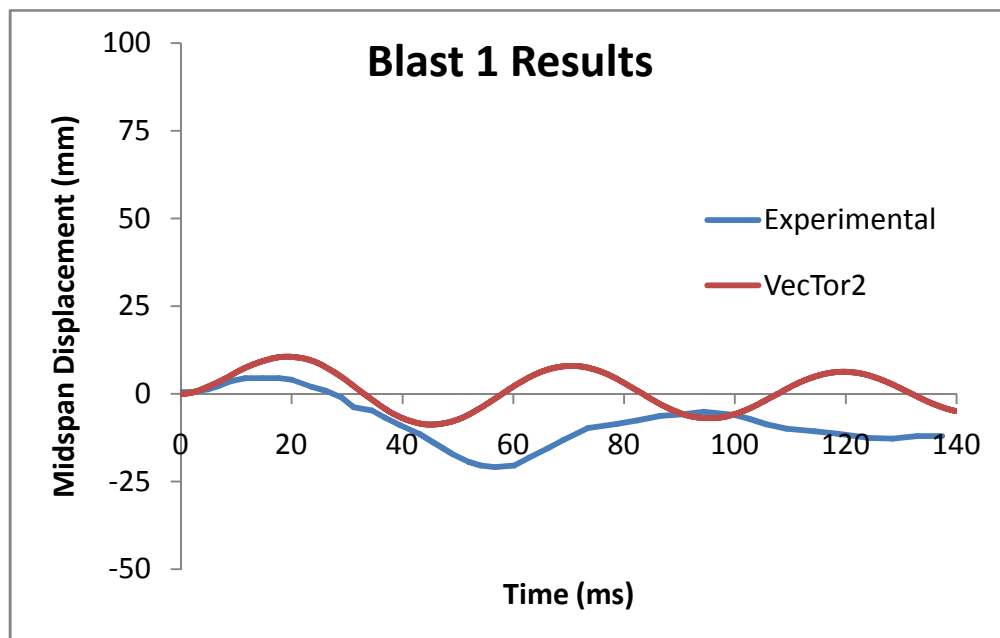


Figure 4-15: VecTor2 and experimental results for University of Texas Blast 1 (post-tensioned panel, VecTor2 model has some fixity, no SRE).

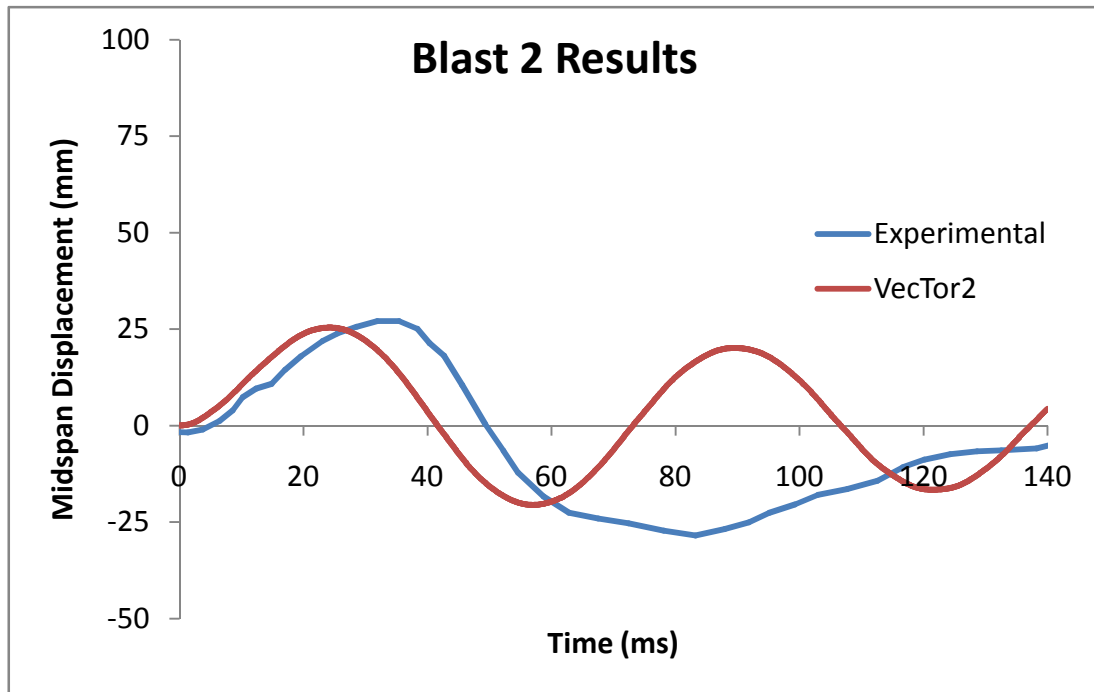


Figure 4-16: VecTor2 and experimental results for University of Texas Blast 2 (post-tensioned panel, VecTor2 model has some fixity, no SRE).

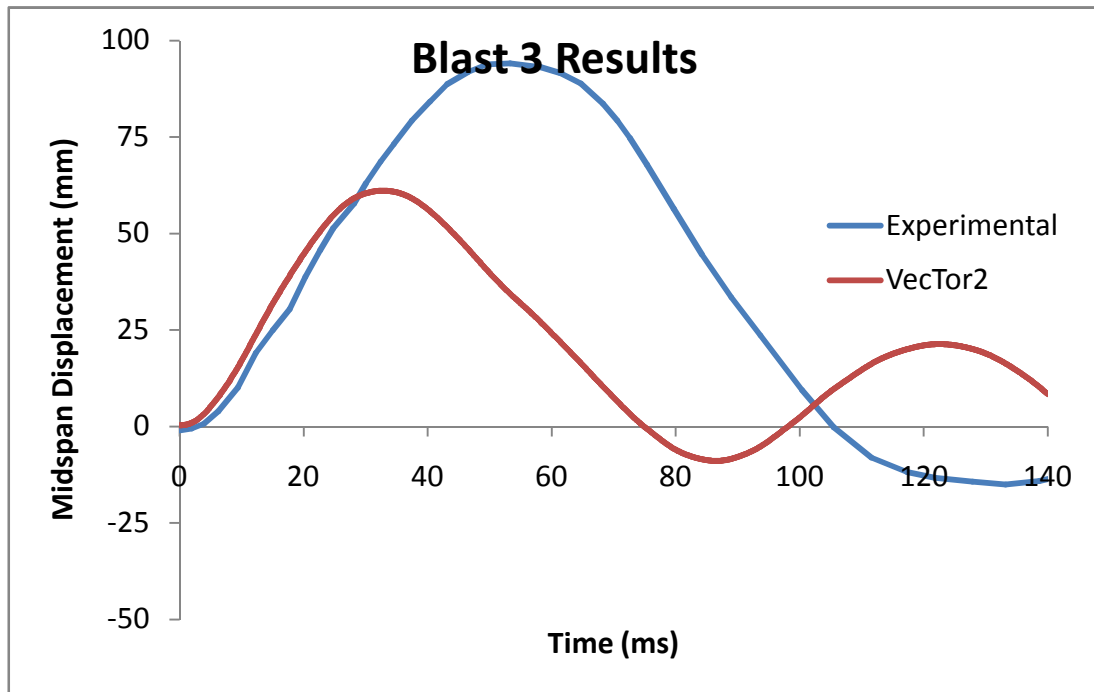


Figure 4-17: VecTor2 and experimental results for University of Texas Blast 3 (post-tensioned panel, VecTor2 model has some fixity, no SRE).

For Blast 1, the experimentally observed deflection-time histories for the two panels were similar in terms of both period and peak displacement. In terms of cracking, more damage was reported for the post-tensioned specimen. Concentrated cracks located at midspan on the tension side were reported. The crack pattern from VecTor2 is shown in Figure 4-18.

The experimentally observed peak displacement for Blast 2 was 27.2 mm. It was expected that the response of the pre- and post-tensioned specimens would be similar, but the post-tensioned specimen sustained more damage. In terms of displacement-time response, the period for the post-tensioned specimen was also longer than that of the pre-tensioned specimen, indicating lower stiffness. This could be due to issues with the anchorage and loss of prestress. In addition to the post-tensioned specimen having a larger reported peak deflection, more cracks were reported. After Blast 2, distributed cracking was observed along the face of the post-tensioned specimen, while there was only minor cracking visible on the pre-tensioned specimen. The crack pattern from the VecTor2 analysis of the post-tensioned specimen is shown in Figure 4-19.

Looking at the experimental displacement-time histories for Blast 1 and Blast 2, shown in Figure 4-15 and Figure 4-16, there is a large discrepancy between the observed post-peak responses and the post-peak responses predicted by VecTor2. This trend was observed in the pre-tensioned specimen as well and, as mentioned in Section 4.2.2, may be due to issues with the supports. Since the slabs were not severely damaged by the first two blasts, the displacement-time history predicted by the VecTor2 analyses was the expected behavior.

Experimentally, a peak displacement of 94.5 mm was reported for Blast 3. The period of the post-tensioned panel was also longer, and more damage was observed. This is an unexpected result, given the fact that both panels were prestressed to the same initial stress. Based on observations made following testing, the method of prestressing is likely the cause of the large difference in displacements. It was observed that after panel failure, splitting cracks were present at the anchorage locations on the post-tensioned panel (Dunkman et al., 2009), and this could explain part of the apparent loss in prestress. An excessive loss of prestress did not occur in the VecTor2 analyses for the post-tensioned specimen. For this reason, the VecTor2 peak displacement for Blast 3 was much less than experimentally observed. The VecTor2 crack pattern is shown in Figure 4-20.

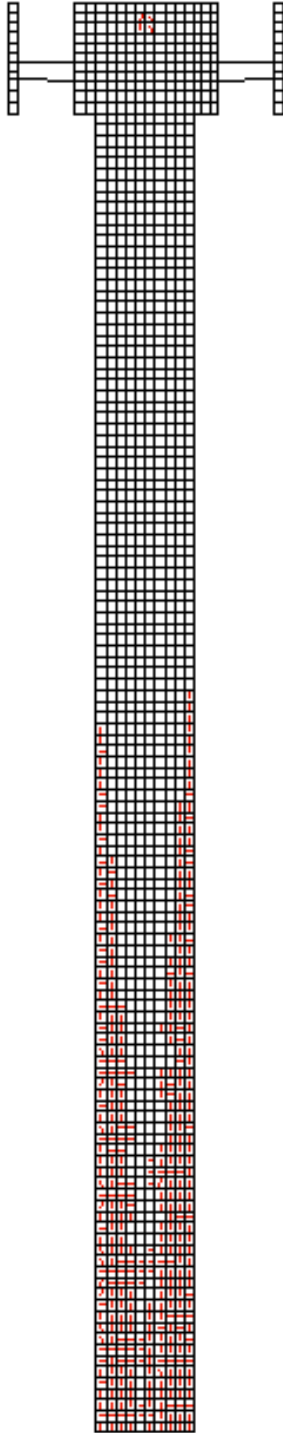


Figure 4-18:
Crack pattern from
VecTor2 for
University of Texas
Blast 1
(post-tensioned;
residual).

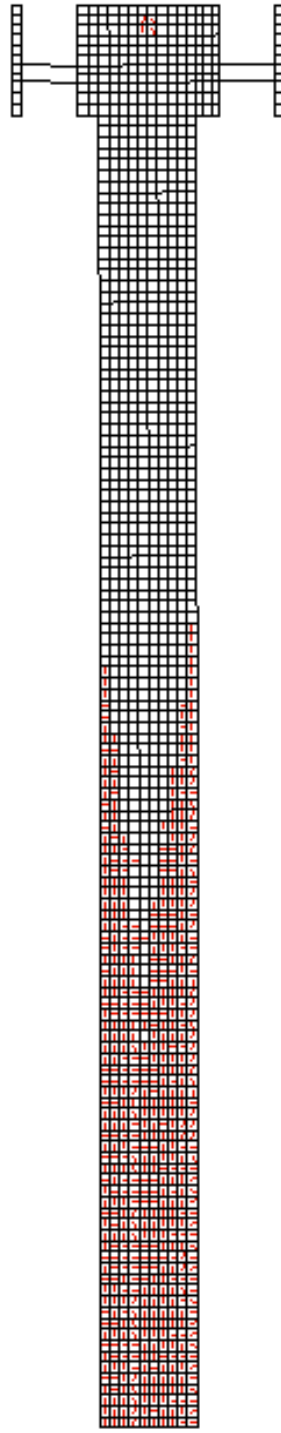


Figure 4-19:
Crack pattern from
VecTor2 for
University of Texas
Blast 2
(post-tensioned;
residual).

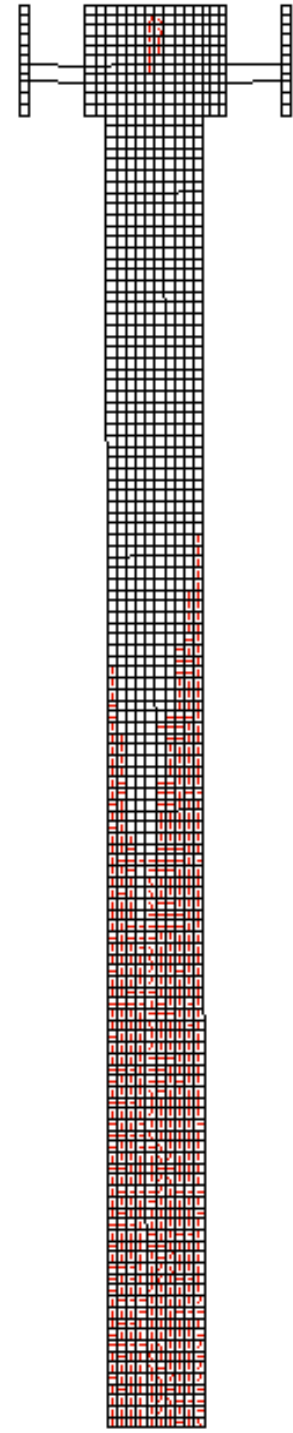


Figure 4-20:
Crack pattern from
VecTor2 for
University of Texas
Blast 3
(post-tensioned;
residual).

4.2.3.1 Comparison of Peak and Residual Crack Widths for Post-tensioned University of Texas Specimen

The crack widths calculated by VecTor2 for the post-tensioned panel were basically the same as those calculated for the pre-tensioned panel.

At the peak of Blast 1, for the post-tensioned panel, crack widths ranged from approximately 1.0 mm to 4.9 mm. The crack pattern at peak is shown in Figure 4-21. Residual crack widths were at most 0.1 mm and were distributed on the front and back face of the panel, as shown in Figure 4-18.

The residual crack widths after Blast 2 were also relatively small. Again, the majority of cracks were of negligible width, with 0.1 mm being the maximum crack width. At peak, the calculated crack widths ranged from 5.6 mm to 25.5 mm. The crack pattern is shown in Figure 4-22.

After Blast 3 residual crack widths were approximately 0.1 mm. Unlike the pre-tensioned panel, there were no larger cracks present at the location of the prestressing. At peak, crack widths ranged from 10 mm to 97.6 mm; the crack pattern is shown in Figure 4-23. The crack widths calculated at the time of peak displacement for the post-tensioned panel, for Blast 3, were larger than those calculated for the pre-tensioned panel.

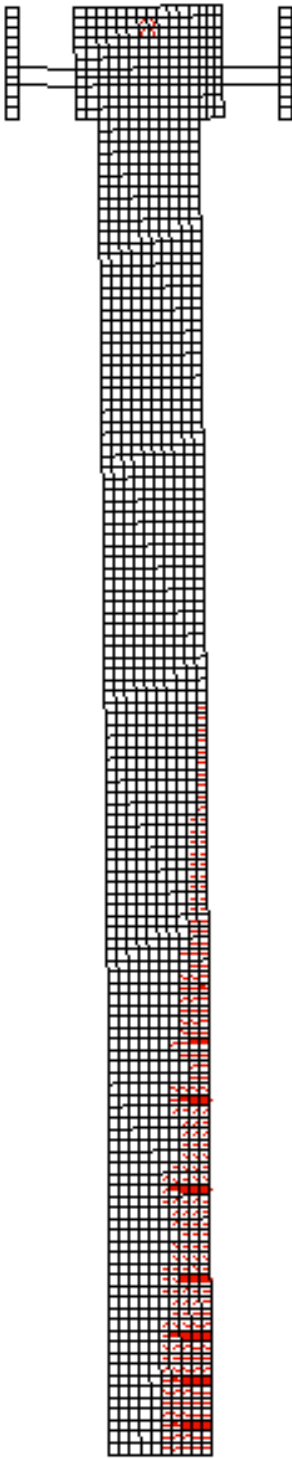


Figure 4-21:
Crack pattern from
VecTor2 for
University of Texas
Blast 1
(post-tensioned; at
peak).

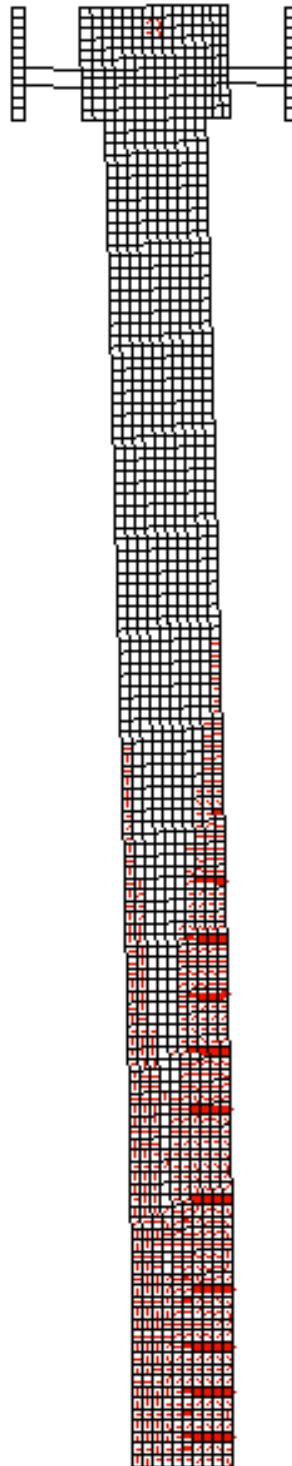


Figure 4-22:
Crack pattern from
VecTor2 for
University of Texas
Blast 2
(post-tensioned; at
peak).

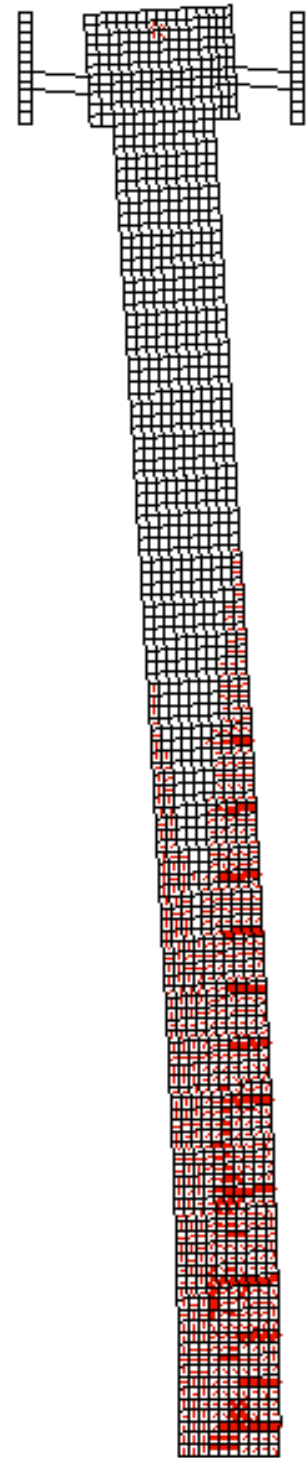


Figure 4-23:
Crack pattern from
VecTor2 for University
of Texas Blast 3
(post-tensioned; at
peak).

4.2.4 Summary

Presented in Sections 4.2.2 and 4.2.3 were the results of VecTor2 analyses of shock-tube tested simply supported prestressed concrete panels. The results were compared to experimental results as well as SDOF analysis results (Dunkman et al., 2009). Overall, the results predicted by VecTor2 agreed with the experimental results for the pre-tensioned slab, with less than 8% difference between the analytical and experimental peak deflections for Blasts 2 and 3. The crack patterns predicted by VecTor2 also agreed well with experimental results.

In terms of strain rate effects, the analyses were carried out prior to the updating of the DIF formulations. Based on the results of a previous investigation (Saatci and Vecchio, 2009) it was determined that incorporating strain rate effects for both steel and concrete overestimated the strength and resulted in an overly stiff response. It is likely that the damping used could be decreased had strain rate effects been considered for the steel. Regardless, the results obtained by VecTor2 agree well with the experimental results and correlate well with SDOF results as well.

4.3 University of Ottawa Specimen

The second test series used for dynamic analysis verification of VecTor2 was a simply supported reinforced concrete slab tested in a shock tube at the University of Ottawa. This slab was also subjected to three individual blasts of increasing intensity. Slab dimensions were 2440 x 2440 x 75 mm, with a simply supported span of 2232 mm (Jacques, 2011). At the supports the slab was clamped between two angles and bolted to the shock tube frame. The 38 x 38 x 4.8 mm and 50 x 50 x 4.8 mm steel angles represent a simply-supported condition, and are modeled with only one compression-only truss bar on either side of the slab. The slab was reinforced with 11 6.3 mm diameter reinforcing wires on each face in both the horizontal and vertical directions. The compressive strength of the concrete was 60 MPa (Jacques, 2011).

The experimental results reported include the pressure-time history, displacement-time history, and photographs of the crack patterns. Displacements were measured using LVDTs located at the midspan, at the supports, and at intermediate positions. The reflected pressures were measured using two piezoelectric pressure sensors, located on the walls of the shock tube 50 mm away from the specimen. The VecTor2 results that are compared in this section are the displacement-time histories and crack patterns.

4.3.1 Finite Element Model

As mentioned above, the slab dimensions were 2440 x 2440 x 75 mm, with a clear span of 2232 mm. Half of this specimen was modeled, with the nodes at midspan restrained against movement in the y-direction, using 7 x 10 mm elements. The following steel properties were specified: yield strength of 580 MPa, ultimate strength of 670 MPa, yield strain of 2.8×10^{-3} , and ultimate strain of 196×10^{-3} . For concrete, the tensile strength, elastic modulus, and strain at peak stress were calculated based on the reported compressive strength. The finite element model is shown in Figure 4-24.

For concrete, the Hoshikuma model was used. All other material models were VecTor2 default models. Rayleigh damping was employed. Starting with 1% and 5% specified for the first two modes, damping was decreased until the results became unstable. Strain rate effects were not considered, for the reasons discussed in Section 4.2.4 and Section 2.2.2.1. The time-step used was 0.1 ms.

The reported pressure-time histories were used in the analyses. The pressure-time histories for Blast 1, 2, and 3 are shown in Figure 4-25, Figure 4-26, and Figure 4-27, respectively. The peak pressures and impulses are summarized in Table 4-4.

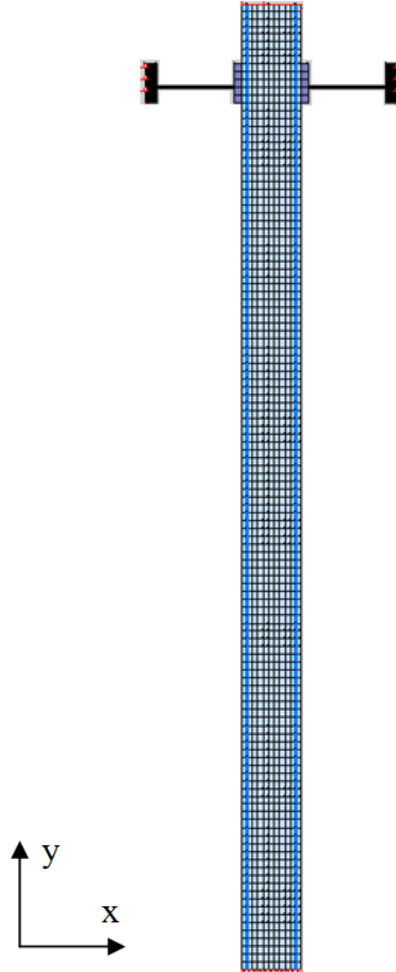


Figure 4-24:
Finite element model for University of Ottawa specimen.

Table 4-4: University of Ottawa Specimen Blast Pressures and Impulses

Blast	Pressure (kPa)	Impulse (kPa-s)
1	15.4	0.123
2	28.2	0.204
3	100.5	0.811

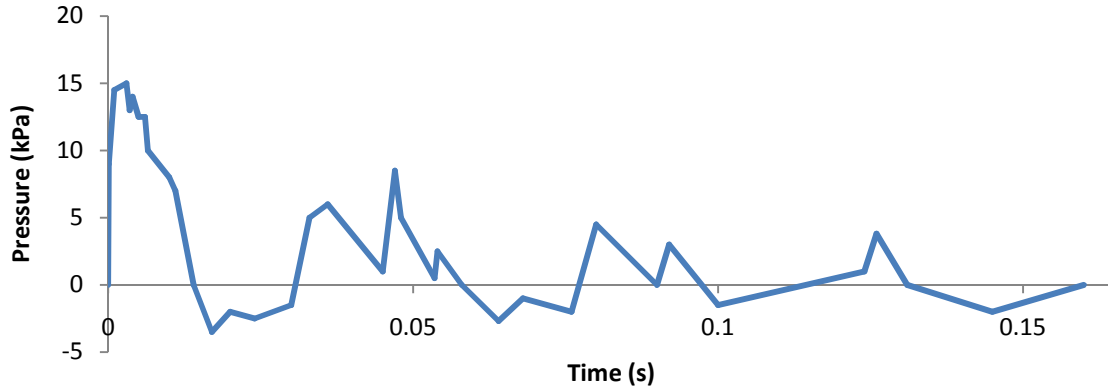


Figure 4-25: VecTor2 pressure-time history for University of Ottawa Blast 1.

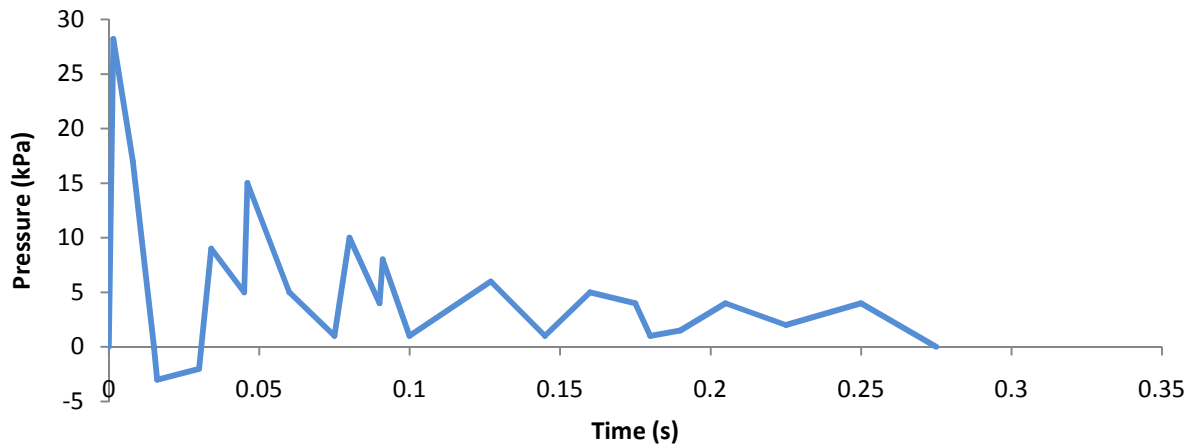


Figure 4-26: VecTor2 pressure-time history for University of Ottawa Blast 2.

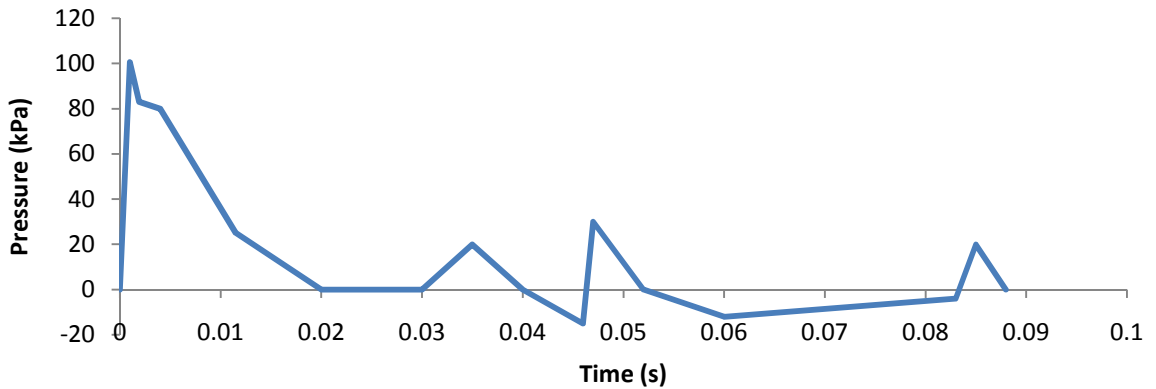


Figure 4-27: VecTor2 pressure-time history for University of Ottawa Blast 3.

4.3.2 Results

Numerous analyses were carried out in order to determine the smallest amount of damping that would yield stable results. Displacement results for the analyses with 0.5% and 0.75% damping for the first two modes are presented in Table 4-5, where the VecTor2 results are compared to both the experimental results and the results from a SDOF analysis carried out by Jacques (2011). For the SDOF analysis, a simplified triangular load was not used; rather, the load applied was modeled after the experimental pressure-time histories. Strain rate effects were considered in the SDOF analysis.

Table 4-5: Displacement Results for University of Ottawa Specimen

Analysis	Blast 1		Blast 2		Blast 3	
	Peak Displacement (mm)	% Error	Peak Displacement (mm)	% Error	Peak Displacement (mm)	% Error
Experimental	6.9	-	16.3	-	197.5	-
SDOF (w/ Strain Rate) (Jacques, 2011)	8.9	28.99	18.6	14.11	217.8	10.28
VecTor2	6.5	-5.80	17.2	5.52	181.6	-8.1

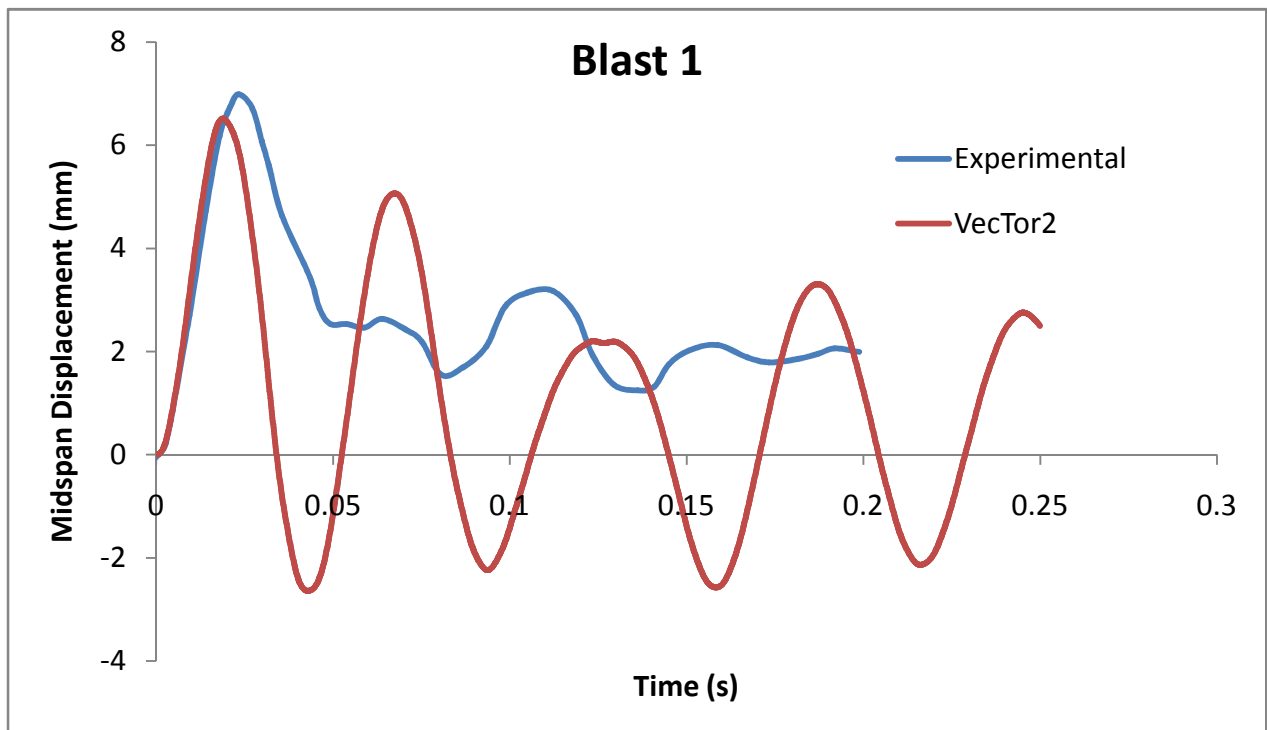


Figure 4-28: Comparison of VecTor2 and experimental response for University of Ottawa Blast 1.

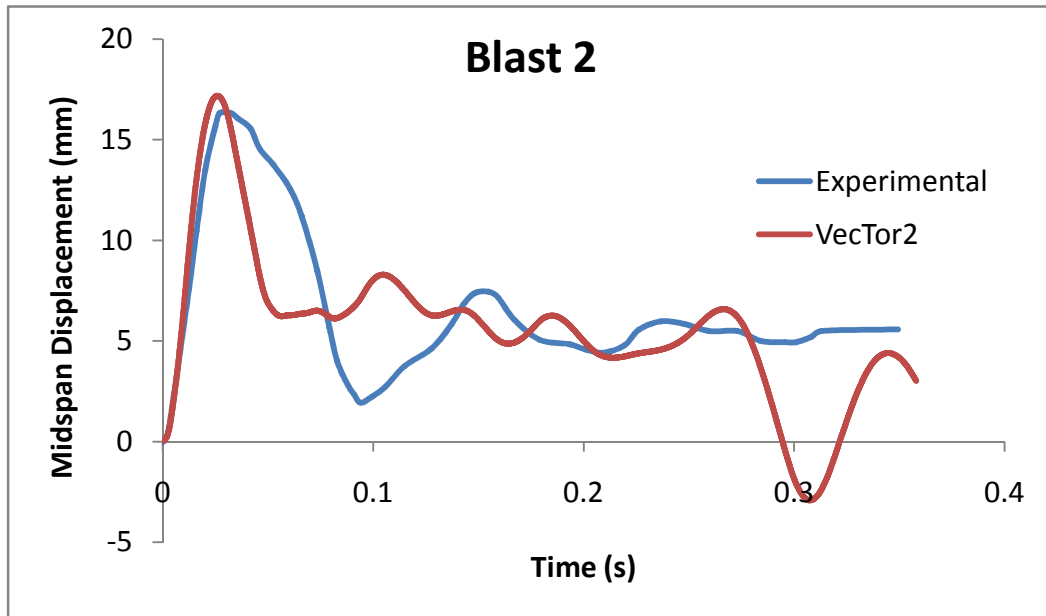


Figure 4-29: Comparison of VecTor2 and experimental response for University of Ottawa Blast 2.

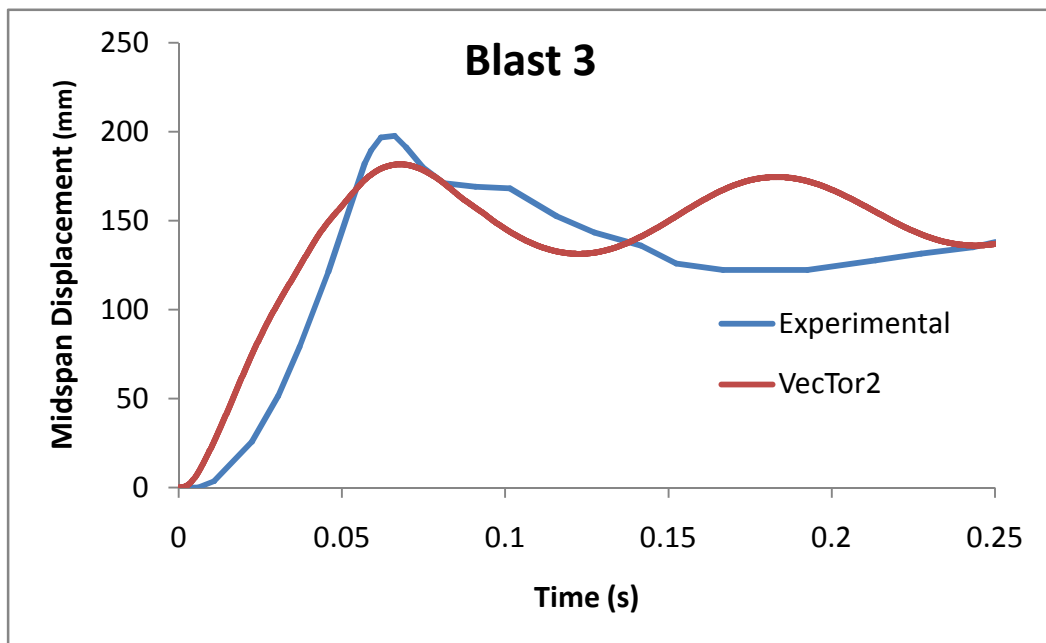


Figure 4-30: Comparison of VecTor2 and experimental responses for University of Ottawa Blast 3.

The VecTor2 displacement-time response for Blast 1 is compared to the experimental response in Figure 4-28, and it can be seen that the VecTor2 response is slightly stiffer than the experimental response. As well, looking at the first descending portion of the experimental response, it appears that the response is affected by the second peak in the Blast 1 pressure-time history. While this part of the blast was modeled in VecTor2, it didn't have much of an effect on the response, based on the observations that the first cycle of the experimental response has a longer period than predicted by VecTor2. It is possible that there was some inaccuracy in the recording of the tertiary impulses or that the pressure-time history that was measured (and subsequently used in VecTor2) is not the same as what the slab experienced. As well, no experimental rebound displacement was reported, but there was rebound in the VecTor2 prediction.

In terms of cracking, a small flexure crack was reported, running along the mid-span of the slab (Jacques, 2011). Other than this single crack, no other damage was observed. VecTor2 predicts no major damage from Blast 1. The VecTor2 crack pattern shows a distribution of small 0.1 mm wide cracks on both faces of the slab, mostly concentrated around the midspan. The crack pattern from the VecTor2 analysis, is shown in Figure 4-31.

The VecTor2 displacement-time response for Blast 2 is compared to the experimental response in Figure 4-29. While the peak displacements are similar, in the post-peak section the VecTor2 response is again slightly stiffer than experimental. As well, the first cycle of the experimental response again exhibits a longer period than that predicted by VecTor2. Although, the response after the first period is similar in terms of shape and magnitude of displacement, the VecTor2 results are shifted in time compared to the experimental results. One of the other differences between the VecTor2 and experimental responses is the sustained displacement of about 7 mm experimentally compared to the drop in displacement in the VecTor2 response. In the blast modeled in VecTor2, the pressure was decreased to zero at 0.275 seconds, which is why the displacement decreases suddenly at that point. A continuation of the VecTor2 response would show the displacement oscillating and eventually damping to negligible residual displacement. In the experimental pressure-time history, though, the pressure doesn't actually decrease to zero at that location, but appears to remain constant at approximately 2-3 kPa for the reported length of time. For comparison purposes, an analysis was carried out assuming that the pressure did not

decrease to zero, and the predicted displacement leveled out at approximately 5.3 mm, and no negative displacement was observed.

In terms of experimentally observed cracking, a single crack was reported along the midspan, and ran approximately two-thirds of the span before extending to the corner of the panel. This is an unusual crack pattern, and it was hypothesized that it was likely a result of damage to the slab prior to testing (Jacques, 2011). As expected, this crack pattern was not observed in the VecTor2 results, and the crack widths predicted by VecTor2 were small. The VecTor2 crack pattern is shown in Figure 4-32. This large single crack at midspan of the slab could also help account for the discrepancy between the experimental and the numerical results. Issues with the supports were also reported (Jacques, 2011), and may have also contributed to the difference between the analytical and experimental results.

The VecTor2 and experimental responses for Blast 3 are compared in Figure 4-30. Again, the VecTor2 response is stiffer than experimental, likely due to the larger crack at midspan. A residual displacement of 141.5 mm was reported (Jacques, 2011), while VecTor2 predicts a residual displacement of 154.3 mm (approximately 9% higher).

Damage reported from Blast 3 included rupture of 50% to 60% of the steel reinforcement, with the remainder of the reinforcement being well into the strain-hardening region (Jacques, 2011). Since there is only one crack present, this is not surprising. It appears that a large plastic hinge developed at midspan early on. In the numerical analysis, no rupture of the steel occurred (this is one of the conditions for analysis stability in the current VecTor2 formulation), and cracking was distributed along the entire length of the span, as shown in Figure 4-33, with the cracks at midspan ranging from 3 mm to 7 mm in most areas. VecTor2 also calculated crack widths of over 90 mm, which is likely due to the fact that the default crack spacing was used.

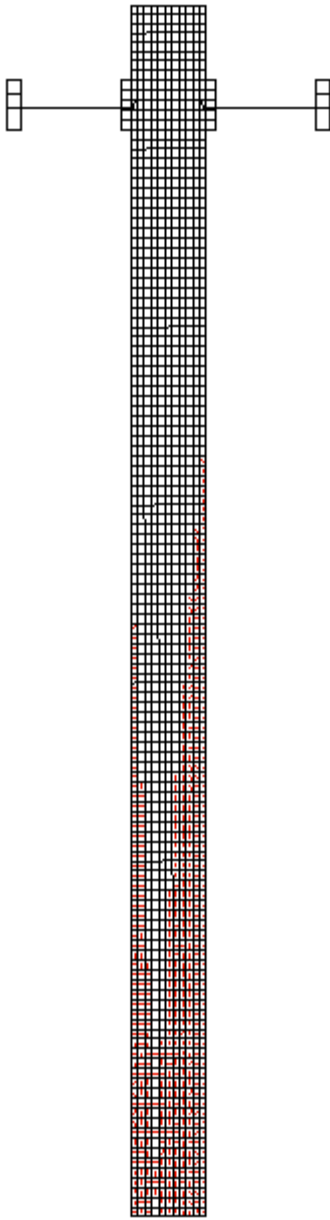


Figure 4-31:
VecTor2 crack pattern
for University of Ottawa
Blast 1
(residual).

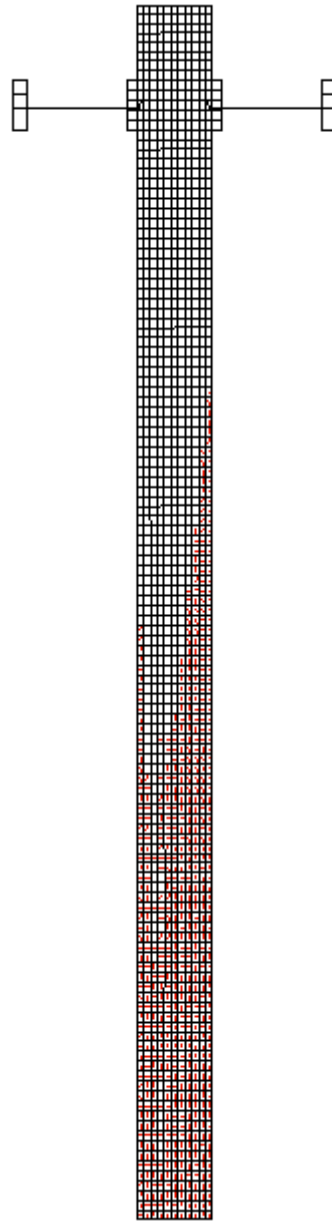


Figure 4-32:
VecTor2 crack pattern
for University of Ottawa
Blast 2
(residual).

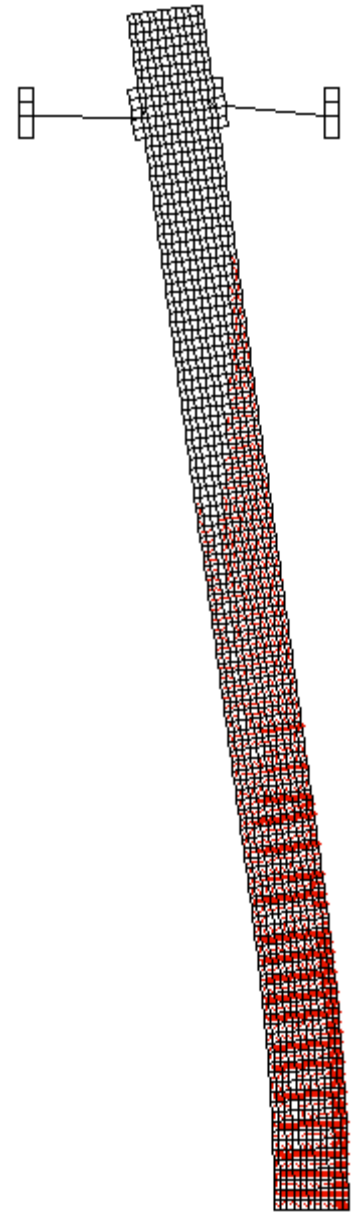


Figure 4-33:
VecTor2 crack pattern for
University of Ottawa
Blast 3
(residual).

4.3.2.1 Comparison of Peak and Residual Crack Widths for University of Ottawa Specimen

As mentioned in the previous section, for Blast 1, VecTor2 calculated residual crack widths with a maximum value of 0.1 mm. At peak, VecTor2 calculated crack widths in the range of 1.5 mm to 2.4 mm; the crack pattern at peak is shown in Figure 4-34.

The residual crack widths after Blast 2 were 0.1 mm on average. The maximum crack widths at peak ranged from 2.5 mm to 6.6 mm. The crack pattern, at the time of peak displacement for Blast 2, is shown in Figure 4-35.

After Blast 3, VecTor2 calculated residual crack widths ranging from 3.0 mm to 7.0 mm in most areas, and from 27.4 mm to 91.5 mm in some locations close to the midspan. These residual crack widths are close to the crack widths calculated at the time of peak displacement. The crack pattern at peak, shown in Figure 4-36, had maximum crack widths ranging from 12 mm to 94.7 mm. As mentioned in the previous section, these large crack widths may be due to the fact that the default crack spacing was used.

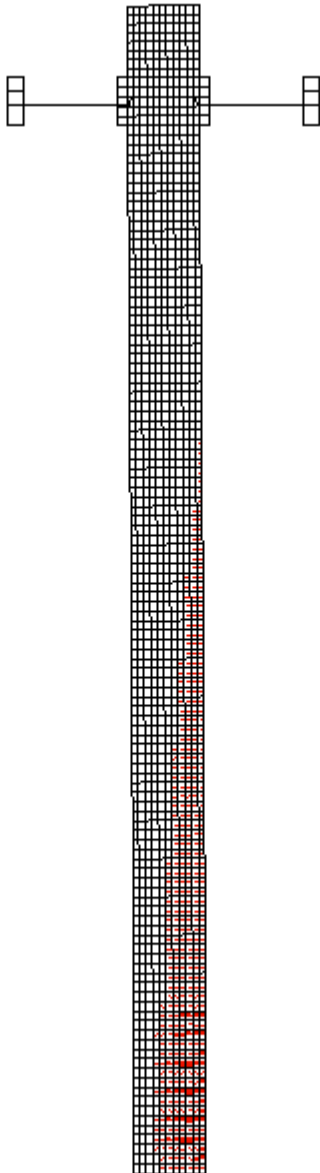


Figure 4-34:
VecTor2 crack pattern for
University of Ottawa
Blast 1
(at peak).

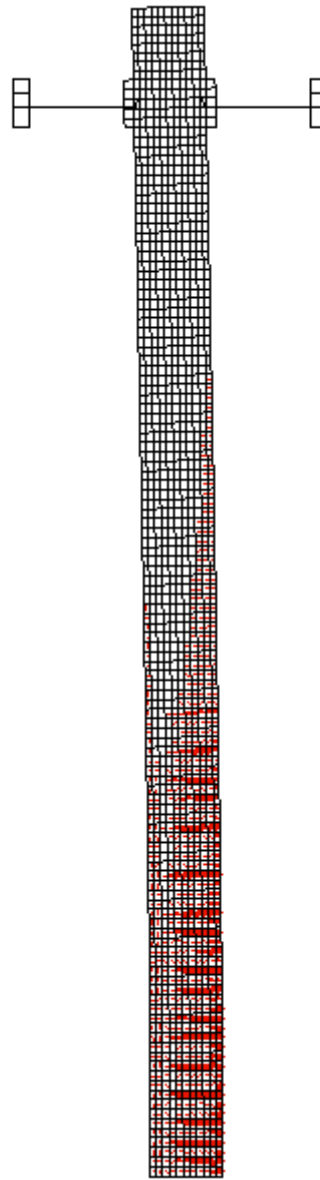


Figure 4-35:
VecTor2 crack pattern
for University of Ottawa
Blast 2
(at peak).

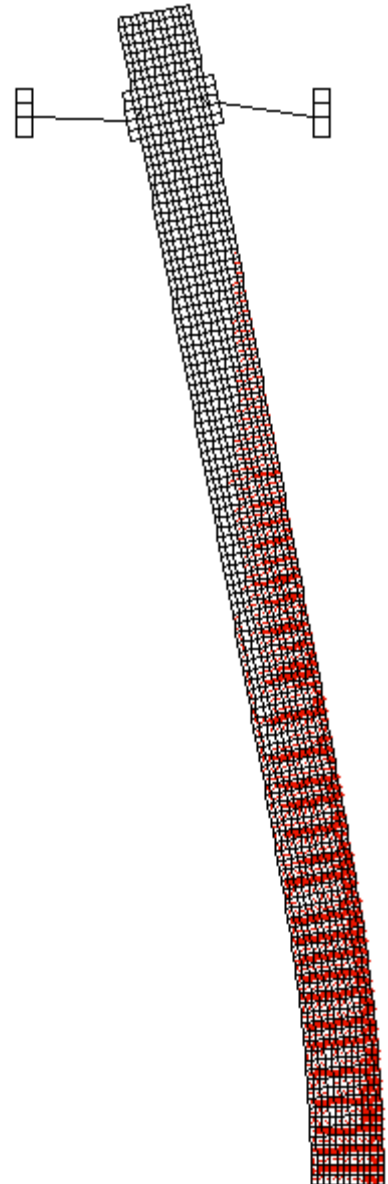


Figure 4-36:
VecTor2 crack pattern for
University of Ottawa Blast 3
(at peak).

4.3.3 Summary

To summarize the analyses for this specimen, good agreement was observed between the experimental and VecTor2 peak displacements, although there was some difference in stiffness. Experimentally observed damage was unusual, with a single crack forming at midspan early on in the experiment. This single crack likely explains the rupture of such a large portion of the reinforcement. One of the other trends observed was that the first cycle of the experimental response had a longer period than predicted by VecTor2 for all blasts. This could be due to a number of factors, including the unusual crack pattern, the issues at the supports, and the effects of tertiary peaks in the blast pressure-time history. Since support displacements were not provided, it was assumed that the supports were essentially pins, restraining lateral movement, but allowing unrestricted rotation.

4.4 U.S. Army Doubly-Reinforced Shock Tube Specimens

4.4.1 Introduction

Ten reinforced concrete panels were tested using the Blast Load Simulator (BLS) at ERDC-Vicksburg. These specimens were 1/3-scale panels, doubly reinforced with #3 reinforcing bars that were either Grade 60 reinforcement or High-Strength-Low-Alloy Vanadium (HSLA-V) reinforcement. The concrete strengths were 4 ksi (26.7 MPa) and 15.5 ksi (107 MPa). The panels were simply supported in the longitudinal direction, and unsupported in the lateral direction (Robert and Johnson, 2009).

The objective of this test series was to investigate the effects of using the vanadium micro-alloyed high-strength steel reinforcement with high strength concrete. Different combinations of steel and concrete material types were used and are summarized in Table 4-6. The specimens modeled in VecTor2 were Specimens 3, 5, 6, and 9; these specimens were modeled because blast pressure-time histories were provided.

Table 4-6: Experimental Matrix for Doubly Reinforced Shock Tube Tests at ERDC-Vicksburg [adapted from Robert and Johnson, 2009]

Slab	Concrete		Steel	
	26.7 MPa	107 MPa	Grade 60	HSLA-V
1		X		X
2		X		X
3		X		X
4		X	X	
5		X	X	
6	X			X
7	X			X
8	X			X
9	X		X	
10	X		X	

The peak pressures and impulses for each specimen modeled are summarized in Table 4-7.

Table 4-7: US Army Two-Way Specimens Peak Pressure and Impulse

Specimen	Peak Pressure (kPa)	Impulse (kPa-sec)
3	395	7.78
5	391	7.42
6	391	7.35
9	351	6.67

4.4.2 Specimen Details and VecTor2 Modeling

The 1/3-scale reinforced concrete panel dimensions were 64 x 33.75 x 4 in (1626 x 857 x 102 mm), with a simply supported span of 52 in (1321 mm). The specimen dimensions and reinforcement layout are shown in Figure 4-37. In VecTor2, half of the specimen was modeled. The longitudinal (in-plane) reinforcement was modeled using discrete truss elements, with a total area of 639 mm², representing nine #3 reinforcing bars each with an area of 71 mm². A concrete cover of 25 mm was used, consistent with the concrete cover used in numerical modeling of this test series done in conjunction with the tests (Thiagarajan et al, 2011; Vasudevan, 2012). Horizontal in-plane reinforcement (in the out-of-plane direction in VecTor2) was modeled as smeared with the reinforcement ratio specified as 0.43 % over the entire slab. The reinforcement properties used in VecTor2 were derived from the stress-strain curves shown in Figure 4-38. For the concrete properties, the reported concrete compressive strength was used to calculate all other properties, based on common empirical relations. The concrete material properties and steel properties are summarized in Table 4-8. The VecTor2 model is shown in Figure 4-39. Crack spacing of 100 mm was also specified, due to issues with the stability of initial analyses.

In the experiment, the supporting frame was intended to provide a simply supported condition. On the side opposite the blast face, the frame consisted of a 6 x 8 in (152 x 203 mm) structural steel tube on the top and bottom. On the blast face, 3 x 3 in (75 x 75 mm) steel tubes were used to hold the specimen in position. Since the main supports were the steel tubes used on the back face, these were used to determine the location of the supports in VecTor2. In VecTor2, a restraint in the direction of the impulse was placed 100 mm from the top of the slab, at the centre of the structural tube. The nodal restraints replace the compression-only truss bars used in the University of Texas and University of Ottawa analyses.

In terms of applying the impulse to the specimen, nodal loads were applied to the nodes within the 52 in (1321 mm) free span. The applied loading was derived from the reported pressure-time histories. The pressure profiles for Specimens 3, 5, 6, and 9 are shown in Figure 4-40, Figure 4-41, Figure 4-42, and Figure 4-43, respectively.

Default concrete material properties were used in the analyses with the exception of the concrete stress-strain curve, for which the Hoshikuma model was used. In terms of damping, the same

damping ratios were specified for all four analyses. The minimum amount of damping required to maintain stability was determined for the critical specimen (Slab 6), and that damping ratio was used for all analyses. The damping ratios specified for the first and second modes were 3% and 5%, respectively. These damping ratios are high compared to those used for the University of Texas and Saatchioglou specimens, however the magnitude of the blast impulses in this test series were much larger.

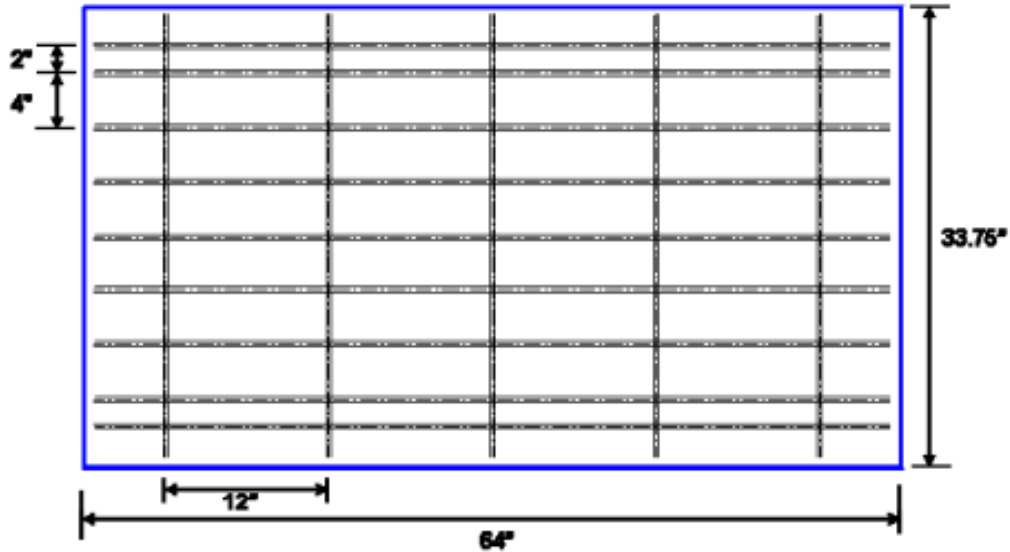


Figure 4-37: Specimen details for doubly reinforced specimens tested at U.S. Army ERDC (Robert et al., 2009).

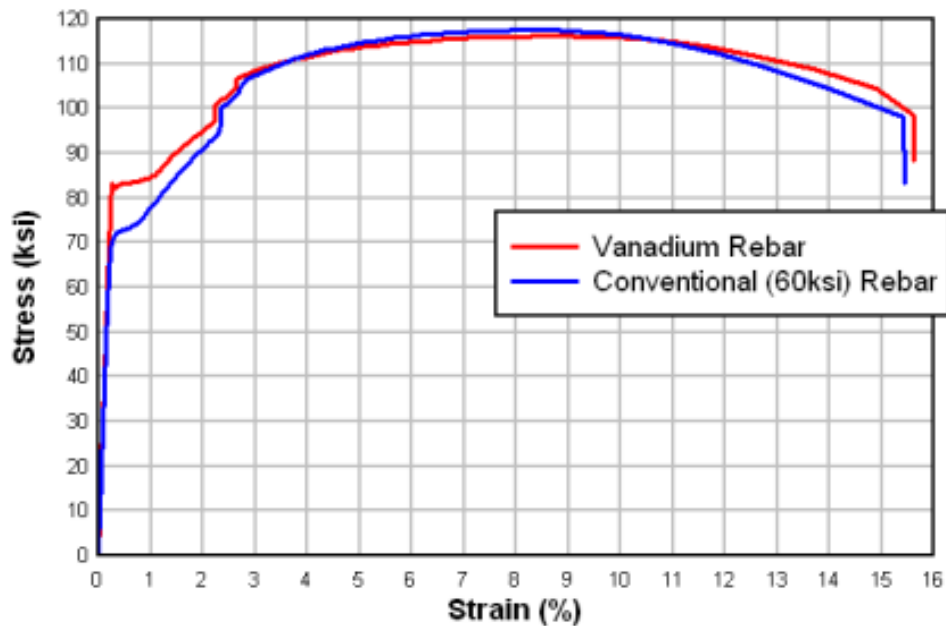


Figure 4-38: Stress-strain curves for vanadium and conventional reinforcement (Robert et al., 2009).

Table 4-8: Reinforcement and Concrete Material Properties for Doubly-Reinforced US Army Specimens

Concrete Properties			
Normal Strength		High Strength	
f_c (MPa)	27.6	f_c (MPa)	107
f_t (MPa)	1.73	f_t (MPa)	3.41
E_c (MPa)	24300	E_c (MPa)	41240
ε_0 ($\times 10^{-3}$)	1.94	ε_0 ($\times 10^{-3}$)	3.03
ν	0.210	ν	0.261
Reinforcing Steel Properties			
Conventional Reinforcement		High Strength Low Alloy Vanadium Reinforcement	
f_y (MPa)	496	f_y (MPa)	572
f_u (MPa)	810	f_u (MPa)	807
E_s (MPa)	198576	E_s (MPa)	212000
ε_s ($\times 10^{-3}$)	5	ε_{sh} ($\times 10^{-3}$)	10
ε_u ($\times 10^{-3}$)	85	ε_u ($\times 10^{-3}$)	85

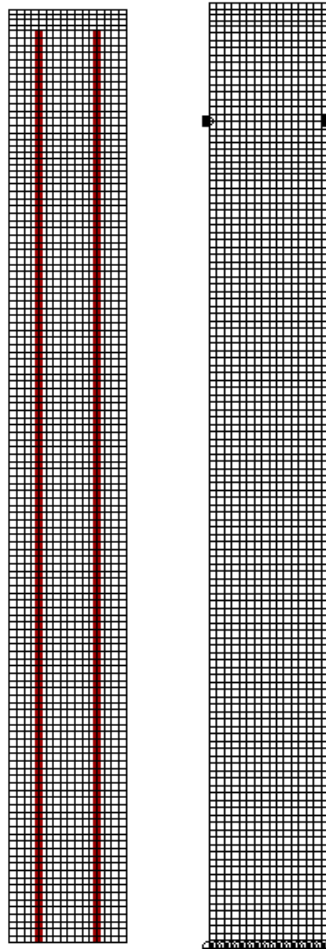


Figure 4-39: VecTor2 model for US Army doubly reinforced specimens; reinforcement (left), supports (right).

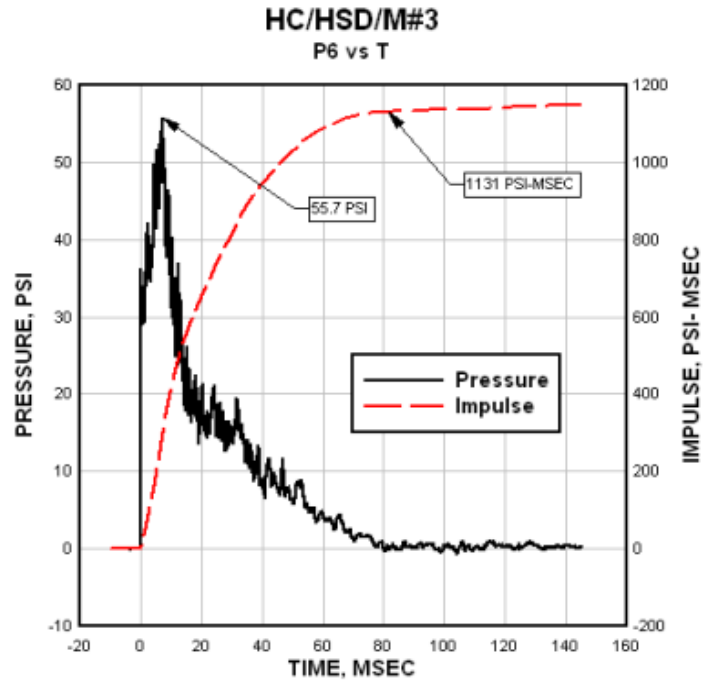


Figure 4-40: Slab 3 experimental pressure-time and impulse-time history (Robert et al., 2009).

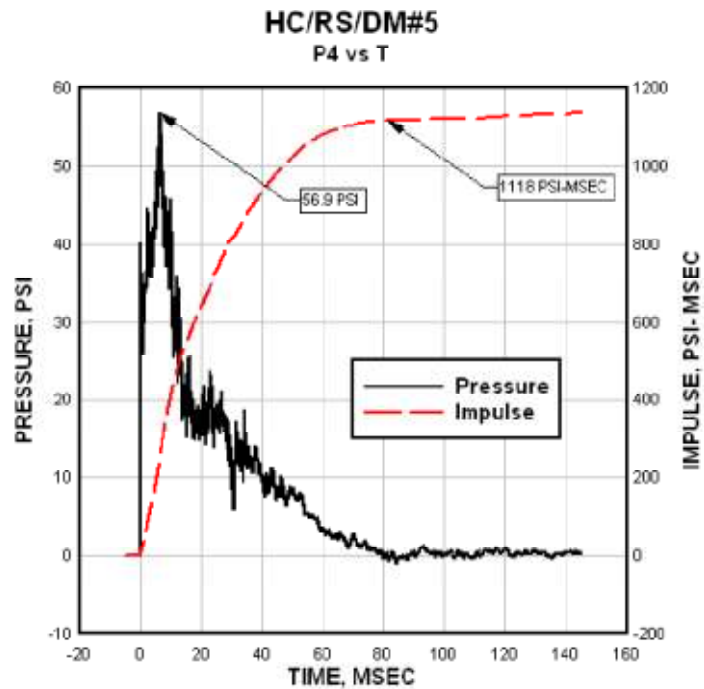


Figure 4-41: Slab 5 experimental pressure-time and impulse-time history (Robert et al., 2009).

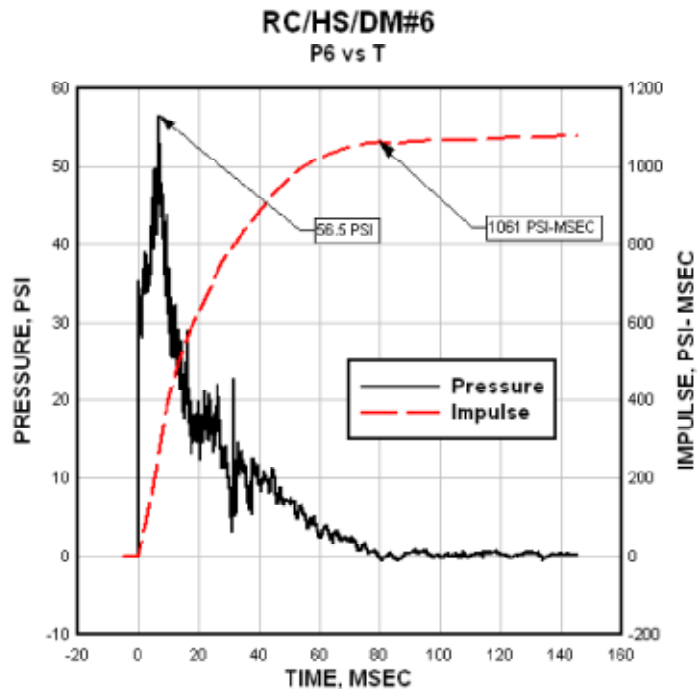


Figure 4-42: Slab 6 experimental pressure-time and impulse-time history (Robert et al., 2009).

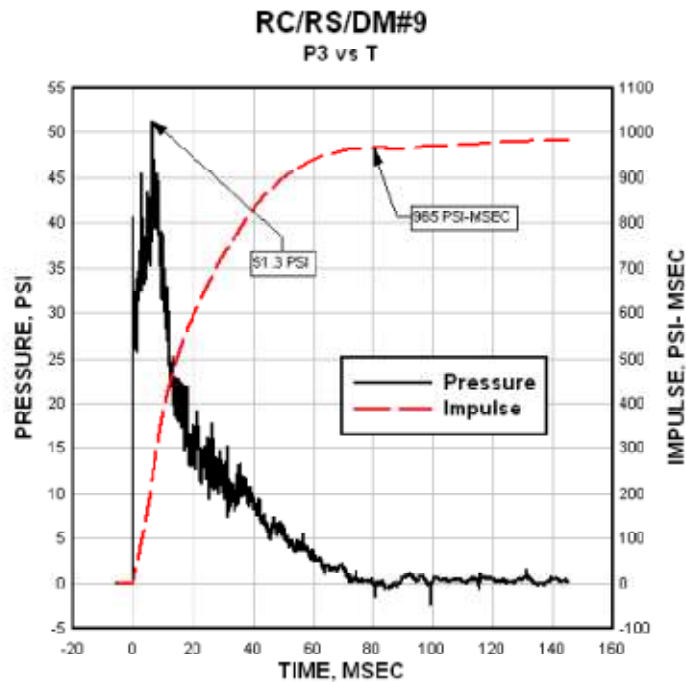


Figure 4-43: Slab 9 experimental pressure-time and impulse-time history (Robert et al., 2009).

4.4.3 Displacement Results and Discussion

Peak displacements are compared in Table 4-9, and displacement-time graphs are shown in Figure 4-44 through Figure 4-47. For Slab 5, the first peak was compared to VecTor2 results due to the fact that, in general, subsequent peaks are less reliable than the initial peak.

Table 4-9: Displacement Comparison for U.S. Army Slabs

Slab	Displacements		
	Experimental	VecTor2	% Error
3	121.1	110.6	-8.7
5	134.2	112.3	-16.3
6	136.7	227.1	66.1
9	231.8	201.8	-13.0

Given the magnitude of these simulated blasts, the results obtained by VecTor2 are good; displacements are within approximately 16% for three of the specimens. Looking at the results obtained for Specimen 6, it appears that the high strength low-alloy steel had a large effect on the experimental results, whereas in the VecTor2 analyses the high strength low-alloy steel behaved very similarly to the conventional reinforcement. The VecTor2 result was anticipated due to the similarity between the stress-strain curves for the two types of steel. The ultimate stresses are almost identical, and the yield stress of the high strength steel is only slightly higher than that of the conventional reinforcement.

It is observed that the VecTor2 response is initially stiffer than experimentally observed for these specimens. This is possibly partly due to the simplification of the support conditions to a single pin from the structural steel tube support frame used experimentally. In the experimental report it was noted that the slabs were initially simply-supported, however as deflections increased the ends of the slabs caught on part of the supports and a simple/fixed support condition existed (Robert and Johnson, 2009).

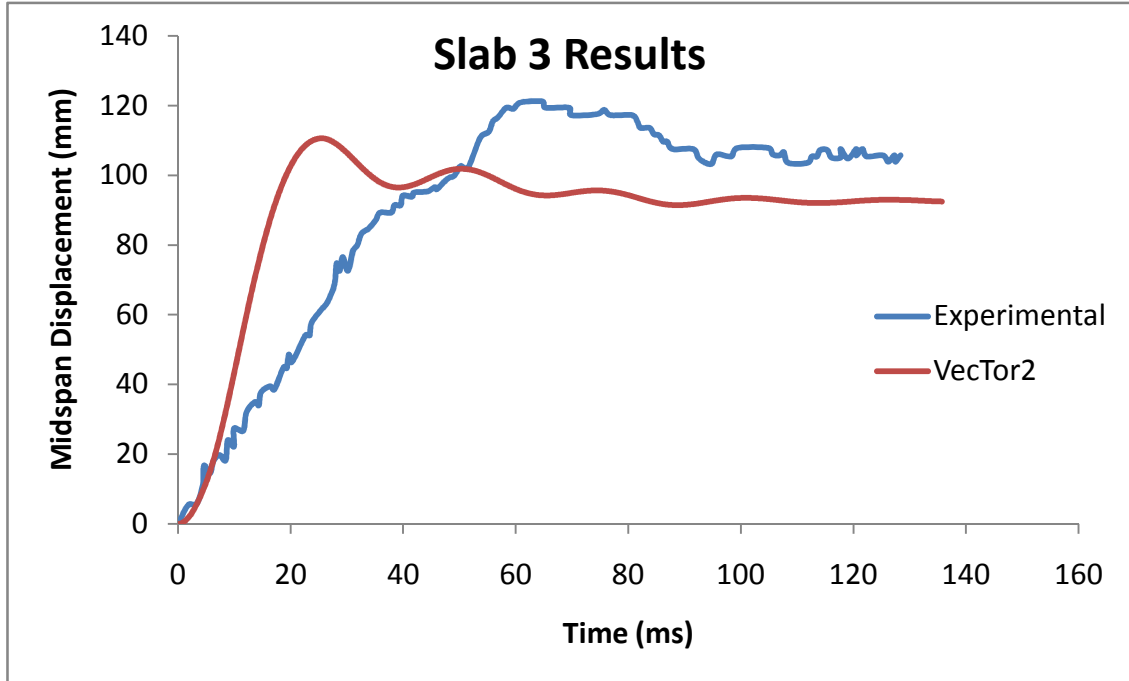


Figure 4-44: US Army Slab 3 results comparison.

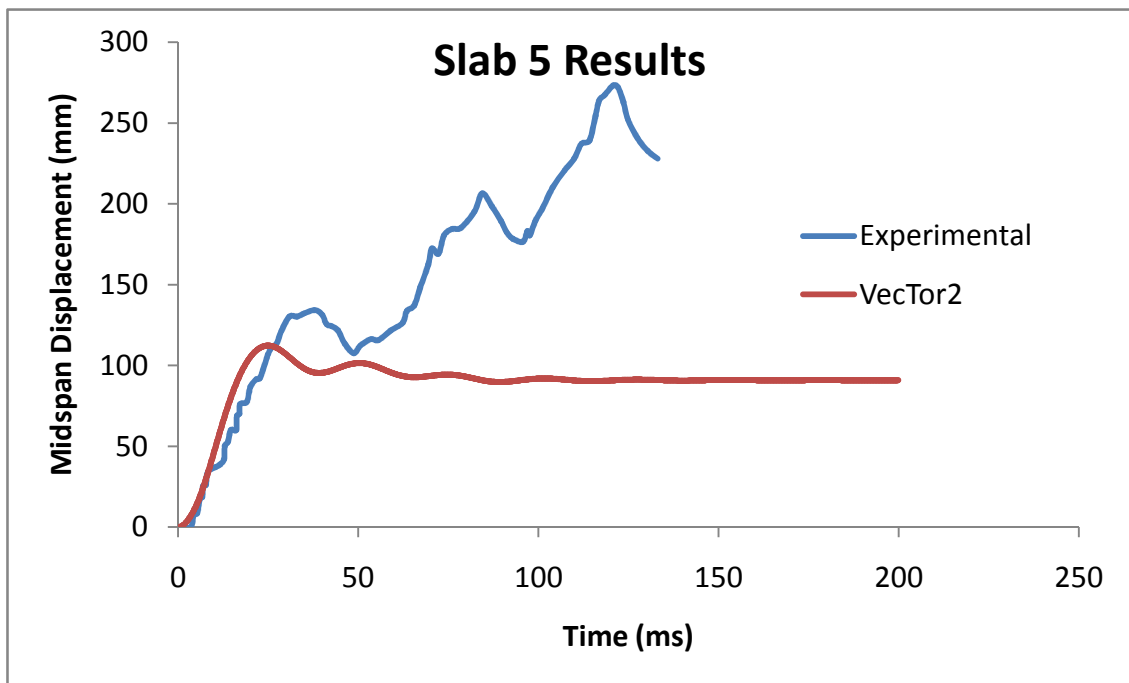


Figure 4-45: US Army Slab 5 results comparison.

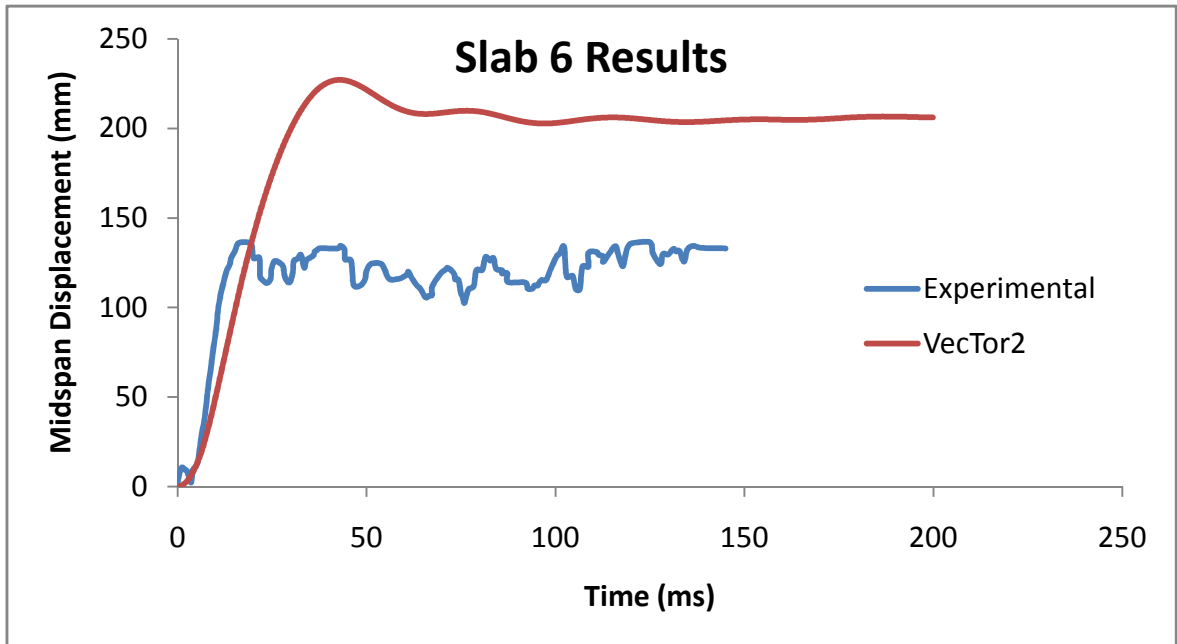


Figure 4-46: US Army Slab 6 results comparison.

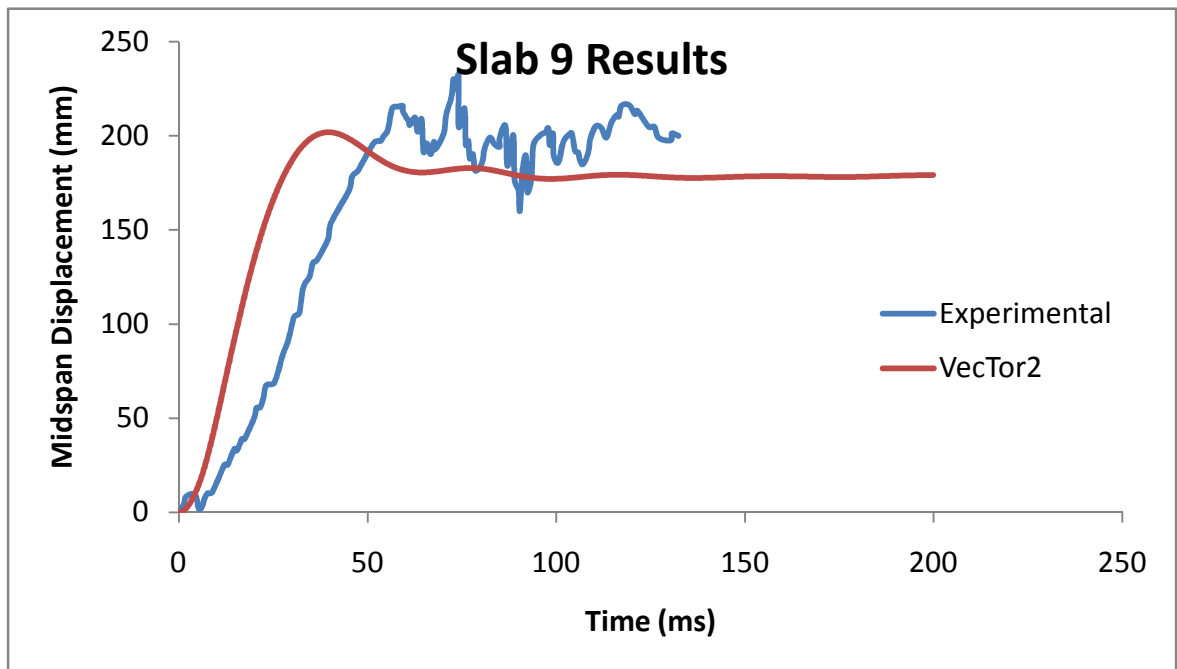


Figure 4-47: US Army Slab 9 results comparison.

4.4.4 Discussion of Slab Damage

Slab 3 consisted of both high-strength concrete and high-strength low-alloy vanadium reinforcement. The VecTor2 crack pattern for Slab 3 is shown in Figure 4-48, and the experimental damage is shown in Figure 4-49. Maximum observed crack widths were not reported; the slab damage was discussed in qualitative terms only. For Slab 3, VecTor2 predicted heavy cracking on the front face, with a maximum crack width of 5.7 mm. As shown in Figure 4-48, cracking was concentrated around the midspan, which is consistent with the experimental damage. The crack widths ranged from 0.01 mm (dark blue) to 5.7 mm (light green).

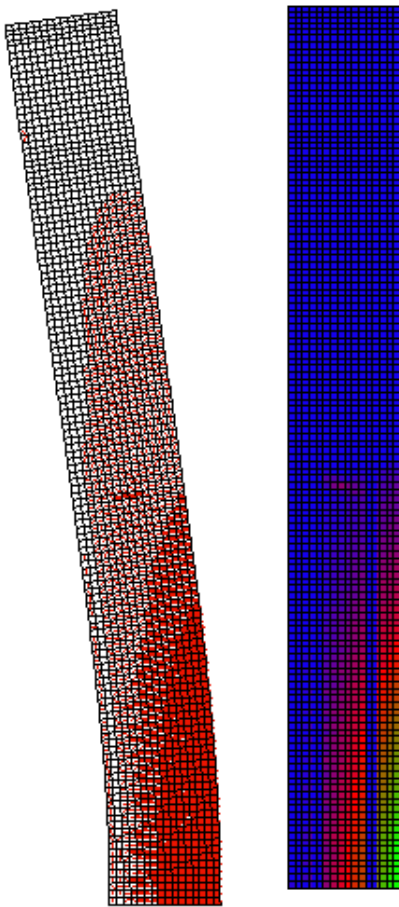


Figure 4-48:
Residual crack pattern predicted
by VecTor2 for Slab 3
(left: crack pattern; right: crack
widths).



Figure 4-49:
Experimental damage to front face of
Slab 3 (Robert and Johnson, 2009).

Slab 5 consisted of high-strength concrete and conventional reinforcement. Because of this, it was expected that the damage to Slab 5 would be slightly more severe than the damage to Slab 3, considering that the peak pressure and impulse imparted to each slab were similar. The damage predicted by VecTor2 is shown in Figure 4-50. While the crack pattern predicted for Slab 5 was similar to that predicted for Slab 3, the maximum crack widths for Slab 5 were slightly larger. The crack widths ranged from 0.01 mm (dark blue) to 6.1 mm (light green). The experimental damage is shown in Figure 4-51. The majority of cracks were concentrated about the midspan, and damage appears to be more severe than the damage sustained by Slab 3. The VecTor2 results appear to be consistent with the experimental results.

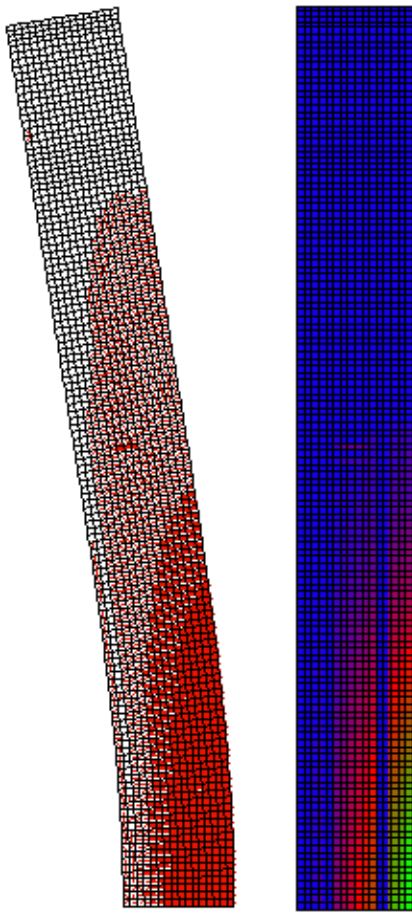


Figure 4-50:
Residual crack pattern predicted by
VecTor2 for Slab 5
(left: crack pattern; right: crack
widths).

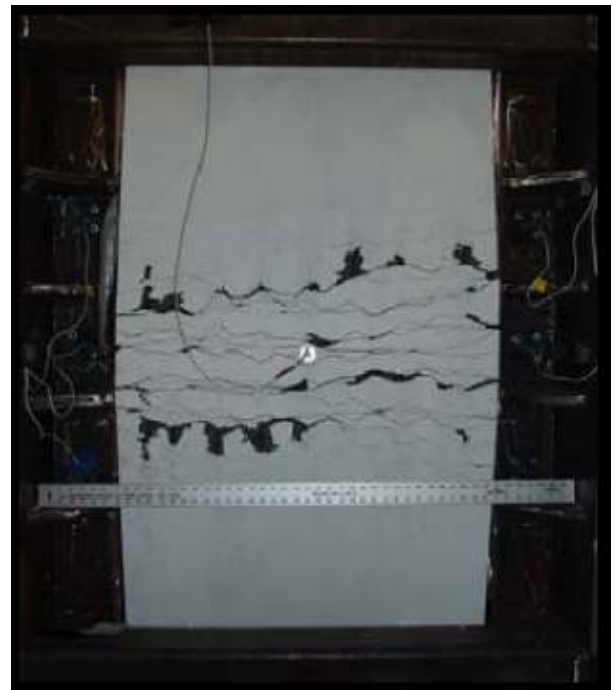


Figure 4-51:
Experimental damage to front face of
Slab 5 (Robert and Johnson, 2009).

Slab 6 consisted of regular strength concrete and high-strength low-alloy vanadium steel reinforcement. As mentioned in Section 4.4.3, based on the similarity of the stress-strain curves for the conventional and high-strength steel, it was expected that the damage to the slabs would be controlled primarily by the concrete strength and that the steel would play a smaller role in differentiating the slabs. In terms of damage to the slab, both the analytical and experimental results appear to support this assertion. VecTor2 predicted crack widths up to 12.8 mm (light green) on the front face of the slab, with the majority of cracks concentrated around the midspan as shown in Figure 4-52. In addition to cracking of the front face, VecTor2 also predicted damage to the back face of the slab. VecTor2 predicted large compressive strains around the midspan on the back face, indicating that some crushing was occurring. These compressive strains led to instability later in the analysis. As shown in Figure 4-53, severe damage to Slab 6 was also observed experimentally.

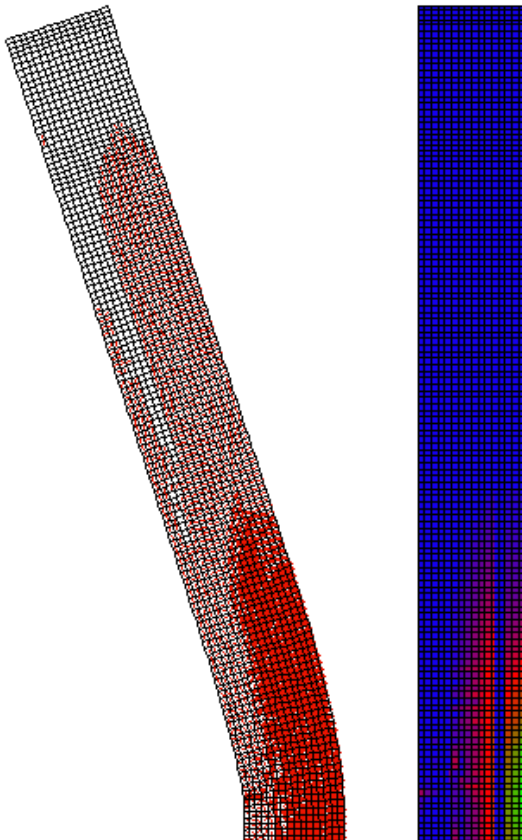


Figure 4-52:
Residual crack pattern predicted by
VecTor2 for Slab 6
(left: crack pattern; right: crack
widths).



Figure 4-53:
Experimental damage to front face of
Slab 6 (Robert and Johnson, 2009).

Slab 9 consisted of regular strength concrete and conventional reinforcement. Although the peak pressure and impulse imparted to Slab 9 was lower than that applied to Slab 3 and Slab 5, it was anticipated that Slab 9 would be more severely damaged than both of those slabs due to the fact that it consisted of regular strength concrete. VecTor2 predicted damage to both the front and back faces of the slab, as shown in Figure 4-54. On the front face, crack widths reached 10.3 mm (light green). Crushing of the back face was also predicted. The experimental damage to Slab 9 is shown in Figure 4-55.

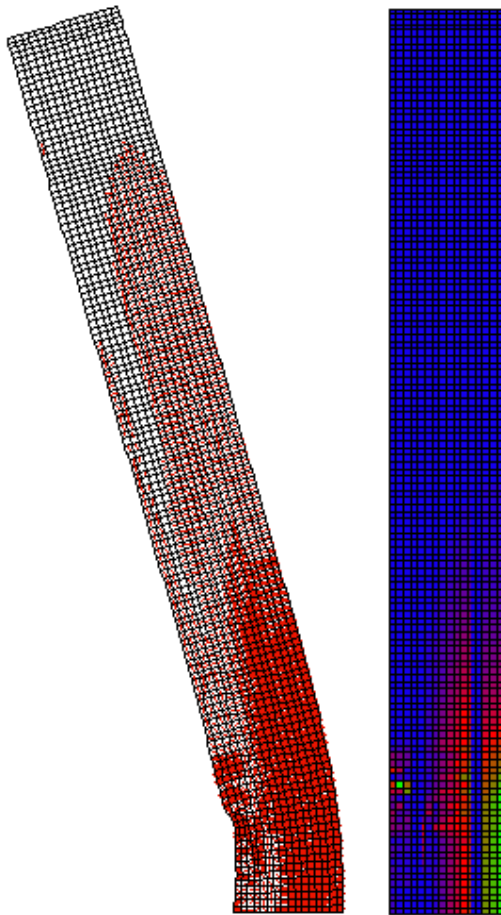


Figure 4-54:
Residual crack pattern predicted by
VecTor2 for Slab 9
(left: crack pattern; right: crack widths).



Figure 4-55:
Experimental damage to front face of
Slab 9 (Robert and Johnson, 2009).

4.4.5 Summary of Doubly-Reinforced U.S. Army Slabs

The four specimens discussed in this section were shock tube tested panels subjected to very high impulse loadings. The average peak pressure and impulse for these tests were 382 kPa and 7.31 kPa-sec, respectively. In terms of displacement-time response, all specimens experienced very large peak displacements and, all were heavily damaged.

Overall, VecTor2 did a good job predicting the peak displacements and also did a fair job predicting the level of damage. In terms of relative damage, VecTor2 matched the experimental results quite well.

In terms of crack widths, it is apparent that specifying a crack spacing caused a decrease in crack widths. In the University of Ottawa modeling, for Blast 3, VecTor2 predicted maximum crack widths in the range of 90 mm. In that analysis, crack spacing was not specified, and the default crack spacing was used. For the impulse magnitudes of the University of Texas and University of Ottawa specimens, good results were achieved without specifying crack spacing. However, for the blast magnitudes of these four specimens, it was necessary to specify crack spacing.

4.5 U.S. Army Singly-Reinforced Shock Tube Specimens

4.5.1 Introduction

The specimens discussed in this section were part of a study carried out at ERDC-Vicksburg using the Blast Load Simulator, and were part of a blast simulation contest sponsored by the American Concrete Institute (ACI) and University of Missouri-Kansas City (UMKC) School of Computing and Engineering. The goal of the contest was to predict the response of four singly-reinforced reinforced concrete slabs under blast loading.

Two sets of three slabs were tested, and in each set there were two unique blast load profiles. Since there was a duplicate specimen in each test series, a total of four specimens were modeled. The first set of specimens, Specimens 2 and 6, consisted of normal strength concrete (34 MPa) and conventional reinforcement (414 MPa). The second set of test specimens, Specimens 1 and 5, consisted of high strength concrete (100 MPa) and high strength reinforcement (570 MPa). Table 4-10 summarizes the peak pressures and impulses for each specimen.

Table 4-10: US Army Singly-Reinforced Specimens Peak Pressure and Impulse

Specimen	Peak Pressure (kPa)	Impulse (kPa-sec)
1	342.7	6.895
2	339.1	6.205
5	275.1	5.24
6	282.4	5.309

4.5.2 Specimen Details and VecTor2 Modeling

These specimens had the same dimensions as the doubly-reinforced specimens discussed in the previous section; the slab dimensions were 64 x 33.75 x 4 in (1626 x 857 x 102 mm). The reinforcement consisted of #3 bars on the back face of the slab, opposite the blast face. The reinforcement is shown in Figure 4-56. In VecTor2, half of the specimen was modeled, and the longitudinal reinforcement was modeled using discrete truss elements with a total area of 639 mm², representing the nine #3 (US) bars. The horizontal bars were modeled as smeared, and were only specified over a portion of the slab starting at the back face (the face furthest from the blast). The reinforcement ratio used was 0.215%. The reinforcement properties were derived from the stress-strain curves provided by the competition organizers, shown in Figure 4-57. The concrete properties were calculated based on the concrete compressive strengths provided. The concrete and steel material properties used in the analyses are summarized in Table 4-11. A crack spacing of 100 mm was specified; this is the same crack spacing used in the doubly reinforced analyses. The VecTor2 model is shown in Figure 4-58.

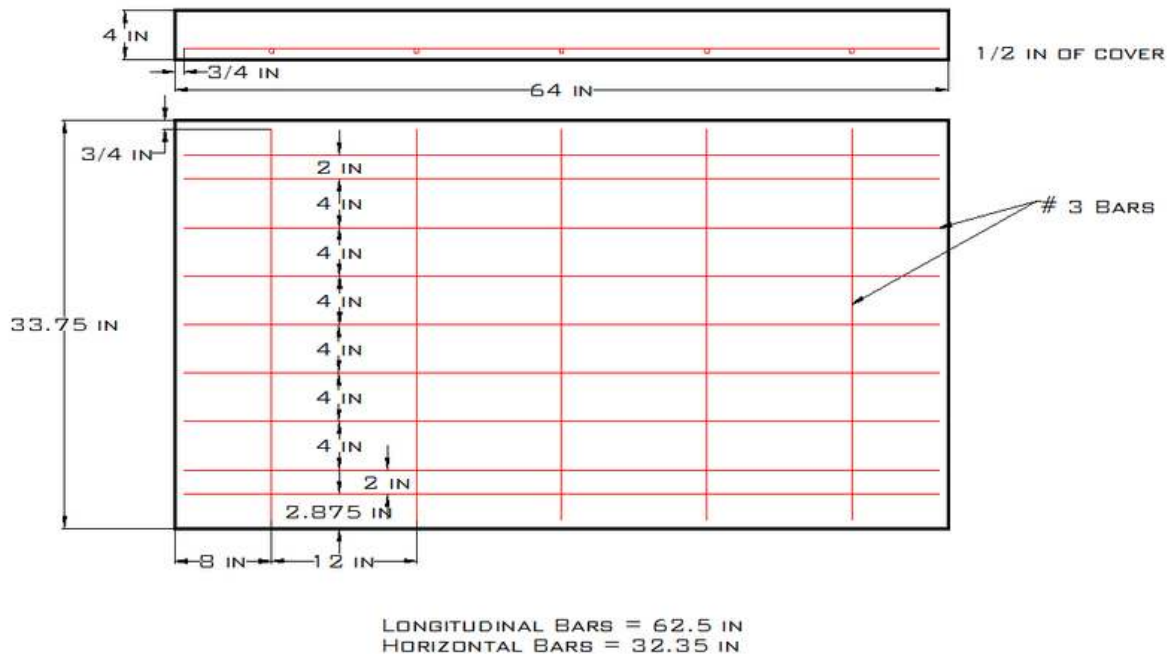


Figure 4-56: Specimen details for singly-reinforced specimens tested at ERDC-Vicksburg (UMKC, 2012).

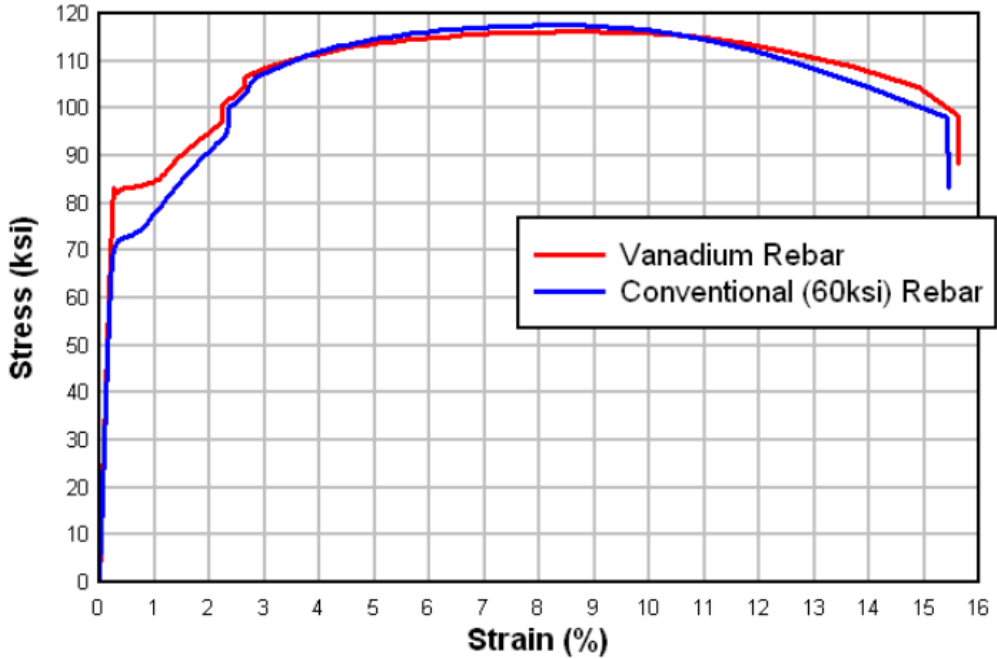


Figure 4-57: Stress-strain curves for vanadium (high strength) and conventional reinforcement (UMKC, 2012).

Table 4-11: Reinforcement and Concrete Material Properties for Singly-Reinforced U.S. Army Specimens

Concrete Properties			
Normal Strength		High Strength	
f_c (MPa)	37	f_c (MPa)	80
f_t (MPa)	2.01	f_t (MPa)	2.95
E_c (MPa)	27100	E_c (MPa)	36590
ϵ_0 ($\times 10^{-3}$)	2.10	ϵ_0 ($\times 10^{-3}$)	2.70
ν	0.210	ν	0.261
Reinforcing Steel Properties			
Conventional Reinforcement		High Strength Low Alloy Vanadium Reinforcement	
f_y (MPa)	496	f_y (MPa)	572
f_u (MPa)	810	f_u (MPa)	807
E_s (MPa)	198576	E_s (MPa)	212000
ϵ_{sh} ($\times 10^{-3}$)	5	ϵ_{sh} ($\times 10^{-3}$)	10
ϵ_u ($\times 10^{-3}$)	85	ϵ_u ($\times 10^{-3}$)	85

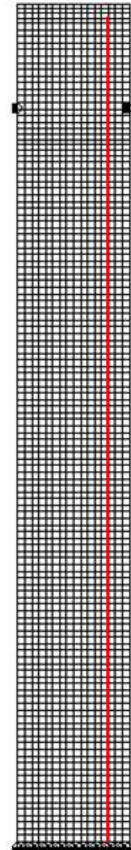


Figure 4-58: VecTor2 model for US Army singly-reinforced slabs (UMKC, 2012).

The supports conditions for this test series were the same as those used in the doubly-reinforced tests discussed in the previous section. They are shown in Figure 4-59 and Figure 4-60. In VecTor2, a simply-supported condition was modeled by specifying a restraint in the direction of the impulse at the centre of the structural tube supporting the back face of the slab.

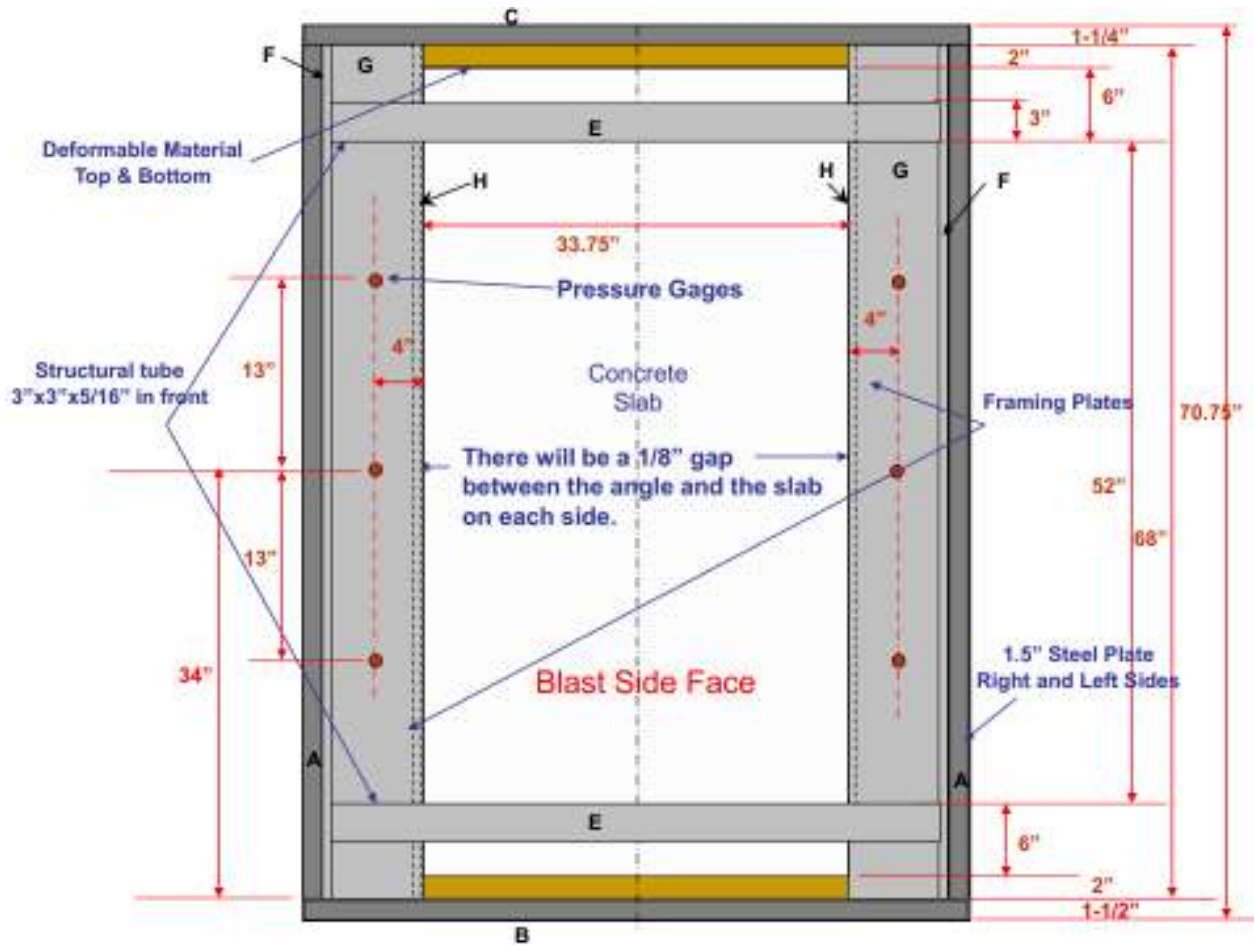


Figure 4-59: Support conditions for blast side of US Army specimens (UMKC, 2012).

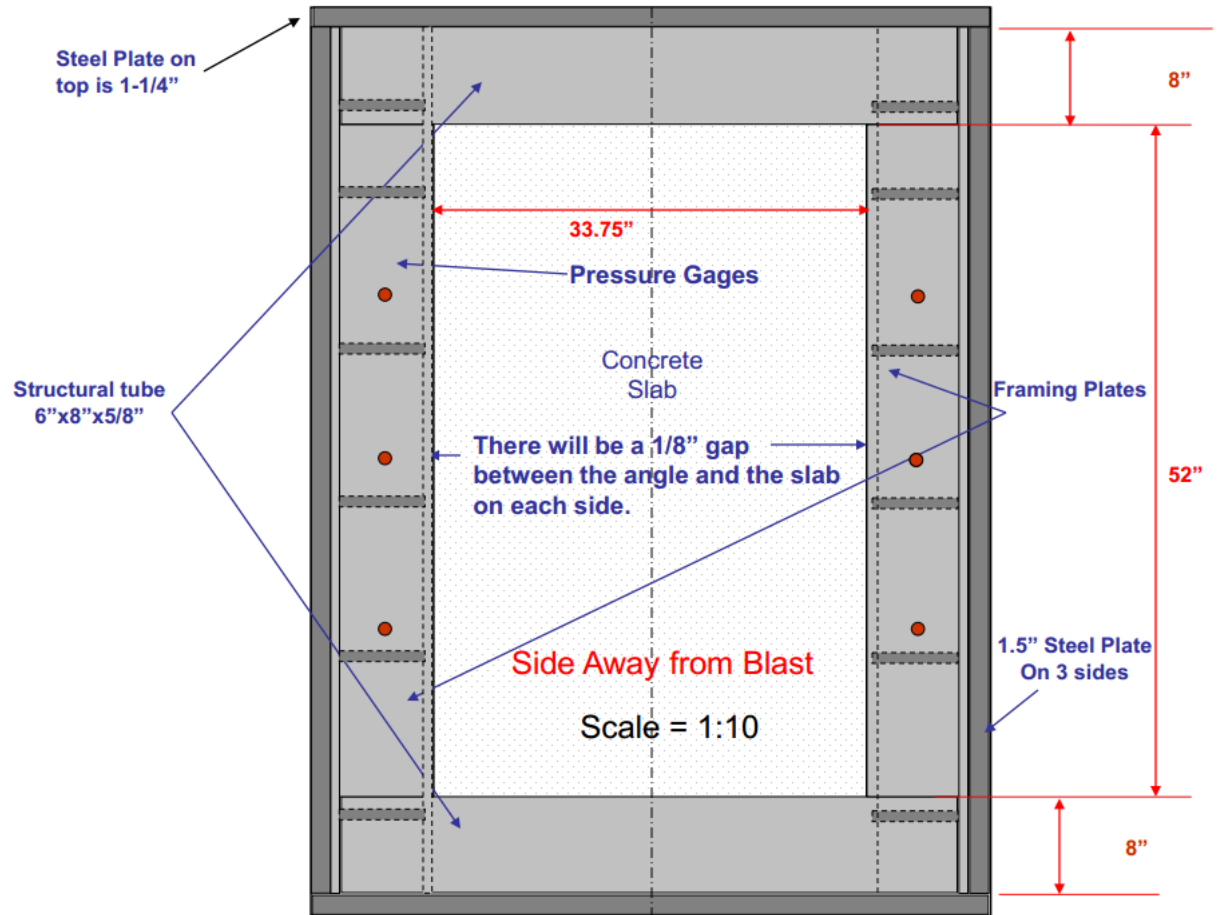


Figure 4-60: Support conditions for non-blast side of US Army specimens (UMKC, 2012).

Nodal loads were used to apply the impulse force. The applied loads were derived from the reported pressure-time histories, shown in Figure 4-61 and Figure 4-62.

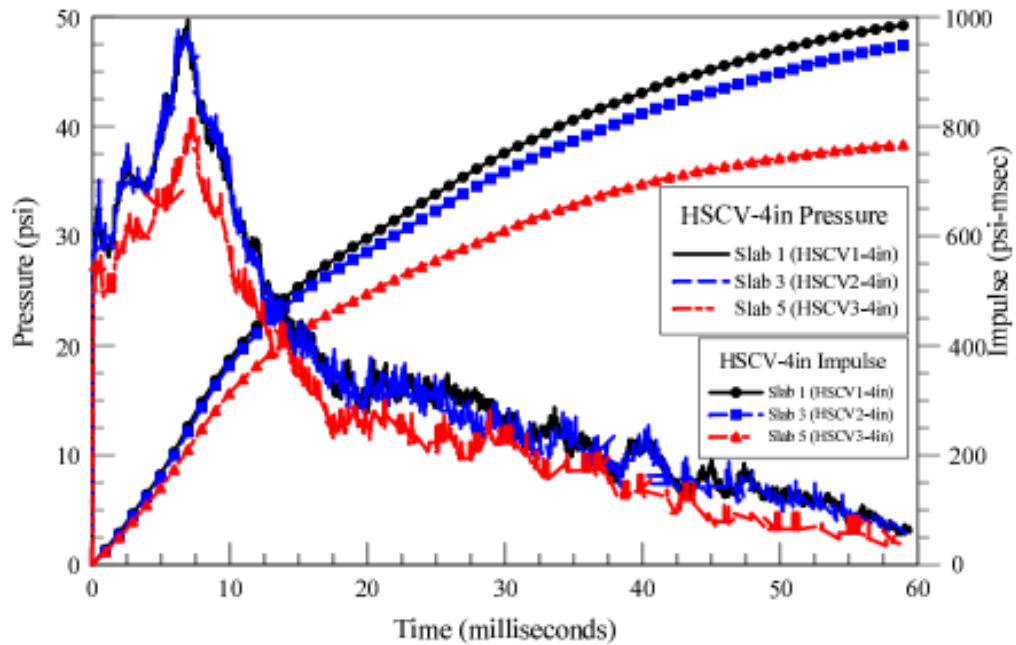


Figure 4-61: Experimental pressure-time histories for high strength specimens (UMKC, 2012).

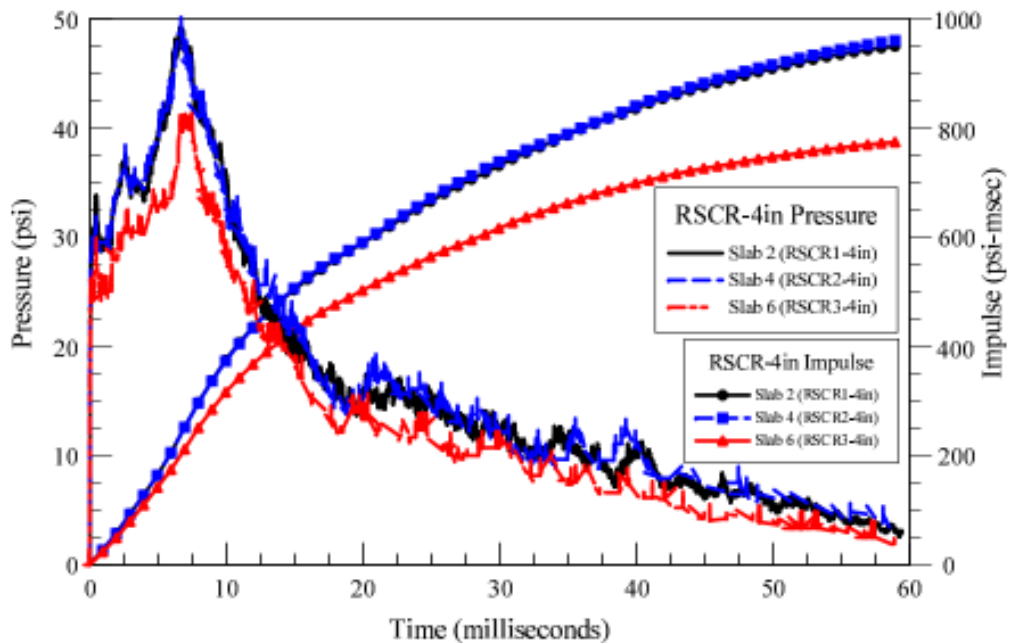


Figure 4-62: Experimental pressure-time histories for regular strength specimens (UMKC, 2012).

Default concrete material properties were used, except for the concrete stress-strain curve, for which the Hoshikuma model was used. Strain rate effects were not considered. In terms of damping, the same damping ratios were used for all four analyses. For the first mode, 3% damping was specified; for the second mode, 5% damping was specified.

Despite the high damping, stability issues arose due to crushing on the blast face of the specimens. Rather than increase the damping further, which would decrease the displacements significantly, element erosion was implemented for Slabs 1, 2, and 6. Since the instability appeared to be arising due to extremely large compressive strains in a few discrete locations on the blast face of the slabs, an erosion criterion based on the maximum compressive strain was implemented. A number of analyses were done in an effort to set the erosion strain high enough such that it had a minimal impact on the analysis results; the erosion criterion decided upon was a principal compressive strain of 10×10^{-3} . Introducing element erosion eliminated the instability issue, but undoubtedly affected the analysis results. This effect will be discussed in the results section.

4.5.3 Results and Discussion

This test series was associated with a blind prediction competition, which concluded in January 2013; the experimental results have not yet been released. The calculated peak displacements are summarized in Table 4-12, and the displacement-time histories predicted by VecTor2 are shown in Figure 4-63.

Table 4-12: Peak and Residual Displacements for Singly-Reinforced Reinforced Concrete Shock Tube Tested Slabs

Slab	Results		
	Time of Peak Displacement (ms)	Peak Displacement (mm)	Residual Displacement (mm)
1	59.0	144.7	138.4
2	77.9	267.7	265.4
5	23.6	75.4	56.5
6	66.6	169.5	162.7

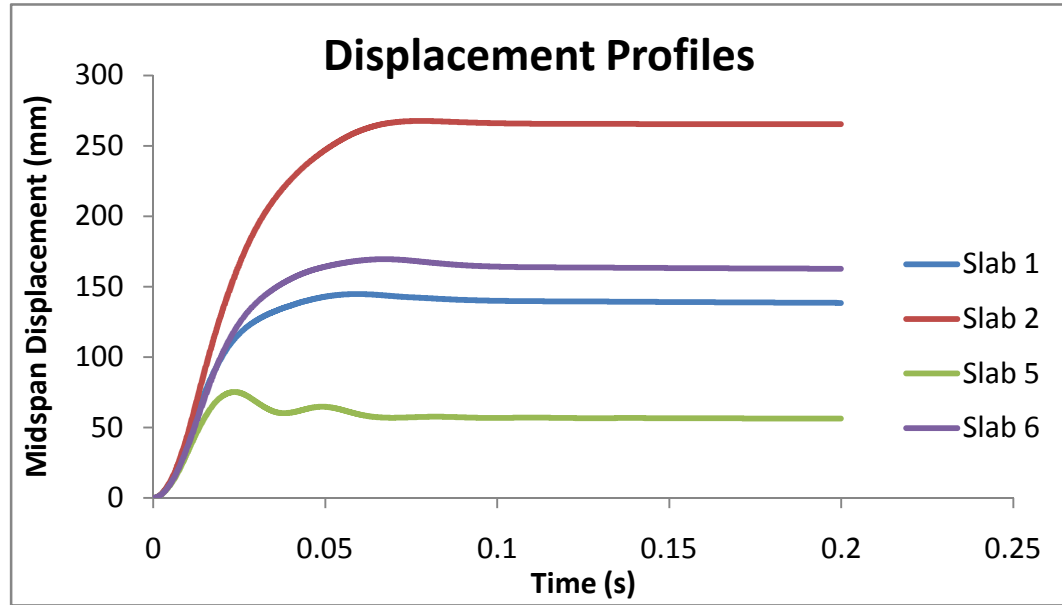


Figure 4-63: Displacement-time histories for singly-reinforced shock-tube tested reinforced concrete panels.

In all four of the analyses, the longitudinal reinforcement yielded and reached stresses of just under the ultimate stress. In addition to yielding, in Slabs 1, 2, and 6 there was some crushing on the blast face. In these three analyses, a few isolated areas of highly compressive strains developed on the blast face of the slab, and initially caused stability issues. As mentioned previously, due to the very high compressive strains that occurred on the impact face of the slab, element erosion was introduced, eliminating the instability issues that had been observed in the initial analyses. However, introducing element erosion clearly affected the analysis results. As can be seen in the displacement profiles, there is no post-peak damping/oscillation for Slabs 1, 2, and 6; these are the analyses in which element erosion was used. The reasons for the change in post-peak response are not yet known.

Based on the stress-strain curves, the two types of steel are quite similar, and analysis results have also shown that they behave quite similarly. It doesn't appear that the Vanadium steel played a major role in increasing specimen strength; the concrete strength was the most influential parameter.

Comparing the displacement results for Slabs 2 and 6, both of which had normal strength concrete and conventional reinforcement, it is clear that the displacement response is sensitive to

the pressure and impulse. Because of this, one of the sources of error inherent in these types of analyses is the load profile. Error in measuring the blast pressure profile may affect the analysis results dramatically and result in a large discrepancy between analytical and experimental results.

Another source of error is the modeling of the supports. The supports were not modeled explicitly, and were simplified as pin supports at the centre of the steel tube support frame. While the supports for the University of Texas and University of Ottawa specimens, discussed in Sections 4.2 and 4.3, were modeled using compression-only truss bars, the effect was basically the same as if pin supports were used. The compression-only truss bar areas were large enough that movement in the direction of the impulse was restrained, while rotation remained unrestrained. In order to simplify the modeling for the US Army specimens, the compression-only truss bars were replaced with pins.

Comparing the results for Slabs 1 and 5, both of which had high strength concrete and vanadium reinforcement, to the results for Slabs 2 and 6, the effect of using high strength materials, particularly high strength concrete, can be seen. The blast pressure profiles for Slab 1 and Slab 2 are basically the same, and the peak displacement for Slab 2 (normal strength) is almost double that of Slab 1 (high strength); the peak displacement of Slab 6 (normal strength) is more than double that of Slab 5 (high strength).

The damage to Slab 1 is shown in Figure 4-64. The maximum crack width at peak was 10.7 mm, shown in green. This crack width was observed at midspan and also in another location away from midspan. The other cracks were approximately 4.0 mm to 6.5 mm on average; this range of crack widths is shown in red. The principal compressive strains are shown to illustrate the elements that were eroded. In the principal compressive strain picture, the elements that are not green have been eroded.

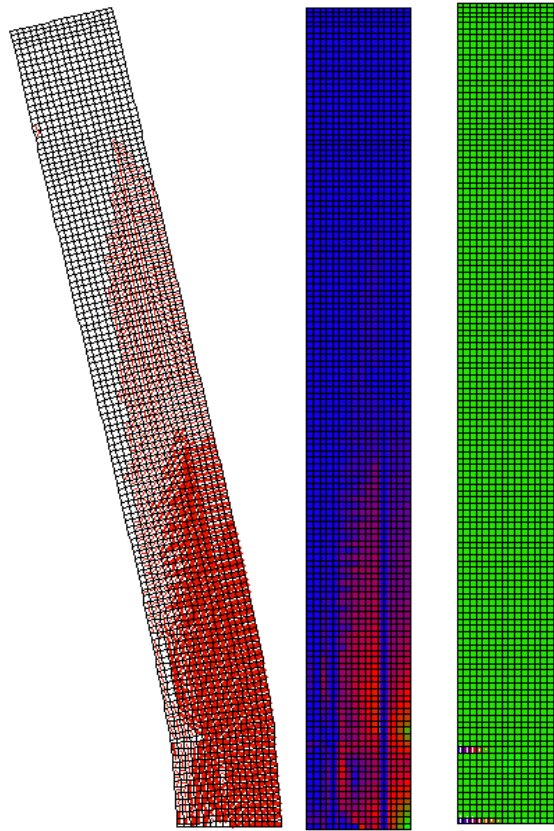


Figure 4-64: Crack pattern at peak predicted by VecTor2 for Slab 1 (left: crack pattern; centre: crack widths; right: principal compressive strain).

The calculated damage to Slab 2 is shown in Figure 4-65. The maximum crack width was 12.5 mm at peak; this maximum crack width occurred at midspan, and at other locations near midspan, and is shown in green. The average crack widths away from midspan, ranged from 3.1 mm to 8.9 mm.

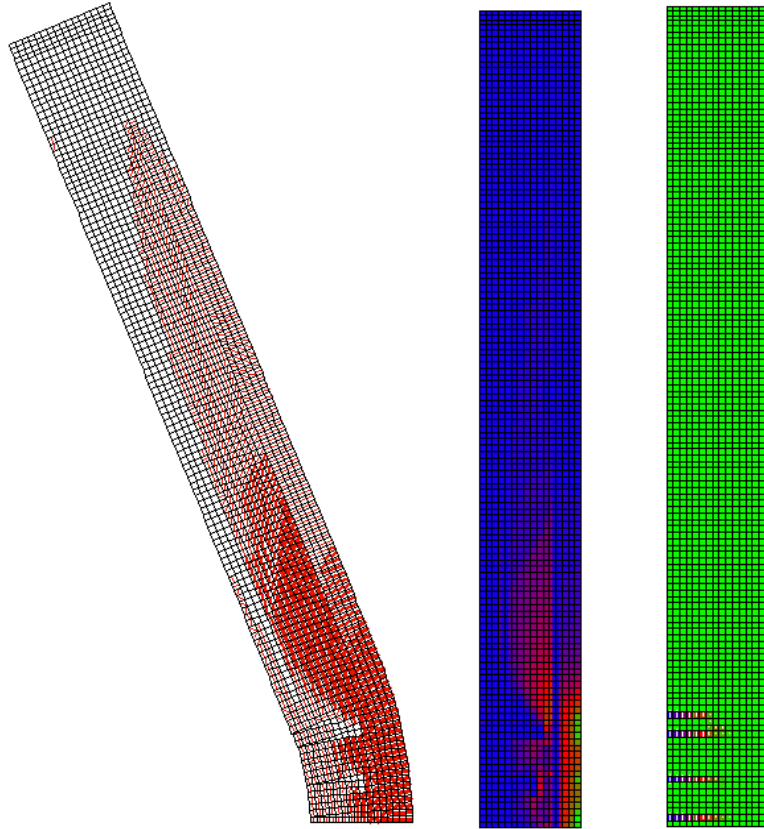


Figure 4-65: Crack pattern at peak predicted by VecTor2 for Slab 2 (left: crack pattern; centre: crack widths; right: principal compressive strain).

The damage at peak, for Slab 5, is shown in Figure 4-66. The maximum crack width was 4.3 mm. Along the front face of the slab, away from the blast face, the crack widths ranged from 3.2 mm to 4.3 mm (shown in green). In other locations the crack widths ranged from 1.1 mm to 3.0 mm.

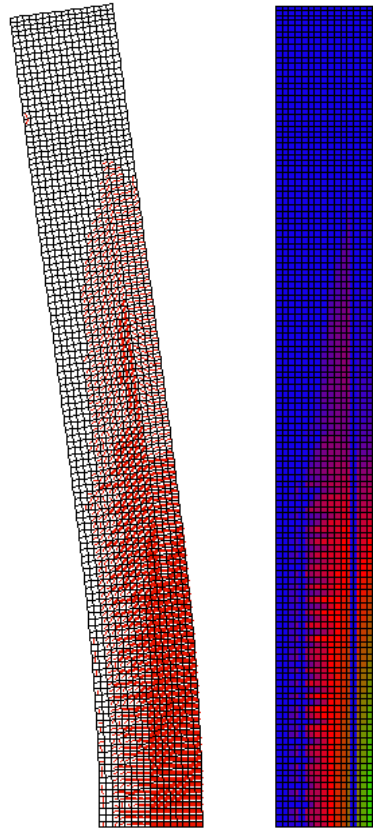


Figure 4-66: Crack pattern at peak predicted by VecTor2 for Slab 5 (left: crack pattern; right: crack widths).

The damage at peak for Slab 6 is shown in Figure 4-67. The maximum crack width, shown in green, was 9.9 mm. The average crack widths were 3.3 mm to 5.8 mm, shown in red.

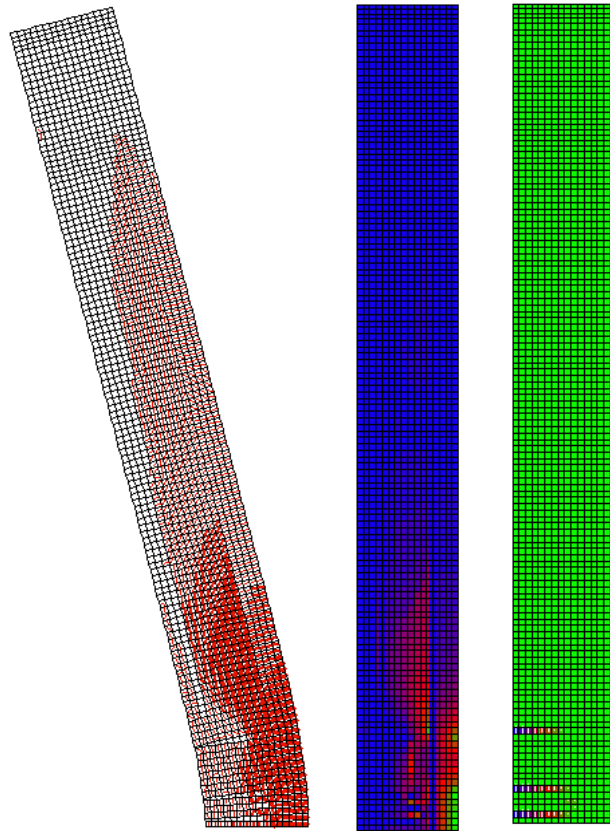


Figure 4-67: Crack pattern at peak predicted by VecTor2 for Slab 6 (left: crack pattern; centre: crack widths; right: principal compressive strain).

As illustrated by the crack patterns for the four slabs, the use of element erosion not only had an effect on the peak displacements and the displacement-time histories, but also on the crack patterns predicted by VecTor2. Element erosion was used in the analyses for Slabs 1, 2, and 6, and the crack patterns for these three specimens are distinctly different from the crack pattern predicted for Slab 5. The cracks for Slab 5 are evenly distributed, decreasing from a peak width at midspan to cracks of negligible widths away from the midspan. The crack patterns for Slabs 1, 2, and 6 are not as even. In each of these slabs, the maximum crack widths occur both at midspan and also in other locations, with cracks of smaller width in-between.

In terms of element erosion, while the erosion criterion used in these analyses eliminated the instability that was occurring, it is not recommended that this criterion be implemented permanently in VecTor2. Further analyses should be done, using many specimens, to determine a more general erosion criterion.

4.6 Summary and Discussion of 2D Verification Studies

The modeling of structures subjected to blast loading is complex, with many influencing variables including material properties, support conditions, and applied load. The effect of the peak pressure, shape of the pressure-time history, and total impulse are all important factors which contribute to the response of the specimen. Shock tube experiments present additional complexities in terms of the interaction of the shock tube wall with the blast, the impact of the negative phase on the structure and the method of measuring the pressure and impulse delivered to the slab. Yet another consideration is the assumption that the load applied to the specimen is a uniformly distributed pressure. While the shock tube is designed to impart a uniform pressure to the specimen, it may be the case that the pressure is larger in some locations than others, which will affect the peak displacement.

The use of strain rate effects is also an important consideration. In the SDOF analyses that accompanied the University of Texas and University of Ottawa experiments, strain rate effects were used. In previous dynamic studies carried out using VecTor2, it had been found that incorporating strain rate effects resulted in an overly stiff response since the confining stresses generated by the inertia of the structure already provide for some apparent gain in strength (Saatci and Vecchio, 2009). For the University of Texas specimen, the peak displacements for the simply-supported case decreased by approximately 15% when strain rate effects were included. For the University of Ottawa specimen, the peak displacements for two of the blasts were already underestimated, and it appears that introducing strain rate effects would be unconservative. Given the issues encountered in the experiment, additional analyses to determine the effect of accounting for strain rate effects were not carried out.

Given the uncertainty associated with modeling blast loading, the results obtained for the first two verification studies are quite good. With one exception, all peak displacements are within 10% of the experimental values, which is considered an acceptable margin of error for a complex modeling problem.

The results obtained for the doubly-reinforced U.S. Army slabs are also good, considering the impulse magnitudes. While there was some discrepancy between the VecTor2 and experimental stiffnesses, the peak displacements calculated by VecTor2 were within approximately 15% of the experimental peak displacements for three of the slabs. In terms of modeling, there were two

changes from the approach taken in modeling the University of Texas and University of Ottawa specimens. Firstly, much higher damping was required. Damping ratios of 3% and 5% were used for the first two modes in the U.S. Army analyses, compared to less than 1% for the first two modes in the University of Texas and University of Ottawa simulations. Secondly, it became necessary to specify crack spacing. The specification of crack spacing made the results more stable, meaning that damping did not have to be increased further.

5 Modeling of IRIS_2012 Specimens

5.1 Introduction

The IRIS_2012 workshop was a follow-up to IRIS_2010, the objective of which was to conduct a benchmark study to evaluate existing techniques for analyzing structures under impact loads. Participants in IRIS_2010 performed analyses of one of the Meppen tests, and also submitted blind simulation results for two additional impact tests. The blind simulation tests consisted of one soft and one hard missile impact, conducted at VTT in Finland. In the soft missile impact test, known as VTT-B1, the reinforced concrete target experienced minor flexural damage. In the hard missile test, VTT-P1, the missile completely perforated the slab. A total of twenty eight teams from twenty countries participated in IRIS_2010, and a wide range of results were submitted for the two blind simulations. For the flexural test, where the experimental peak displacement was approximately 30 mm, results for peak displacement ranged from less than 10 mm to greater than 60 mm. In the hard missile test, there were many teams that did not predict perforation, even when using programs capable of predicting such a result. For both the flexural and punching tests, there was a large amount of scatter in the numerical results (see Figure 5-1 and Figure 5-2).

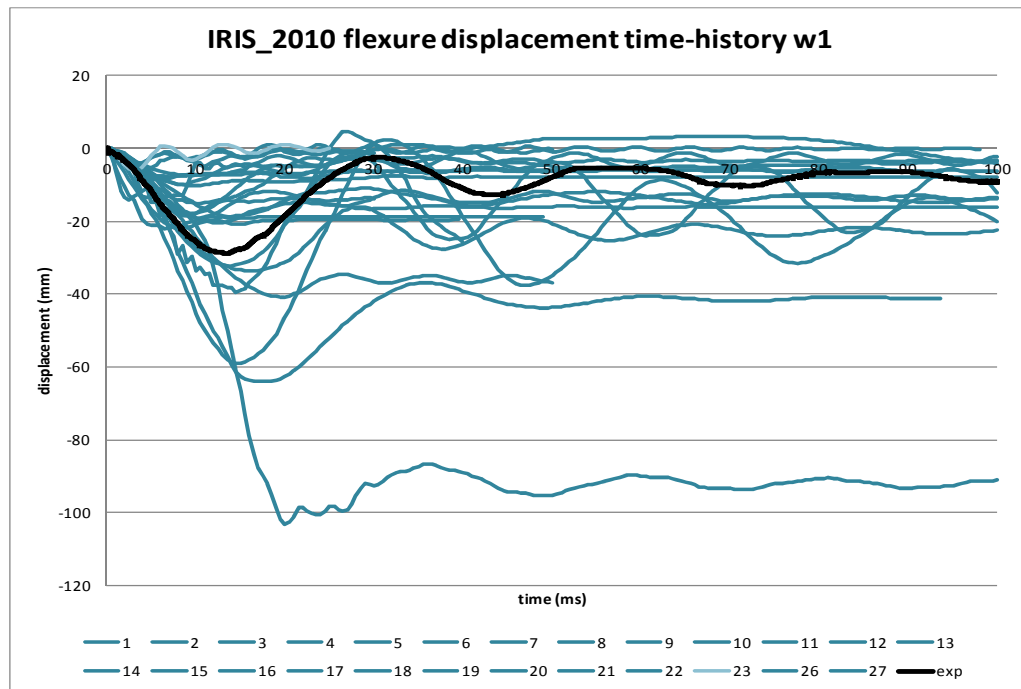


Figure 5-1: Centre displacement history of VTT-B1 (blind simulation results from IRIS_2010).

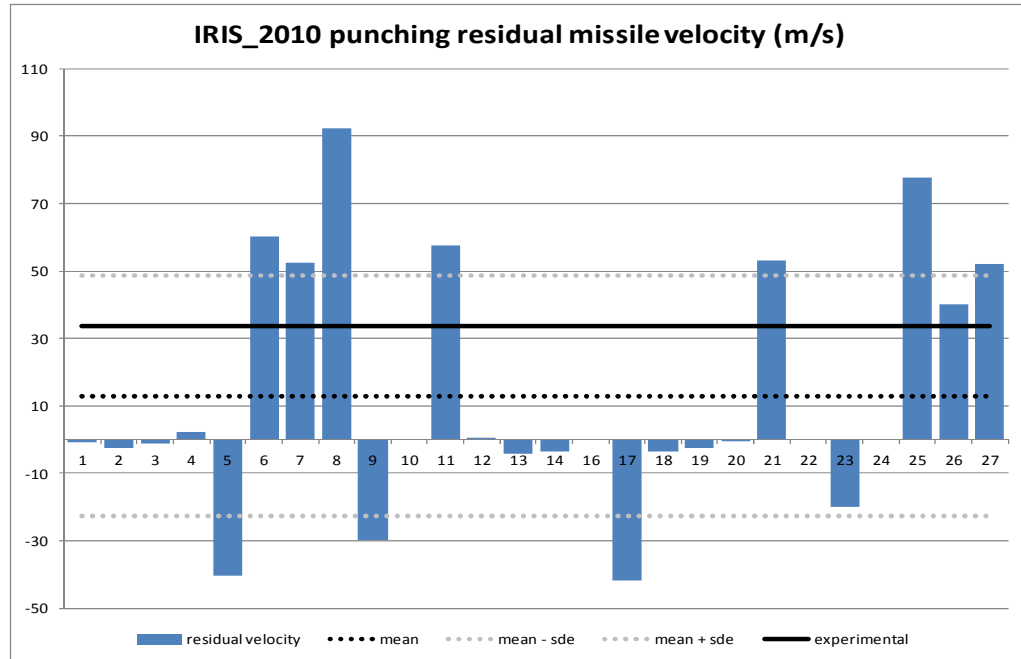


Figure 5-2: VTT-P1 missile residual velocity (blind simulation results from IRIS_2010).

The purpose of IRIS_2012 was to model the two VTT tests again, using a single set of material properties. The primary goal was to reduce the scatter observed in the IRIS_2010 numerical results. The hope was that using a single set of material properties, which included triaxial test results to be used for the calibration of material models, would accomplish this. The second goal of IRIS_2012 was to promote simplified analytical tools that can be used in conjunction with more complex analysis tools to provide a reliable prediction of the behavior of reinforced concrete structures under impact loading conditions. The modeling results discussed in this chapter represent a simplified approach.

In this chapter, the results of three sets of analyses are presented. Firstly, the results of triaxial test simulations are presented, followed by the results for VTT-B1 and VTT-P1.

5.2 IRSN Triaxial Tests

The IRSN uniaxial and triaxial concrete test series was carried out at the University Joseph Fourier in Grenoble, as part of the doctoral work of M. Vu (2007). A total of nine concrete cylinders, each with a diameter of 70 mm and a height of 140 mm, were tested. Three specimens were unconfined, and six specimens were tested under four different levels of confinement. Confinement was applied through the use of a confining fluid, and a latex membrane was used to prevent the fluid seeping into the concrete. The specimen data are summarized in Table 5-1.

Table 5-1: IRSN Triaxial Specimen Data

Specimen	1	2	3	4	5	6	7	8	9
Confining Pressure (MPa)	-	-	-	15.5	15.5	26	26	47	100
Cylinder Height (mm)	139.2	138.7	139.3	139.6	138.5	137.6	139.3	139.1	140.7
Cylinder Diameter (mm)	69.9	69.9	69.9	69.9	70	69.9	70.2	70.0	69.9

As suggested by the organizing committee of the IRIS_2012 workshop, IRSN Specimens 2, 4, 7, 8, and 9 were modeled in VecTor2, both at the material and structural levels. At the material level, a single element was used to eliminate the possibility of instability due to element interactions. For the structural-level modeling, a mesh of 2 x 2 mm elements was used. For concrete confined strength, the two material models examined were the Kupfer/Richart and Montoya/Ottosen models. The following four models were investigated for concrete dilatation: Fixed Poisson Ratio, Variable—Kupfer, Montoya 2003, and Montoya with Limit. For each specimen and analysis type, a total of eight analyses were performed, allowing for all combinations of confined concrete strength and concrete dilatation models to be examined. Details of the confinement and dilatation models can be found in Wong et al. (2012).

It is important to note that for all these analyses, only four concrete material parameters were specified: compressive strength, modulus of elasticity, strain at peak stress, and Poisson's ratio. As well, in terms of material models used, the concrete stress-strain model used was Hoshikuma, and all other material models were default models. The only material models that varied between analyses were the concrete confinement and concrete dilatation models.

5.2.1 Model Details

A quarter of the cylinder was modeled in VecTor2 and, since VecTor2 is a 2D program, the cylinder cross section was simplified to a square one of equivalent area. Confinement was modeled in two ways. To model in-plane confinement, nodal forces were applied such that the sum of the forces divided by the area was equal to the confinement pressure. The out-of-plane confinement was modeled using smeared reinforcement. The smeared reinforcement was specified such that the confining pressure was equal to ρf_y of the steel. The ultimate strain of the steel was specified such that the strain hardening portion of the curve was very shallow and the steel stress remained 400 MPa throughout the simulation. The model parameters are summarized in Table 5-2 and Table 5-3. The concrete strength, modulus, and Poisson ratio reported experimentally were used in the analyses.

Table 5-2: VecTor2 Triaxial Test Model Data

Specimen	Confinement (MPa)	Width (mm)	Height (mm)	Area (mm ²)	Equiv. Width (mm)	Model Width (mm)	Model Height (mm)	Steel (%)	Nodal Load (kN) (2x2 mesh)
2	-	69.9	138.7	3833.1	61.9	31.0	69.4	-	-
4	15.5	69.9	139.6	3833.1	61.9	31.0	69.8	3.9	0.9
7	26	70.2	139.3	3865.0	62.2	31.1	69.6	6.5	1.6
8	47	70.0	139.1	3844.0	62.0	31.0	69.6	11.8	2.8
9	100	69.9	140.7	3841.9	62.0	31.0	70.4	25.0	6.1

Table 5-3: Material Properties Specified in VecTor2 Triaxial Analyses

Concrete			Steel	
Material Property	Specimen 2	Specimens 4, 7, 8, and 9	f_y (MPa)	400
f'_c (MPa)	69	66.93	f_u (MPa)	405
E (MPa)	29663	29670	e_y ($\times 10^{-3}$)	2
ν	0.22	0.223	e_{sh} ($\times 10^{-3}$)	2.05
ϵ_0 ($\times 10^{-3}$)	2.5	2.5	$\Delta\epsilon_p$ ($\times 10^{-3}$)	3

5.2.2 Analysis Results

The numerical results for all eight sets of analyses for each specimen are presented in this section. The stress-strain curves for the material model combination of Montoya/Ottosen for confining pressure and Variable-Kupfer for concrete dilatation are shown; at the structural level, this combination of material models yielded the longest post-peak responses. For all analyses, the peak stress is indicated, as well as the strain at peak stress. For the structural-level analyses, results are also compared to the associated material-level test. Table 5-4 summarizes the experimental results.

Table 5-4: Triaxial Experiment Results

Specimen	Confining Lateral Stress (MPa)	Peak Axial Stress (MPa)
2	-	69
4	15.5	130
7	26	165
8	47	225
9	100	400

5.2.2.1 Material-Level Results

This section summarizes the material-level results for the triaxial tests. The model used at the material level is shown in Figure 5-3. As mentioned previously, confinement was modeled in two ways, through the use of nodal forces for in-plane confinement and smeared reinforcement for out-of-plane confinement. The load in the vertical direction was applied with nodal displacements, in increments of 0.001 mm.

In all simulations at the material level, an appreciable amount of post-peak response was captured. In addition to the results obtained using the Montoya/Ottosen (confinement) and Variable-Kupfer (dilatation) models, stress-strain results will also be presented for the Kupfer/Richart (confinement) and Montoya 2003 (dilatation) simulations, which were closest to the experimental results.

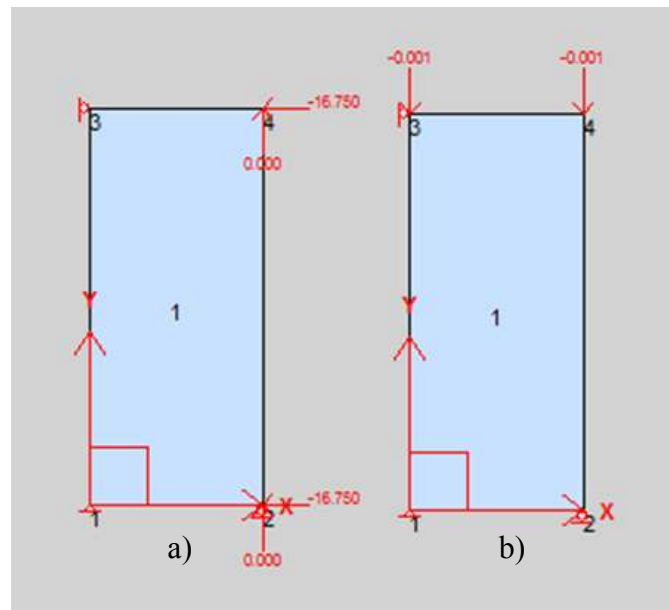


Figure 5-3: VecTor2 triaxial compression test material-level model [a) confinement load; b) nodal loads].

The remainder of this section summarizes the VecTor2 material-level results and compares them to the experimental triaxial results. In the tests, the vertical displacements were measured using an LVDT. The horizontal strain, J_0 , was measured locally using a strain gauge. The strain gauge location is shown in Figure 5-4.

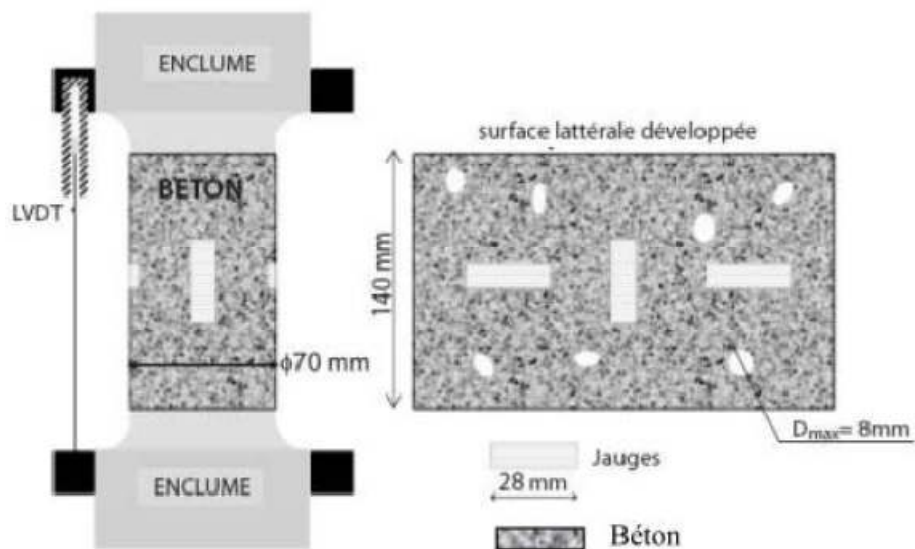


Figure 5-4: Triaxial test strain gauge locations (Vu, 2007).

Specimen 2: Unconfined

The results from each combination of material models were identical for the unconfined compression test. The peak stress was 69 MPa, at a strain of 2.48×10^{-3} . The VecTor2 stress-strain response is compared to the experimental one in Figure 5-5. The VecTor2 results match the experimental results, despite the apparent shift in the stress-strain curves. There was likely a lag in the LVDT system or slack in the LVDT before the specimen was compressed. A strain at peak stress of 5×10^{-3} is not reasonable for unconfined concrete. Concrete with a compressive strength of approximately 70 MPa reaches the peak stress at a strain of approximately 2.5×10^{-3} .

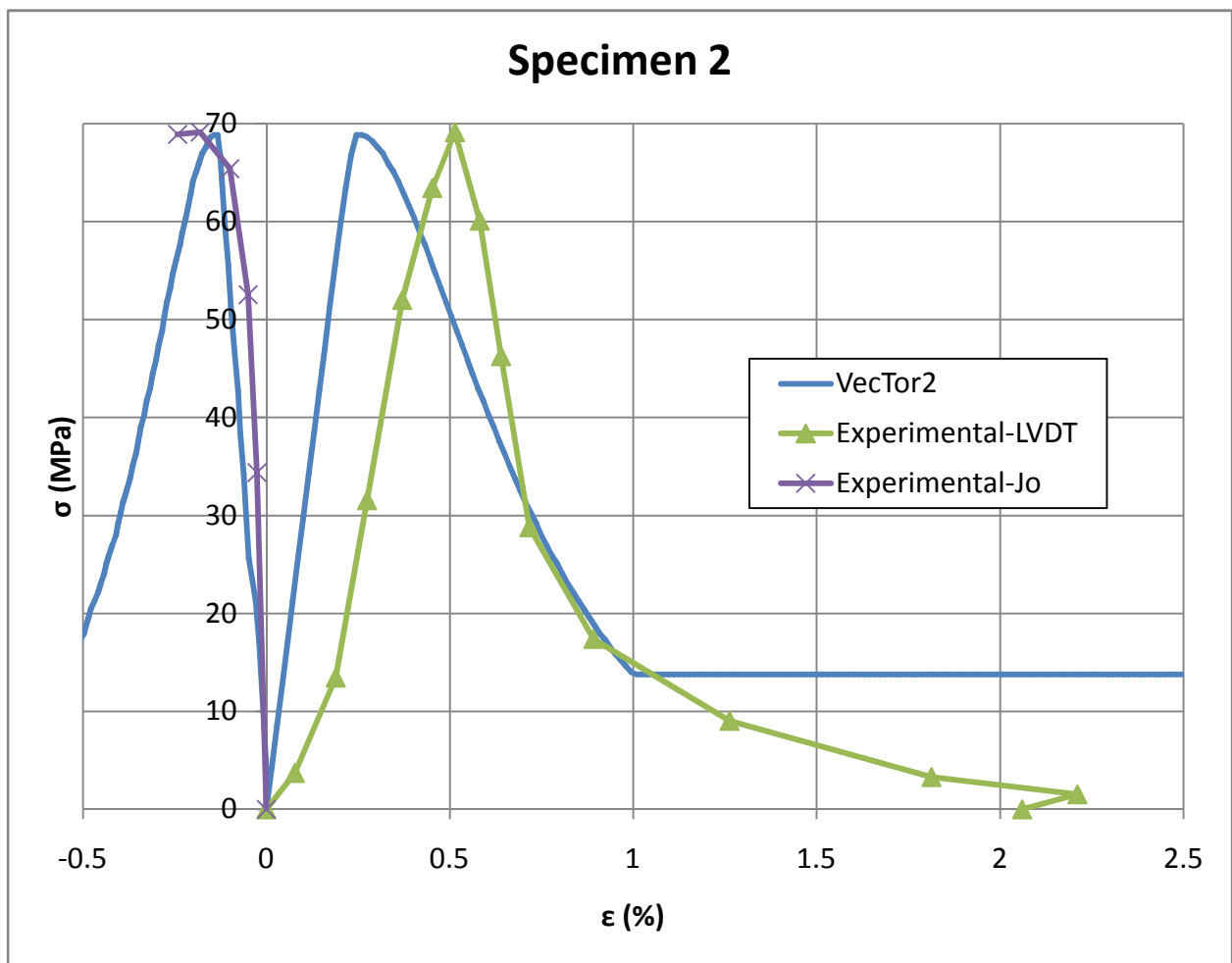


Figure 5-5: Specimen 2: comparison of VecTor2 and experimental stress-strain results.

Specimen 4: 15.5 MPa Confinement

The analysis results are summarized in Table 5-5. No increase in peak stress was attained when the Fixed Poisson Ratio dilatation model was used, although all other dilatation models yielded good results. The stress-strain results from VecTor2 are compared to the experimental results in Figure 5-6. At this level of confinement, the difference between the two sets of material models is minimal. The Montoya/Ottosen confinement model reached a slightly higher peak stress, but both results are comparable to the experimental stress-strain curves.

Table 5-5: Stress-Strain Results for All Specimen 4 Material-Level Analyses

Concrete Confined Strength Model	Concrete Dilatation Model	Peak Stress (MPa)	Strain at Peak Stress (me)
Kupfer/Richart	Fixed Poisson Ratio	74.9	4.4
	Variable-Kupfer	125.4	13.5
	Montoya 2003	124.4	13.5
	Montoya with Limit	124.4	13.5
Montoya/Ottosen	Fixed Poisson Ratio	98.5	6.9
	Variable-Kupfer	128.5	11.6
	Montoya 2003	127.9	11.5
	Montoya with Limit	127.9	11.5

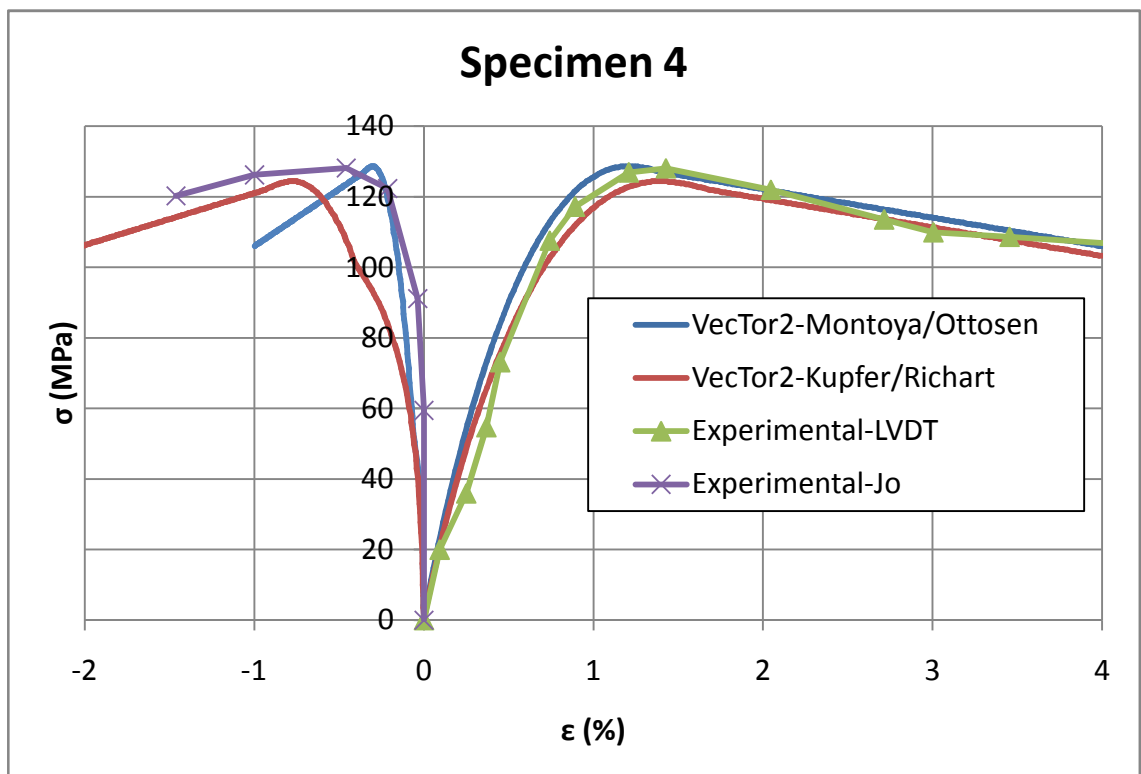


Figure 5-6: Specimen 4: comparison of VecTor2 and experimental stress-strain results.

Specimen 7: 26 MPa Confinement

The results from the analyses for Specimen 7 are summarized in Table 5-6 and the stress-strain curves are compared in Figure 5-7. While the Fixed Poisson Ratio allowed for some strength enhancement, the increase was insufficient. Practically identical results were obtained when the Kupfer/Richart confined concrete strength model was used, regardless of whether the Variable-Kupfer, Montoya-2003, or Montoya with Limit concrete dilatation model was used. Similarly, the Variable-Kupfer and Montoya concrete dilatation models produced identical results when paired with the Montoya/Ottosen confined concrete strength model.

Table 5-6: Stress-Strain Results for All Specimen 7 Material-Level Analyses

Concrete Confined Strength Model	Concrete Dilatation Model	Peak Stress (MPa)	Strain at Peak Stress (me)
Kupfer/Richart	Fixed Poisson Ratio	77.4	5.2
	Variable-Kupfer	164.6	21.4
	Montoya 2003	162.5	21.3
	Montoya with Limit	162.5	21.3
Montoya/Ottosen	Fixed Poisson Ratio	109.5	9.9
	Variable-Kupfer	158.0	17.8
	Montoya 2003	156.5	17.7
	Montoya with Limit	156.5	17.7

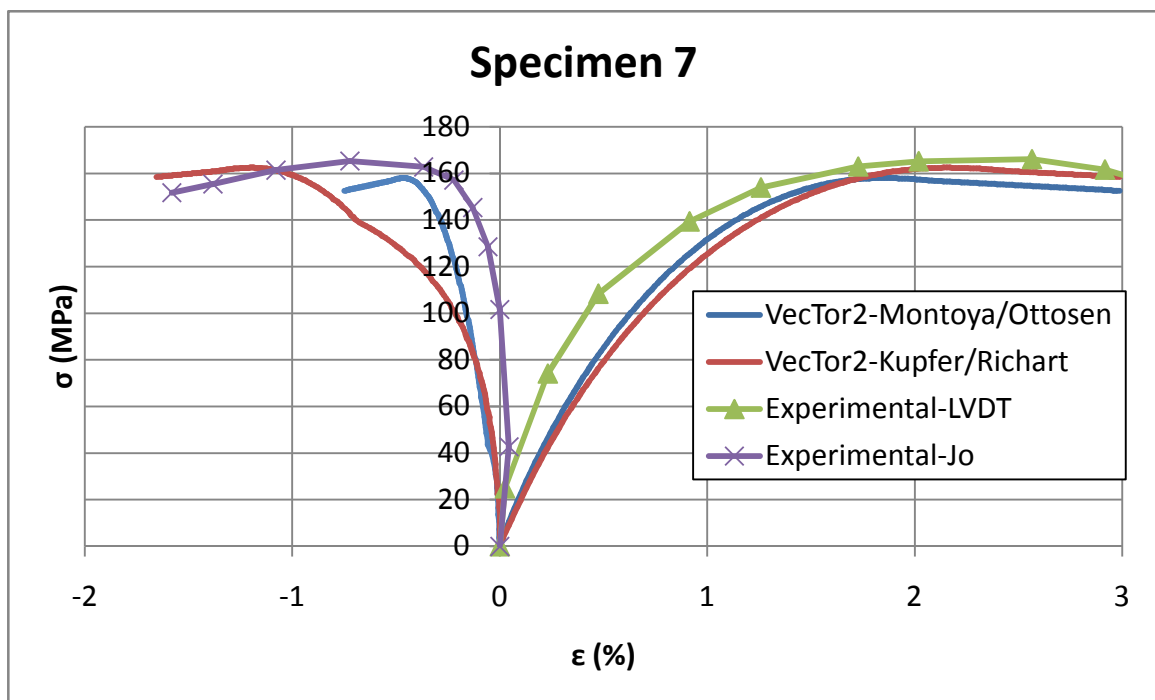


Figure 5-7: Specimen 7: comparison of VecTor2 and experimental stress-strain results.

Specimen 8: 47 MPa Confinement

The results from the analyses for Specimen 8 are summarized in Table 5-7 and compared to experimental results in Figure 5-8. In terms of which material model combinations yielded the best results, the same trends as observed in Specimens 4 and 7 are seen here. It was observed in the Specimen 7 results that the Montoya/Ottosen model slightly underpredicted the peak stress (in the cases where strength enhancement due to confinement was achieved). The same observation can be made about the Specimen 8 results, and the difference between the VecTor2 and experimental results is more pronounced.

Table 5-7: Stress-Strain Results for All Specimen 8 Material-Level Analyses

Concrete Confined Strength Model	Concrete Dilatation Model	Peak Stress (MPa)	Strain at Peak Stress (me)
Kupfer/Richart	Fixed Poisson Ratio	73.7	5.3
	Variable-Kupfer	212.7	25.0
	Montoya 2003	219.8	25.0
	Montoya with Limit	219.8	25.0
Montoya/Ottosen	Fixed Poisson Ratio	108.2	16.1
	Variable-Kupfer	189.0	24.9
	Montoya 2003	198.3	25.0
	Montoya with Limit	198.3	25.0

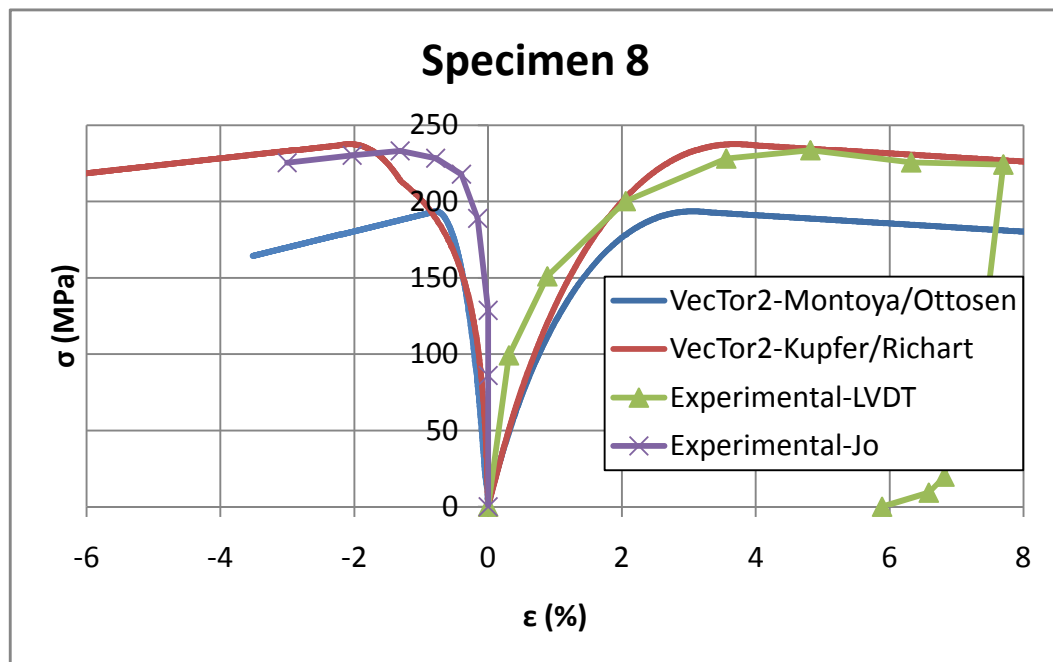


Figure 5-8: Specimen 8: comparison of VecTor2 and experimental stress-strain results.

Specimen 9: 100 MPa Confinement

The results of the VecTor2 analyses for Specimen 9 are summarized in Table 5-8 and the stress-strain curves are compared to the experimental curves in Figure 5-9. At this high level of confinement, the Kupfer/Richart model overpredicted the peak strength slightly, while the Montoya/Ottosen confined strength model underestimated the strength enhancement due to confinement. Stable results were not obtained when the Fixed Poisson Ratio dilatation model was used.

Table 5-8: Stress-Strain Results for All Specimen 9 Material-Level Analyses

Concrete Confined Strength Model	Concrete Dilatation Model	Peak Stress (MPa)	Strain at Peak Stress (me)
Kupfer/Richart	Fixed Poisson Ratio	-	-
	Variable-Kupfer	410.1	72.6
	Montoya 2003	424.4	73.6
	Montoya with Limit	424.4	73.6
Montoya/Ottosen	Fixed Poisson Ratio	-	-
	Variable-Kupfer	277.4	59.9
	Montoya 2003	295.1	60.8
	Montoya with Limit	295.1	60.8

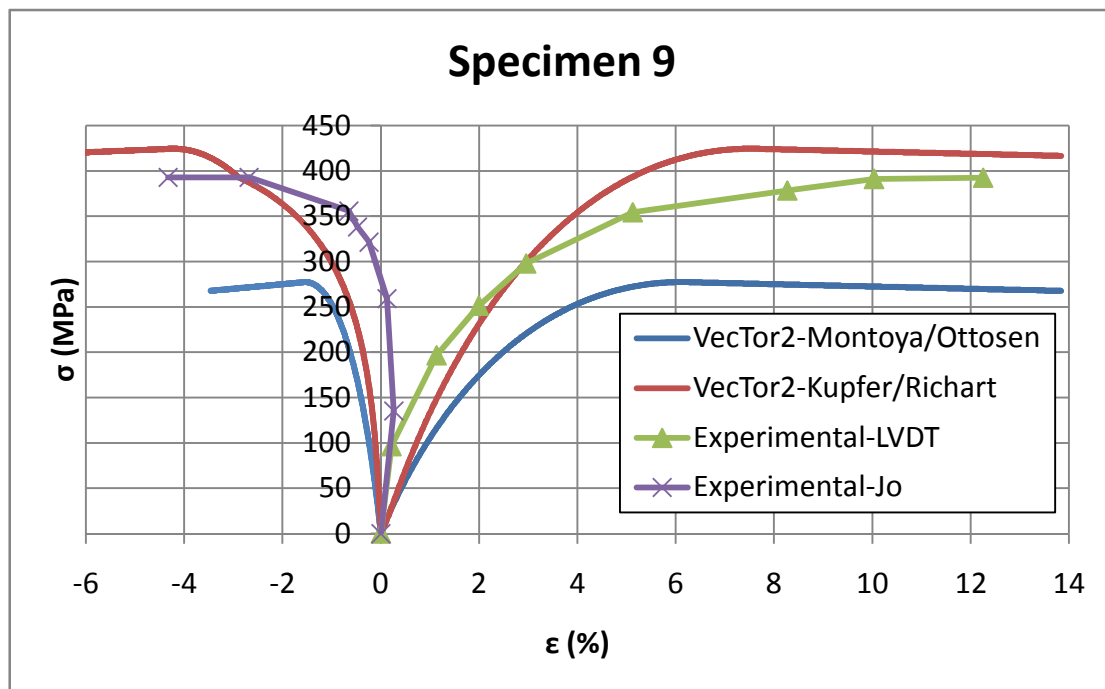


Figure 5-9: Specimen 9: comparison of VecTor2 and experimental stress-strain results.

5.2.2.2 Summary of Material-Level Triaxial Test Results

The tables in this section summarize the VecTor2 material-level results for the four confined specimens. Table 5-9 summarizes the results from analyses where the Montoya/Ottosen concrete confinement model was used with the Montoya 2003 concrete dilatation model. Table 5-10 summarizes the results obtained using the Kupfer/Richart confinement model with the Montoya 2003 dilatation model. Table 5-11 and Table 5-12 summarize the results obtained using the Variable-Kupfer dilatation model.

Table 5-9: Results for Montoya/Ottosen Confinement Model with Montoya 2003 Dilatation

Specimen	f_{cc-exp} (MPa)	$f_{cc-calc}$ (MPa)	$f_{cc-calc}/f_{cc-exp}$
4	128	127.9	0.999
7	165	156.5	0.948
8	232	198.3	0.855
9	400	295.1	0.738
Mean			0.885
COV			0.130

Results obtained using the Montoya/Ottosen confinement model with the Montoya 2003 dilatation model agree well with the experimental data. Very good agreement is seen in Specimens 4 and 7, where the confining pressures were 15.5 MPa and 26 MPa, respectively. The results for Specimens 8 and 9 are also reasonably good, considering that the confining pressure is quite high, and well above the range of confining pressures for which the confinement model was intended.

Table 5-10: Results for Kupfer/Richart Confinement Model with Montoya 2003

Specimen	f_{cc-exp} (MPa)	$f_{cc-calc}$ (MPa)	$f_{cc-calc}/f_{cc-exp}$
4	128	124.4	0.972
7	165	162.5	0.985
8	232	219.8	0.947
9	400	424.4	1.061
Mean			0.991
COV			0.049

The results obtained when the Kupfer/Richart confinement model was used with the Montoya 2003 dilatation model match the experimental results more closely than when the Montoya/Ottosen confinement model is used. The COV of 0.049 is good. Good agreement is observed for all four specimens. As well, the peak stress was not universally underestimated as was the case for the results shown in Table 5-9.

Table 5-11: Results for Montoya/Ottosen Confinement Model with Variable-Kupfer Dilatation

Specimen	f_{cc-exp} (MPa)	f_{cc-calc} (Mpa)	f_{cc-calc}/f_{cc-exp}
4	128	128.5	1.004
7	165	158.0	0.958
8	232	189.0	0.815
9	400	277.4	0.694
Mean			0.867
COV			0.163

The results obtained using the Montoya/Ottosen confinement model and the Variable-Kupfer dilatation model are comparable to those obtained using the same confinement model and the Montoya 2003 dilatation model. Again, very good agreement is observed between the experimental results and the VecTor2 results for Specimens 4 and 7. The peak stress for Specimen 9, though, is underestimated by approximately 30%. Given that the discrepancy between experimental data and VecTor2 results is small for the other three specimens, these results are considered to be acceptable.

Table 5-12: Results for Kupfer/Richart Confinement Model with Variable-Kupfer

Specimen	f_{cc-exp} (MPa)	f_{cc-calc} (MPa)	f_{cc-calc}/f_{cc-exp}
4	128	125.4	0.980
7	165	164.6	0.998
8	232	212.7	0.917
9	400	410.0	1.025
Mean			0.980
COV			0.047

It can be seen that the results obtained when the Kupfer/Richart confinement model was used with the Kupfer dilatation model are very similar to the results obtained from the Kupfer/Richart confinement model and Montoya 2003 dilatation model. Good agreement between the experimental and VecTor2 results is observed for all four specimens, with a mean $f_{cc-calc}/f_{cc-exp}$ of 0.98 and a COV of 0.047.

Both the Montoya/Ottosen and Kupfer/Richart confinement models and the Kupfer and Montoya 2003 concrete dilatation models are suitable for modeling confined concrete. In general, good agreement was observed between VecTor2 and experimental results for Specimens 4, 7, and 8. When the Montoya/Ottosen confinement model was used, the strength of Specimen 9 was underestimated, however good agreement was obtained when the Kupfer/Richart model was used. At the material level, all combinations of confinement and dilatation models displayed appreciable post-peak responses.

Based on the results, a number of conclusions can be drawn. Firstly, for unconfined specimens, as expected, the Kupfer/Richart and Montoya/Ottosen confined concrete strength models will produce identical results, regardless of the concrete dilatation model employed. Secondly, a fixed Poisson ratio is not suitable for modeling confined concrete. This dilatation model was unable to capture the strength enhancement due to confinement at low levels of confinement, and yielded unstable results at high levels of confinement. Based on the simulations performed, the Kupfer/Richart and Montoya/Ottosen confined concrete model can be paired with the Variable-Kupfer, Montoya 2003, and Montoya with Limit concrete dilatation models to adequately model confinement.

It was also observed that for the levels of confinement examined, the Montoya 2003 and Montoya with Limit dilatation models yielded identical results. As well, at higher levels of confinement, the Kupfer/Richart model overpredicted the peak stress, while the Montoya/Ottosen model underestimated the peak stress. Finally, it was observed that the Montoya 2003 and Montoya with Limit dilatation models resulted in higher peak stresses than the Variable-Kupfer model, an effect which became more pronounced as confinement increased.

5.2.2.3 Structural-Level Triaxial Results

The model used in the structural-level analyses is shown in Figure 5-10. In terms of confinement, nodal loads and smeared reinforcement were used. Similar to the material-level analysis, vertical displacements were applied to the top surface of the model. For the structural-level analyses, displacements were applied in increments of 0.0002 mm.

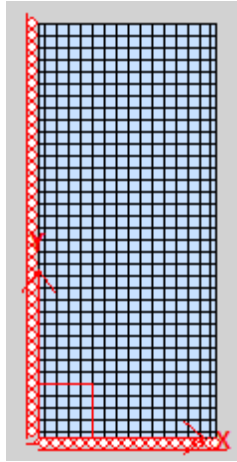


Figure 5-10: VecTor2 triaxial compression test structural-level model

In the material-level analyses, it was observed that the Kupfer/Richart and Montoya/Ottosen confinement models could be used to model confined concrete when paired with the Variable-Kupfer, Montoya 2003, and Montoya with Limit concrete dilatation models. Table 5-13 summarizes the results of the structural-level analyses, and compares them to the material-level results. In this section, the crack patterns at failure are also shown. In the experiments, it was observed that at higher confining pressures, the failure planes became more horizontal. This trend was observed in the VecTor2 results.

Table 5-13: Results of Structural-Level Triaxial Analyses in VecTor2

Concrete Dilatation Model	Concrete Confined Strength Model	Specimen	Confining Pressure (MPa)	Peak Stress (MPa)	Strain at Peak Stress (me)	% Difference in Peak Stress from Material Level
Variable-Kupfer	Kupfer/Richart	2	-	68.5	2.41	-0.8
		4	15.5	124.3	12.71	-0.9
		7	26	162.4	19.20	-1.3
		8	47	226.0	31.90	6.3
		9	100	409.0	70.33	-0.3
	Montoya/Ottosen	2	-	68.9	2.70	-0.3
		4	15.5	128.4	11.21	-0.1
		7	26	157.2	17.52	-0.5
		8	47	193.4	28.73	2.4
		9	100	276.4	58.18	-0.4
Montoya 2003	Kupfer/Richart	2	-	68.5	2.41	-0.8
		4	15.5	119.4	10.87	-4.0
		7	26	124.5	9.53	-23.4
		8	47	149.7	12.14	-31.9
		9	100	302.4	30.00	-28.8
	Montoya/Ottosen	2	-	68.5	2.41	-0.8
		4	15.5	128.2	11.12	0.2
		7	26	156.0	17.24	-0.3
		8	47	202.2	29.25	1.9
		9	100	291.6	55.80	-1.2

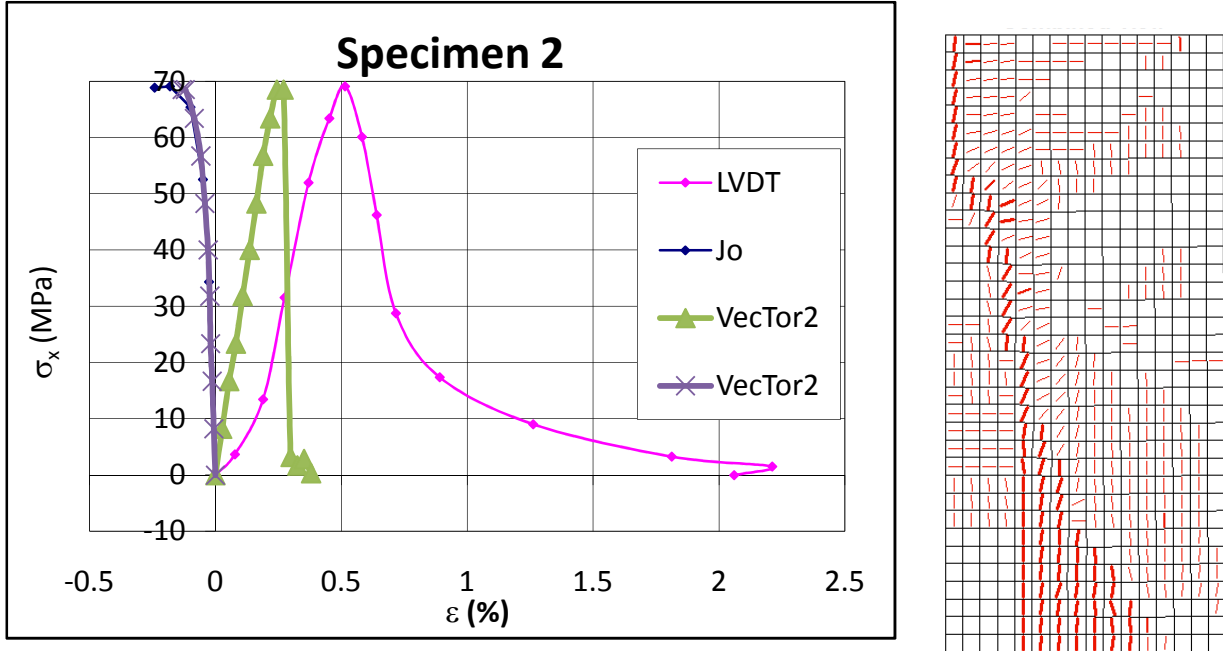


Figure 5-11: Results from analyses using Montoya/Ottosen & Variable-Kupfer.

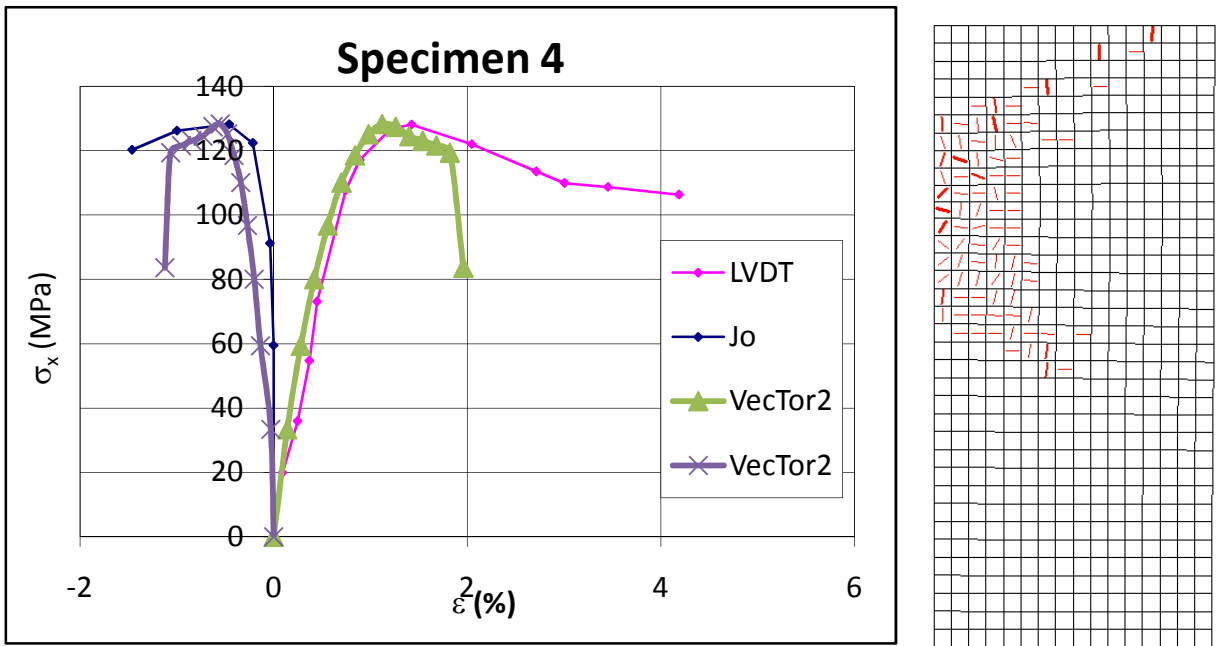


Figure 5-12: Results from analyses using Montoya/Ottosen & Variable-Kupfer.

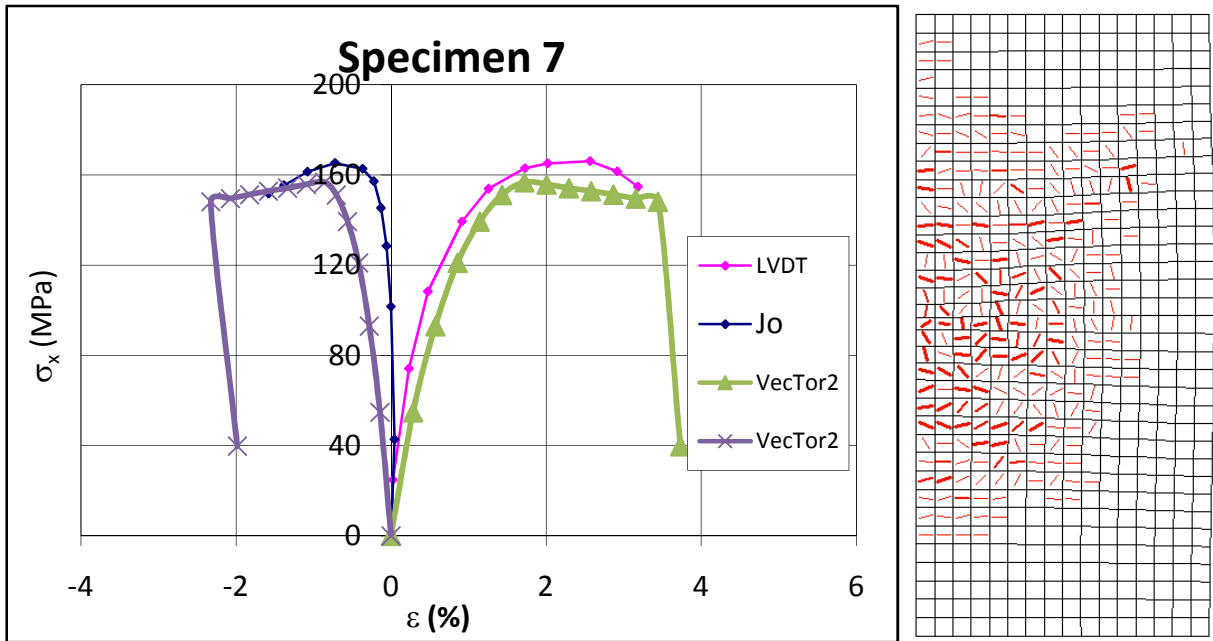


Figure 5-13: Results from analyses using Montoya/Ottosen & Variable-Kupfer.

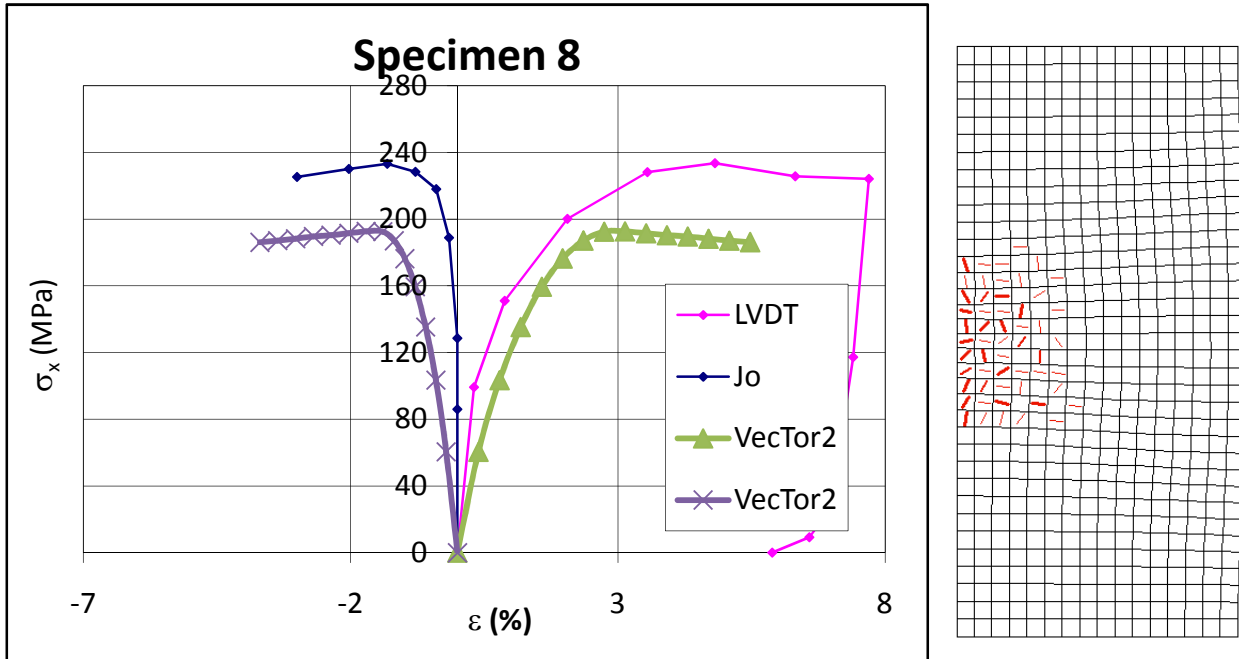


Figure 5-14: Results from analyses using Montoya/Ottosen & Variable-Kupfer.

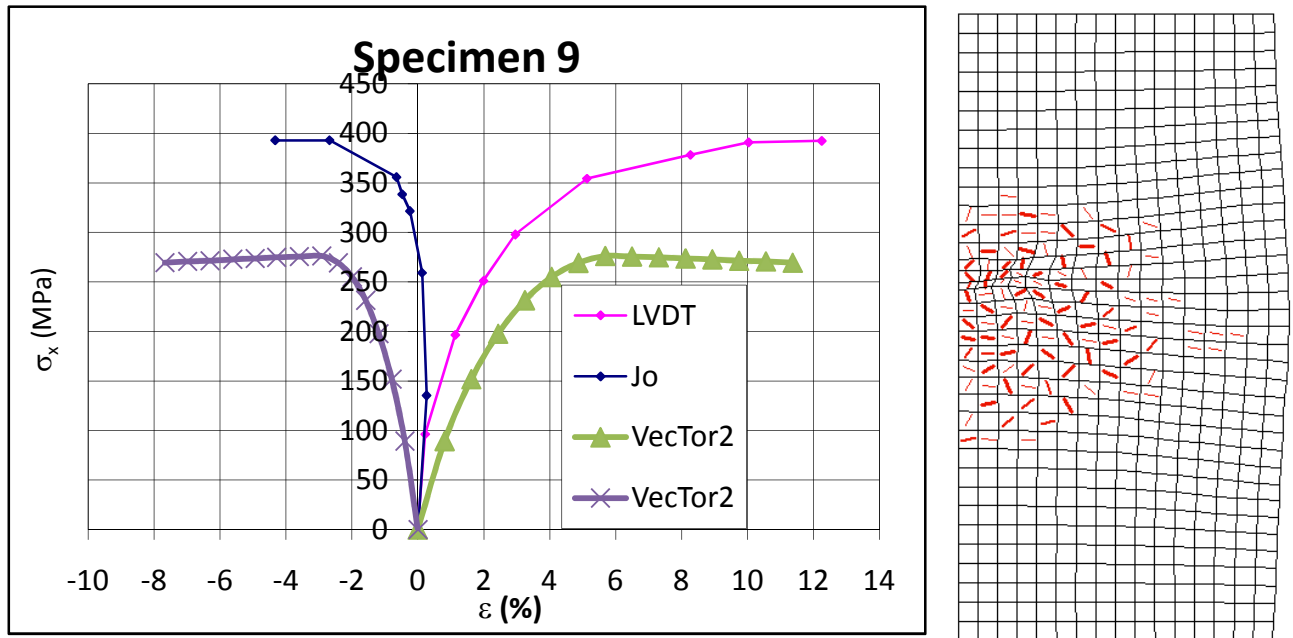


Figure 5-15: Results from analyses using Montoya/Ottosen & Variable-Kupfer.

The same general trends that were observed in the material-level analyses were seen in the structural-level analyses. For the analyses where the Variable-Kupfer dilatation model was used, the Kupfer/Richart confined strength model consistently calculated a higher peak stress than the Montoya/Ottosen model, and at higher levels of confinement overpredicted the concrete strength. For higher levels of confinement, the Montoya/Ottosen confined strength model significantly underpredicted the confined strength of the concrete.

For the analyses where the Montoya 2003 dilatation model was used in conjunction with the Kupfer/Richart confinement model, instability at the structural level caused the peak stress to be underestimated at all levels of confinement. However, when the Montoya 2003 dilatation model was paired with the Montoya/Ottosen confinement model, the peak stresses obtained were approximately the same as those that were observed in the material-level analyses.

Compared to the material-level analyses, the structural-level results exhibited a shorter post-peak response due to localization of damage. However, as illustrated in the figures above, an appreciable post-peak response was still achieved.

Future work should be focused primarily on improving the post-peak response of the Kupfer/Richart concrete confinement model. This model matched the experimental results well for all specimens, but lacked post-peak response.

Based on the material- and structural-level analysis results, the recommended concrete confinement model is the Kupfer/Richart model, which can be used with any of the three dilatation models discussed.

5.3 VTT-B1 Flexural Specimen

5.3.1 Introduction

The test modeled in this section was carried out by IRSN and VTT in early 2010, and was part of a test series which consisted of four impact tests on reinforced concrete targets. For the two flexural tests in the series, B1 and B2, hollow deformable stainless steel missiles were impacted against 2082 x 2082 x 150 mm reinforced concrete panels. The panels were simply supported on four sides, as shown in Figure 5-16, with a distance of 2000 mm between the supports in both directions and a nominal concrete strength of 50 MPa.

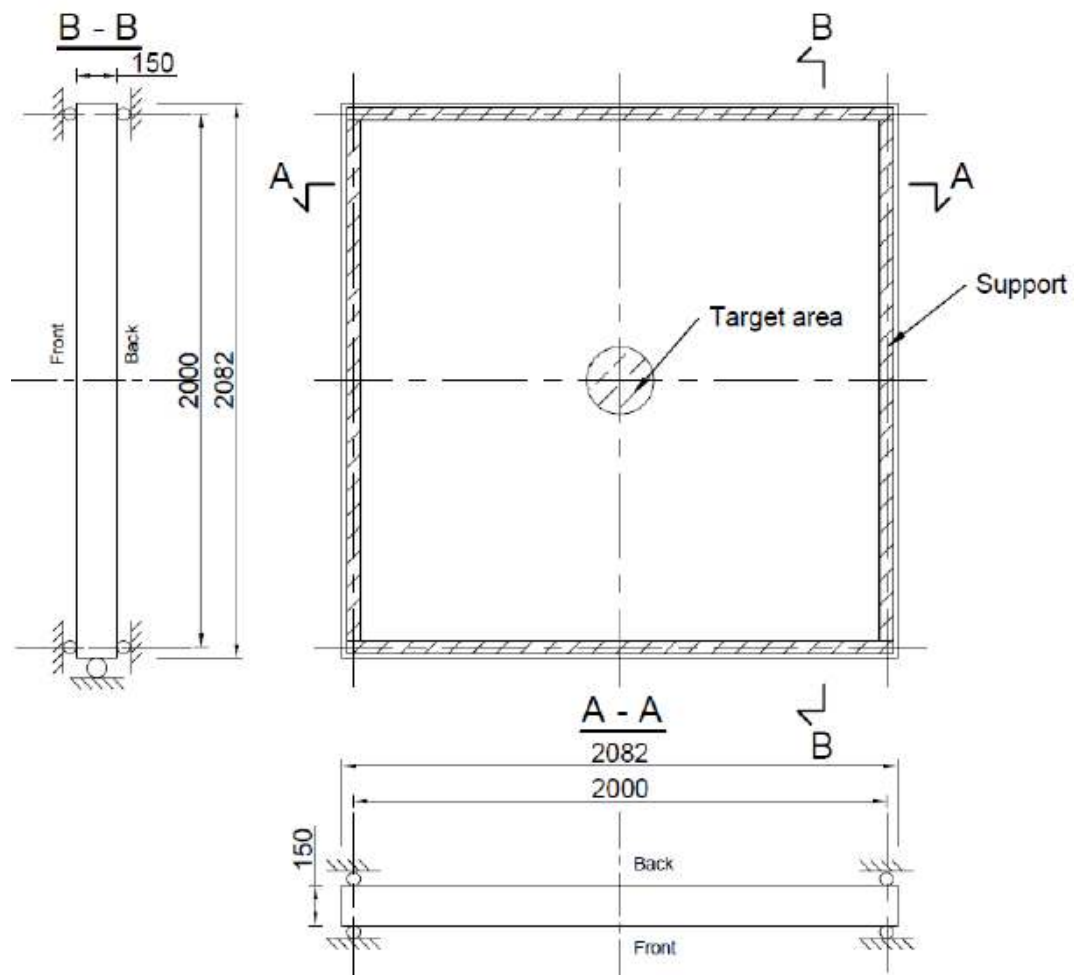


Figure 5-16: VTT-B1 dimensions and support conditions (Vepsä, 2010a).

Reinforcement consisted of 6 mm diameter bars at a spacing of 55 mm, with shear reinforcement provided in the form of 6 mm diameter stirrups. Figure 5-17 and Figure 5-18 show the reinforcement details. For the B1 and B2 tests, which were meant to be identical, the design missile mass and impact velocity were 50 kg and 110 m/s, respectively. The missile is shown in Figure 5-19.

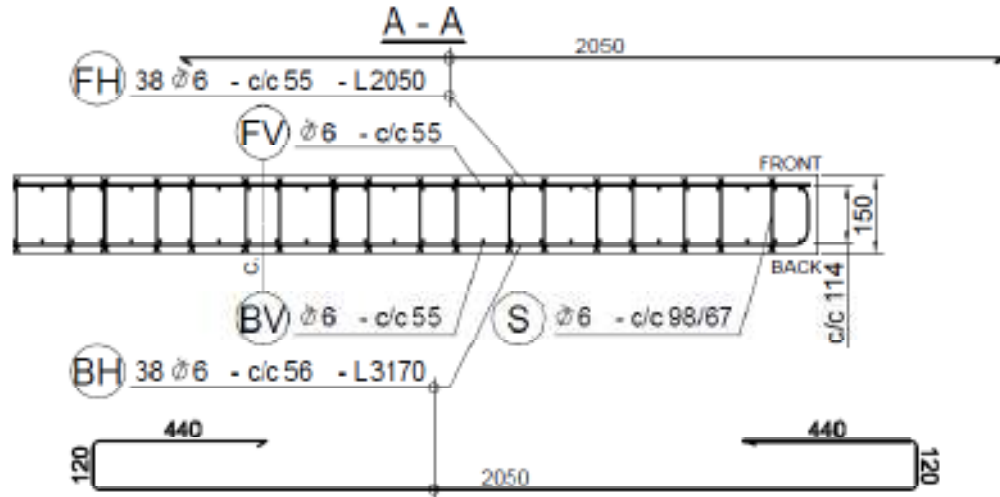


Figure 5-17: Horizontal cross section of VTT-B1 (Vepsä, 2010a).

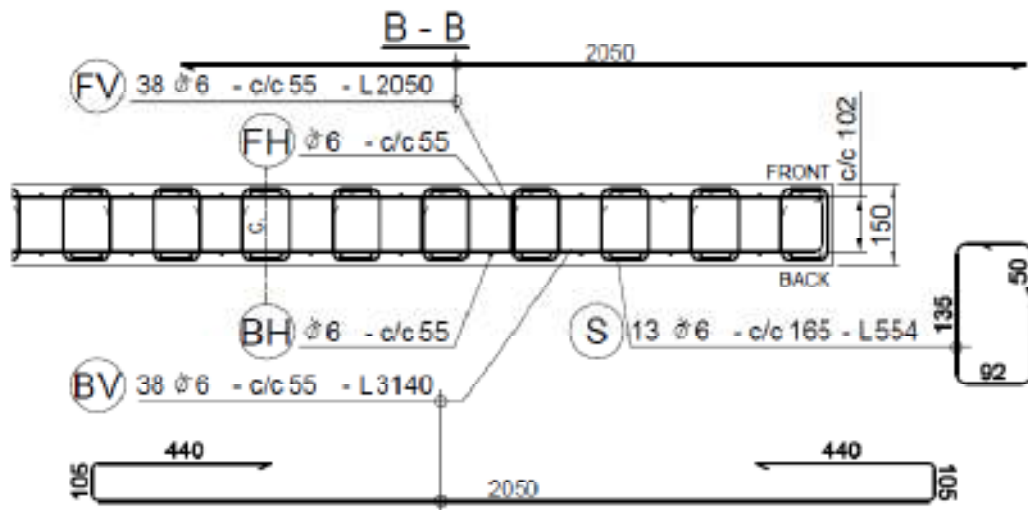


Figure 5-18: Vertical cross section of VTT-B1 (Vepsä, 2010a).

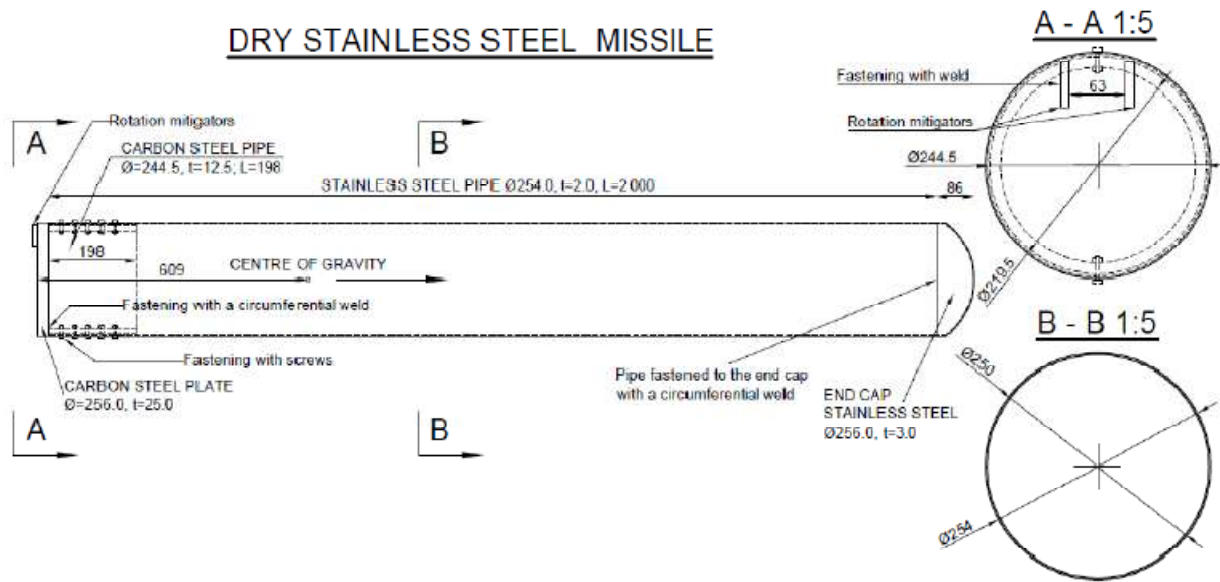


Figure 5-19: VTT-B1 missile (Vepsä, 2010a).

The VTT-B1 flexural specimen was modeled using both VecTor2 and VecTor3. Default material behaviour models were used in most cases (the exception being the use of the Hoshikuma concrete stress-strain curve), in keeping with the goal of employing simplified modeling procedures. In addition, only the concrete compressive strength was taken from the experimental material properties. All other properties were derived from f'_c using common empirical relations. No attempt was made to refine the analyses by adjusting the material models or material properties.

5.3.2 VecTor2 Missile Modeling

First, the missile was explicitly modeled in VecTor2 using a combination of steel elements and compression-only truss bars. Compression-only truss bars were used due to the fact that the VecTor suite of programs do not yet support contact elements. The force histories determined in the compression-only truss bars were then used in the VecTor3 modeling of the specimen.

5.3.2.1 Mesh and Simplifying Assumptions

The model used in VecTor2, including the missile and target, is shown in Figure 5-20. A total of 1963 nodes, 1777 rectangular elements, 31 triangular elements (at the nose of the missile), and

188 truss elements were used to model the slab and missile. A close-up of the target is shown in Figure 5-21.

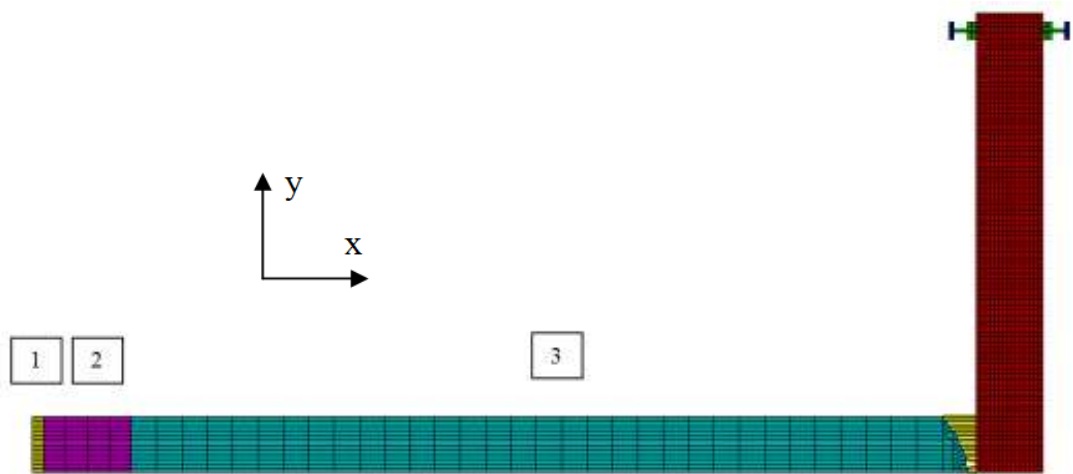


Figure 5-20: VecTor2 VTT-B1 mesh including missile and target.

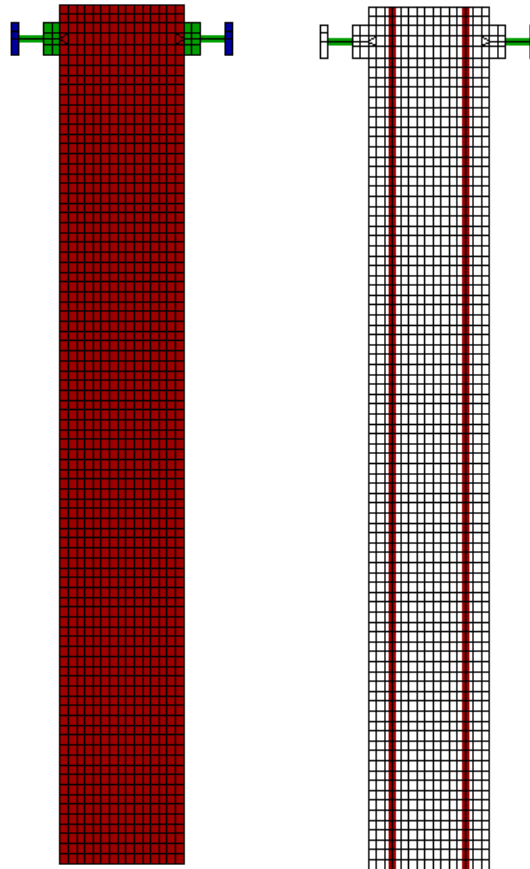


Figure 5-21: Close-up of VecTor2 VTT-B1 target [a) mesh; b) reinforcement].

In addition to simplifying the model to 2D, half of the slab was modeled due to the fact that it was symmetric in terms of both geometry and loading. The bottom edge of the model, representing the midspan of the slab, was restrained against movement in the y-direction to represent this symmetry. For the supports, compression-only truss bars were used. An area of 1000 mm² was used for these truss bars, which restrained movement of the supports in the horizontal direction, but allowed for rotation of the slab and vertical displacements to occur without restraint.

The concrete target was modeled using rectangular concrete elements. For the slab model, a depth of 2.082 m out-of-plane was used. For the vertical in-plane reinforcement, discrete truss elements were used; horizontal in-plane reinforcement (in the out-of-plane direction in VecTor2) was modeled as smeared. The material properties used in the analyses are summarized in Table 5-14.

Table 5-14: Material Properties for VTT-B1 Analyses

Concrete		Steel	
f_c (MPa)	55.2	d_b (mm)	6
ε₀ (x10⁻³)	2.33	A_b (mm²)	28.3
f_t (MPa)	2.45	A_{total} (mm²)	1071
E (MPa)	31600	ρ (%; in-plane,z-dir)	0.686
		ρ (%; transverse)	0.5
		E (MPa)	200000
		f_v (MPa)	650
		f_u (MPa)	715
		ε_{sh} (x10⁻³)	3.3
		ε_u (x10⁻³)	70

The average element size for the concrete target was 10 x 12 mm. With this element size, there were 15 elements through the thickness of the slab, which was assumed to be acceptable given that the response was expected to be flexural in nature and not shear-critical. The elements used had an aspect ratio of approximately 1.2, which was judged to be sufficiently close to the preferred aspect ratio of 1. The density of the concrete was assumed to be 2400 kg/m³ when calculating the lumped masses.

The soft missile was modeled using structural steel elements, and the missile forces were transferred to the concrete target using a total of 12 compression-only truss bars. The compression-only truss bars were used in lieu of contact elements, which are currently not

available in VecTor2. Compression-only truss bars transfer compressive forces to the target and allow the missile to rebound from the target without pulling it. On average, the aspect ratio of the elements in the stainless steel tube section of the missile was 5 to 6, with the average element being approximately 10 x 57 mm. For the missile, lumped masses also had to be specified. Half of the actual missile mass was used, since only half of the slab was modeled. The mass of the stainless steel cap, stainless steel pipe, carbon steel pipe, and carbon steel plate were taken to be 0.65 kg, 12.5 kg, 6.795 kg, and 5.05 kg, respectively. Each of the lumped masses in the missile was assigned an initial velocity of 110 m/s.

Note that this study is the first time VecTor2 has been used to model a soft impact. Buckling of thin-walled steel elements is not rigorously considered in the VecTor programs, and thus instability issues arose when modeling the missile. In order to capture more of the response, simplified element erosion in the missile was used. Once the fracture strain of steel was exceeded in an element, the element was eroded (i.e, rendered inactive). Making this change did not greatly affect the slab displacement. A decrease in slab peak displacement of approximately 2 mm was observed when element erosion was introduced, which was determined to be acceptable for these preliminary analyses, since the results had been largely unstable with no missile erosion. Further, the compression-only truss bar forces for the analysis with erosion were compared to the initial analysis, and the truss bar profiles for the two analyses were essentially the same. It is also noted that although the missile nose was modeled with a rounded nose, the use of the compression-only truss bars along the nose of the missile effectively made the missile blunt.

The missile itself was modeled in three sections. The back end of the missile was assigned a thickness in the out-of-plane direction of 254 mm, the full diameter of the missile, since that part of the missile was a solid section. The thickness of the carbon pipe near the back of the missile was 29 mm, twice the wall thickness. Similarly, the thickness of the remainder of the missile was 4 mm. The missile properties are summarized in Table 5-15.

The b/t ratios for the different sections of missile were calculated using the slenderness formulation used for steel tubes.

The missile sections indicated in Table 5-15 correspond to the missile sections shown in Figure 5-20.

Table 5-15: VTT-B1 Missile: VecTor2 Missile Properties

Missile Truss Properties		Missile Body Properties					
		1		2		3	
A_{truss} (mm ²)	47	F_y (MPa)	350	F_y (MPa)	350	F_y (MPa)	350
Number of Trusses	12	F_u (MPa)	633	F_u (MPa)	633	F_u (MPa)	633
E_{truss} (MPa)	200000	e_{sh} (x10 ⁻³)	1.8	e_{sh} (x10 ⁻³)	1.8	e_{sh} (x10 ⁻³)	1.8
F_y (MPa)	350	e_u (x10 ⁻³)	454	e_u (x10 ⁻³)	454	e_u (x10 ⁻³)	454
F_u (MPa)	633	E (MPa)	200000	E (MPa)	200000	E (MPa)	200000
e_{sh} (x10 ⁻³)	1.8	Thickness (mm)	254	Thickness (mm)	29	Thickness (mm)	4
e_u (x10 ⁻³)	454	b/t (buckling)	N/A	b/t (buckling)	9.5	b/t (buckling)	160

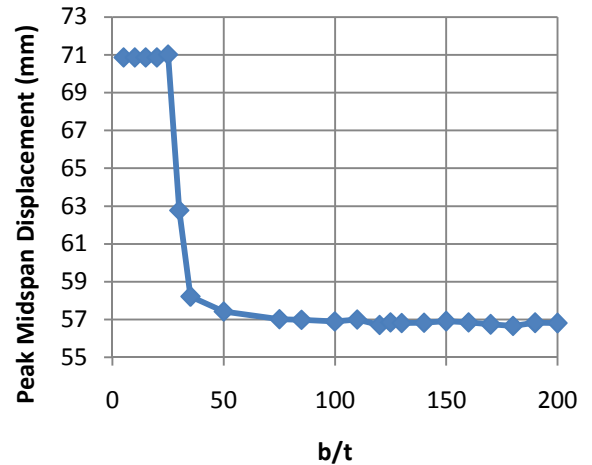
5.3.2.2 Effect of b/t Ratio

In an effort to understand the effect of the missile model on the response of the specimen, numerous analyses were performed using different b/t ratios for the hollow section of the missile. In VecTor2, b/t is the ratio of the unsupported length to diameter, and buckling occurs in elements with b/t ratios greater than 5, beginning when the compressive strain exceeds the specified yield strain. It is expected that as the unsupported length to diameter increases, the load-carrying capacity will decrease.

These analyses were performed prior to element erosion being introduced, and the area of the compression-only truss bars was held constant. The results of this series of analyses are summarized in Table 5-16 and Figure 5-22. For low b/t ratios, in the range of 5 to 20, the peak midspan displacement was approximately 70 mm. For b/t ratios greater than approximately 35, the peak displacement decreased to approximately 50 mm. The transition b/t ratio was approximately 30.

Table 5-16: Effect of b/t on Peak Displacement

b/t	Δ_{\max}	b/t	Δ_{\max}
5	70.9	110	57.0
10	70.9	120	56.7
15	70.9	125	56.9
20	70.9	130	56.8
25	71.0	140	56.8
30	62.8	150	56.9
35	58.2	160	56.8
50	57.4	170	56.7
75	57.0	180	56.7
85	57.0	190	56.8
100	56.9	200	56.8

**Figure 5-22: Effect of b/t on peak displacement of VTT-B1 target.**

5.3.2.3 Load Profile

In order to determine the appropriate load profile to use for the VecTor3 analyses, different compression-only truss bar areas were used in the VecTor2 simulations and the effect on damage to missile and maximum slab displacement (in VecTor2) were identified. The area of all 12 truss bars was the same in each analysis. The effect of truss bar area on missile damage was assessed in terms of the displacement of the back of the missile. It was found that increasing the area of the truss bars increased the displacement of the back of the missile. While the truss bar area had an effect on the missile displacement, changing the truss bar area had virtually no effect on the displacement profile of the slab. In all cases, the maximum displacement of the slab was approximately 45 mm, with a deviation of about 1 mm. While the slab displacement in each case was almost identical, the maximum force in the truss bars dramatically increased as the area increased. Despite the increase in initial force, the truss bar forces always returned to the same backbone load curve regardless of area. Because of this, the load profile was chosen such that the displacement obtained using nodal forces in VecTor2, for the same target, was 45 mm. That is, an impulse load using nodal forces was defined such as to give the same response as obtained when the missile was explicitly modeled.

5.3.2.4 VecTor2 Missile Results

This section summarizes the missile results. Figure 5-23 shows the displacement-time history of the back of the missile during impact. Figure 5-24 shows the velocity-time history of the back of the missile during impact. Notice that the velocity of the back of the missile does not decrease to zero until approximately 30 ms after impact. Figure 5-25 and Figure 5-26 show the forces in the compression-only truss bars and the impulse derived from those forces. The peak load is 350 kN, while the total impulse is 2.35 kNs; these values are for half of the slab. In terms of the damage to the missile, the missile is pictured at $t=10.1$ ms and $t=20.2$ ms. The duration of the shock was determined to be 20.2 ms, which was the point at which the front of the missile started to rebound. Figure 5-27 shows the stress contours in the missile at $t=10.1$ ms. The original length of the missile was 2111 mm. At $t=10.1$ ms, the buckled length of the missile was approximately 171.4 mm, leaving an unbuckled length of 1939.6 mm. The buckled portion of the missile is shown in dark blue. The dark blue elements at the front of the missile were deactivated. The displaced shape of the missile at $t=10.1$ ms is illustrated in Figure 5-28. At $t=20.2$ ms, the buckled region had increased to 630 mm, illustrated in Figure 5-29. The displaced shape is shown in Figure 5-30.

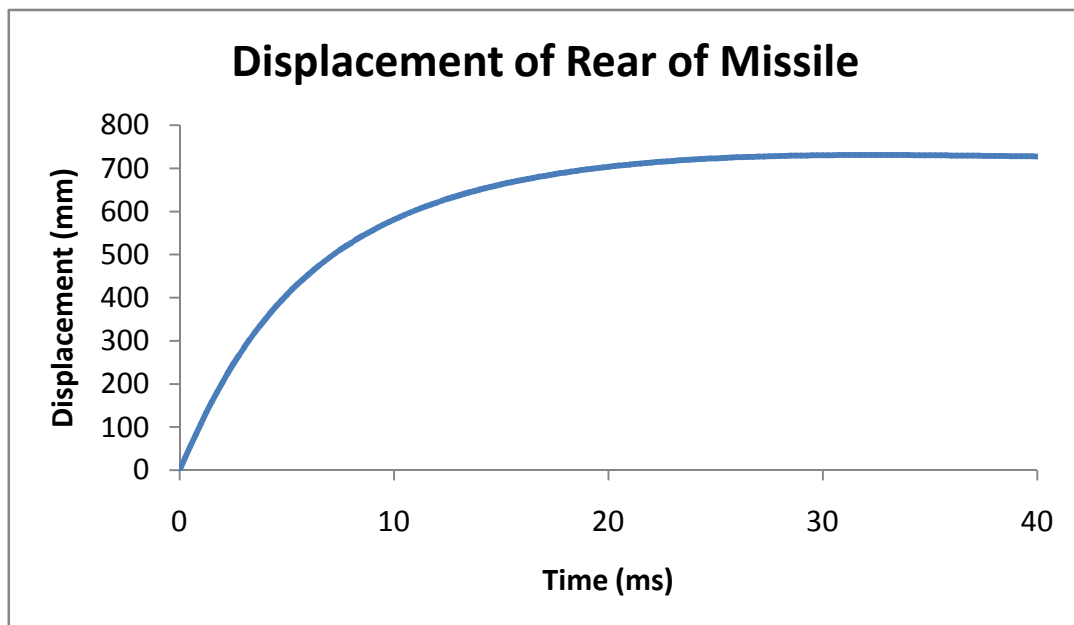


Figure 5-23: Displacement-time history of rear of missile from VecTor2 analysis of VTT-B1.

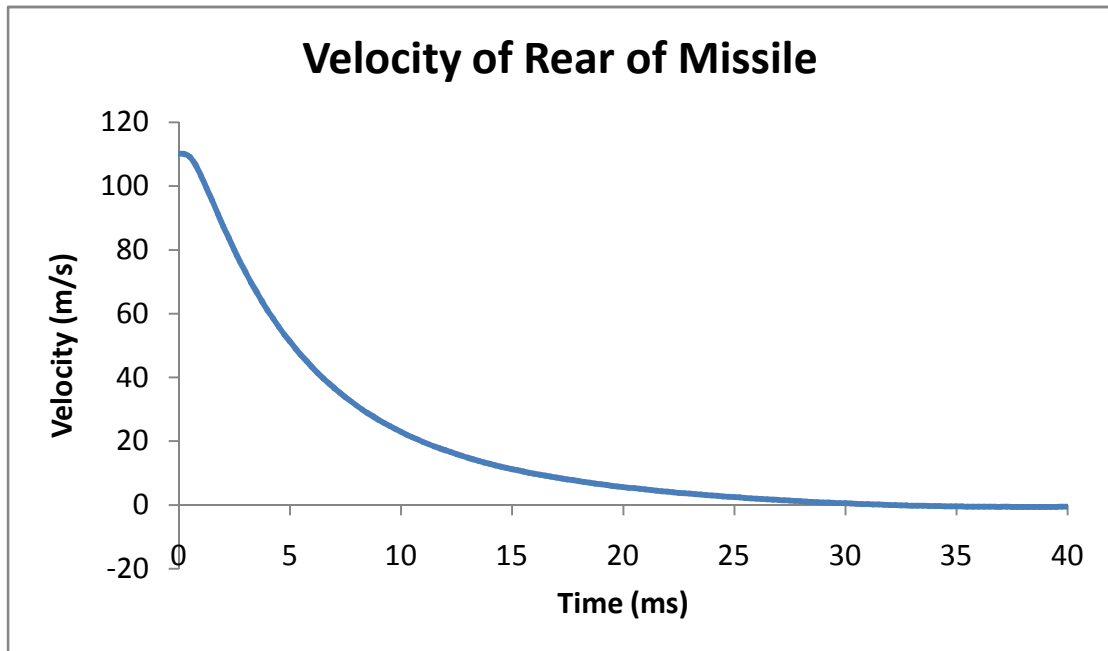


Figure 5-24: Velocity-time history of rear of missile from VecTor2 analysis of VTT-B1.

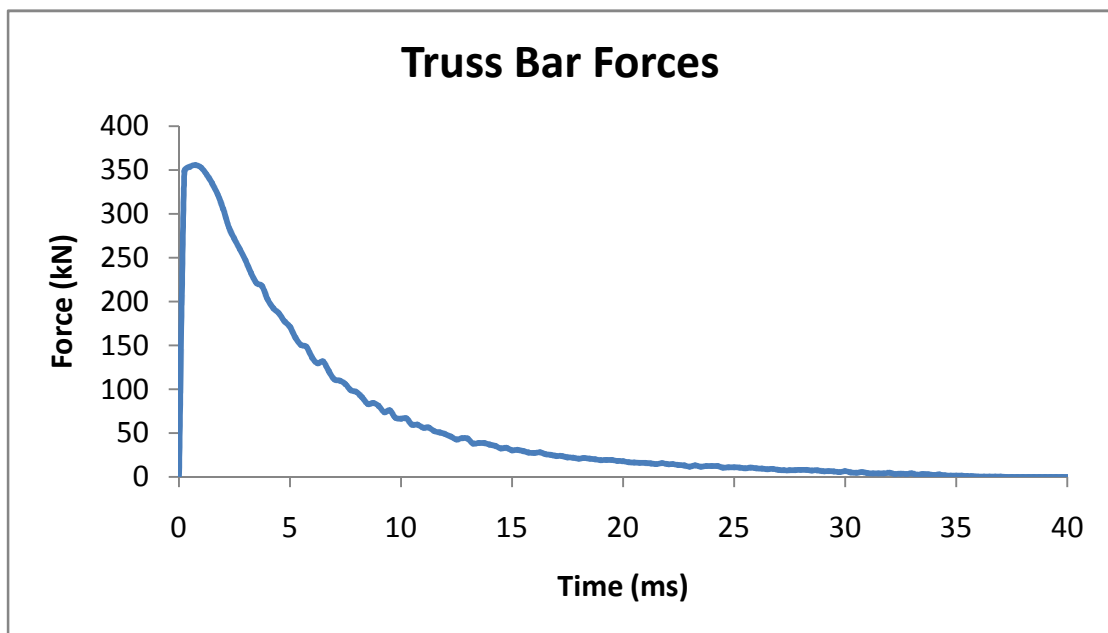


Figure 5-25: Load-time history in compression-only truss bars from VecTor2 analysis of VTT-B1.

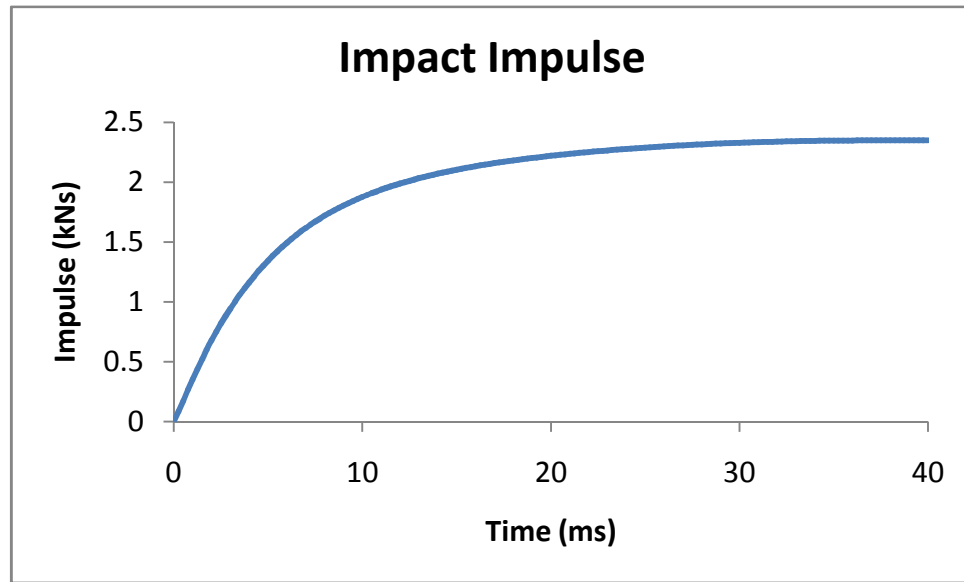


Figure 5-26: Impulse derived from truss bar forces from VecTor2 analysis of VTT-B1.



Figure 5-27: Stress contours of VTT-B1 missile at $t=10.1$ ms (half-way through impact).



Figure 5-28: Displaced shape of VTT-B1 missile at $t=10.1$ ms (half-way through impact).



Figure 5-29: Stress contours of VTT-B1 missile at $t=20.2$ ms (end of impact).



Figure 5-30: Displaced shape of VTT-B1 missile at $t=20.2$ ms (end of impact).

5.3.3 Modeling of Impact Using Nodal Forces

Analyses were done in VecTor2 and VecTor3 using the load profile derived from the truss bar forces. The VecTor2 analyses were performed to illustrate the effect of mesh density on the displacement results.

5.3.3.1 VecTor2 Modeling

Three different mesh sizes were used in the VecTor2 modeling using nodal forces. The fine mesh, shown in Figure 5-31, is the same mesh that was used in the analysis where the missile was modeled explicitly. The coarsest mesh, shown in Figure 5-32, has the same mesh density as the VecTor3 model. For the fine mesh, the average element size was 10x12 mm, and there were a total of 15 elements through the thickness of the slab. The coarse mesh has an average element size of 15x54 mm. The aspect ratio for the coarse mesh is much larger than optimal, and was used due to computation and modeling constraints. The coarse mesh has a total of 10 elements through the thickness. A third analysis in VecTor2 was performed to determine the effect of element aspect ratio only, since between the coarse and fine mesh, both the element aspect ratios and number of elements through the thickness are quite different. The mesh used for this analysis is shown in Figure 5-33. For all analyses, damping ratios of 0.25% and 1% were used for modes 1 and 2, respectively.

In these preliminary analyses the concrete cover used was 30 mm. The peak displacement for the fine mesh was 45.1 mm. When the element aspect ratio was kept to approximately 1, and the number of elements through the thickness was reduced from 15 to 10, the peak displacement decreased to 44.1 mm. Finally, the peak displacement for the coarse mesh was 42.2 mm.

Based on these three analyses, it can be observed that while the number of elements through the thickness of the slab has some effect, going from 15 to 10 elements did not have an overwhelming effect on the peak displacement. Going from a square element, with an aspect ratio of 1, to an element with an aspect ratio of 3.6 had a larger effect on the peak displacement, decreasing it by approximately 2 mm.

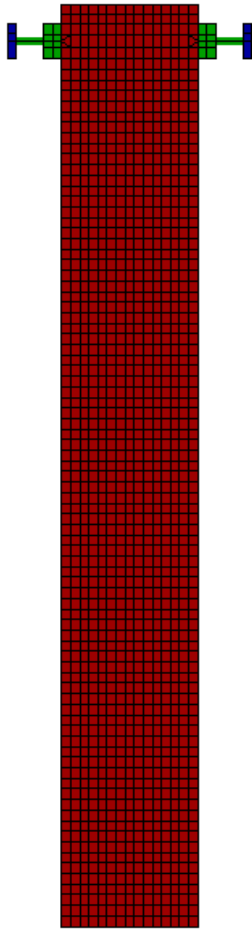


Figure 5-31: VecTor2 VTT-B1 target fine mesh.

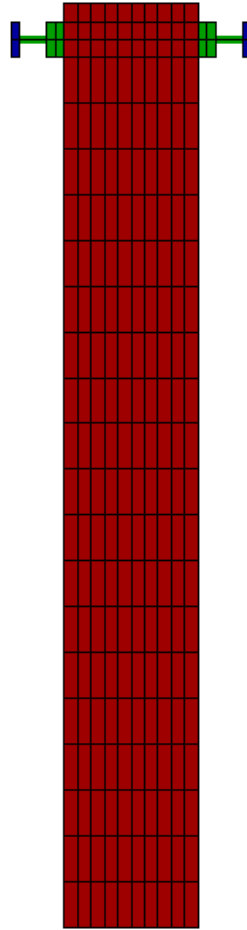


Figure 5-32: VecTor2 VTT-B1 target coarse mesh.

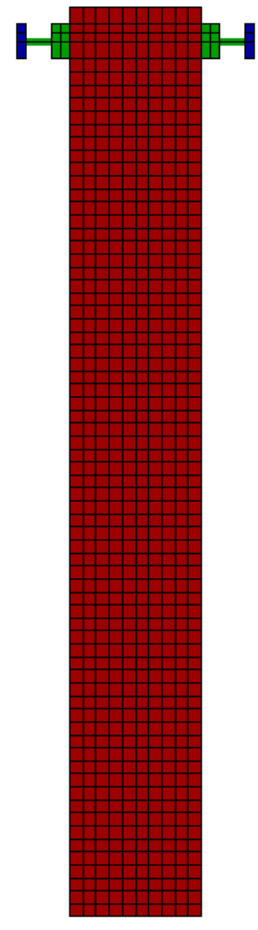


Figure 5-33: VecTor2 VTT-B1 target coarse mesh (aspect ratio=1).

5.3.3.2 VecTor3 Modeling

The concrete target alone was modeled in VecTor3 and the load profile defined in the VecTor2 analyses by modeling the missile explicitly was adapted to the VecTor3 analyses. A total of 4851 nodes, 4000 8-node rectangular concrete elements, and 1520 2-node truss bar elements were used in modeling the flexural specimen. The in-plane reinforcement was modeled using truss bar elements, while the transverse reinforcement was modeled as smeared through the concrete elements. The concrete cover to the longitudinal reinforcement on the front and back was 15 mm. The damping ratios for the first and second modes were 0.25% and 1%, respectively. For the supports, only the degree of freedom in the direction of impact was restrained. Double symmetry was assumed, and those planes of symmetry were restrained in the appropriate directions. The mesh is shown in Figure 5-34. The same material properties for the

concrete and steel that were specified for the target in the VecTor2 model were used for the VecTor3 model. The nodes loaded with the impulse force and the total load applied to the quarter slab are illustrated in Figure 5-35.

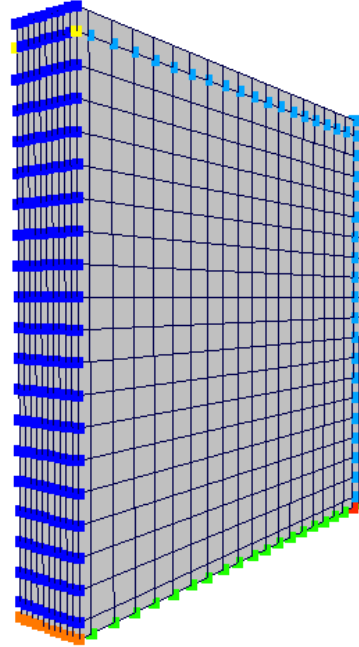


Figure 5-34: VecTor3 VTT-B1 mesh.

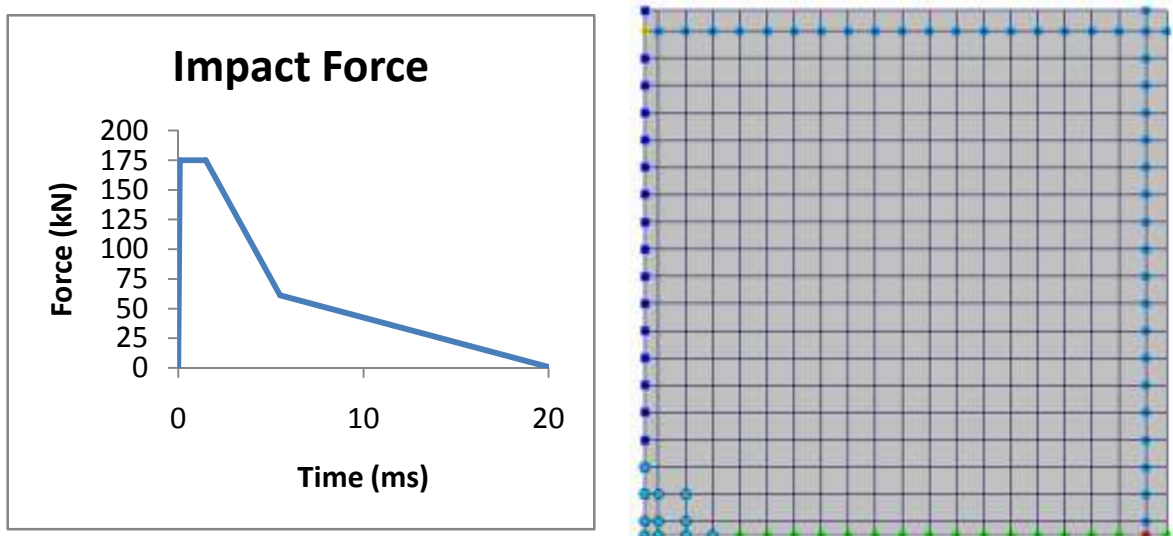


Figure 5-35: Load applied to quarter slab and loaded nodes in VecTor3 VTT-B1 (indicated in blue in the lower left corner of the mesh).

5.3.3.3 Comparison of VTT-B1 Displacement Results

Table 5-17 compares the VecTor3 peak displacement with the displacement from VecTor2 using the same mesh density. In VecTor3, a quarter of the slab was modeled and was supported on two sides. Half of the slab was modeled in VecTor2, and the support condition was simplified to simply-supported on one edge only. In both of these analyses, the concrete cover was 15 mm.

Table 5-17: Displacement Results for VecTor2 and VecTor3 VTT-B1 Analyses Using Nodal Loads

Results	Experimental	VecTor2 (Coarse Mesh)	VecTor3	
			20x20x10	20x20x10 w/ Strain Rate
Max Displacement (mm)	28.89	38.7	32.83	27.06
Time of Max. Disp. (ms)	13.50	18.7	10.80	9.90

A detailed comparison of VecTor3 results to experimental results is given in Appendix A; reinforcement strains, concrete strains, displacements, and support forces from the base analysis are compared to experimental results. Analyses were also done considering strain rate effects for both the concrete and the steel (using CEB strain rate formulations) and for steel only (using CEB 1988). The displacements from those analyses and the base analysis are compared to experimental peak displacements at each displacement sensor location in Table 5-18. The three sets of displacement results indicate that incorporating strain rate effects for the concrete has a much larger effect than incorporating strain rate effects for steel. As well, when strain rate effects were considered for the concrete, displacements at all sensor locations were underestimated by VecTor3, suggesting that it may be overly conservative to consider concrete strain rate effects and that confinement may already provide some increase in strength. As discussed previously, other impact analyses carried out using the VecTor programs have led to the same conclusions.

Table 5-18: Comparison of Displacements for VecTor3 VTT-B1 Analyses With and Without Strain Rate Effects

Sensors (back face)			Peak Displacements						
Name	x (mm)	y (mm)	Experimental	VecTor3 (base)	% Error	VecTor3 (Strain Rate)	% Error	VecTor3 (Steel SR)	% Error
W1	0	0	28.89	32.83	13.64	27.06	-6.32	31.95	10.59
W2	250	250	20.38	22.80	11.90	19.01	-6.74	22.31	9.47
W3	250	0	21.96	26.13	19.01	21.81	-0.68	25.56	16.39
W4	385	385	15.27	17.26	13.03	14.44	-5.43	16.91	10.74
W5	385	0	19.53	21.94	12.32	18.35	-6.04	21.48	9.98

Figure 5-36 compares the VecTor3 displacement-time response to the experimental response at the centre of the slab. While the peak displacement was higher for the base simulation, both VecTor3 analyses exhibit a shorter period than observed experimentally. This may partly be a result of how the supports were modeled. One of the other reasons for this is the loading function used. The peak load from VecTor2 was higher than predicted by the Riera method, and the loading function obtained from VecTor2 was much more heavily weighted to the beginning of the impact, with the load decaying more quickly. Figure 5-37 compares the load obtained from VecTor2 to the load predicted using the Riera method (Borgerhoff et al., 2011).

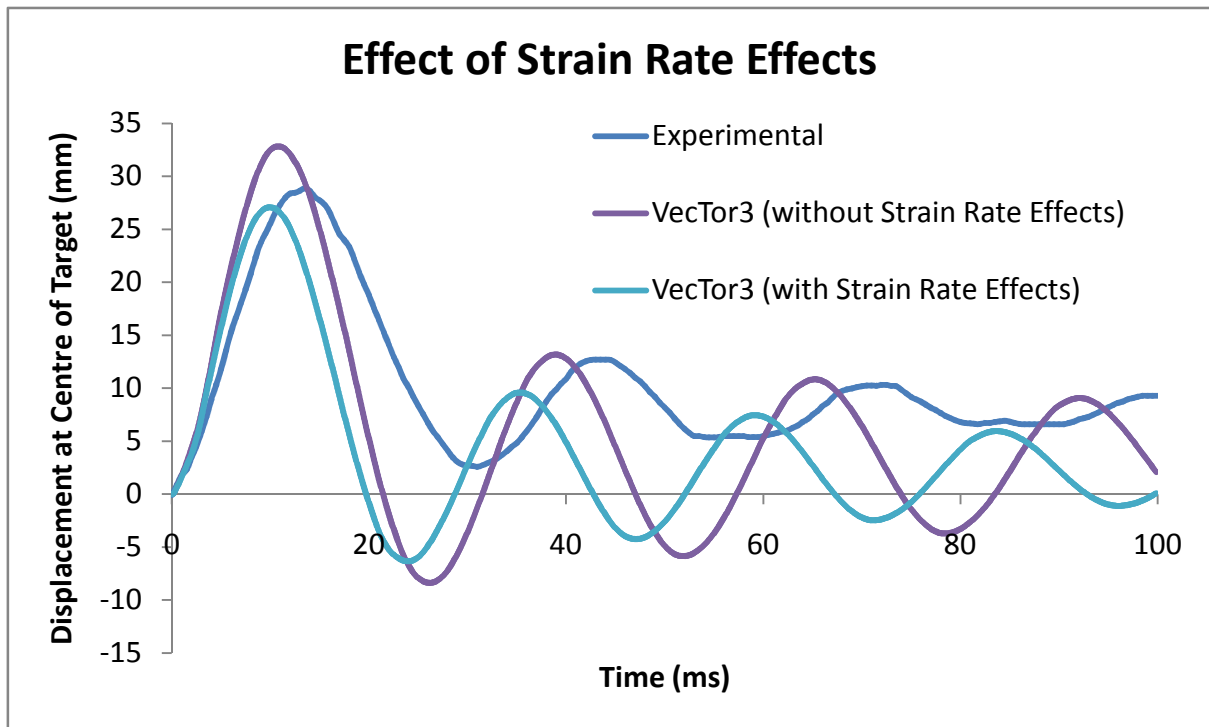


Figure 5-36: Comparison of VecTor3 and experimental displacement-time response for centre of VTT-B1.

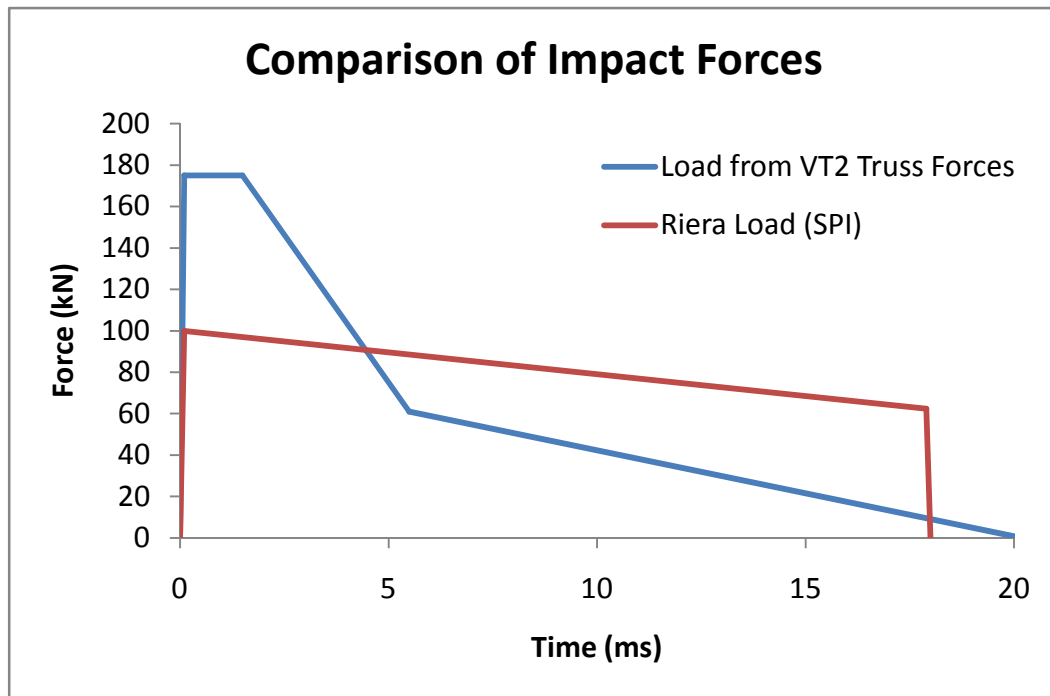


Figure 5-37: Comparison of VecTor2 truss forces to Riera load for VTT-B1.

Figure 5-38 shows the displacement-time response obtained in VecTor3 when the Riera load was used. In this analysis, the peak midspan displacement was slightly underestimated. The peak displacement predicted by VecTor3 was 27.2 mm, compared to the experimental peak of 28.9 mm. However, if a finer mesh was used, the displacement predicted by VecTor3 would be closer to the experimental result. Comparing the period predicted by VecTor3 and the period observed experimentally, the period is more accurately predicted when using the Riera load.

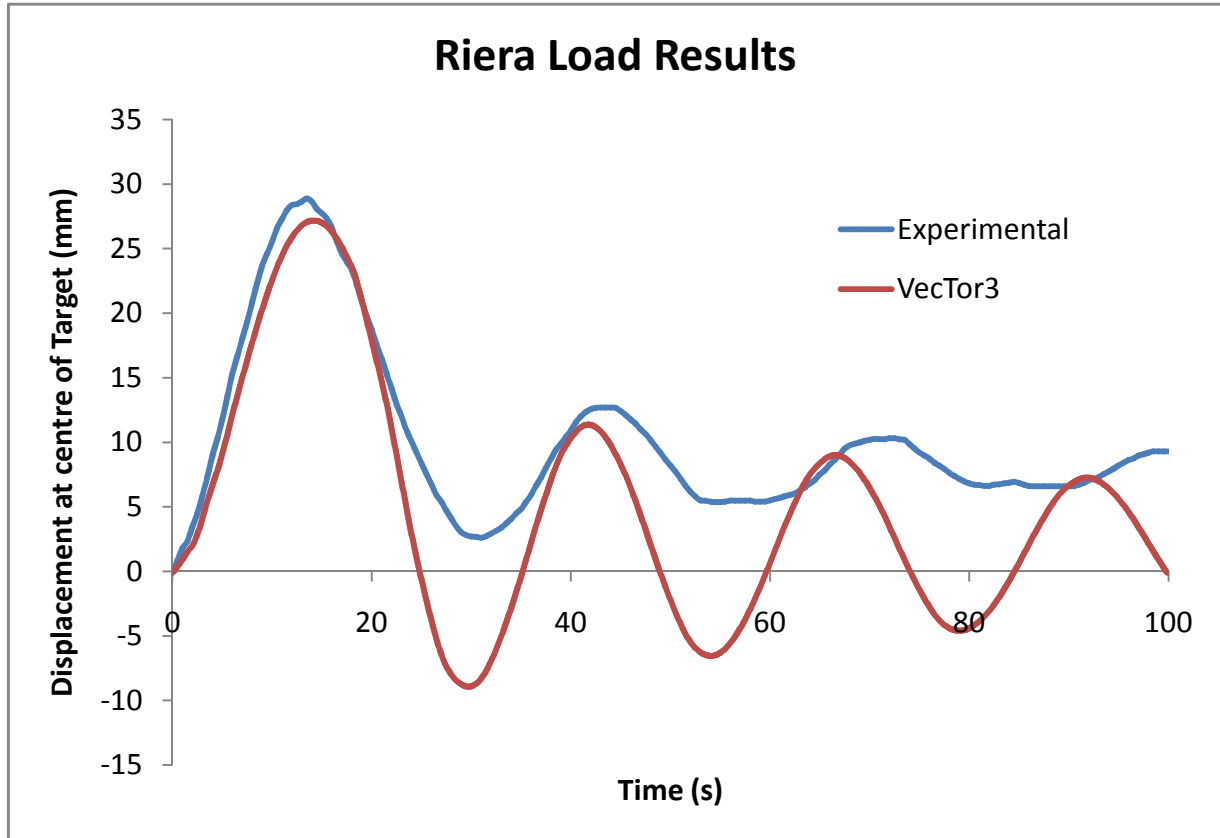


Figure 5-38: Displacement-time response for centre of VTT-B1 using Riera load in VecTor3.

5.3.3.4 Effect of Concrete Cover and Mesh Size

This section discusses the effect of concrete cover on the displacement results for the B1 specimen. In the experiment, the concrete cover was 15 mm with the reinforcement provided in two mats, one in each principal direction. Due to constraints in the model, the reinforcement in the VecTor3 analyses was specified all at the same depth, and this may have resulted in a slight underestimation of displacements. Because of this, and to examine the effect of reinforcement depth on peak displacements, an analysis was performed using the same mesh and material properties, with the only difference being that the depth to all reinforcement was 30 mm from each face. The results of this analysis are compared to the experimental results and the results obtained with a concrete cover of 15 mm in Table 5-19.

Table 5-19: Displacement Comparison for VecTor3 Analysis of VTT-B1 With Reinforcement Depths of 15 mm and 30 mm

Sensor	Peak Displacement Results					Difference in Displacement (mm)
	Experimental	20x20x10 Mesh (cover=15 mm)		20x20x10 Mesh (cover=30 mm)		
		VecTor3 (base)	% Difference	VecTor3 (base)	% Difference	
W1	28.89	32.83	13.6	34.38	19.0	1.55
W2	20.38	22.80	11.9	24.16	18.6	1.36
W3	21.96	26.13	19.0	27.55	25.5	1.42
W4	15.27	17.26	13.0	18.37	20.3	1.12
W5	19.53	21.94	12.3	23.14	18.5	1.21

The results shown above indicate that while the depth to reinforcement does influence the results slightly, the error introduced by having both layers of reinforcement at the same depth is likely small. The maximum difference between peak displacements, with a difference in reinforcement depth of 15 mm is only 1.55 mm.

The effect of mesh density will now be examined with respect to analyses done using VecTor3. For the base analyses, 10 elements were used through the thickness of the slab. In keeping with the goal of carrying out a simplified analysis, a simulation was also done using a very coarse mesh, with only four elements through the depth of the slab. For this analysis the depth to reinforcement was 30 mm, and strain rate effects were not considered. The peak displacement at W1, the centre of the slab, was 28.6 mm, compared to 34.4 mm obtained using a

finer mesh. This result is consistent with the understanding that a finer mesh is typically less stiff and yields larger displacements.

5.3.3.5 VecTor3 Deformed mesh and Crack Patterns

This section illustrates the crack patterns and displaced shapes obtained from the base VecTor3 analysis for the flexural specimen. The figures in this section are from $t=10.8$ ms, the time of maximum displacement at the centre of the slab. Figure 5-39 illustrates the deformed mesh and displacement contours for the front face of the slab. Figure 5-40 and Figure 5-41 are views of the vertical and horizontal sections.

Looking at the crack pattern on the front face, Figure 5-42, there is light flexural cracking but no major damage. Figure 5-43, showing the crack pattern on the back face, also illustrates flexural damage. On the back face of the slab, the maximum crack width calculated by VecTor3 at the time of peak displacement was 7 mm. The average crack widths ranged from 0.5 mm to 3 mm.

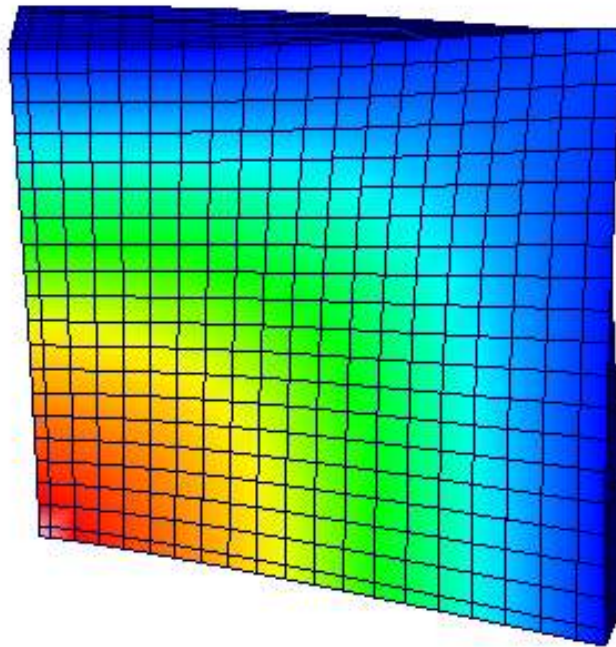


Figure 5-39: VecTor3 VTT-B1 deformed mesh at $t=10.8$ ms (front face).

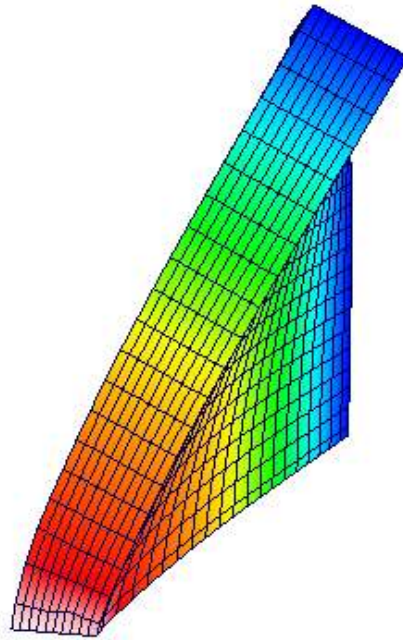


Figure 5-40: VecTor3 VTT-B1 deformed mesh at $t=10.8$ ms (vertical section).

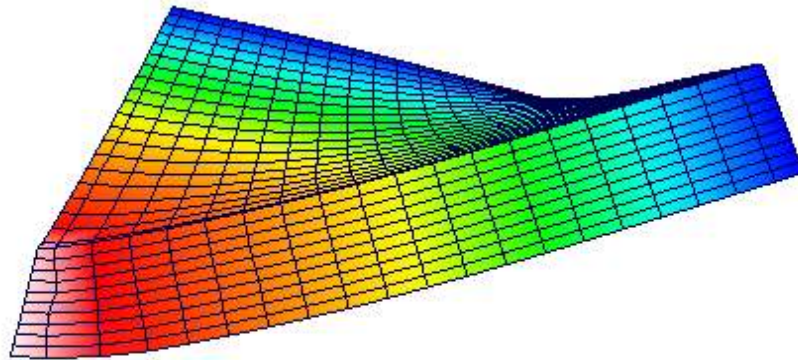


Figure 5-41: VecTor3 VTT-B1 deformed mesh at $t=10.8$ ms (horizontal section).

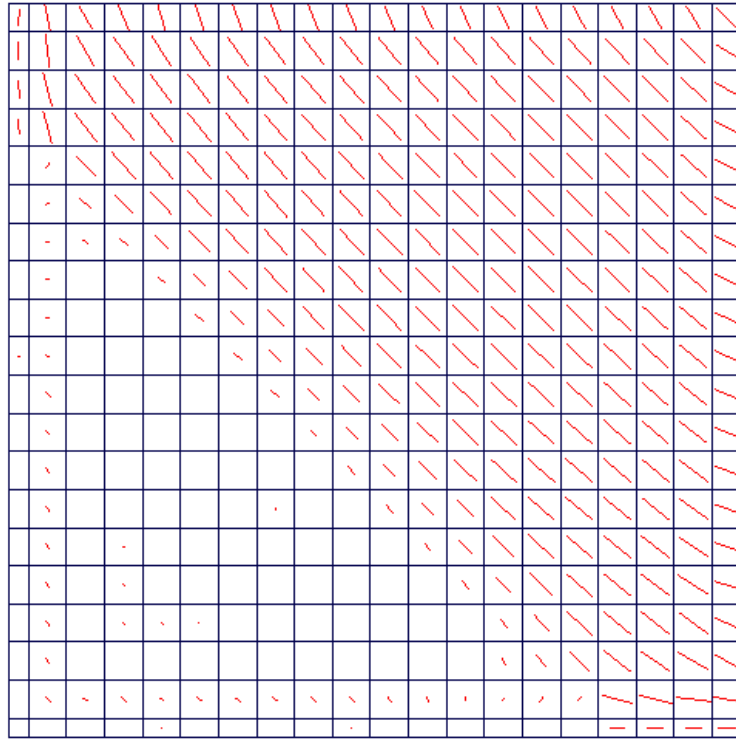


Figure 5-42: Crack pattern on front face of VTT-B1 at $t=10.8$ ms (centre of slab, point of impact, located in lower left corner).

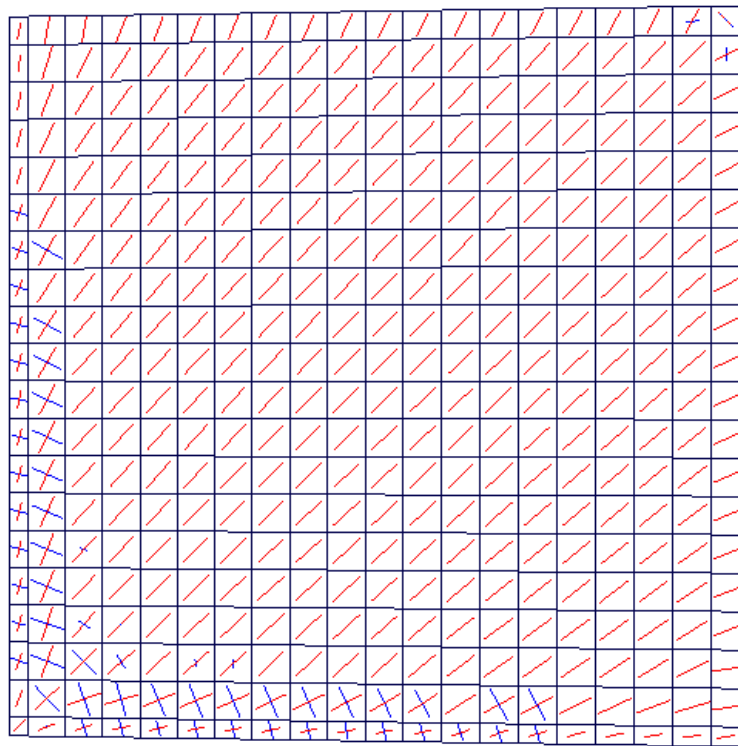


Figure 5-43: Crack pattern on back face of VTT-B1 at $t=10.8$ ms (centre of slab, point of impact, located in lower left corner).

5.3.3.6 Comparison of VecTor3 and Experimental Results

This section compares the displacement and reinforcement strain profiles at the centre of VTT-B1 and discusses the reaction forces. In Section 5.3.3.3 the displacement results at the centre of the target were discussed. An extended displacement-time response of the centre of the slab, for the base VecTor3 analysis without strain rate effects and using the load derived from VecTor2 impact modeling, is shown in Figure 5-44.

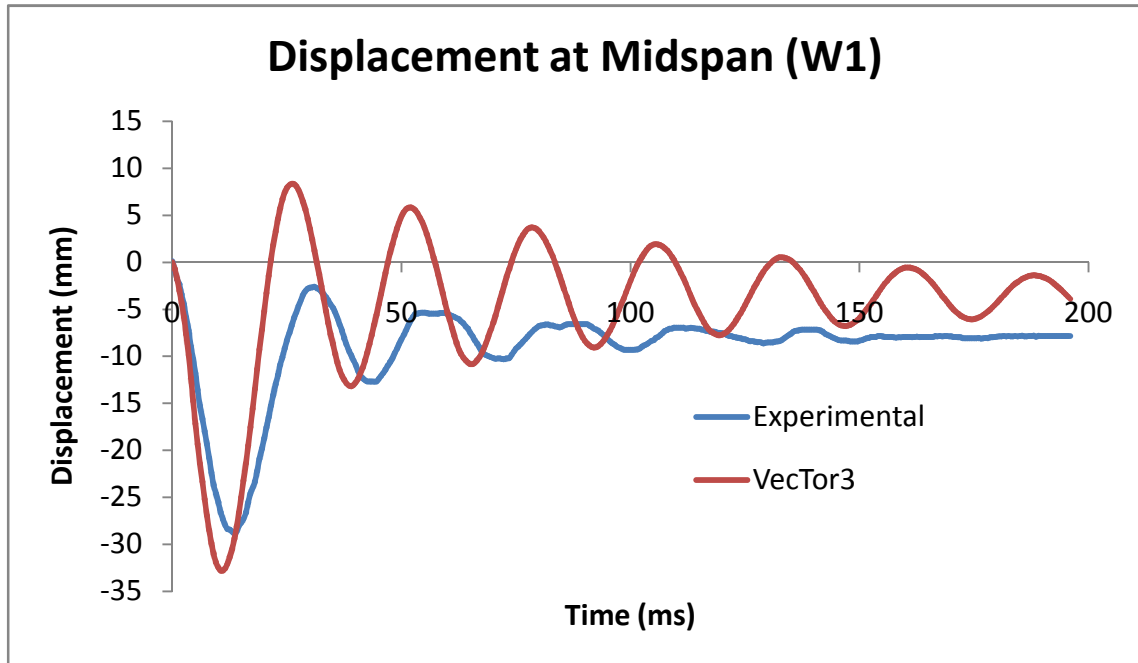


Figure 5-44: Comparison of VecTor3 and experimental displacement responses for centre of VTT-B1

It was observed in Section 5.3.3.3 that for the base model, while the peak displacement and rebound displacement were over-predicted by VecTor3, the period was shorter. Two possible reasons for this were stated. Firstly, in the VecTor3 analyses, the actual details of the supports were not explicitly modeled. The supports were idealized by restraining all nodes along the panel perimeter in the direction of the impact. In the experiment, while a steel tube was provided as a support along all four edges, there were four main supporting posts, one in each corner. The simplified modeling of the supports may have made the model stiffer than the target was in the experiment. Secondly, it was noted that there was likely error in the loading function used, since it was derived from a VecTor2 analysis where buckling of the missile was approximated. In comparing the load function derived from the VecTor2 impact to the Riera load it was observed that the load predicted by VecTor2 was weighted more heavily toward the beginning of the

impact, the peak force was almost double that of the Riera load, and the load from VecTor2 decreased much more rapidly than the Riera load. A comparison of the displacement-time responses at the centre, obtained from the base analysis and from an analysis using the Riera load, was also presented in Section 5.3.3.3 (see Figure 5-38). It was observed that when the Riera load was used, the peak displacement predicted by VecTor3 was closer to the measured displacement, the initial stiffness more closely matched the experiment, and the period was closer to the experimental period.

Compared in Figure 5-45 are the VecTor3 and experimental reinforcement strains for the reinforcement located at the back of the slab, 27.5 mm (horizontally) away from the centre of the slab. In terms of peak strain, the strain predicted by VecTor3 matches the experimentally measured strain fairly well. Comparing the post-peak responses, the periods are similar, though the period predicted by VecTor3 is slightly shorter. Also, the experimental strain damps out faster than predicted by VecTor3. The most noticeable difference, though, is the difference between the measured residual strain and the residual strain predicted by VecTor3. VecTor3 predicts negligible residual strain, while the experimental residual strain was approximately 20×10^{-3} .

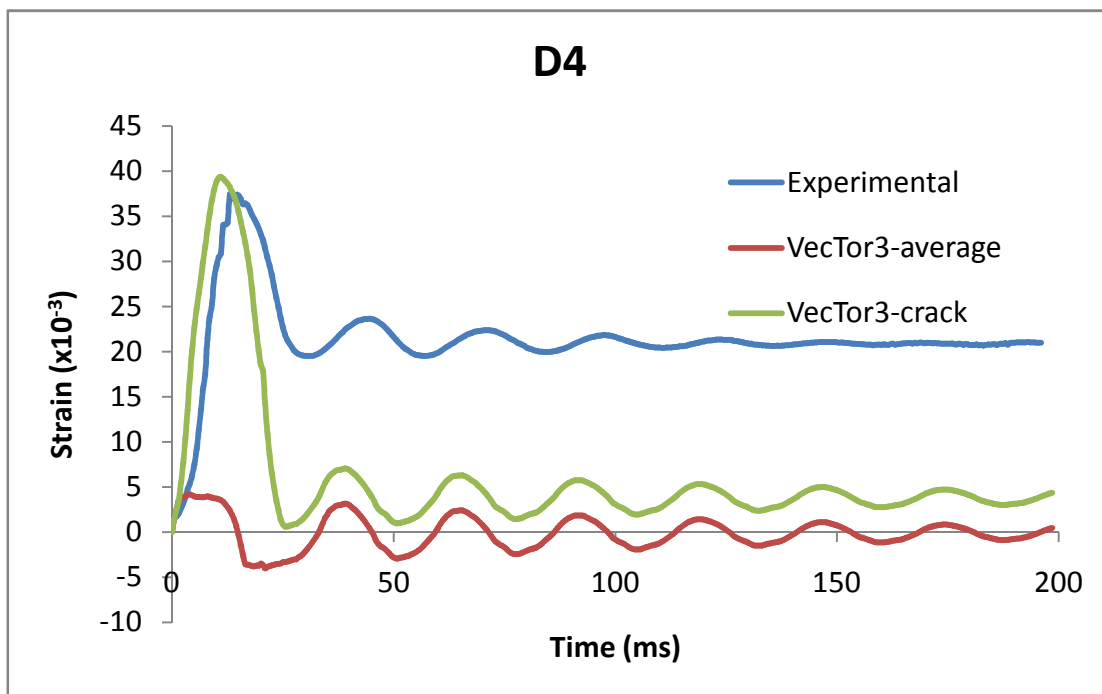


Figure 5-45: Comparison of reinforcement strains at midspan of VTT-B1

The measured and predicted support forces are compared in Figure 5-46, and the comparison of the impulse at the support, derived from the reaction forces, is shown in Figure 5-47.

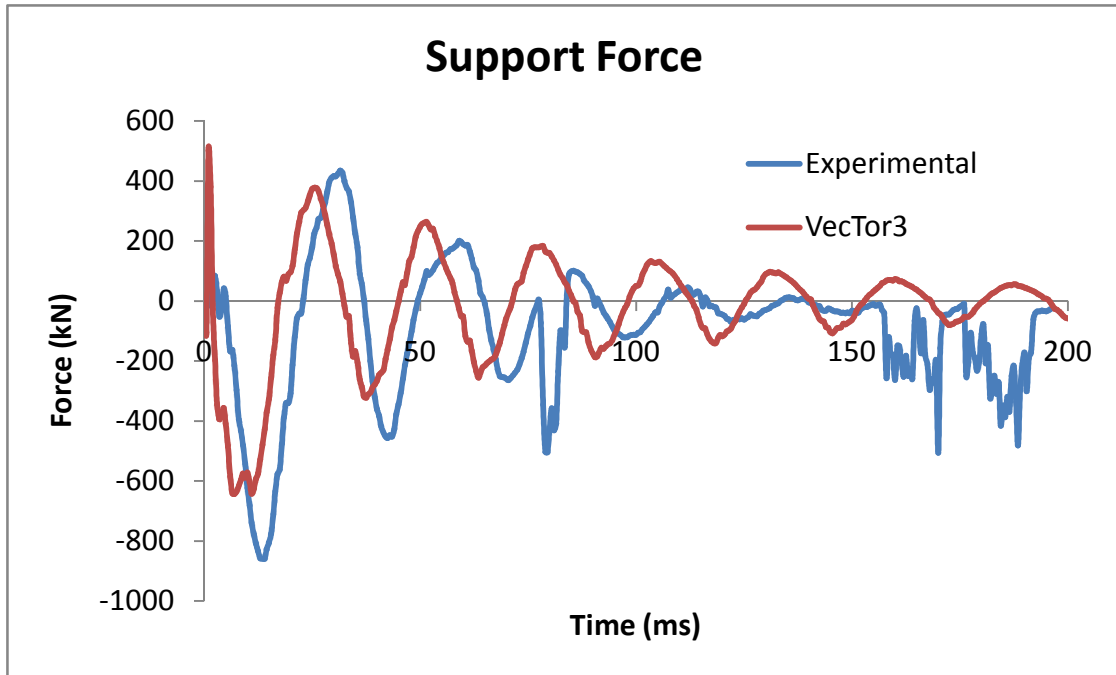


Figure 5-46: Comparison of support forces for VTT-B1

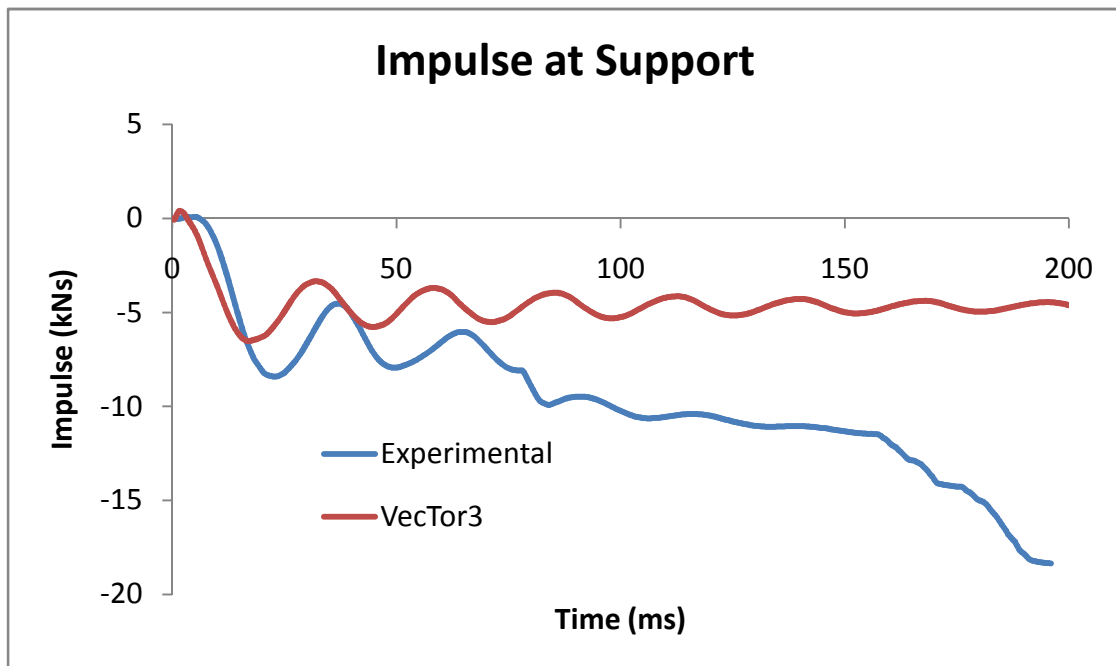


Figure 5-47: Comparison of impulse at support for VTT-B1

Looking at Figure 5-46, the peak experimentally measured support force was just over 800 kN, while VecTor3 predicted a peak force of approximately 600 kN. The second and third experimental peaks are also slightly higher than predicted by VecTor3. For the first 75 ms, the experimental and analytical periods are similar, with the VecTor3 reaction force lagging slightly behind the experimental one, but having basically the same shape. Aside from the few spikes later in the response, the support force measured experimentally damps out faster than the VecTor3 support forces.

The impulses compared in Figure 5-47 were derived from the measured (or calculated) support forces. The differences mentioned above when comparing the support forces also account for the difference between the experimental and predicted impulses.

5.3.4 Summary of VTT-B1 Modeling

The VTT-B1 flexural specimen was modeled using VecTor2, a program for the nonlinear finite element analysis of two-dimensional reinforced concrete membrane structures, and VecTor3, a program for the analysis of reinforced concrete three-dimensional solid structures. The missile and target were first modeled in VecTor2, and a load profile was derived from the VecTor2 analysis. A three-dimensional analysis of a quarter of the slab was then carried out using VecTor3 and, for the most part, the results obtained from VecTor3 were comparable to the experimental results for the B1 specimen.

It was observed that the period of the response from VecTor3 was shorter than the experimental period, indicating higher stiffness, although the peak displacement predicted by VecTor3 was higher. The cause of this issue was thought to be the loading function, so an analysis was done using a load function derived using the Riera method. Compared to the load obtained from VecTor2, the Riera load has a lower peak, but the force decreases much more gradually. When the VecTor3 response using the Riera load was compared to experimental, the peak displacement was slightly lower, but the period was closer. It is noted that a larger displacement would be obtained from VecTor3 if a finer mesh was used or if the same number of elements through the thickness was used but the element aspect ratio was closer to 1. As well, both layers of steel were specified at a depth of 15 mm. Analyses have shown that separating the steel layers would increase the displacement only slightly. Despite the effect that these small changes to the

modeling would have on the results, it is concluded that the modeling of the missile is the largest source of error, and that the response of the concrete target was captured adequately.

In terms of the concrete response, comparing the displacement-time responses obtained from VecTor3 to those observed in the experiment, there is not enough hysteretic damping. The rebound displacement predicted by VecTor3 was much larger than observed experimentally. Looking at the reinforcement strains predicted by VecTor3, shown in Appendix A, the peak strains generally agree well with the experimental measurements, although the residual strains are not as consistent. Comparing the concrete strain to the strain measured experimentally, it is important to note that the strain values from VecTor3 have error in them due to the fact that the aspect ratio for the elements is so large. It is possible that a mesh with elements having an aspect ratio closer to 1 would do better in predicting the concrete strains. The VecTor3 mesh was determined by the in-plane reinforcement layout and the desire to have 10 elements through the thickness of the slab. Computational constraints limited the total number of elements, which resulted in the high element aspect ratio.

5.4 VTT-P1 Punching Specimen

The VTT-P1 punching test was commissioned by the CNSC and carried out at VTT. The goal of this test was to obtain perforation of a concrete wall by a non-deformable missile, with the residual velocity being as close to zero as possible. The wall dimensions were 2100 x 2100 x 250 mm, and the target values for the missile mass and impact velocity were 135 m/s and 47 kg. The target dimensions and support conditions are shown in Figure 5-48 and the missile is shown in Figure 5-49.

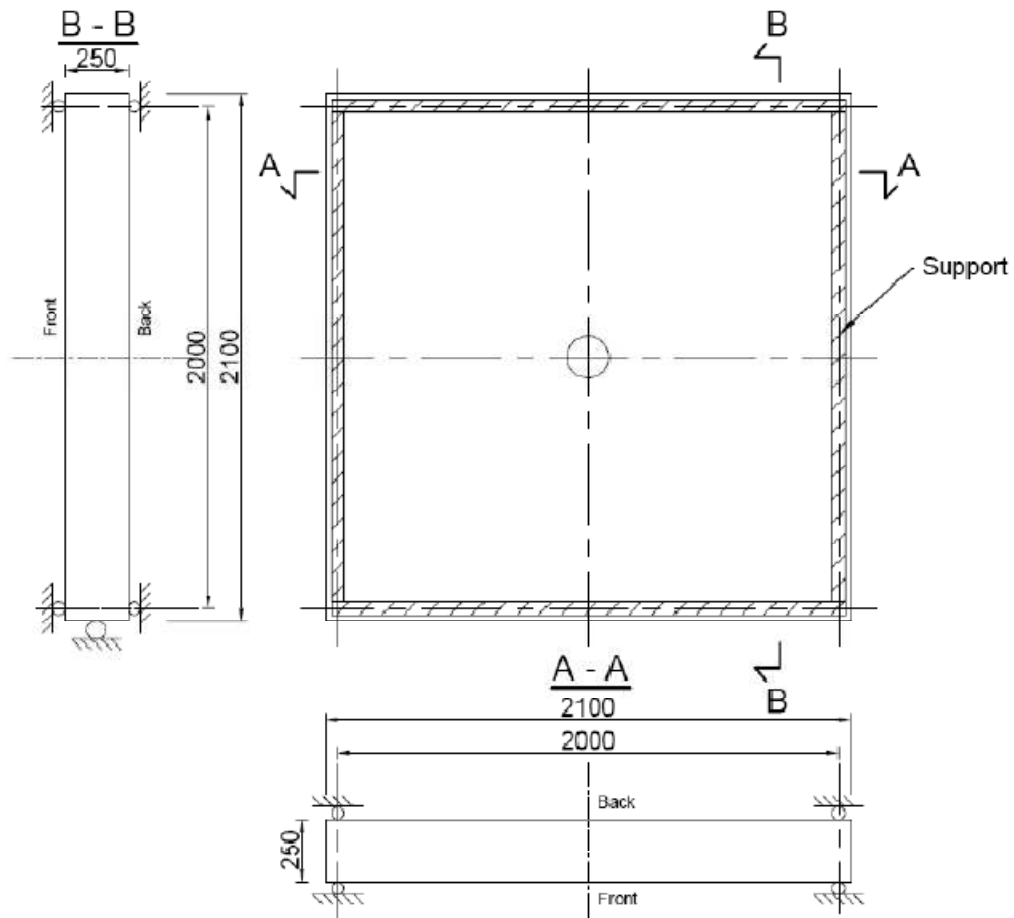


Figure 5-48: VTT-P1 dimensions and support conditions (Vepsä, 2010b).

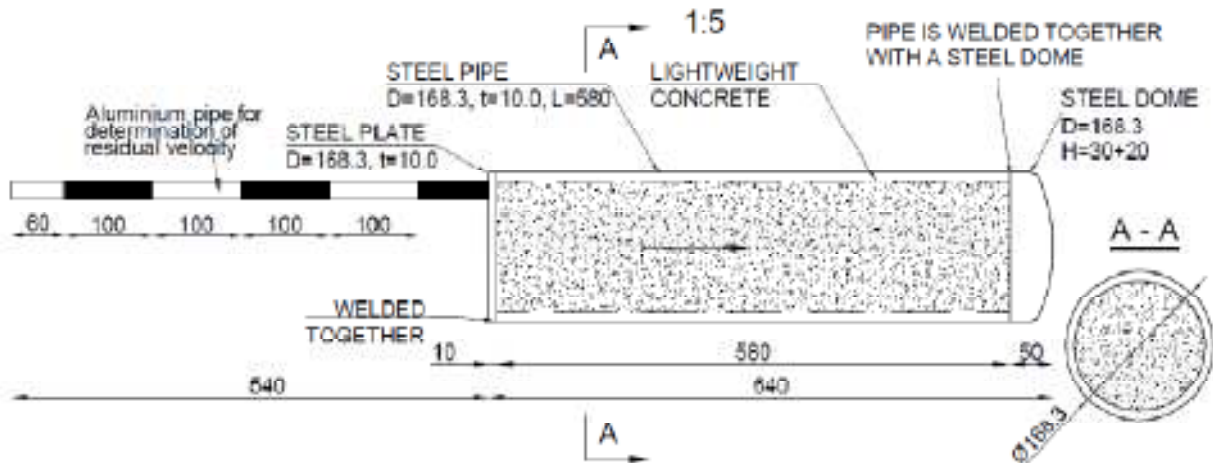


Figure 5-49: VTT-P1 missile (Vepsä, 2010b).

The concrete strength was 60 MPa, and the reinforcement in the in-plane directions, illustrated in Figure 5-50 and Figure 5-51, consisted of 10 mm diameter bars spaced at 90 mm. No shear reinforcement was provided.

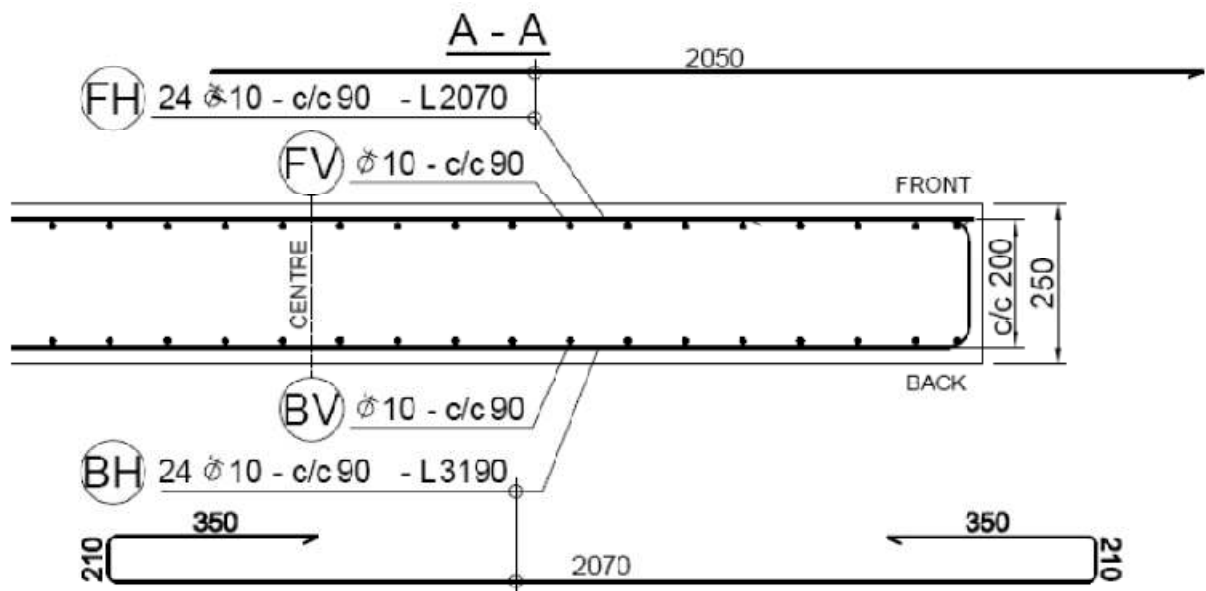


Figure 5-50: Horizontal cross section of VTT-P1 (Vepsä, 2010b).

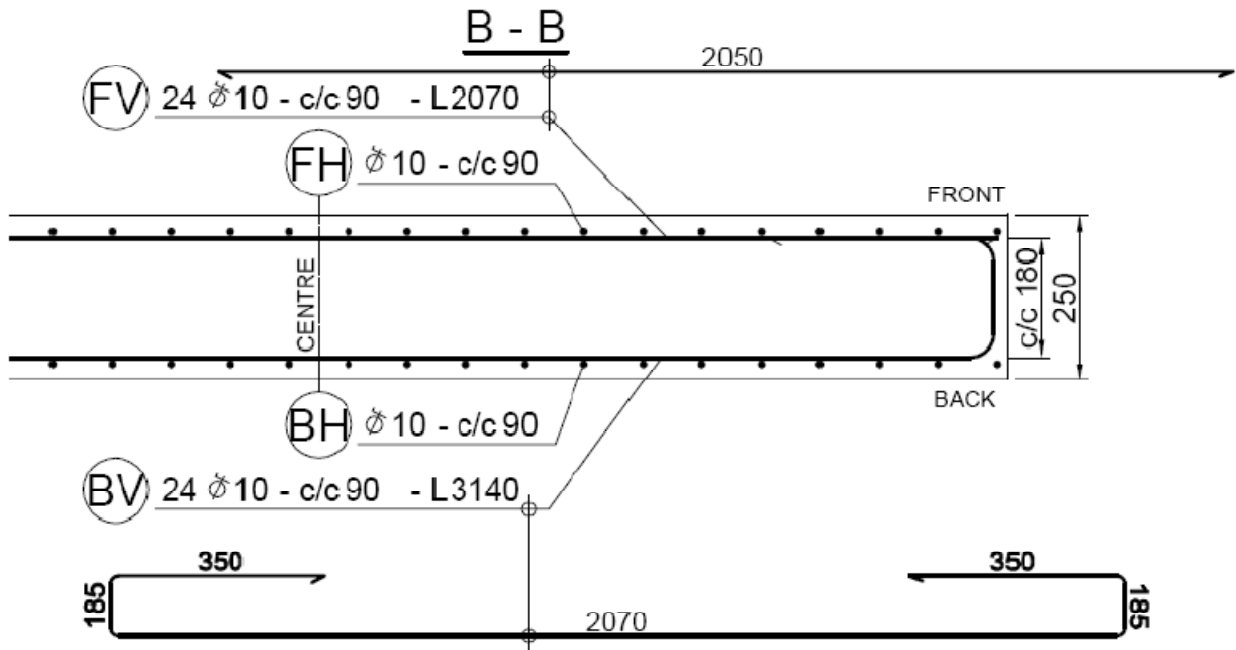


Figure 5-51: Vertical cross section of VTT-P1 (Vepsä, 2010b).

The VTT-P1 punching specimen was modeled using both VecTor2 and VecTor3. Default material behaviour models and analysis parameters were used in most cases. The exception was the concrete stress-strain curve, for which the Hoshikuma model was used. Similar to the modeling for VTT-B1, half of the specimen was modeled in VecTor2, and a quarter of the specimen was modeled in VecTor3.

5.4.1 VecTor2 Modeling

As with the flexural specimen, a model was first constructed in VecTor2 to determine the load applied to the slab. The model of the missile and target is shown in Figure 5-52, and the material properties used for the missile are summarized in Table 5-20.

A total of 3294 nodes, 3063 rectangular elements, 87 triangular elements, and 219 truss bar elements were used in the model. Within the target, the average element size was 10 x 10 mm. There were 25 elements through the depth, which is considered appropriate for a specimen where shear mechanisms are likely to dominate. The typical element size for the missile was also 10 x 10 mm.

In the VecTor2 model for this specimen, both concrete and steel elements were used, to represent the concrete-filled missile. A total of 8 compression-only truss bars were used to transfer the

force from the missile to the target. The area of the compression-only truss bars sum to the cross-sectional area of the missile (each truss bar has an identical area), and softer impacts were not examined for this specimen. The material properties are summarized in Table 5-21. The horizontal in-plane reinforcement was modeled as smeared and the reinforcement ratio was calculated to be 0.72% based on the given reinforcement layout of 10 mm bars spaced at 90 mm in each direction and face.

Compression-only truss bars for the supports were not used in this case. Movement was restricted in the direction of impact at the support locations. The support locations are shown in Figure 5-53. A time-step of 1×10^{-5} seconds was used. This time-step was chosen because a larger time-step may not have captured the compression-only truss forces as accurately, and smaller time-steps resulted in unstable results in VecTor3.

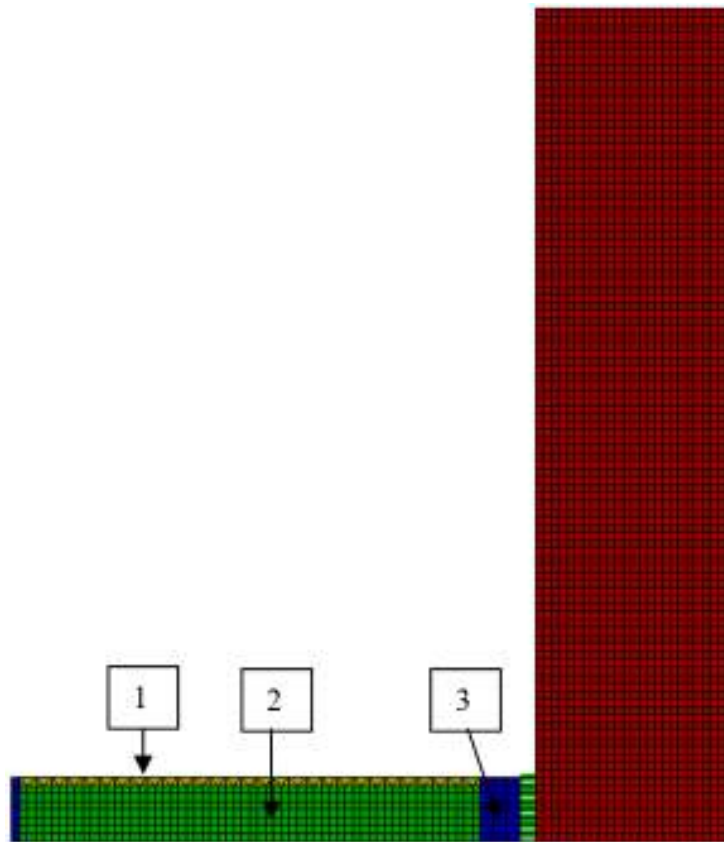


Figure 5-52: VecTor2 mesh of VTT-P1 missile and target.

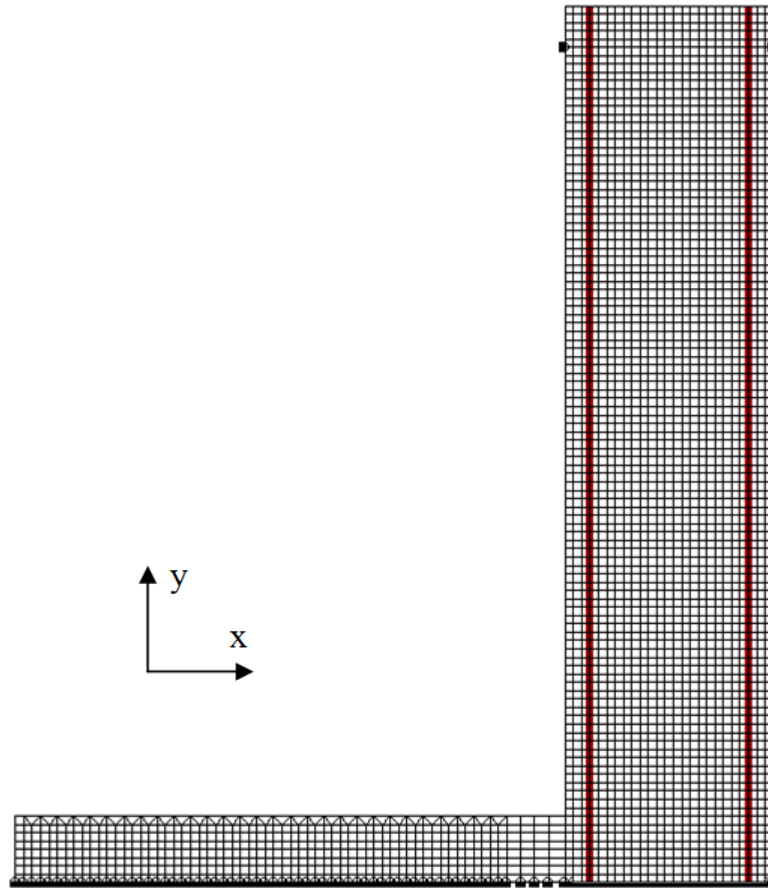


Figure 5-53: VecTor2 VTT-P1 support and reinforcement locations.

Table 5-20: VTT-P1 Missile Properties

Missile Truss Properties		Missile Body Properties					
		1 (steel)		2 (concrete)		3 (steel)	
A_{truss} (mm ²)	1235	F_y (MPa)	355	f'_c (MPa)	60	F_y (MPa)	355
Number of Trusses	9	F_u (MPa)	600	f'_t (MPa)	4.04	F_u (MPa)	600
E_{truss} (MPa)	200000	e_{sh} (x10 ⁻³)	3	E (MPa)	29429	e_{sh} (x10 ⁻³)	3
F_y (MPa)	355	e_u (x10 ⁻³)	220			e_u (x10 ⁻³)	220
F_u (MPa)	600	E (MPa)	200000			E (MPa)	200000
e_{sh} (x10 ⁻³)	3	Thickness (mm)	160	Thickness (mm)	160	Thickness (mm)	160
e_u (x10 ⁻³)	220	b/t (buckling)	N/A	b/t (buckling)	N/A	b/t (buckling)	N/A

Table 5-21: VTT-P1 Target Properties

Concrete Properties		Steel Properties	
f'_c (MPa)	60	d_b (mm)	10
ϵ_0 ($\times 10^{-3}$)	2.24	A_b (mm^2)	78.5
f'_t (MPa)	2.56	A_{total} (mm^2)	1884
E (MPa)	32610	ρ (%; in-plane, z-dir)	0.718
		E (MPa)	200000
		f_v (MPa)	540
		f_u (MPa)	605
		ϵ_{sh} ($\times 10^{-3}$)	30
		ϵ_u ($\times 10^{-3}$)	114

While the VecTor2 analysis cannot simulate behaviour in situations where the missile punches completely through the target, the crack pattern can be examined to determine whether punching is likely to occur. The crack pattern obtained for VTT-P1, showing maximum damage to the slab, is shown in Figure 5-54.

The truss forces from the VecTor2 analysis and the load profile used for the VecTor3 analysis are shown below in Figure 5-55. Both analyses were carried out using a time-step of 1×10^{-5} seconds, and 0.25% and 1% damping for modes 1 and 2, respectively.



Figure 5-54:
VecTor2 VTT-P1
crack pattern.

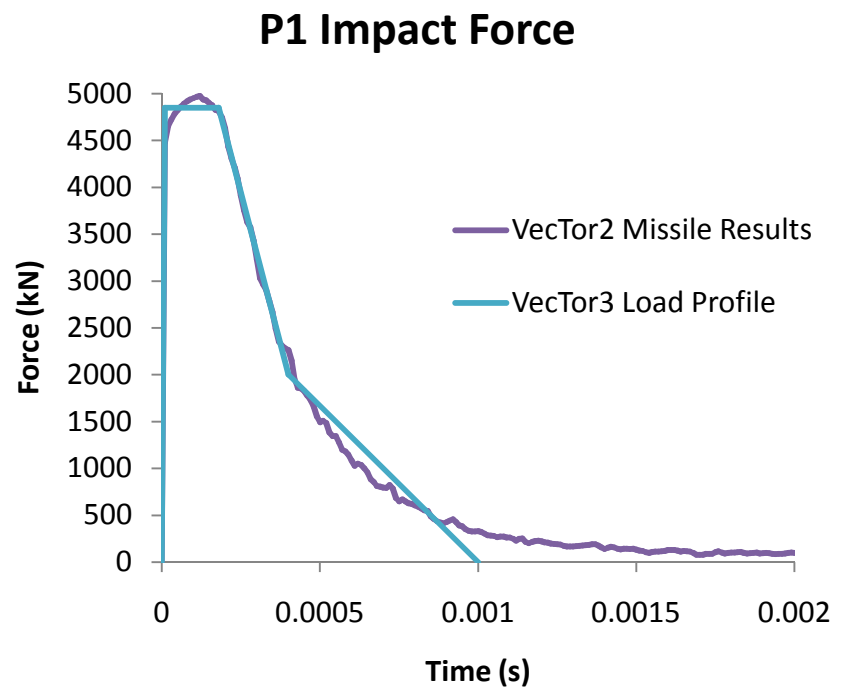


Figure 5-55: Load profile from VecTor2 truss forces and VecTor3 VTT-P1 analyses.

5.4.1.1 VecTor2 Missile Results

Experimentally, there was little damage sustained by the missile. Some crushing of the front of the concrete-filled missile was observed. Figure 5-56 shows the stress contours, predicted by VecTor2, of the missile after impact. It too indicates little damage. The dark blue colour is indicative of large compressive strains, and it is likely that the front part of the missile has experienced some crushing.

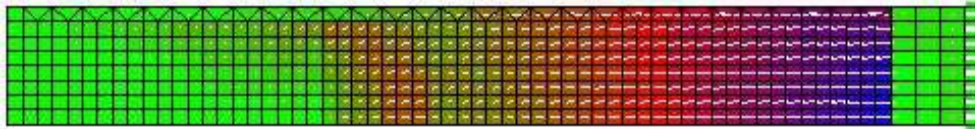


Figure 5-56: Stress contours in concrete-filled VTT-P1 missile after impact.

The displacement and velocity-time profiles of the back of the missile are shown in Figure 5-57 and Figure 5-58. The load profile derived from the compression-only truss bars is shown in Figure 5-59, and the impulse imparted to the target is shown in Figure 5-60. The peak force in the P1 impact is 4.8 MN for the half-specimen modeled, over 10 times the peak force obtained from the B1 model. Note, though, that the total impulse imparted in the P1 modeling is less. In B1, the impulse was approximately 2.3 kNs, whereas the impulse in P1 is 2.0 kNs.

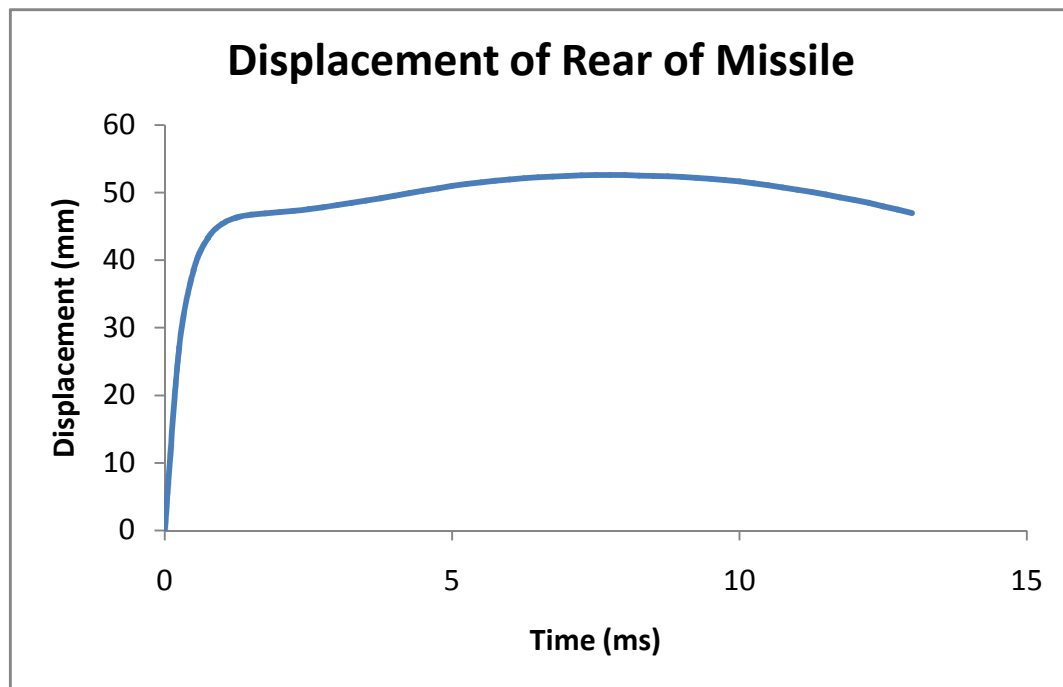


Figure 5-57: Displacement-time history of back of missile in VecTor2 VTT-P1 analysis.

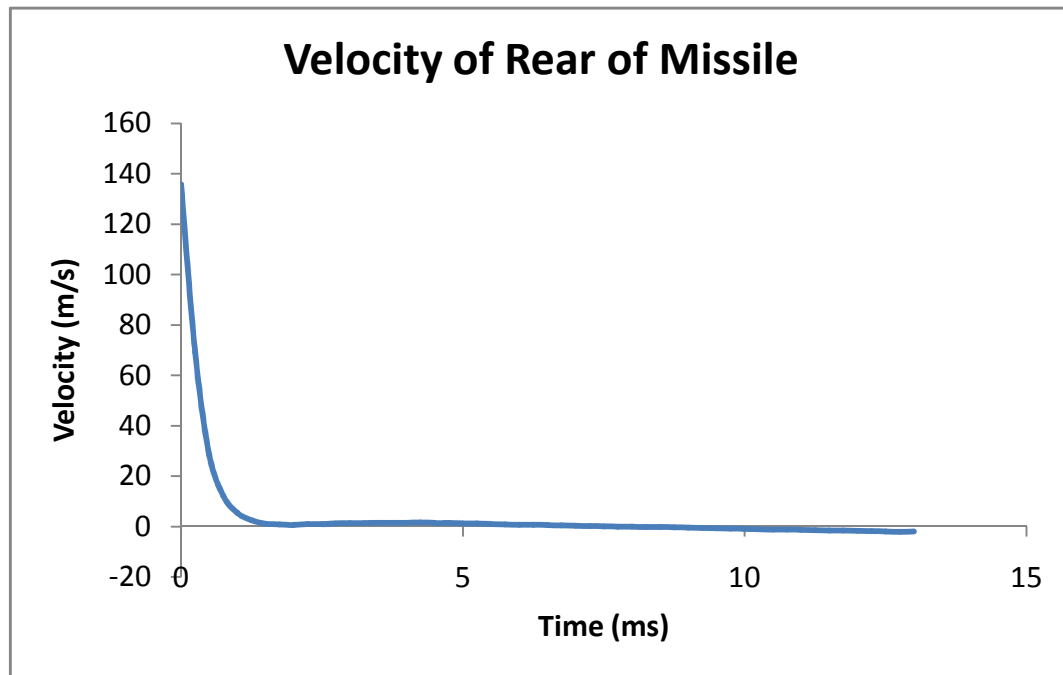


Figure 5-58: Velocity-time history of back of missile in VecTor2 VTT-P1 analysis.

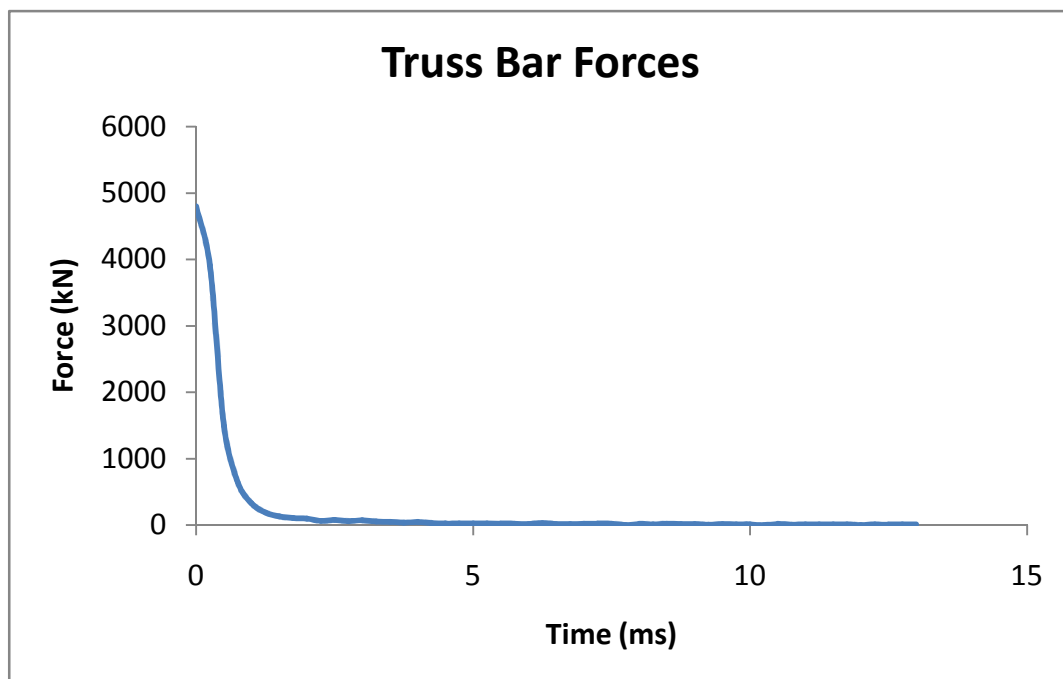


Figure 5-59: Load-time history from truss forces in VecTor2 VTT-P1 analysis.

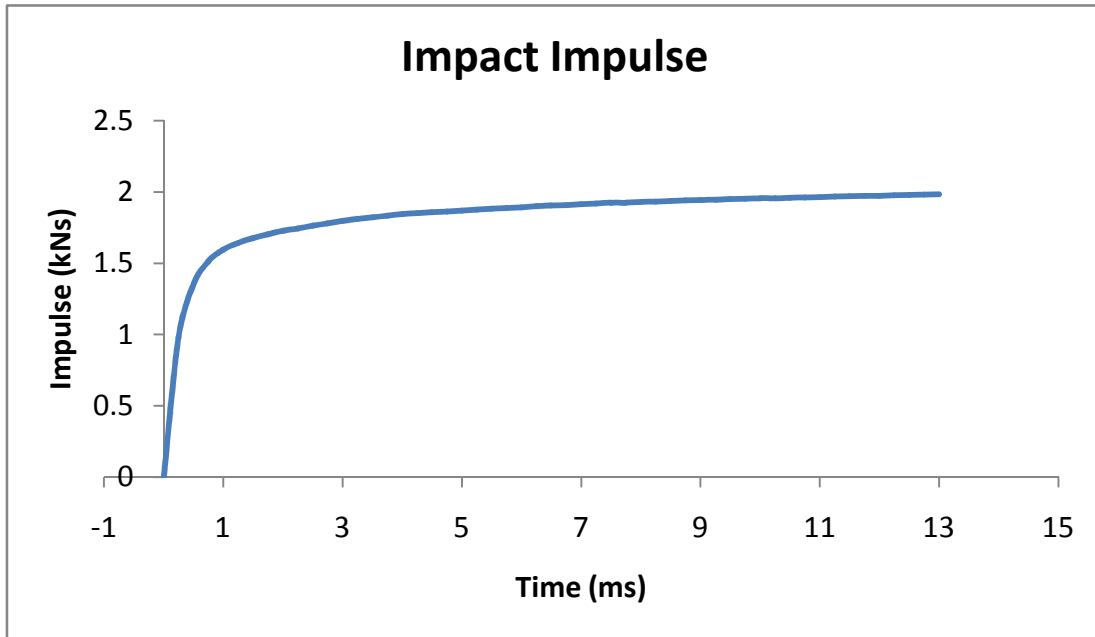


Figure 5-60: Impulse from truss forces in VecTor2 VTT-P1 analysis.

5.4.2 VecTor3 Modeling

A total of 6336 nodes, 5290 rectangular elements for the concrete, and 1104 truss elements for the reinforcement were used to model the punching specimen. Only the target was modeled and the impact was applied to the slab using the nodal forces. For the supports, only the degree of freedom in the direction of impact was restrained. Double symmetry was assumed, and those faces on the axes of symmetry were restrained in the appropriate directions. The mesh is shown in Figure 5-61. The cover used was 25 mm for the front and back faces. The nodes loaded with the impulse force and the load applied to each node are illustrated in Figure 5-62.

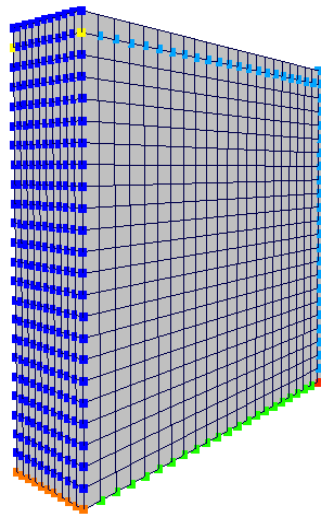


Figure 5-61: VecTor3 VTT-P1 model.

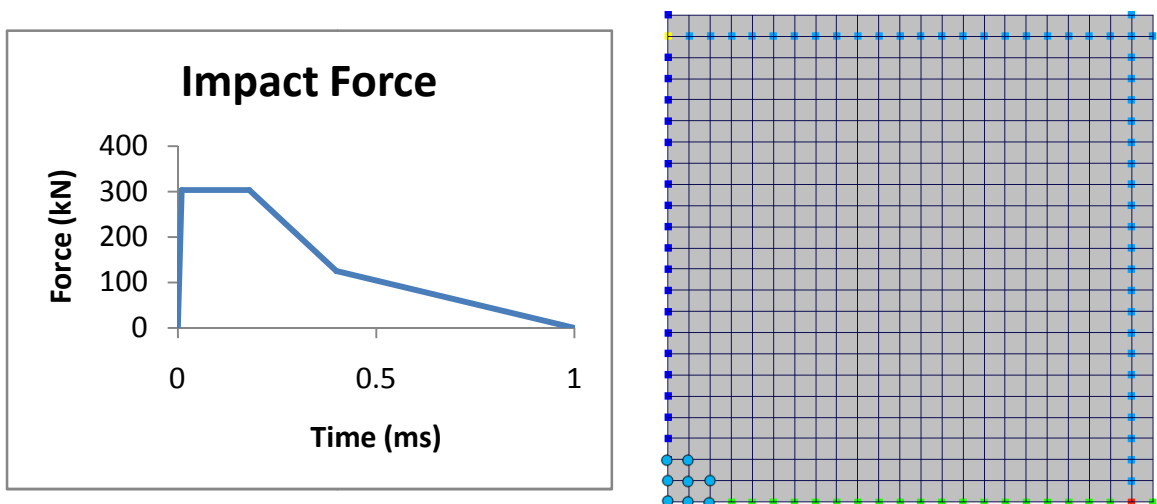


Figure 5-62: VTT-P1 loaded nodes and load profile.

5.4.3 VecTor3 Results

In the experiment, VTT-P1 was perforated, and the missile had a residual velocity of 34 m/s. The damage to the target is shown in Figure 5-63.

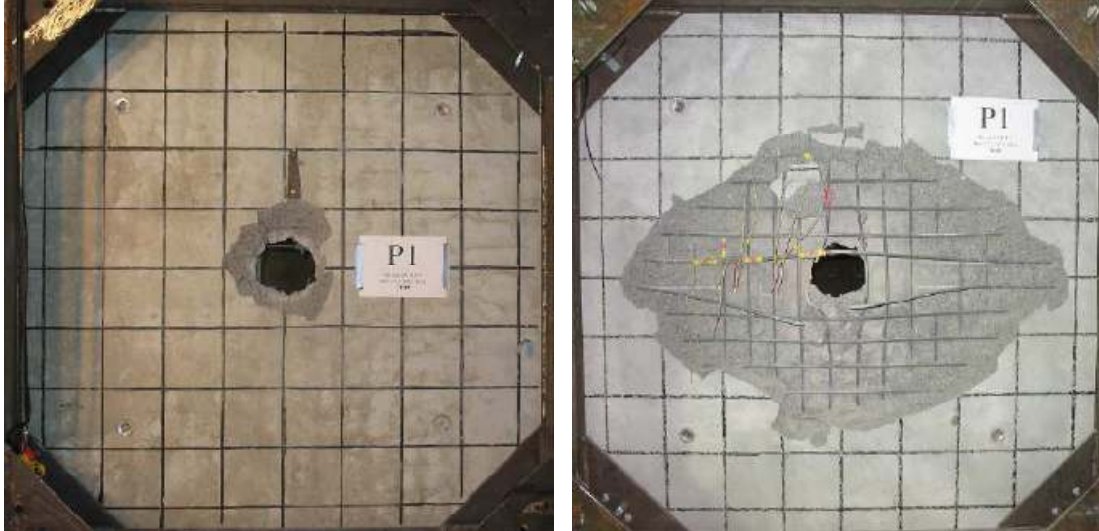


Figure 5-63: VTT-P1 experimental damage (Vepsä, 2010b)
[left: front; right: back]

As shown in Figure 5-64, the predicted displacement response of the centre of VTT-P1, a peak displacement of approximately 85 mm is reached 8 ms into the analysis, and displacements slowly decrease for the remainder of the analysis. A residual displacement of about 40 mm is observed after 100 ms. For the base analysis, the results are stable.

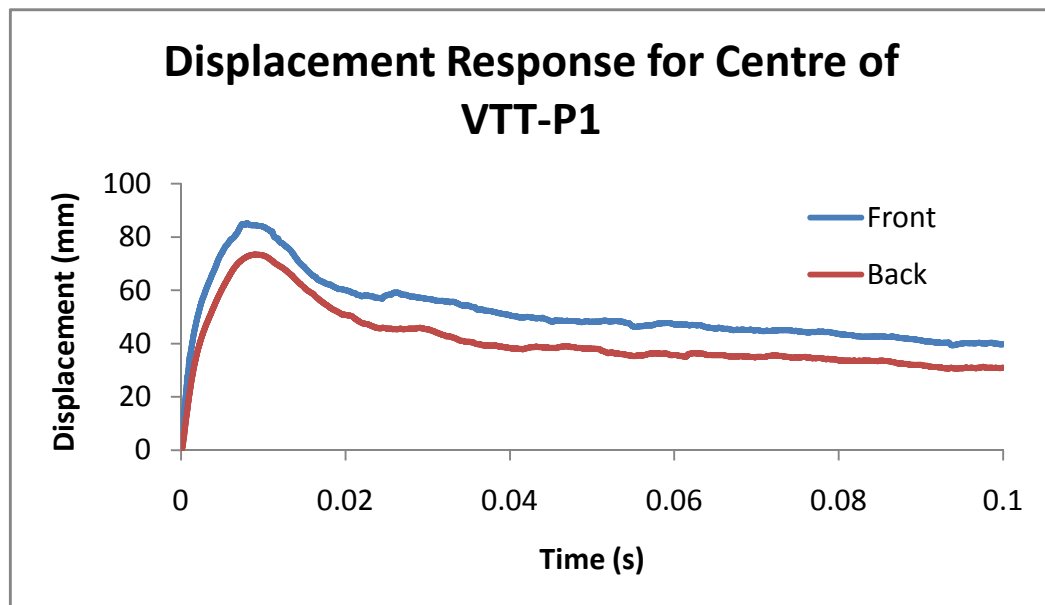


Figure 5-64: Displacement response, predicted by VecTor3, for centre of VTT-P1.

The displacements at each sensor location predicted by VecTor3 are compared to experimental displacements in Table 5-22. There is less agreement between the displacements in this specimen compared to the flexural specimen, and this is likely due to a combination of error in the loading function and not having local damage or element erosion taken into account.

Table 5-22: Comparison of VecTor3 and Experimental VTT-P1 Displacements

Sensor			Peak Displacements (mm)		
Name	Distance from Centre (mm)		Experimental	VecTor3	Theoretical/Experimental Peak Displacement
	x	y			
Centre	0	0	Perforation	85.23	-
W2	0	230	3.96	34.03	8.59
W3	300	230	3.6	13.52	3.76
W4	460	230	3.31	10.88	3.29
W5	600	230	2.5	8.09	3.24

Detailed comparisons to experimental results are shown in Appendix B. Here, the deformed mesh and displacement profiles along the length of the slab are examined to determine whether a punching failure is occurring, or would occur if local damage were included.

Figure 5-65 shows the deformed mesh at $t=7.9$ ms, which is the time of maximum displacement of the centre of the slab. Displacements are very high in the area of impact and are comparatively very small outside of the punching region. The length of the punching zone is more apparent in Figure 5-66 and Figure 5-67, which show the displacement profiles along the front and back edges of the slab, along the horizontal line of symmetry. Examining Figure 5-66, a punching zone approximately 300 mm wide is apparent. If the entire slab were modeled, there would be a 600 mm wide punching zone. Inside of this punching zone, at the center, the maximum displacement is approximately 80 mm. Outside of the punching zone, displacements are approximately 8 times less, and the maximum displacement outside of the punching region is about 10 mm. Comparing the displacements at t_{\max} and $t_{\max/2}$, it is apparent that the slab is starting to separate or fail. At t_{\max} , which is the time of maximum displacement of the center of the slab, the area inside the punching zone is still moving in the direction of impact, while the part of the slab outside of the punching zone is rebounding. The same observations can be made in Figure 5-67. It is also observed that the punching cone has widened once it has reached the back face, and the punching cone is now approximately 400 mm wide.

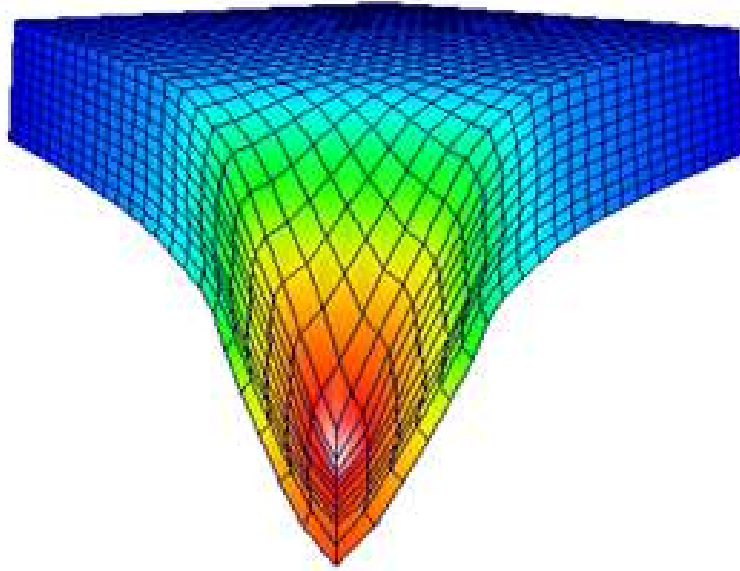


Figure 5-65: Deformed VecTor3 VTT-P1 mesh at time of maximum displacement ($t=7.9$ ms).

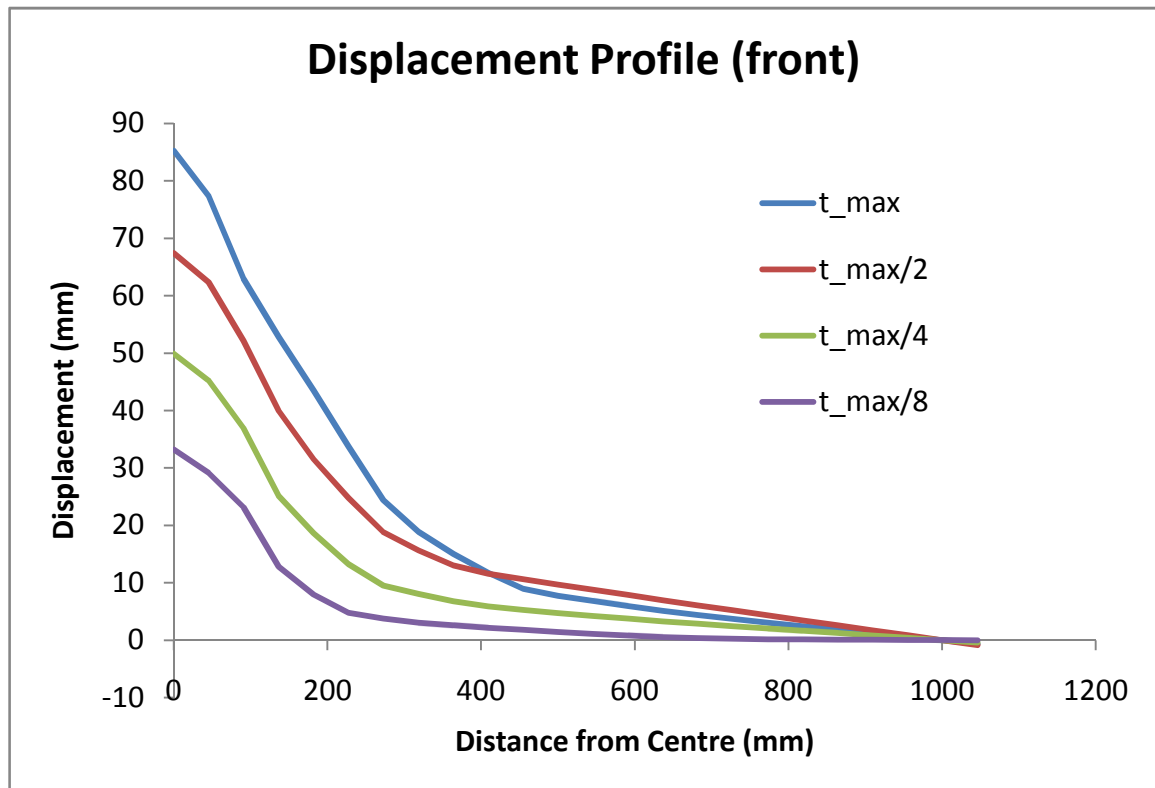


Figure 5-66: Displacement profile along front of slab for different stages in the VecTor3 VTT-P1 simulation.

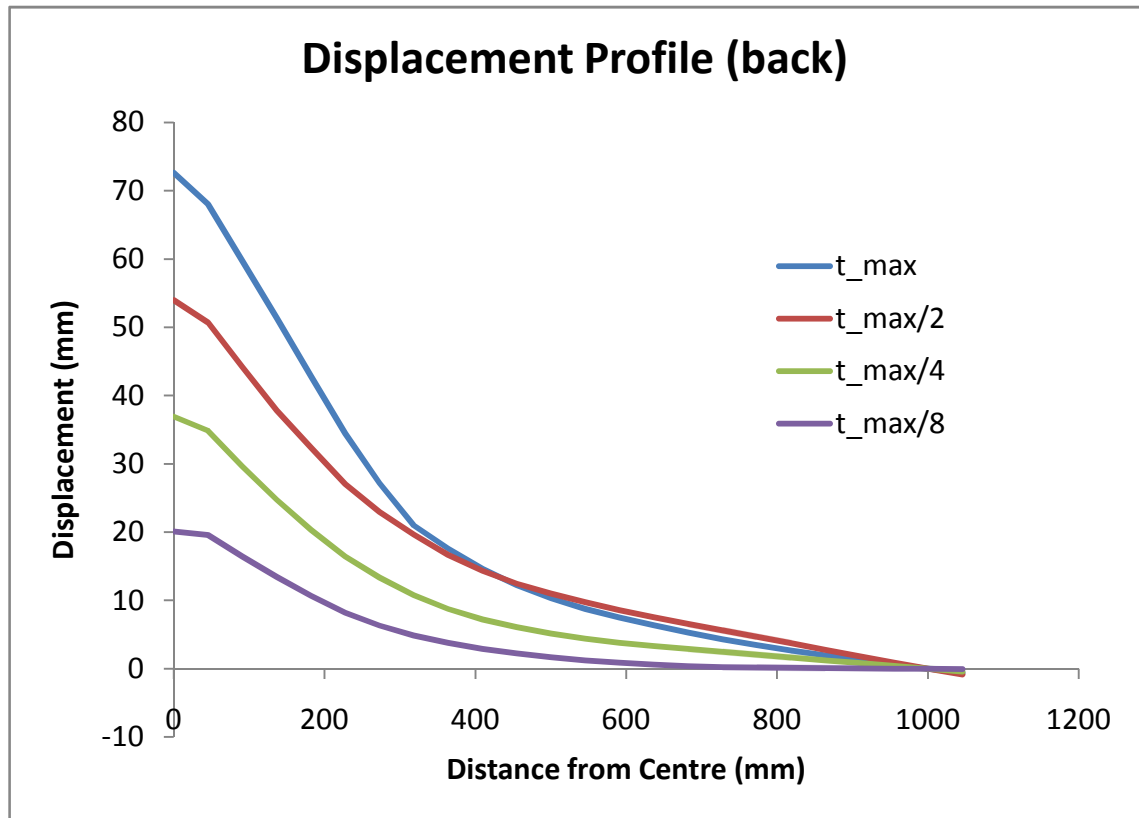


Figure 5-67: Displacement profile along back of slab for different stages in the VecTor3 VTT-P1 simulation.

The crack patterns can also be used as indicators of the type of damage. Figure 5-68 shows the crack pattern of the front face of the wall at $t=7.9$ ms. The centre of the slab and the point of impact is the lower left corner, and there is clearly extensive damage in that region. The crack pattern for the back of the slab, shown in Figure 5-69, also shows extensive damage in the impact region with flexural damage outside of it. Figure 5-70 and Figure 5-71 show crack patterns on vertical and horizontal cross sections. Shear cracking is the predominant type of damage in both figures.

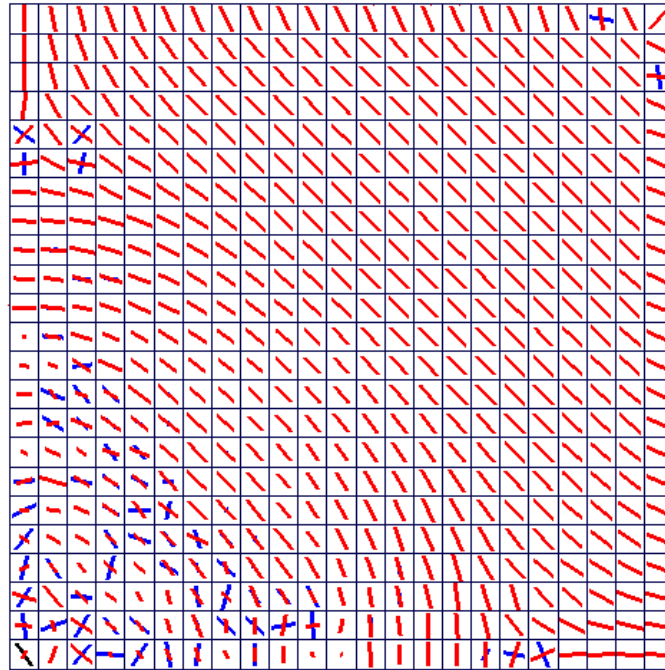


Figure 5-68: Crack pattern of front face of VTT-P1 at $t=7.9$ ms (centre of slab, and point of impact, located in lower left corner).

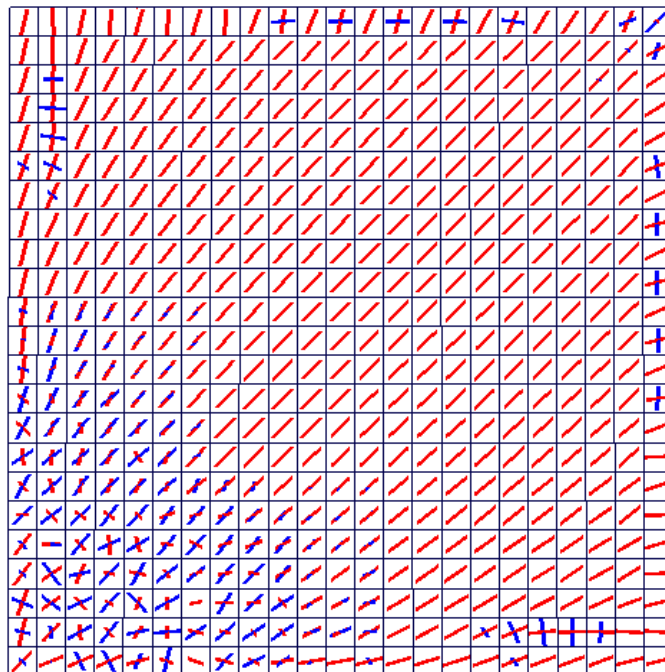


Figure 5-69: Crack pattern of back face of VTT-P1 at $t=7.9$ ms (centre of slab located in lower left corner).

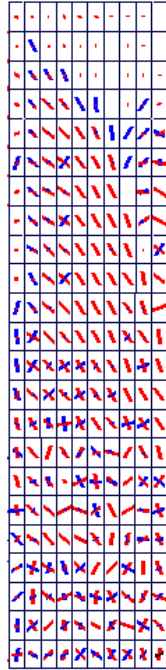


Figure 5-70: Crack pattern of vertical cross section of VTT-P1 at $t=7.9$ ms.

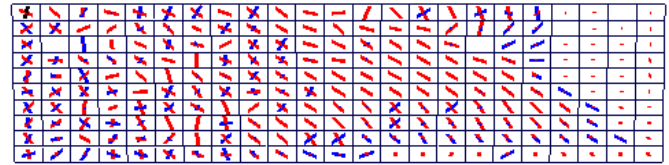


Figure 5-71: Crack pattern of horizontal cross section of VTT-P1 at $t=7.9$ ms.

5.4.4 Summary of VTT-P1 Modeling

The VTT-P1 punching specimen was modeled in VecTor2 and VecTor3. The missile was first modeled in VecTor2 and the force obtained from the VecTor2 analysis was used in the VecTor3 simulation. Perforation could not be modeled, since local damage or element erosion is not yet incorporated in the VecTor programs. Crack patterns, deformed meshes, and displacements along the length of the slab were examined to determine the behavior. Punching behavior was observed, with very large displacements in the punching region and relatively small displacements outside of the 300 mm wide punching zone. The crack patterns also reflected punching behavior, with heavy damage in the region of impact.

When the displacements were compared to experimental results, VecTor3 displacements were approximately 3-4 times larger at three sensor locations, but at a sensor location 230 mm away from the centre of the slab, the displacement predicted by VecTor3 was approximately 10 times larger than the experimental displacement. There are a few factors that may contribute to the discrepancy between the analytical and experimental results. Firstly, without element erosion, the crack pattern and deflected shapes must be relied on to determine if punching failure is likely or not. Secondly, in the absence of element erosion, highly damaged elements remain in the model with little or no stiffness, and this may lead to more energy being transferred to the surrounding elements. It is also noted that since nodal forces were used to approximate the impact, a set amount of energy is put into the slab regardless of damage to the slab. Finally, it is possible that a higher load is being applied to the slab than was applied during the experiment. There is uncertainty in the load applied to the slab because of the lack of element erosion in VecTor2 and the influence of the area of the compression-only truss bars in the determination of the impact load for the VecTor3 analysis.

The VTT-P1 punching specimen results highlight the need to account for local damage in order to be able to model penetration and perforation. As well, the need for contact elements is apparent. Again, contact elements are required to model the impact properly and to model perforation.

5.5 Observations from IRIS_2012 Modeling

The purpose of participating in IRIS_2012 was to determine the ability of the VecTor programs, VecTor2 and VecTor3 in particular, to model medium-velocity impacts. Triaxial cylinder tests were also modeled to evaluate the concrete confinement models implemented in VecTor2. Over the course of the IRIS_2012 workshop, the results obtained by VecTor2 and VecTor3 were compared to analyses done using complex hydrocodes such as LS-DYNA and ABAQUS.

In terms of the triaxial tests, VecTor2 did an excellent good job in capturing the increase in peak stress with confinement. The Kupfer/Richart confinement model accurately predicted the peak stress at all levels of confinement. The Montoya/Ottosen model also did an acceptable job at modeling concrete confinement. At lower and medium levels of confinement, the Montoya/Ottosen confinement model predicted the peak stress accurately, but at 100 MPa confinement, the model underestimated the peak stress. In general, the VecTor2 results were as good as or better than those obtained using LS-DYNA and ABAQUS.

For VTT-B1, results obtained by VecTor3 are comparable to those obtained by more complex codes, and were achieved using far fewer nodes. The large difference between the concrete strains predicted by VecTor3 and the experimentally reported concrete strains is likely due to the high aspect ratio of the elements, and is probably not indicative of the level of accuracy that could be achieved using VecTor3.

For VTT-P1, most hydrocodes used by other teams for IRIS_2012 analyses predicted perforation of the target, and VecTor3 does not currently have the ability to do so. Punching behaviour was observed, and it is likely that perforation will be predicted once local damage models are incorporated into the program.

The main objective of modeling the two impact specimens, VTT-B1 and VTT-P1, was to identify the areas of future research for the VecTor programs and to highlight deficiencies. Firstly, contact elements should be incorporated into the VecTor programs. The introduction of contact elements would eliminate the need to use compression-only truss bars and to apply the impact using nodal loads. For the punching specimen in particular, this would likely mean that less energy would be transferred to the target, and the damage would likely be contained more locally around the point of impact. Secondly, VecTor2 has recently been updated with different

formulations for strain rate effects, as well as with the option to consider strain rate effects for either the steel or concrete alone. These formulations still need to be verified and tested in VecTor3 before they are used. Finally, as mentioned in Section 5.2 the Kupfer/Richart concrete confinement model provided the best results when modeling the triaxial test specimens, however it lacked post-peak response at the structural level. Work should be done to elongate the post-peak response for this model.

5.6 Missile Modeling in VecTor3

Analyses were also done for the VTT-P1 specimen where the missile was explicitly modeled in VecTor3. The hard missile was modeled using three layers of steel elements and, for simplicity, a square missile was used. One quarter of the missile mass was used, since a quarter of the panel was modeled, and an initial velocity of 135 m/s was assigned to each missile node. Short compression-only truss bars were used to connect the missile to the slab. Steel element buckling is not yet available in VecTor3 and, because of this, the soft missile was not modeled. In addition, the object of the modeling of these specimens was, first of all, to capture the target response. Results shown in Section 5.3 illustrated that VecTor3 was able to adequately capture the flexural response.

5.6.1 P1 Modeling

For the P1 specimen, the hard missile was modeled with a total of 12 elements and the slab mesh was kept the same as was used with nodal loads for the impact. For the slab, the same material properties as described in Section 5.4 were used, and the model is shown in Figure 5-72. The time-step used was 1×10^{-5} seconds and the damping ratios used were 0.25% for the first mode and 1% for the second mode.

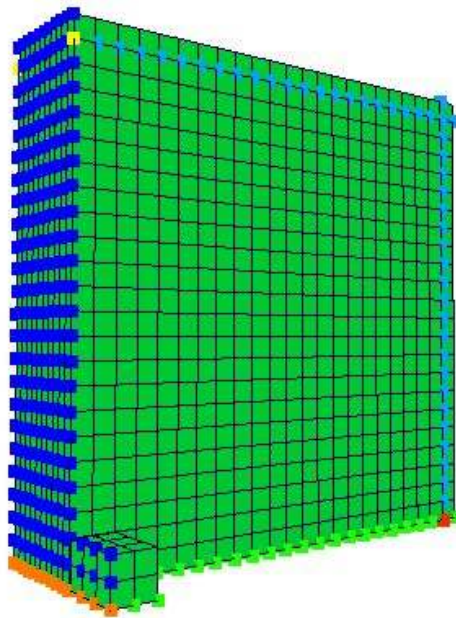


Figure 5-72: VecTor3 VTT-P1 model (missile and slab).

5.6.2 P1 Results

The results for P1 are summarized in this section. The displacement and velocity profiles for the back of the missile are shown. As well, the forces from the nine compression-only truss bars are summarized and presented, as are the missile impact force and impulse imparted to the slab.

In terms of slab results, peak displacements are summarized for four of the displacement sensor locations. The deformed mesh and crack patterns are shown, at the time of maximum displacement at the centre of the slab, and crack patterns for that load stage are also presented. Similar to the modeling using nodal loads, the displacement profiles for the front and back of the slab are shown, and are compared to the displacement profiles obtained using nodal loads.

5.6.2.1 Missile Results

The missile displacement and velocity profiles are shown in Figure 5-73 and Figure 5-74. From these two plots, one can see that the analysis was stopped after approximately 3 ms, and that at that time the back of the missile had displaced approximately 85 mm and had a velocity of 10 m/s. The analysis was stopped due to rupture of the reinforcement at the centre of the slab in the reinforcing mat furthest from the impact face. After the first reinforcement ruptured, the analysis became unstable due to decreased convergence; because of this, results obtained after rupture are not as reliable and are not used. In this analysis, since the reinforcement ruptured before the missile was stopped by the slab, it is likely that the missile is perforating the slab, or would perforate if local damage were included.

The impact load is shown in Figure 5-75, and the missile impulse is shown in Figure 5-76. The load profile was derived from the average stresses in the compression-only truss bars. As shown, the majority of the impulse occurs in the first 0.25 ms, due to the first couple of peaks in the force profile. Note also that although the peak impact force calculated for P1 is over 80 times larger than the peak force for B1, the calculated impulse is approximately the same. This illustrates the relative influence of peak pressure and impulse on the target's response.

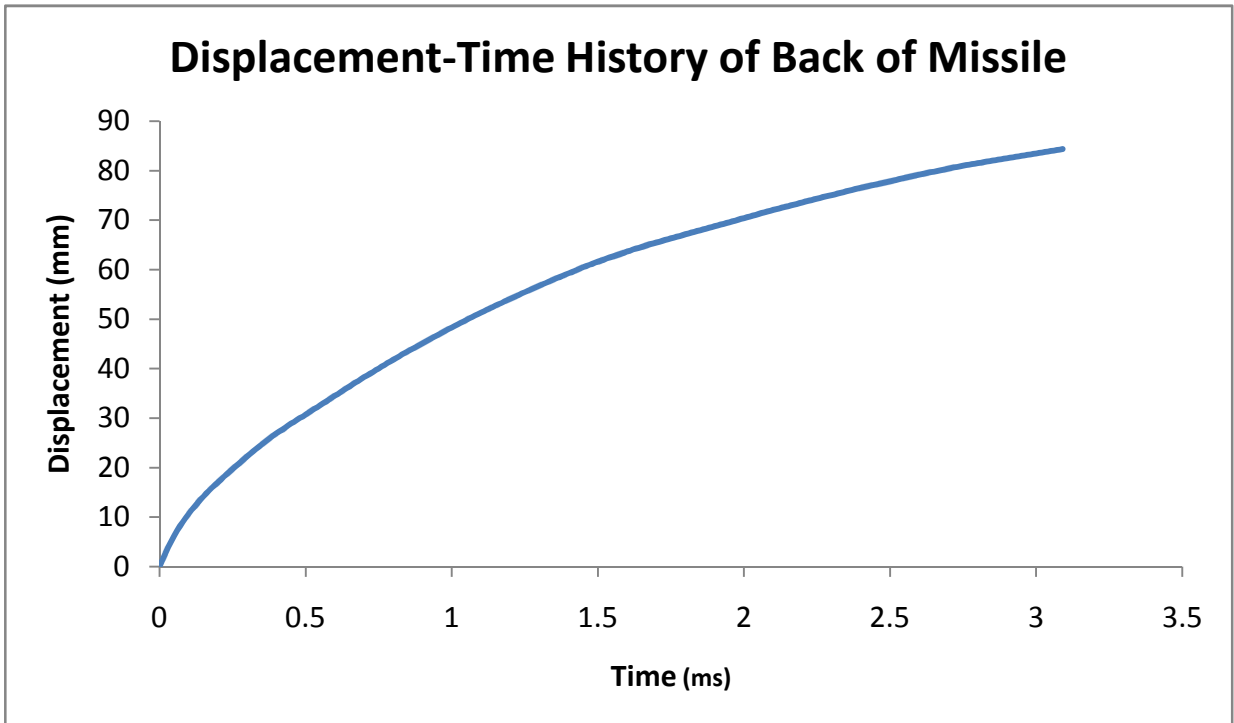


Figure 5-73: Displacement-time profile for VTT-P1 missile in VecTor3.

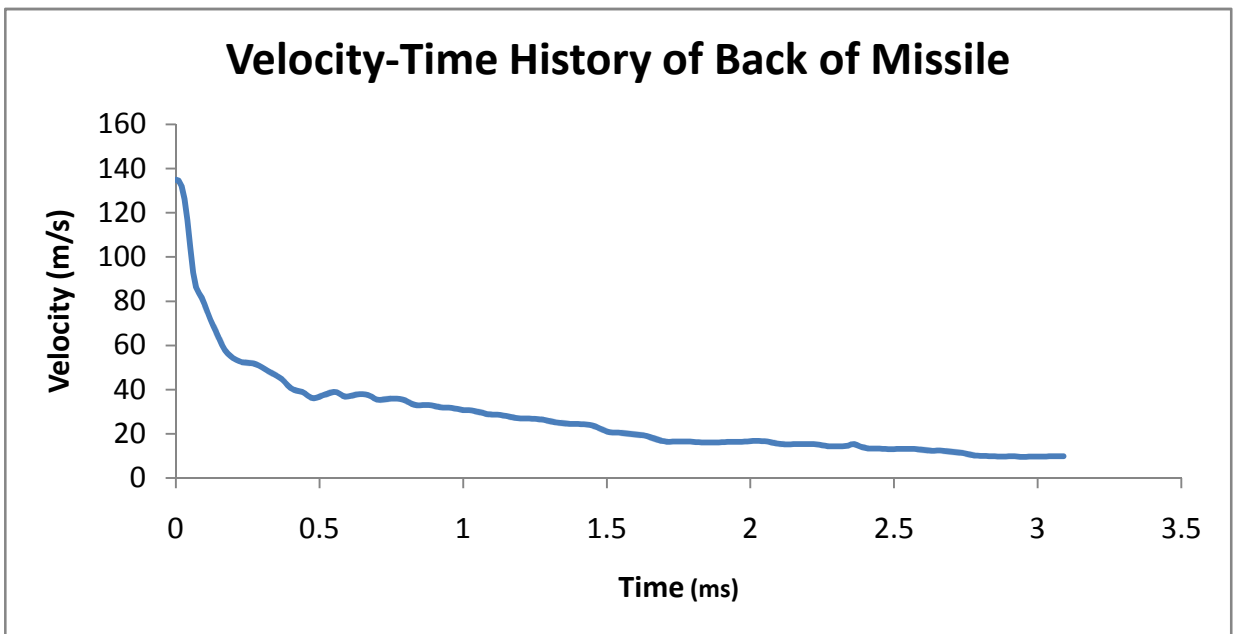


Figure 5-74: Velocity-time profile for VTT-P1 missile in VecTor3.

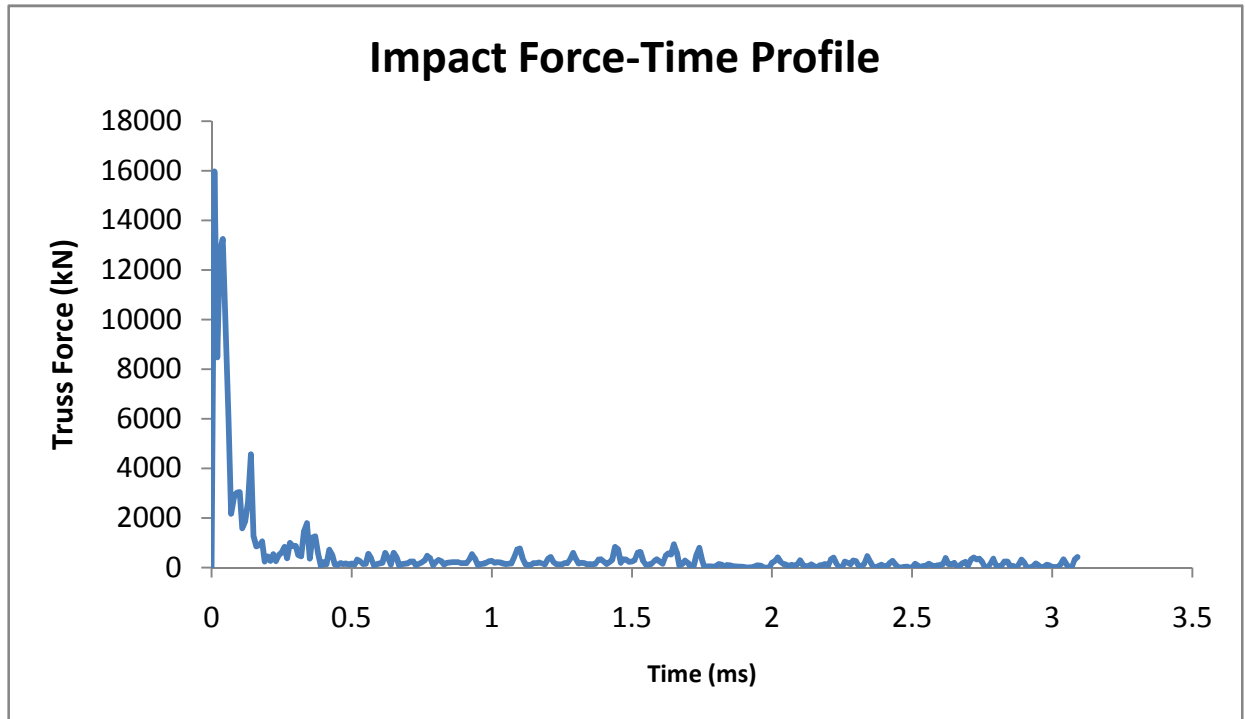


Figure 5-75: Impact force-time profile for VTT-P1 missile in VecTor3.

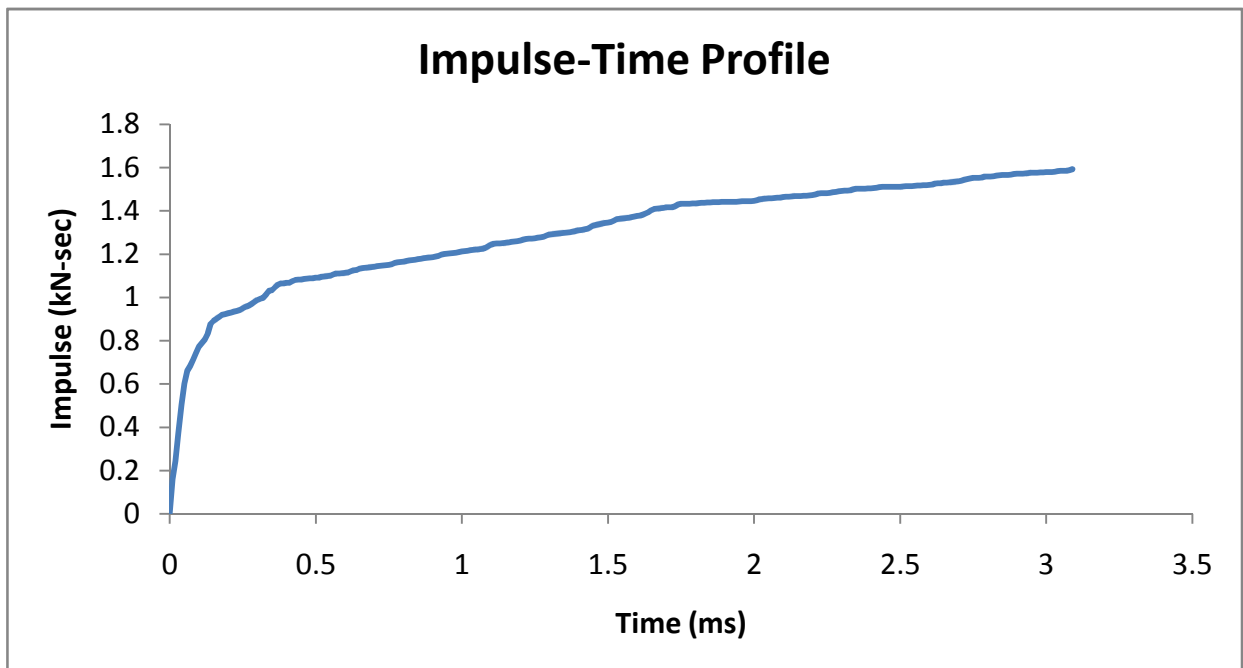


Figure 5-76: Impulse-time profile for VTT-P1 missile in VecTor3.

5.6.2.2 Slab Results

The peak slab displacement was 87.4 mm at 3.09 ms. This peak displacement occurred at the centre of the slab, under the point of impact. In the experiment, perforation occurred and so the corresponding displacement would be infinitely large. The displacements at that time, at four displacement sensor locations, are summarized in Table 5-23.

Table 5-23: Comparison of VecTor3 (With Missile Modeled) and Experimental Displacements for VTT-P1

Sensor	Peak Displacements (mm)		
	Experimental	VecTor3	Theoretical/Experimental Peak Displacement
W2	3.96	35.05	8.85
W3	3.6	11.33	3.15
W4	3.31	6.34	1.92
W5	2.5	4.84	1.94

When nodal loads were used to model the impact, it was observed that VecTor3 overestimated the displacements at all sensor locations. The same result was obtained in this analysis. VecTor3 displacements are larger than experimental displacements at all sensor locations.

The deformed mesh, at 3.09 ms, is shown in Figure 5-77. The crack patterns for the front and back of the slab are also shown in Figure 5-78 and Figure 5-79.

From the displacement results and the deformed mesh, one can see that while there was still heavy damage predicted by VecTor3 in the impact region, the analytical results show more of a spreading of the shear cone compared to the tight shear cone that was observed in the experiment. This may be partly due to the lack of local damage models, the large element size, or a combination of both factors.

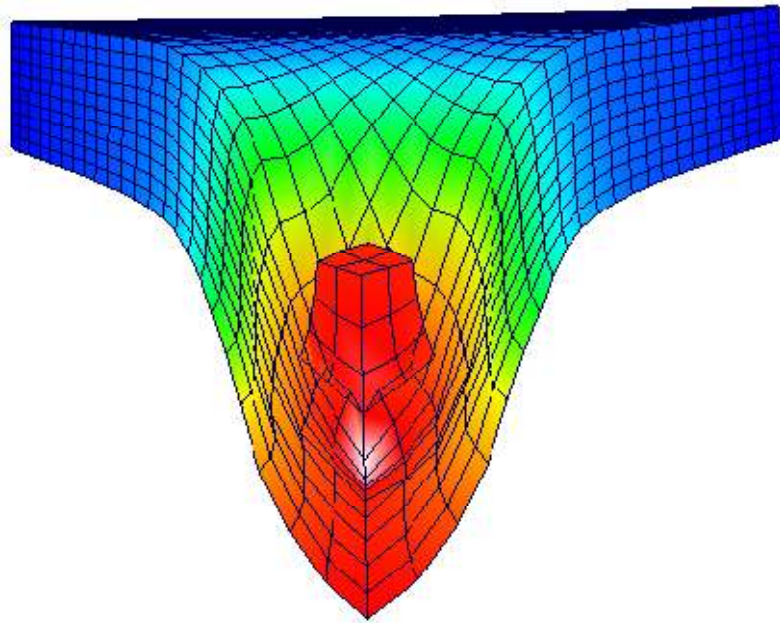


Figure 5-77: Deformed VTT-P1 mesh at $t=3.09$ ms (with missile modeled).

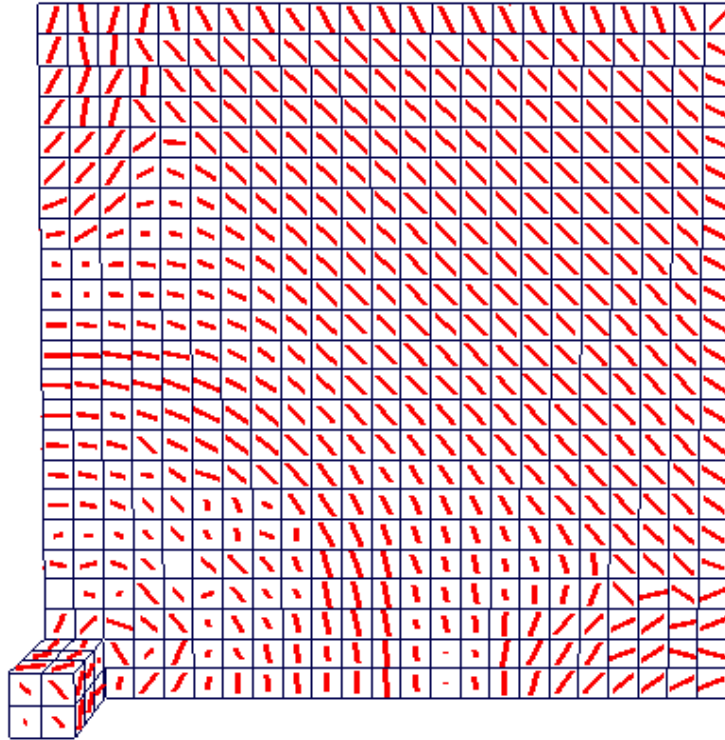


Figure 5-78: Crack pattern on the front of VTT-P1 at $t=3.09$ ms (with missile modeled).

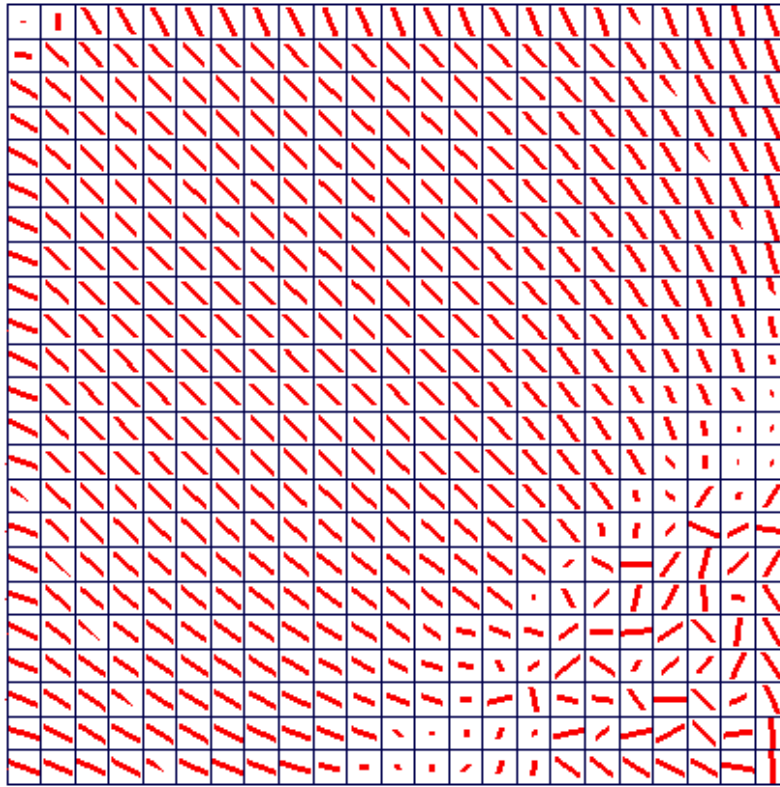


Figure 5-79: Crack pattern on the back of VTT-P1 at $t=3.09$ ms (with missile modeled).

The displacement profiles for the front and back of the slabs are shown in Figure 5-80 and Figure 5-81. The displacement profiles are compared to those obtained using nodal loads in Figure 5-82, Figure 5-83 and Figure 5-84. Both displacement profiles show a distinct punching zone, which widens to approximately 600 mm (1.2 m zone of punching for the entire slab) towards the end of the analysis. Inside of the punching zone, displacements reach up to 87 mm, while outside of the punching zone, displacements are less than 10 to 20 mm. Comparing the displacement profiles for the analysis with nodal loads to the analysis where the missile was modeled explicitly, it appears that damage inside the punching zone is more severe when the missile is modeled explicitly. Figure 5-84 compares the ratio of displacements between the two models and shows that displacements have increased more inside the punching zone. As well, an analysis was done using nodal loads where the loaded area was square. There was no difference in the results from that analysis and the original analysis.

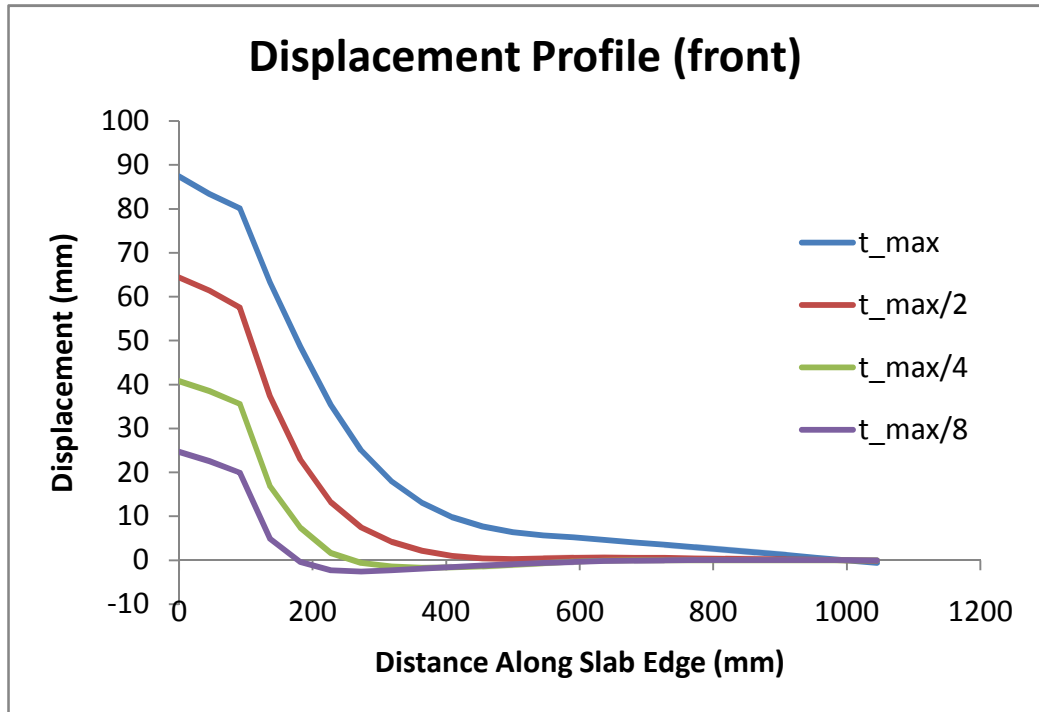


Figure 5-80: Displacement profile along front edge of VTT-P1 from VecTor3 analysis with missile modeled.

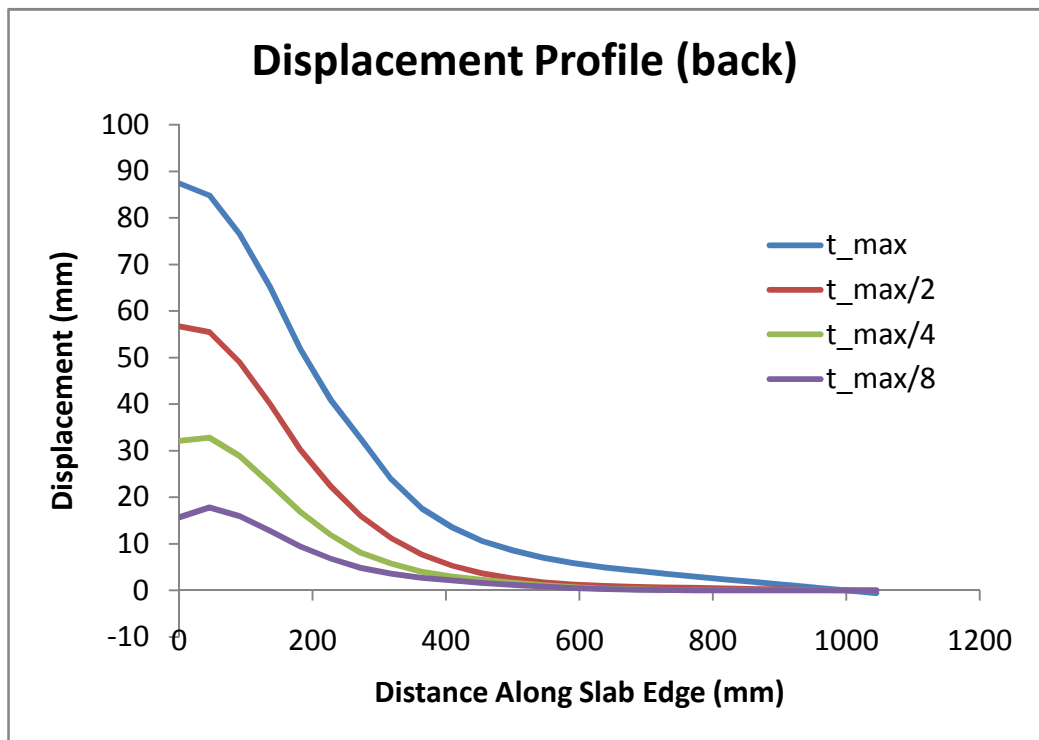


Figure 5-81: Displacement profile along back edge of VTT-P1 from VecTor3 analysis with missile modeled.

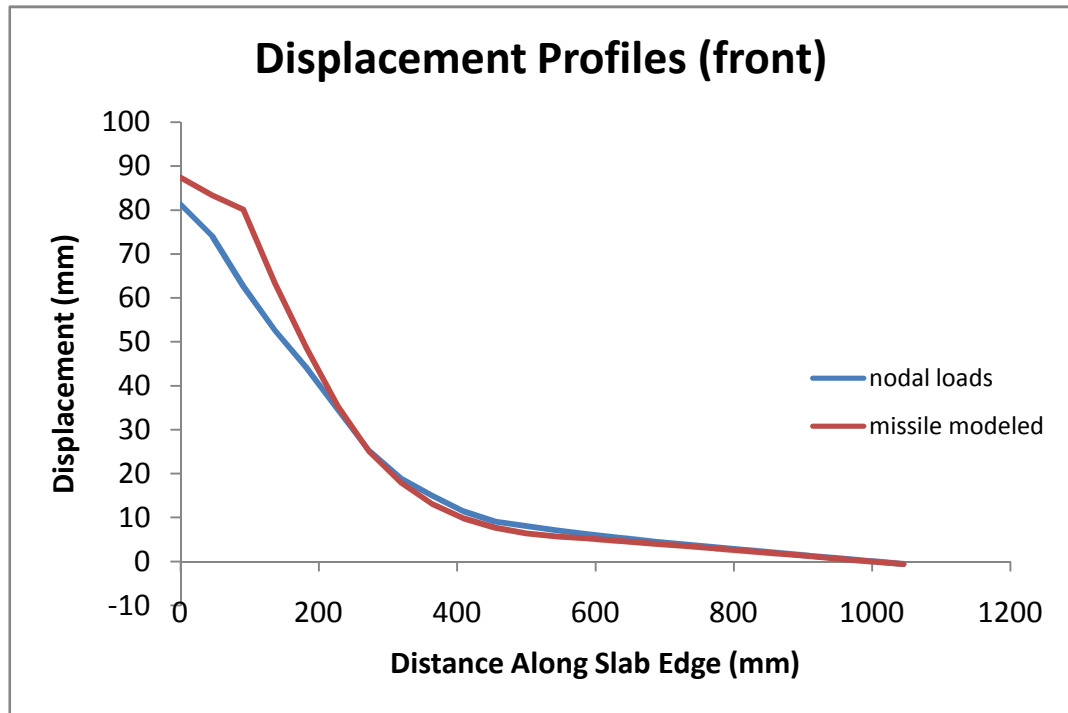


Figure 5-82: Comparison of displacement profiles at max displacement for front of VTT-P1.

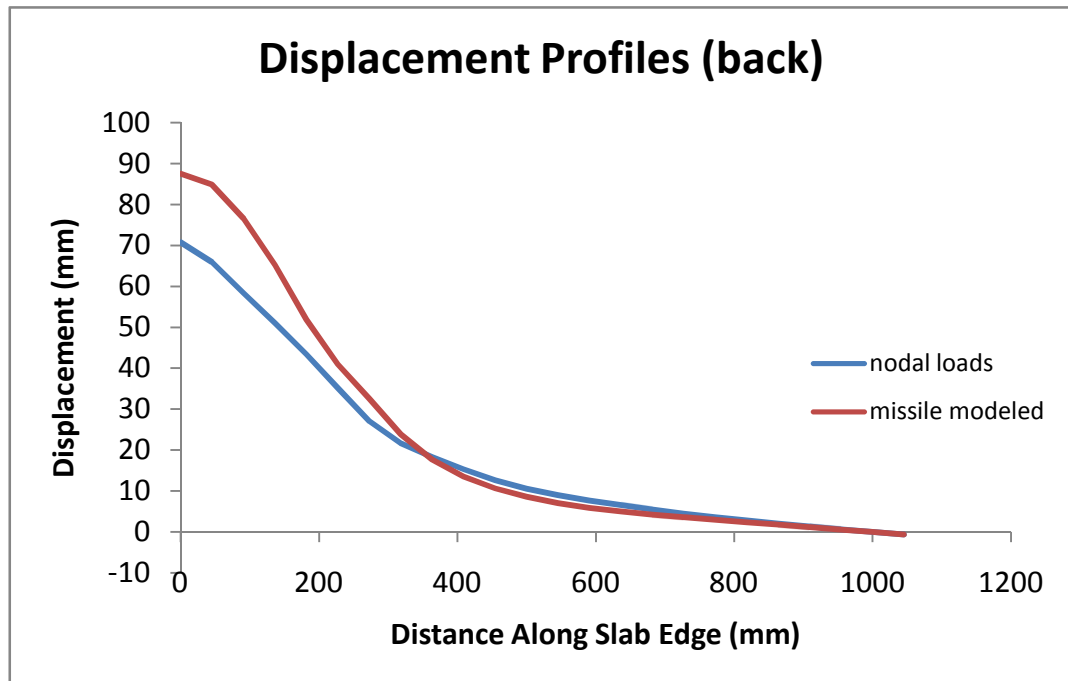


Figure 5-83: Comparison of displacement profiles at max displacement for back of VTT-P1.

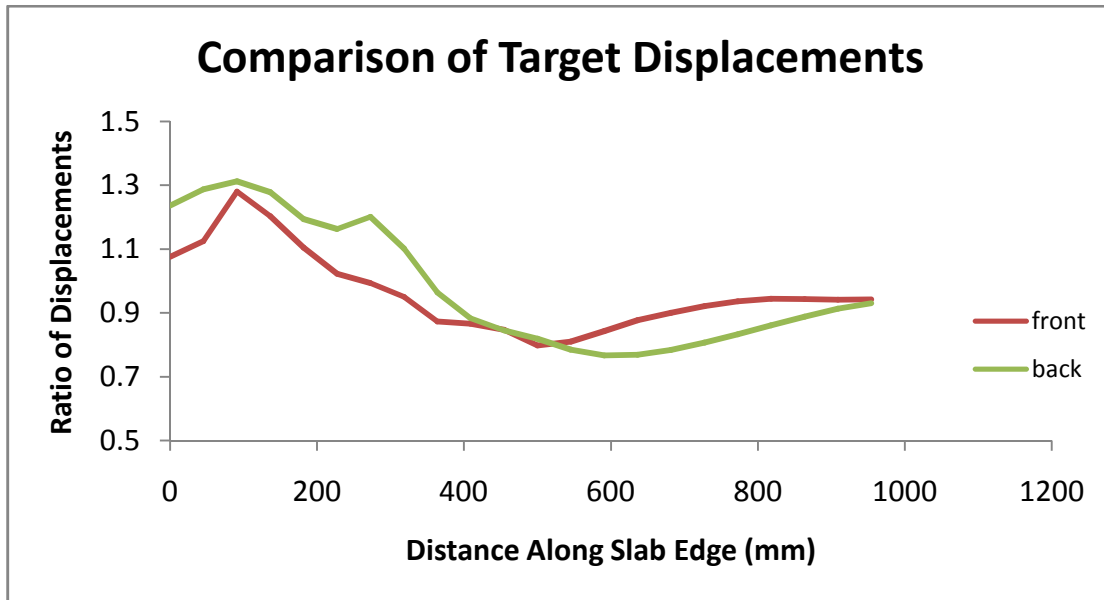


Figure 5-84: Comparison of displacements between VecTor3 P1 models.

5.6.3 Summary of P1 VecTor3 Modeling with Missile

This section summarizes the modeling of the P1 specimen, where the missile was modeled explicitly. The missile was modeled with three layers of four solid steel elements. Compression-only truss bars were used to connect the missile to the slab.

The maximum displacement was 87.4 mm at 3.09 ms. At 3.09 ms, one of the longitudinal truss bars at the back of the slab, within the punching region and close to the point of impact, ruptured. After the first truss bar ruptured, a number of other truss bars ruptured and the analysis became unstable. The analysis was considered stable up to the point of reinforcement rupture. At the time of rupture, the instantaneous velocity of the front of the slab was 15.29 m/s and the velocity of the back of the missile was 9.83 m/s. The initial missile velocity was 135 m/s.

The displacement profiles and the deformed mesh exhibit punching behaviour, which is the same type of behaviour that was observed experimentally. As has been mentioned previously, perforation occurred in the actual test. Although VecTor3 cannot explicitly model perforation, the punching behaviour observed in this analysis, along with the rupture of the reinforcement, may indicate that perforation is likely.

6 Modeling of Prestressed Impact Specimens

6.1 Test Series I

6.1.1 Introduction

In addition to VTT-P1, a number of other hard missile impact tests were carried out at the VTT testing facility. Two test programs were carried out; the goal of the first series was to assess the effect of prestressing and transverse reinforcement on the punching resistance of concrete elements. A total of six slabs having the same geometry and base reinforcement as P1 were tested, and the damage to the specimens with prestressing and transverse reinforcement was compared to a reference reinforced concrete wall with the same reinforcement as P1.

All six specimens in this test series were subjected to medium velocity impacts, where the impact velocities were less than perforation velocities determined using empirical formulae. Impact velocities are summarized in Table 6-1; the specimen concrete strengths and reinforcement are also indicated. The impact mass used was the same type used in the P1 test. A concrete filled missile, weighing approximately 47 kg, was used in each test (Orbovic, N. et al., 2009).

6.1.2 Test Specimens and Modeling Approach

All specimens were 2100 x 2100 x 250 mm square slabs, simply supported on all four sides, with a clear span of 2.0 m in each direction. The base in-plane reinforcement, present in each specimen, was identical to that of P1 and consisted of 10 mm bars spaced at 90 mm in each principal direction on each face. For the specimens with transverse (i.e., out-of-plane) reinforcement, 12 mm diameter bars, placed at the intersections of the in-plane reinforcement, were used. Both the in-plane and transverse reinforcement had a nominal yield strength of 500 MPa. Prestressing was introduced using 26.5 mm diameter bars, each with an area of 548 mm², spaced at 180 mm. These bars were placed in plastic sleeves to prevent contact with the concrete. The prestressing bars had a nominal yield strength of 1030 MPa, and were prestressed to 820 MPa, approximately 80% of yield. The layout of the prestressing bars and transverse reinforcement is shown in Figure 6-1 and Figure 6-2.

In terms of modeling, VecTor3 was used to model all specimens, with the missile included in the model. As the base model, the same mesh used for the modeling of P1 was used. For the appropriate specimens, transverse reinforcement and prestressing steel were added to the model. The transverse reinforcement was modeled as smeared, and a reinforcement ratio of 1.48% was used. Prestressing was modeled using discrete truss elements and link elements. For the concrete material properties, the reported compressive strength was used, and all other required properties were determined based on the compressive strength using empirical relations. The stress-strain curve provided for the 500 MPa steel used in the P1 specimen was used for both the in-plane and transverse reinforcement of the prestressed specimens. For the prestressing steel, no stress-strain curve was available for the bars used. Based on tensile tests, the yield strength was approximately 1240 MPa and the ultimate strength was 1330 MPa.

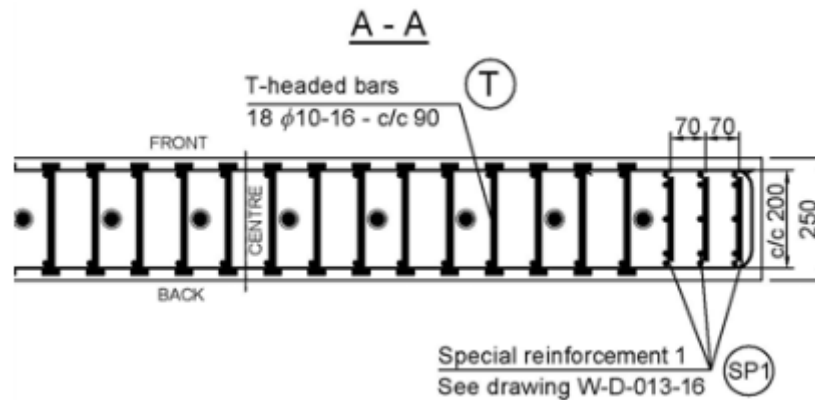


Figure 6-1: Prestressing and transverse steel reinforcement layout (Orbovic, N. and Blahoianu, A., 2011) [horizontal cross section].

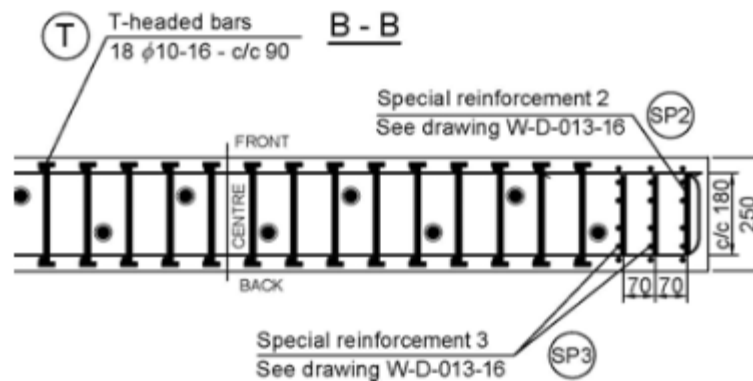


Figure 6-2: Prestressing and transverse steel reinforcement layout (Orbovic, N. and Blahoianu, A., 2011) [vertical cross section].

Table 6-1: Test Series I: Concrete Strength, Missile Velocity, and Specimen Reinforcement

Specimen	Concrete Compressive Strength (MPa)	Reinforcement	Impact Velocity (m/s)
A	48.3	Base in-plane reinforcement only	103
B	52.1	In-plane and 5 MPa prestressing	101.9
C	48.7	In-plane and 10 MPa prestressing	99.4
D	45	In-plane and transverse	99.7
E	45.8	In-plane, transverse, and 5 MPa prestressing	98.4
F	45	In-plane, transverse, and 10 MPa prestressing	98.4

6.1.3 Experimental and Modeling Results

Experimental results were reported in terms of impact depth, scabbing area, cracked area, and residual deflection (Orbovic, N. et al., 2009). Because a smeared crack program was used, it is difficult to compare the cracked area obtained analytically to the cracked area observed experimentally. Analytical results presented will include peak displacement, time of rupture of the first reinforcement, and missile velocity at the time of rupture. The time of rupture is the last load stage that is found to be stable, since soon after the rupture of the first reinforcement the analysis becomes unstable and displacements become exceedingly large. Table 6-2 summarizes the VecTor3 results and compares them to experimental results. In all tests, except for Specimen B, the missile rebounded; the missile was embedded in Specimen B after testing. The experimental results are presented in terms of impact depth.

Figure 6-3 illustrates the VecTor3 displacement-time results for the specimens in Test Series I. A discussion of the results of the analyses will be provided in Section 6.3.

**Table 6-2: Comparison of Experimental and VecTor3 Results for
Prestressed Impact Test Series I**

Specimen	Experimental Impact Depth (mm)	VecTor3 Results		
		Peak Displacement (mm)	Time of Reinforcement Rupture (ms)	Missile velocity at rupture (m/s)
A	120	76.86	4.29	6.17
B	130	83.19	5.49	3.35
C	110	87.76	6.41	4.66
D	38	81.52	18.44	-1.16
E	47	70.06	9.24	-3.70
F	74	76.99	11.59	-1.99

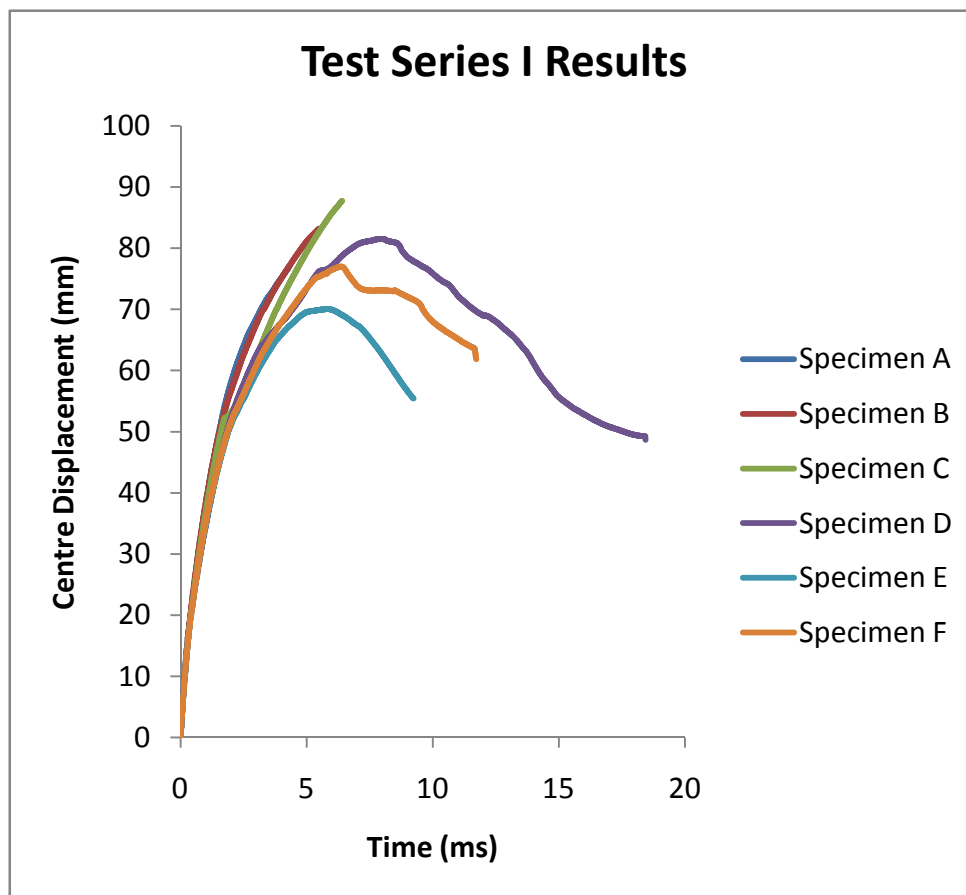


Figure 6-3: VecTor3 Prestressed Test Series I Results.

6.2 Test Series II

6.2.1 Introduction

The second test series consisted of four specimens. The goal of this test series was also to evaluate the effect of transverse reinforcement and prestressing on the response of reinforced concrete slabs to medium velocity hard missile impacts.

The specimens were all 2100 x 2100 x 250 mm. The results of the tests in this series are compared to a reference specimen, reinforced only with the base in-plane reinforcement, identical to the reinforcement in P1. All specimens were impacted with a 47 kg missile (Orbovic, N. and Blahoianu, A., 2011).

6.2.2 Test Specimens and Modeling

For each of the four specimens, perforation velocities were calculated using three empirical formulae, and the missile velocities chosen were just over the perforation velocities. The compressive concrete strength, reinforcement, and impact velocity for each specimen are summarized in Table 6-3. The transverse reinforcement used in this test series was the same as in Test Series I. Prestressing was also introduced in the same way.

Table 6-3: Test Series II: Concrete Strength, Missile Velocity, and Specimen Reinforcement

Specimen	Concrete Compressive Strength (MPa)	Reinforcement	Impact Velocity (m/s)
G	50.3	In-plane only	110
H	53	In-plane and transverse	144
I	50	In-plane, transverse, and 10 MPa prestressing	139
J	62.9	In-plane, transverse, and 10 MPa prestressing	153

6.2.3 Experimental and Modeling Results

Experimental damage reported included scabbed area and cracked area. Where perforation occurred, the residual velocity was also reported (Orbovic, N. and Blahoianu, A., 2011). Table 6-4 compares the experimental and VecTor3 results. The displacement-time results from the VecTor3 analyses are shown in Figure 6-4.

Table 6-4: Comparison of Experimental and VecTor3 Results for Prestressed Impact Test Series II

Specimen	Experimental Results	VecTor3 Results		
		Peak Displacement (mm)	Time of Reinforcement Rupture (ms)	Missile velocity at rupture (m/s)
G	-residual velocity of 21 m/s	93.8	6.72	4.2
H	-residual velocity of 30 m/s	64.8	1.53	22.9
I	-missile rebounded -seven rebar ruptured -four transverse bars were ejected	101.5	4.7	7.1
J	-missile rebounded -five rebar ruptured -eight transverse bars partially ejected	103.8	4.46	10.0

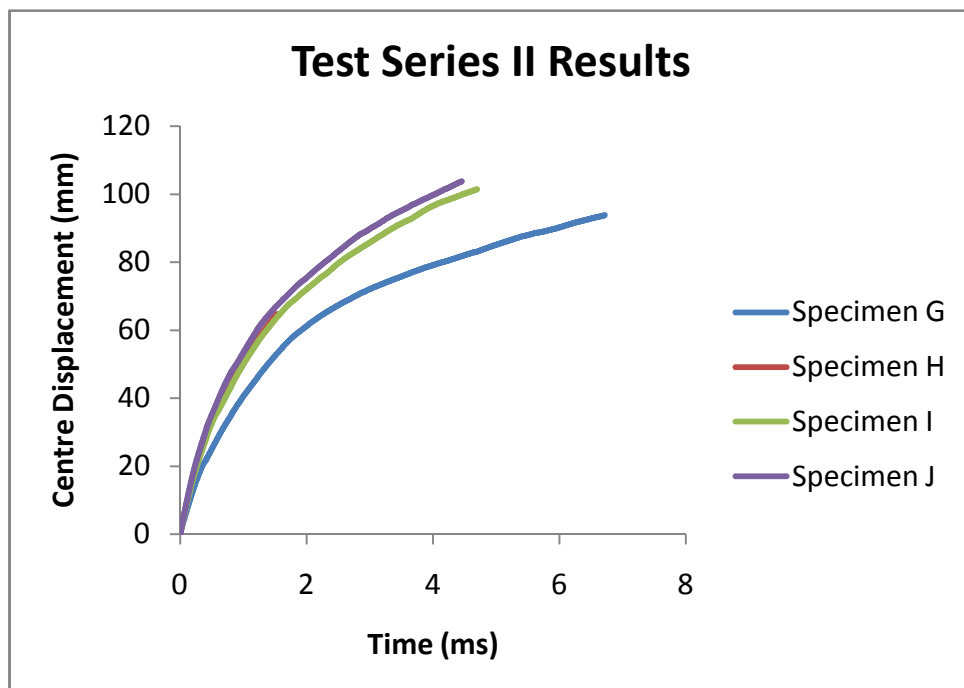


Figure 6-4: VecTor3 Prestressed Test Series II Results.

6.3 Discussion of Hard Missile Modeling in VecTor3

A total of 11 hard missile impacts were modeled in VecTor3. Table 6-5 shows the concrete strength, reinforcement, and missile impact velocity for each specimen, and compares the results in terms of peak displacement, time of reinforcement rupture, and missile velocity at the time of rupture. As mentioned previously, the base in-plane reinforcement for each specimen was the same; each specimen was reinforced with 10 mm diameter bars spaced at 90 mm in both principal directions, on both the front and back faces. The reinforcement specified in Table 6-5 is the reinforcement provided in addition to this base reinforcement. The prestressing of 5 MPa corresponds to a prestress of approximately 410 MPa in the tendons, while the prestressing of 10 MPa corresponds to a prestress of 820 MPa in the tendons. The transverse reinforcement was provided by T-headed bars and was modeled as smeared; the reinforcement ratio was 1.48%.

Table 6-5: Summary of Hard Missile Modeling Results in VecTor3

Specimen	Input Parameters			VecTor3 Results			
	Concrete Strength (MPa)	Reinforcement	Impact Velocity (m/s)	Peak Displacement (mm)	Time of Reinforcement Rupture (ms)	Velocity at Rupture (m/s)	
						Front of Slab	Back of Missile
P1	60	-	135	87.39	3.09	15.29	9.83
A	48.3	-	103	76.86	4.29	5.85	6.17
B	52.1	5MPa prestress	101.9	83.19	5.49	3.83	3.35
C	48.7	10 MPa prestress	99.4	87.76	6.41	4.61	4.66
D	45	Transverse	99.7	81.52	18.44	-109.99	-1.16
E	45.8	5 MPa prestress & transverse	98.4	70.06	9.24	-4.96	-3.70
F	45	10 MPa prestress & transverse	98.4	76.99	11.59	-2.00	-1.99
G	50.3	-	110	93.78	6.72	4.15	4.23
H	53	Transverse	144	64.80	1.53	23.35	22.88
I	50	10 MPa prestress & transverse	139	101.45	4.7	6.69	7.13
J	62.9	10 MPa prestress & transverse	153	103.80	4.46	7.74	9.96

A comparison of the displacement-time histories for all 11 specimens is shown in Figure 6-5.

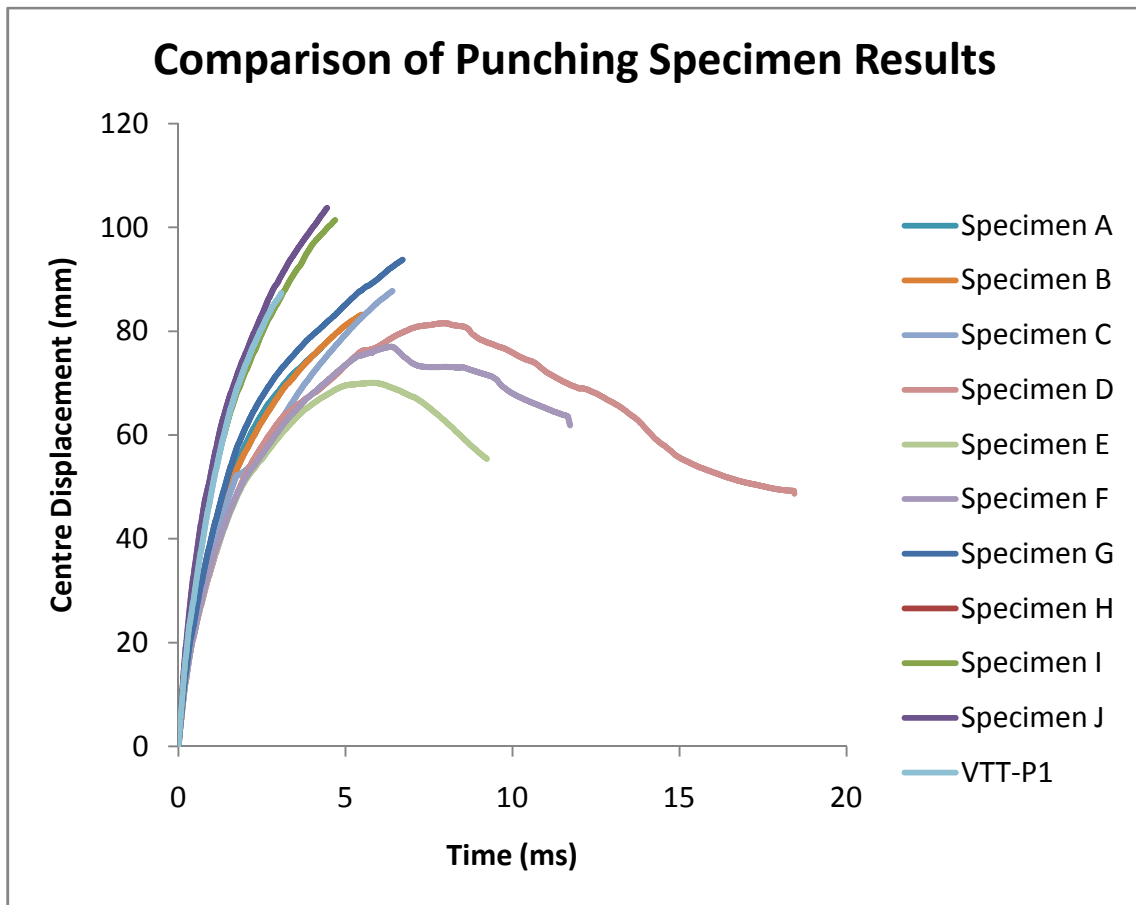


Figure 6-5: Comparison of all hard impacts modeled in VecTor3.

Based on Figure 6-5 and Table 6-5, the VecTor3 analysis results can be divided into two categories: perforation and punching. Perforation specimens are characterized by rupture of the reinforcement before the missile rebounded; punching specimens are characterized by reinforcement rupture while the missile was rebounding. Specimens D, E, and F are punching specimens, while Specimens P1, A, B, C, G, H, I, and J are perforation specimens. The experimental results can also be grouped into categories of punching, severe punching, and perforation. In terms of the experimental results, Specimens D, E, and F belong to the punching category, Specimens A, B, C, I, and J experienced severe punching, and Specimens P1, G, and H are perforation specimens. It is also noted that for some of the specimens that experienced severe punching, although perforation did not occur they were still heavily damaged, with a number of rebar rupturing in some cases.

If the groupings for the analytical and experimental results are compared (see Table 6-6), one can see that, while work is required to refine the results obtained by VecTor3 for hard missile impacts, the correct mode of failure was approximately captured. In terms of the experimental results, for the perforation and severe punching specimens, VecTor3 predicts perforation (based on the fact that the reinforcement ruptured before the peak displacement was reached). For Specimens D, E, and F, VecTor3 does not predict perforation, since the missiles rebounded in VecTor3 for all three of these specimens. Experimentally, these three specimens incurred the least amount of damage, with the penetration depth being less than 75 mm for all three specimens.

Table 6-6: Comparison of Analytical and Experimental Failure Modes for Hard Missile Impacts on 250 mm Thick Reinforced Concrete Targets

Specimen	Failure Mode		Experimental Observations (Orbovic, N. and Blahoiianu, A., 2011)
	Analytical (VecTor3)	Experimental	
P1	Perforation	Perforation	Residual velocity=34 m/s
A	Perforation	Severe punching	Impact depth=120 mm
B	Perforation	Severe punching	Impact depth=130 mm
C	Perforation	Severe punching	Impact depth=110 mm
D	Punching	Punching	Impact depth=38 mm
E	Punching	Punching	Impact depth=47 mm
F	Punching	Punching	Impact depth=74 mm
G	Perforation	Perforation	Residual velocity=21 m/s
H	Perforation	Perforation	Residual velocity=30 m/s
I	Perforation	Severe punching	-seven rebar ruptured -four transverse bars were ejected
J	Perforation	Severe punching	-five rebar ruptured -eight transverse bars partially ejected

6.3.1 Missile Modeling Using Average Strain for Rupture

The analyses summarized earlier in this chapter were performed using the default analysis options in VecTor3. As part of the analysis, at each step, the strain at the crack was compared to the specified rupture strain, and if the rupture strain had been exceeded at the crack, the element was considered ruptured. In eight of the eleven analyses presented, this rupture criterion resulted in failure before the peak displacement was obtained and also required the analyses to be stopped. In order to determine the calculated peak displacement for each specimen, the rupture criterion was changed such that the average strain dictated when the rupture of the element occurred. In addition to changing the rupture criterion to the average strain, element deactivation was also introduced, and the truss elements were removed from the calculations once rupture occurred. Element erosion for the concrete was also introduced; elements were removed once either the tensile or compressive strain exceeded 200×10^{-3} . As a result of these two changes, peak displacements were obtained for ten of the eleven specimens; for Specimen H, rupture still occurred prior to the peak displacement, likely signifying perforation. The new results are summarized in Table 6-7 and Figure 6-6.

In general, VecTor3 predicts the highest peak displacements for those specimens that were perforated experimentally or which had multiple reinforcement rupture. In terms of calculated peak displacements compared to measured impact depths, there is good agreement observed in some specimens, particularly Specimens A and C. Where impact depths were quite small, the VecTor3 residual displacements are sometimes a better indication of impact depth (Specimens D and E). However, there are still some disparities. For example, Specimen B and Specimen D have similar analytical results in terms of both peak and residual displacements, but the experimental results are quite different.

Examining the displacement-time profiles in Figure 6-6, it appears that the introduction of the prestressing steel and transverse reinforcement has a large effect on the shape of the post-peak response. For all three specimens containing only the base reinforcement, the displacements decreased gradually, and linearly, after the peak. In the other specimens, the displacements decreased more quickly and levelled out to a residual displacement sooner.

Table 6-7: Comparison of Analytical and Experimental Results for Hard Missile Impacts with Average Strain Rupture Criterion in VecTor3

Specimen	VecTor3 Peak Displacement (mm)	VecTor3 Residual Displacement (mm)	Ruptured Reinforcement (Yes/No)	Experimental Observations (Orbovic, N. and Blahoianu, A., 2011)
P1	154.5	-	No	Residual velocity=34 m/s
A	116.5	-	No	Impact depth=120 mm
B	92.6	39	No	Impact depth=130 mm
C	114.9	50	No	Impact depth=110 mm
D	95.0	46	No	Impact depth=38 mm
E	85.0	22	Yes	Impact depth=47 mm
F	99.7	-	Yes	Impact depth=74 mm
G	125.1	-	No	Residual velocity=21 m/s
H	Premature failure	-	Yes	Residual velocity=30 m/s
I	138.9	-	Yes	-seven rebars ruptured -four transverse bars were ejected
J	140.0	-	Yes	-five rebars ruptured -eight transverse bars partially ejected

In general, changing the rupture criterion did improve the correlation with the experimental results, when considering VecTor3 predictions of perforation versus punching. Using the average strain rupture criterion, only Specimen H experienced rupture before the missile rebounded; when the strain at the crack was used to determine rupture eight specimens were predicted to be perforated. Experimentally, only three specimens were perforated. It is noted, however, that when the strain at the crack was used more conservative results were obtained. For the specimens that experienced severe punching experimentally, VecTor3 predicted perforation. When the average strain criterion was used, perforation of two specimens was not captured by VecTor3. Also, in terms of correlation between experimental impact depths and analytical peak or residual displacements, changing the rupture criterion from strain at the crack to average strain did not improve the results.

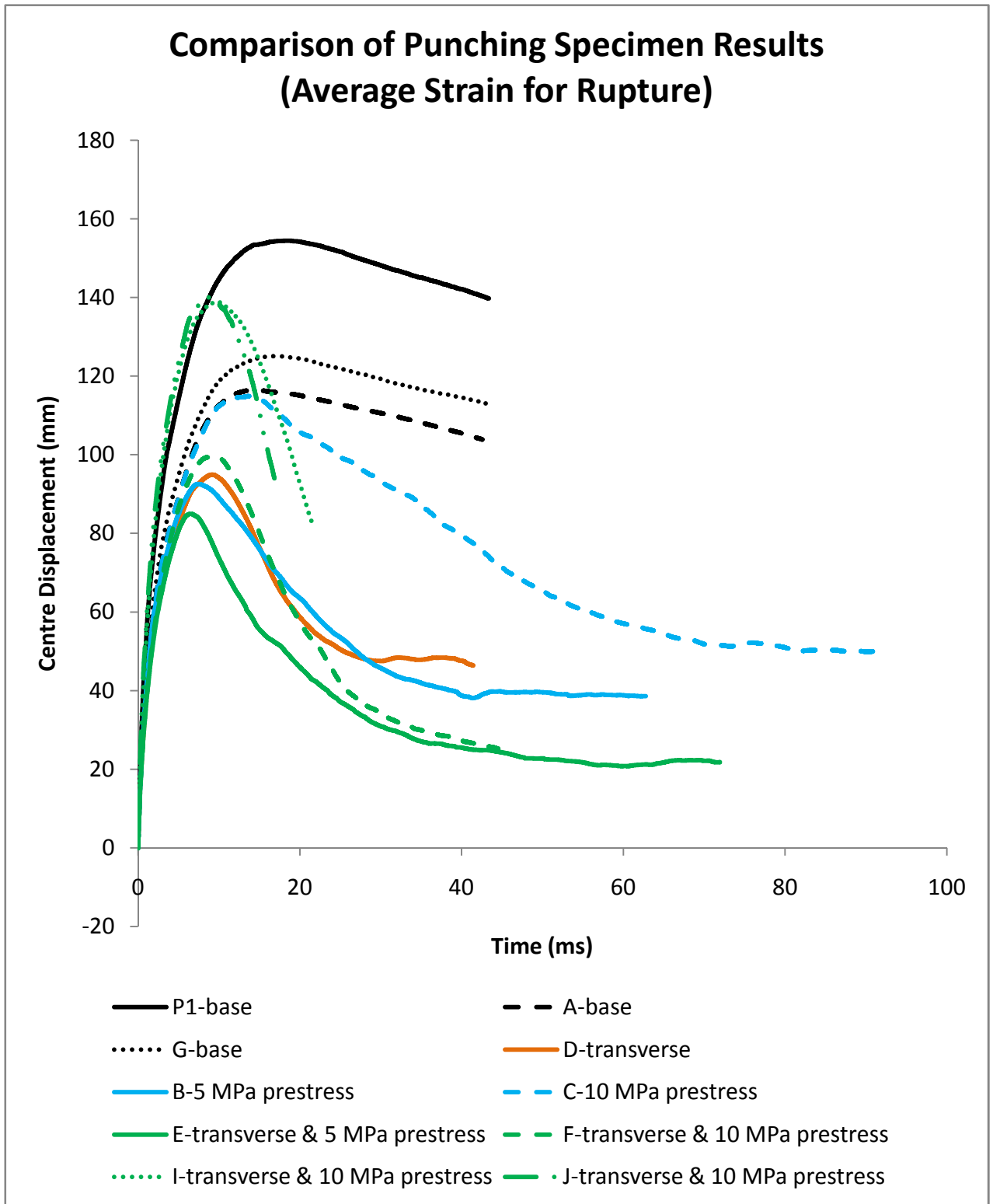


Figure 6-6: Comparison of hard impact results in from VecTor3 analyses with average strain rupture criterion.

7 Conclusions and Lessons Learned

This study represented a preliminary investigation into the current capabilities of VecTor2 and VecTor3 in modeling the response of reinforced concrete structures subjected to blast and impact loading. In order to verify the dynamic analysis capabilities of these programs, and to determine where future work should be focused, a number of different specimens were analyzed. First, shock-tube tested reinforced concrete panels were modeled, followed by one soft missile impact and a series of hard missile impacts. Based on the results of these analyses, a number of observations and conclusions can be made with respect to dynamic loading and dynamic modeling.

One of the first observations that should be made is that the support conditions are extremely important, both in the experimental and analytical results. This point is illustrated particularly well by the University of Texas specimens. In terms of the experimental conditions, it was noted that due to the wedging at the supports, a degree of fixity was introduced. In the VecTor2 analyses, both simply-supported and slightly fixed support conditions were examined. It was observed that the simply-supported model overestimated the peak displacements for all three blasts, whereas the slightly fixed support condition resulted in a more accurate estimation of the peak displacements for all three blasts. With only a small increase in fixity introduced to the model, estimated displacements decreased by over 20%. Support conditions are also important experimentally in terms of rebound displacements. For Blast 1 of the University of Texas test series, the rebound displacement was approximately 25 mm compared to the peak displacement of only 5.6 mm. This very large rebound displacement, as well as the reported displacement-time histories for both specimens, indicates that there were anomalies with the supports.

Another observation that can be made is with respect to the influence of peak pressure and impulse. In Blast 2 and Blast 3 of the University of Texas tests, the peak pressures were approximately 72 kPa and 76 kPa, respectively. The impulses were 0.55 kPa-s and 1.31 kPa-s. The peak displacements for the pretensioned specimen for Blast 2 and Blast 3 were 24.4 mm and 66.4 mm, respectively. In terms of the reported pressure-time history for Blast 3, there were two distinct peaks, an initial peak and a secondary peak at approximately 50 ms. The presence of this secondary peak had a significant influence on both the impulse and peak displacement. It is important that this pressure-time history be modeled properly in numerical simulations, as

evidenced by the VecTor2 results. In VecTor2, the force-time profile was modeled from the reported pressure-time history as well as with a simplified triangular pulse based on the peak pressure and total impulse. The difference between the results obtained with these two force profiles was quite large. For the force-time profile modeled after the experimentally reported pressure-time history, the peak displacement was 76 mm. When simplified to a triangular pulse, the displacement increased to 123 mm. The fact that the shape of the pressure-time history makes such a large difference in the analytical results illustrates the importance of accurately measuring the pressure experimentally.

Finally, one other observation that can be made with the respect to the University of Texas specimens is that the specimen construction is also extremely important. Experimentally, the post-tensioned specimen had a peak deflection of 94.5 mm compared to 66.4 mm for the pretensioned specimen. The analytical results did not agree with these results, and it was speculated that the much larger displacement of the post-tensioned specimen was due to a loss of prestress, due in part to difficulties with the anchorages. In terms of analytical results, it was also observed that the time-step of 0.1 ms was sufficiently small, and decreasing the time-step to 0.01 ms yielded basically the same results.

Alongside the University of Texas panels, as part of the initial 2D impulse loading verification specimens, a reinforced concrete panel tested at the University of Ottawa was modeled in VecTor2. This specimen was also tested in a shock tube, and was subjected to three blasts of increasing intensity. Unlike the pressure-time histories for the University of Texas specimens (particularly for Blast 1 and Blast 2), the University of Ottawa pressure-time histories consisted of multiple tertiary peaks. It is apparent from the experimentally reported displacement-time histories, particularly for Blast 1 and Blast 2, that the tertiary peaks had a significant influence on the specimen response. The tertiary peaks were included in the force-time history used in the VecTor2 analyses, and a significant influence on the computed results was observed.

One other observation that can be made with respect to the 2D shock-tube tested specimens relates to the influence of strain rate effects. In the University of Texas pretensioned specimen, considering strain rate effects for both the steel and the concrete decreased the peak displacement by approximately 10 mm. In the final VecTor2 analyses, strain rate effects were not considered for either steel or concrete. In the SDOF analyses carried out for the University of Texas and

University of Ottawa specimens, done in conjunction with the experiments, strain rate effects were considered for both materials. For SDOF analyses, including strain rate effects can be important, whereas in VecTor2 analyses it seems that including strain rate effects for the concrete is unconservative. While strain rate effects for the steel may be included, it is likely that the increase in the strength of the concrete under high rates of loading is already achieved through inertial effects within the finite element analysis of the continuum.

The University of Texas and University of Ottawa specimens consisted of blasts with peak pressures in the range of 15 kPa to 100 kPa, and impulses in the range of 0.12 kPa-s to 1.31 kPa-s. Four other specimens, tested in the Blast Load Simulator at ERDC-Vicksburg, were modeled in VecTor2, and had peak pressures in the range of 351 kPa to 395 kPa, and impulses in the range of 6.67 kPa-s to 7.78 kPa-s. In general, VecTor2 was able to estimate the peak displacements for these blasts fairly well. VecTor2 was able to predict the large peak displacements observed experimentally, and was also able to capture the large amount of damage that was visible experimentally. There was some discrepancy in the time of peak displacement between the VecTor2 analyses and the experiment. This may be due to the way the supports were modeled or set up in the experiment.

A large part of the work done for this study consisted of modeling triaxial and impact specimens for the IRIS_2012 workshop. A set of five triaxial specimens, each with different levels of confinement pressure, were modeled as well as one soft impact specimen and a series of hard missile impact tests. With the triaxial specimens, for all levels of confinement, good results were obtained using VecTor2. There were some issues with the length of post-peak response at the structural level, but in general the results obtained by VecTor2 agreed well with the experimental results. It was concluded that the Kupfer/Richart and Montoya/Ottosen concrete confinement models and the Variable-Kupfer, Montoya 2003, and Montoya with Limit concrete dilatation models can be used to adequately model confinement.

The VecTor2 and VecTor3 modeling of the VTT-B1 specimen led to a number of conclusions. Firstly, one can conclude that modeling the flexural specimen response using only the concrete compressive strength can yield good results; an excessive number of input properties are not required to carry out a quality simulation. For the VTT-B1 specimen, only the concrete compressive strength reported experimentally was used in the analyses, and the other material

properties were determined using common empirical relations. In terms of significant sources of error, the largest is the missile modeling. Modeling the soft missile was a challenge. Firstly, VecTor2 does not have a rigorous hollow missile buckling model. A rebar buckling formulation was applied to the steel elements comprising the missile, and missile crushing was approximated. Secondly, VecTor2 does not yet have proper contact elements, and the impact load was transferred from the missile to the slab using compression-only truss bars. Additional analyses, performed using the Riera impact load, indicated that the load profile obtained from the VecTor2 analyses was weighted too heavily to the start of the impact; compared to the Riera load, the VecTor2 load profile had a peak which was much higher and decayed more quickly.

Reinforcement locations and the desired number of elements through the depth of the slab resulted in an element aspect ratio that was higher than optimal. For this reason, the effects of mesh density and element aspect ratio were examined to determine whether or not they were a large source of error. A number of analyses were performed in both VecTor2 and VecTor3, and it was concluded that while the mesh density did have an effect on the target response (a finer mesh will tend to return larger displacements), this effect was not large. Another source of error may be the way the supports were modeled; no effort was made to model the supports in detail.

Despite these challenges, good results were achieved for VTT-B1 in terms of peak displacements, strains in the reinforcement, and support reactions. The peak displacements estimated by VecTor3 were generally within 13% of the experimental displacements at five sensor locations. Thus, results suggest that for flexural specimens, the VecTor programs are able to capture the target response adequately. With respect to the missile modeling, it is not the intent of the VecTor programs to be able to model hollow missile buckling in detail. As a “simplified” analysis, it may be best to limit the model to the target alone. Further, if a simplified impact force profile can be easily obtained using the Riera method, it is best to use that load when carrying out a simplified analysis.

Modeling the punching specimens presented the same challenges as VTT-B1 in terms of limitations on mesh density and the use of compression-only truss bars instead of contact elements. The punching specimens also presented the additional challenge of local damage. Experimentally, VTT-P1 was perforated, with a residual missile velocity of approximately 34 m/s. VecTor3 does not yet have local damage or element erosion capabilities, and so

perforation could not be explicitly captured. Despite this, VecTor3 was able to model punching behaviour. For VTT-P1, the displacement profiles for the front and back of the slab were examined at different times in the analysis. These profiles, as well as the deformed mesh, clearly illustrated punching behaviour. Two other series of punching specimens were modeled in VecTor3, and VecTor3 was able to differentiate between different levels of punching.

The analyses discussed in this study were the first step in the development of a simplified analytical tool. The sub-objectives of this study were to verify the dynamic analysis capabilities for soft impacts and for impulsive loading scenarios and to identify where future work was needed, particularly with respect to hard missile impacts. The overall objective was to determine if there is merit in further developing the VecTor programs as a simplified tool for analysis of concrete structures subjected to impact and impulsive loads.

As has been discussed, the results of the University of Texas and University of Ottawa specimen analyses, as well as the results of the analyses done for VTT-B1, indicate that VecTor2 and VecTor3 are able to capture reasonably well the flexural response of targets under impulsive loading and soft missile impacts. Where the majority of work is required is in the modeling of local damage. The simplified analytical tool should be able to model damage up to and including perforation of the target. In order to achieve this, work must be focused on incorporating local damage and element erosion capabilities into the programs. Work will be required to determine what element erosion criterion to use and what strain limits to choose. Preliminary analyses done using the average reinforcement strain as the rupture criterion, instead of the local strain at the crack, also show that the rupture criterion has a large effect on the response and can cause the analytical result to change from perforation to punching. The proper rupture criterion for impact analyses, and the erosion of ruptured truss elements, will also need to be investigated further.

Thus, in summary, the primary conclusions derived from this study are:

1. In the testing and modeling of specimens under extreme dynamic loads, the support conditions exert a significant influence on the results. Proper care should be taken in realistically modeling the support conditions.

2. In the simulation of blast load conditions, the shape of the pressure-time profile also significantly affects the computed responses. Simplification of the profile to a triangular pulse can result in appreciable error.
3. For blast or impact load conditions, the inclusion or exclusion of strain rate effects is also a major influencing factor in the analysis results. Preliminary indications are that, for finite element based analysis, strain rate effects in the concrete are already achieved through confinement and inertia effects, and should not be double-counted through the use of Dynamic Increase Factors for concrete.
4. The VecTor programs currently provide reasonably good accuracy in the modeling of structural elements subjected to blast loading when the behaviour of such elements is primarily flexural in nature.
5. For impact loading conditions where the structural element's response is also primarily flexural in nature, the VecTor programs again provide reasonably accurate analysis capabilities.
6. With impact loading conditions where the missile is deformable, the use of complementary methods (e.g. Riera method) for determining the loading impulse is preferable to explicitly modeling the missile.
7. The VecTor programs currently are unable to fully capture the behaviour of structural elements subjected to hard missile impacts that experience severe local damage or perforation. However, the analysis results indicate that there is potential for improved performance in this regard if various refinements are implemented. Once enhancements are made, the programs will be able to model shear damage from hard missile impacts just as well as flexural damage; as mentioned previously, the strength of the MCFT is its ability to model shear behaviour.
8. As with all finite element simulations, the fineness of the mesh will have some influence on the analysis results. However, the VecTor programs can achieve good results with meshes considerably less fine than normally employed in hydrocode models, resulting in much reduced computation times.

9. The VecTor programs do not require an inordinate number of material parameters to be specified, as is the case with many of the concrete models employed in the commonly used hydrocodes. As few as one concrete material parameter, the compressive strength, can be used.

10. There is merit in further developing the VecTor programs as a simplified tool for analysis of reinforced concrete structures subjected to impulsive or impactive loads. Specific recommendations follow.

8 Recommendations

Based on the VecTor2 and VecTor3 analysis results presented in this study, a number of recommendations can be made for future work:

1. Improvement of the post-peak response for Kupfer/Richart concrete confinement model at the structural level
2. Development and implementation of contact elements
3. Improved consideration of local damage or element erosion
4. Development of VecTor6 (axi-symmetric program)
5. Modeling of steel-concrete (SC) elements

In terms of the concrete confinement models, at the material level, the Kupfer/Richart model yielded the best results, and matched the experimental results very closely. At the structural level, however, the Kupfer/Richart model did not yield sufficient post-peak response. Work should be done to rectify this.

As mentioned with respect to VTT-B1, VTT-P1, and the other punching specimens, the lack of contact elements was a significant challenge and a source of error. In particular, in order to properly model perforation, contact elements should be implemented. In regards to the missile modeling itself, the hard missile was modeled adequately, but the soft missile presented a challenge. However, it is recommended that, instead of trying to model hollow missile buckling, a simplified load profile, such as the load applied using the Riera method, should be used for flexural analyses.

The other significant challenge that arose in the modeling of the punching specimens was the lack of element erosion. Because elements were not eroded, the rupture of a steel truss element had to be used as an indication that perforation was likely. In some cases, truss elements ruptured due to instability issues; however, the majority of steel rupture can be taken to indicate perforation. In order to properly model local damage, up to and including perforation, element erosion should be incorporated into VecTor3.

Finally, for specimens where local damage is likely to predominate, VecTor6 should be developed to include dynamic analysis capabilities. VecTor6 is a nonlinear finite element analysis program for three-dimensional axi-symmetric reinforced concrete structures subjected to quasi-static loading conditions, and is based on the MCFT and DSFM. The program uses a 4-node rectangular torus element with linear displacement fields. Reinforcement is generally modeled as smeared but can be modeled discretely using a ring element. Using VecTor6 would allow a much finer mesh to be used and would allow the modeling to focus on the impact region. It would also allow for faster analysis times.

Modeling of SC elements must also be addressed. Steel-concrete elements have already been implemented in VecTor2, but the formulations have only been verified for static loading conditions thus far. The SC elements in VecTor2 must be verified for dynamic loading conditions. In VecTor3, no analyses of SC panels have been done.

References

ABAQUS, Abaqus Inc., Providence, RI., USA.

ADINA, ADINA R&P Inc., Watertown, MA, USA.

ANSYS AUTODYN. Interactive Non-Linear Dynamic Analysis Software, Version 12, User's Manual. *SAS IP Inc.*, 2009.

AUTODYN, Century Dynamics Inc., Concord, CA, USA.

Borgerhoff, M., Stangenberg, F., and Zinn, R. (2011) "Numerical simulation of impact tests of reinforced concrete slabs with predominant flexural deformation behavior" *Transactions of SMiRT 21*, New Delhi, India.

Comite Euro-International du Beton (1988). Concrete Structures Under Impact and Impulsive Loading. *Bulletin D'Information No. 187*. Lausanne, Switzerland.

Comite Euro-International du Beton (1990). CEB-FIP Model Code 1990. Lausanne, Switzerland.

Comite Euro-International du Beton (2010). *fib* Model Code 2010. Bulletin No. 55. Lausanne, Switzerland

Dancygier, A.N. and Yankelevsky, D.Z. (1996) "High strength concrete response to hard projectile impact". *International Journal of Impact Engineering*. 18(6); 583-599

Dancygier, A.N. (1997) technical note on "effect of reinforcement ratio on the resistance of reinforced concrete to hard projectile impact". *Nuclear Engineering and Design*. 172; 233-245

Dancygier, A.N., Yankelevsky, D.Z., and Jaegermann, C. (2007) "Response of high performance concrete plates to impact of non-deforming projectiles". *International Journal of Impact Engineering*. 34; 1768-1779

Department of the Army (1990) *Structures to Resist the Effects of Accidental Explosions*. TM5-1300. U.S. Government Printing Office, Washington, D.C.

- Dunkman, D.A., Yousef, A.E.A, Karve, P.M., Williamson, E.B. (2009) “Blast performance of prestressed concrete panels”. *Proceedings of the 2009 Structures Congress—Don’t Mess with Structural Engineers: Expanding Our Role* pp 1297-1306
- Esashi, Y., Ohnuma, H., Ito, C., and Shirai, K. (1989) “Experimental Studies on Local Damage of Reinforced Concrete Structures by the Impact of Deformable Missiles: Part 2: intermediate Scale Tests”. *Transactions of the 10th International Conference on Structural Mechanics in Reactor Technology, Anaheim.* pp.265-270
- FHWA (2007). *Evaluation of LS-DYNA Concrete Material model 159.* FHWA Publication. U.S. Department of Transportation
- Fiquet, G. and Dacquet, S. (1977) “Study of the perforation of reinforced concrete slabs by rigid missiles-experimental study, part II”. *Nuclear Engineering and Design.* 41; 103-120
- Goldstein, S., Berriaud, C, and Labrot, R. (1977) “Study of the perforation of reinforced concrete slabs by rigid missiles—experimental study, Part III”. *Nuclear Engineering and Design.* 41; 121-128
- Hanchak, S.J., Forrestal, M.J., Young, E.R., and Ehergott, J.Q. (1992) “Perforation of concrete slabs with 48 MPa (7ksi) and 140 MPa (20 ksi) unconfined compressive strengths”. *International Journal of Impact Engineering.* 12(1); 1-7
- Ho, D. (2004). “Impact response of reinforced concrete: An experimental and numerical investigation.” M.A.Sc. Thesis, University of Toronto, Department of Civil Engineering.
- Hoshikuma, J., Kawashima, K., Nagaya, K. and Taylor, A.W. (1997). “Stress-Strain Model for Confined Reinforced Concrete in Bridge Piers”. *ASCE Journal of Structural Engineering.* 123(5): 624-633
- Itoh, M., Katayama, M., Mitake, S., Niwa, N., Beppu, M., and Ishikawa, N. (2000) “Numerical study on impulsive local damage of reinforced concrete structures by a sophisticated constitutive and failure model”. *Structures Under Shock and Impact VI*
- Jacques, E. (2011) “Blast Retrofit of Reinforced Concrete Walls and Slabs”, *University of Ottawa*, M.A.Sc Thesis, 286 pp.

Jones, N. (1989) “Structural Impact”. Cambridge University Press, UK. 575pp.

Kojima, I. (1991) “An experimental study on local behaviour of reinforced concrete slabs to missile impact”. *Nuclear Engineering and Design*. 130; 121-132

LS-DYNA, Livermore Software Technology Corp., Livermore, CA, USA.

Luccioni, B. and Aráoz, G. (2011) “Erosion criteria for frictional materials under blast load”. *Mecánica Computacional*. 30; 1809-1831.

Magnier, S.A. and Donze, F.V. (1998) “Numerical simulations of impacts using a discrete element method”. *Mechanics of Cohesive-Frictional Materials*. 3; 257-276

Malvar, L.J., and Crawford, J.E. (1998). “Dynamic Increase Factor for Concrete”. *Twenty-Eighth DDESB Seminar*. Orlando, FL.

Malvar, L.J., and Crawford, J.E. (1998). “Dynamic Increase Factor for Steel Reinforcing Bars”. *Twenty-Eighth DDESB Seminar*. Orlando, FL.

Malvar, L.J., Crawford, J.E., Wesevich, J.W., Simons, D. (1997) “A Plasticity Concrete Material Model for DYNA3D”. *International Journal of Impact Engineering*. 19 (9-10): 847-873

Muto,K., Tachikawa, H., Sugano, T., Tsubota, H., Kobayashi, H., Kasai, Y., Koshika, N., and Tsujimoto, T. (1989a) “Experimental Studies on Local Damage of Reinforced Concrete Structures by the Impact of Deformable Missiles: Part 1: Outline of Test Program and Small-Scale Tests”. *Transactions of the 10th International Conference on Structural Mechanics in Reactor Technology, Anaheim*. pp.257-264

Muto,K., Sugano, T., Tsubota, H., Nagamatsu, N., Koshika, N., Okano, M., Suzuki, K., and Ohroi, S. (1989b) “Experimental Studies on Local Damage of Reinforced Concrete Structures by the Impact of Deformable Missiles: Part 3: Full-Scale Tests”. *Transactions of the 10th International Conference on Structural Mechanics in Reactor Technology, Anaheim*. pp.271-278

Muto, K., Sugano, T., Tsubota, H., Koshika, N., Esashi, Y., Ohnuma, H., and Ito, C. (1989c) “Experimental Studies on Local Damage of Reinforced Concrete Structures by the Impact of Deformable Missiles: Part 4: Overall Evaluation of Local Damage”. *Transactions of the 10th International Conference on Structural Mechanics in Reactor Technology, Anaheim*. pp.279-299

Nachtsheim, W. and Stangenberg, F. (1982) “Interpretation of results of Meppen slab tests—comparison with parametric investigations”. *Nuclear Engineering and Design*. 75; 283-290

Nuclear Energy Agency. (2011) “Improving Robustness Assessment Methodologies for Structures Impacted by Missiles (IRIS_2010): Final Report”.

Ohno, T., Uchida, T., Matsumoto, N., and Takahashi, Y. (1992) “Local damage of reinforced concrete slabs by impact of deformable projectiles”. *Nuclear Engineering and Design*. 138; 45-52

Orbovic, N. and Blahoianu, A. (2011) “Tests on Concrete Slabs Under Hard Missile Impact to Evaluate the Influence of Transverse Reinforcement and Pre-stressing on Perforation Velocity”. *Transactions of SMiRT 21*. November 6-11, New Delhi, India.

Orbovic, N., Elgohary, M., Lee, N., and Blahoianu, A. (2009) “Tests on Reinforced Concrete Slabs with Pre-stressing and with Transverse Reinforcement under Impact Loading”. *Proceedings of the 20th International Conference on Structural Mechanics in Reactor Technology (SMiRT 20)*. Espoo, Finland. August 9-17, 2009.

Riech, H. and Rüdiger, E. (1984) “Versuchsergebnisse des Meppener Versuche II/11 bis II/22 (Results of Meppen tests II/11 to II/22)”. 1500408 (RS 467), Technischer Bericht.

Riedel, W., Thoma, K., Hiermaier, S., Schmolinske, E. (1999). “Penetration of Reinforced Concrete by BETA-B-500 Numerical Analysis using a New Macroscopic Concrete Model for Hydrocodes”. *Proceedings of the 9th International Symposium on the Interaction of the Effects of Munitions with Structures*

Riera, J.D. (1968). “On the stress analysis of structures subjected to aircraft impact forces”. *Nuclear Engineering and Design*.; 8: 416-426

Riera, J.D. and Iturrioz, I. (1998) “Discrete elements model for evaluating impact and impulsive response of reinforced concrete plates and shells subjected to impulsive loading”. *Nuclear Engineering and Design*. 179; 135-144

Robert, S.D. and Johnson, C.F. (2009) “Blast Response of Conventional and High Performance Reinforced Concrete Panels”. *Proceedings of the 2009 Structures Congress—Don’t Mess with Structural Engineers: Expanding Our Role* pp 1142-1150

Saatci, S. (2007) “Behaviour and Modeling of Reinforced Concrete Structures Subjected to Impact Loads”. Thesis for Doctor of Philosophy. Department of Civil Engineering, University of Toronto. 316pp

Saatci, S. and Vecchio, F.J. (2009) “Nonlinear Finite Element Modeling of Reinforced Concrete Structures under Impact Loads”. *ACI Structural Journal*. 106 (5): 717-725

Sawamoto, Y., Tsubota, H., Kasai, Y., Koshika, N., and Morikawa, H. (1998) “Analytical studies on local damage to reinforced concrete structures under impact loading by discrete element method”. *Nuclear Engineering and Design*. 179; 157-177

Schwarzkoopp, D., Stangenberg, F., and Zinn, R. “Impact response analysis including missile-structure interaction”. Paper J 0385, *Proceedings of 10th SMiRT Conference*, Anaheim, USA, August 14-18, 1989.

Schwer, L. (2010) *Winfrith Concrete Model Strain Rate Option*. Schwer Engineering & Consulting Services

Schwer, L.E. and Murray, Y.D. (1994). “A Three-Invariant Smooth Cap Model With Mixed Hardening”. *International Journal for Numerical and Analytical Methods in Geomechanics* 18: 657-688

SOFiSTiK, SOFiSTiK AG Analysis Programs, Oberschleissheim, Germany.

Sugano, T., Tsubota, H., Kasai, Y., Koshika, N., Ohnuma, H., von Riesenmann, W.A., Bickel, D.C., and Parks, M.B. (1993a) “Local damage to reinforced concrete structures caused by impact of aircraft engine missiles. Part 1. Test program, method, and results”. *Nuclear Engineering and Design*. 140; 387-405

Sugano, T., Tsubota, H., Kasai, Y., Koshika, N., Itoh, C., Shirai, K., von Rieseemann, W.A., Bickel, D.C., and Parks, M.B. (1993b) "Local damage to reinforced concrete structures caused by impact of aircraft engine missiles. Part 2. Evaluation of test results". *Nuclear Engineering and Design*. 140; 407-423

Tai, Y.S. (2009) "Flat ended projectile penetrating ultra-high strength concrete plate target". *Theoretical and Applied Fracture Mechanics*. 51; 117-128

Teng, T.L., Chu, Y., Chang, F., Shen, B. (2005) "Penetration resistance of reinforced concrete containment structures". *Annals of Nuclear Energy*. 32; 281-298

Thiagarajan, G., Vasudevan, A.K., and Robert, S. (2011) "Numerical Modeling of Concrete Slabs Reinforced with High Strength Low Alloy Vanadium Steel Bars Subjected to Blast Loads". SP281-15. American Concrete Institute.

University of Missouri Kansas City (2012) Blast Blind Simulation Contest 2012. website: <http://sce.umkc.edu/blast-prediction-contest/>

Unosson, M. (2002) *Constitutive equations for concrete materials subjected to high rate of loading*. Licentiate Thesis, Linkoping University, Sweden

Vasudevan, A.K. (2012) "Finite Element Analysis and Experimental Comparison of Doubly Reinforced Concrete Slabs Subjected to Blast Loads". Master of Science in Civil Engineering, University of Missouri-Kansas City.

Vecchio, F.J. and Collins, M.P. (1986) "The Modified Compression-Field Theory for Reinforced Concrete Elements Subjected to Shear". *Journal of the American Concrete Institute*. 83(2):219-231

Vecchio, F.J. (1990) "Reinforced Concrete Membrane Element Formulations". *Journal of Structural Engineering*. 116(3):730-750

Vecchio, F.J. (2000) "Disturbed Stress Field Model for Reinforced Concrete: Formulation". *ASCE Journal of Structural Engineering*. 126(8):1070-1077

Vepsä, A. (2010a) “Experimental tests for bending and punching behavior of reinforced concrete walls under impact loading”. Research Report VTT-R-05587-10. 172pp.

Vepsä, A. (2010b) “Punching behavior of one 250 mm thick reinforced concrete wall under hard impact loading: Revision A”, Research Report VTT-05588-10. 71 pp.

Vu, X.U. (2007) “Caractérisation expérimentale du béton sous fort confinement: influences du degré de saturation et du rapport eau/ciment (Experimental characterization of the concrete behaviour under high confinement: influence of the saturation ratio and the water/cement ratio)”. Doctoral Thesis. Université Joseph Fourier-Grenoble I. 225pp.

Winnicki, A., Pearce, C.J., Bicanic, N. (2000) “Viscoplastic Hoffman consistency model for concrete”, *Computers and Structures* 79: 7-19

Wong, P.S., Vecchio, F.J., Trommels, H. (2012) *VecTor2 & FormWorks User's Manual*.

Zinn, R., Stangenberg, F., Borgerhoff, M., Chauvel, D., and Touret, J. (2007) “Non-linear behaviour of concrete structures under severe impact”. *Proceedings of CONSEC'07 Tours, France*

Appendix-A Comparison of VecTor3 VTT_B1 Results to Experimental Results

This section compares VecTor3 results, for the base case, to the experimental results for displacements, reinforcement strains, concrete strains, and support forces. Figure A-1 and Table A-1 summarize the experimental locations of the displacement sensors. Figure A-2 and Table A-2 summarize the locations of the concrete strain sensors. Figure A-3 and Table A-3 show the locations of the reinforcement strain gauges.

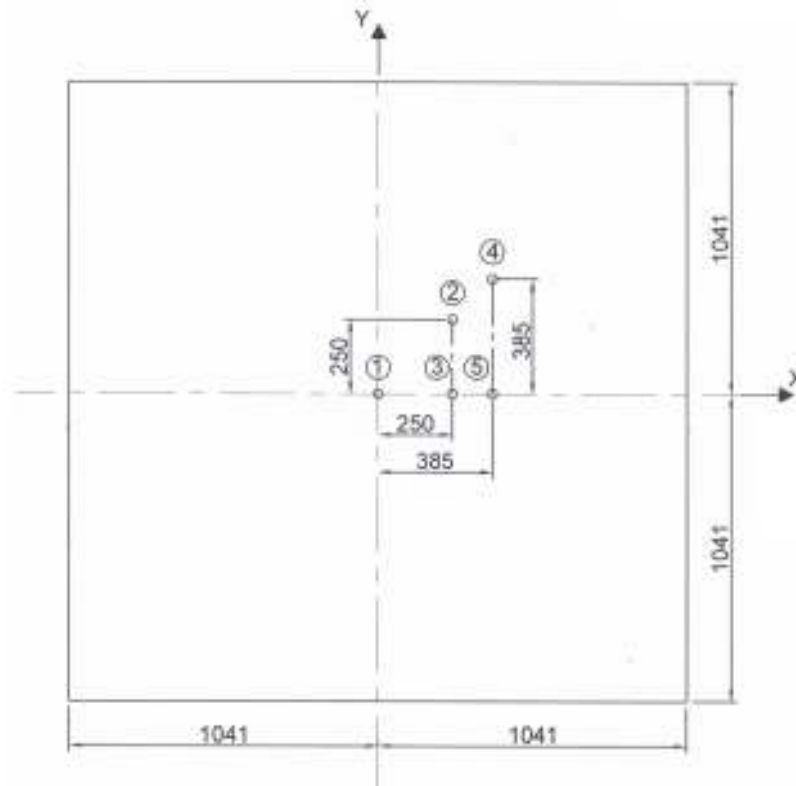


Figure A-1: Displacement sensor locations (Vepsä, 2010a).

Table A-1: Displacement Sensor Locations

Position relative to the center					
point	W1	W2	W3	W4	W5
x (mm)	0	250	250	385	385
y (mm)	0	250	0	385	0
z(mm)	-75	-75	-75	-75	-75
position	rear	rear	rear	rear	rear

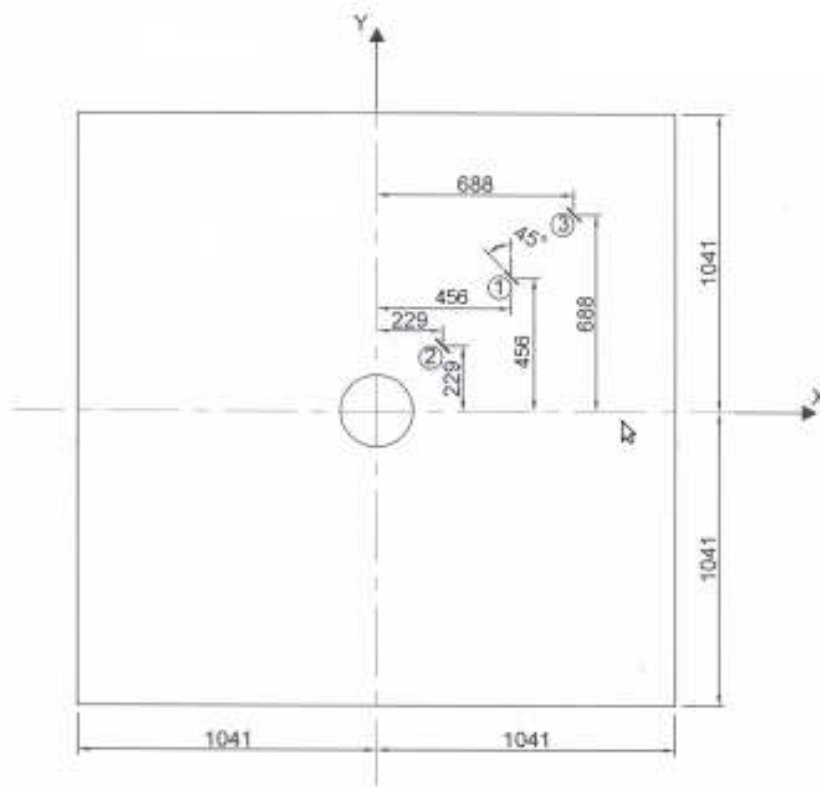


Figure A-2: Concrete strain gauge locations (Vepsä, 2010a).

Table A-2: Concrete Strain Gauge Locations

Position relative to the center			
point	R2	R1	R3
x (mm)	229	456	688
y (mm)	229	456	688
z(mm)	75	75	75
direction	45°	45°	45°
position	front	front	front

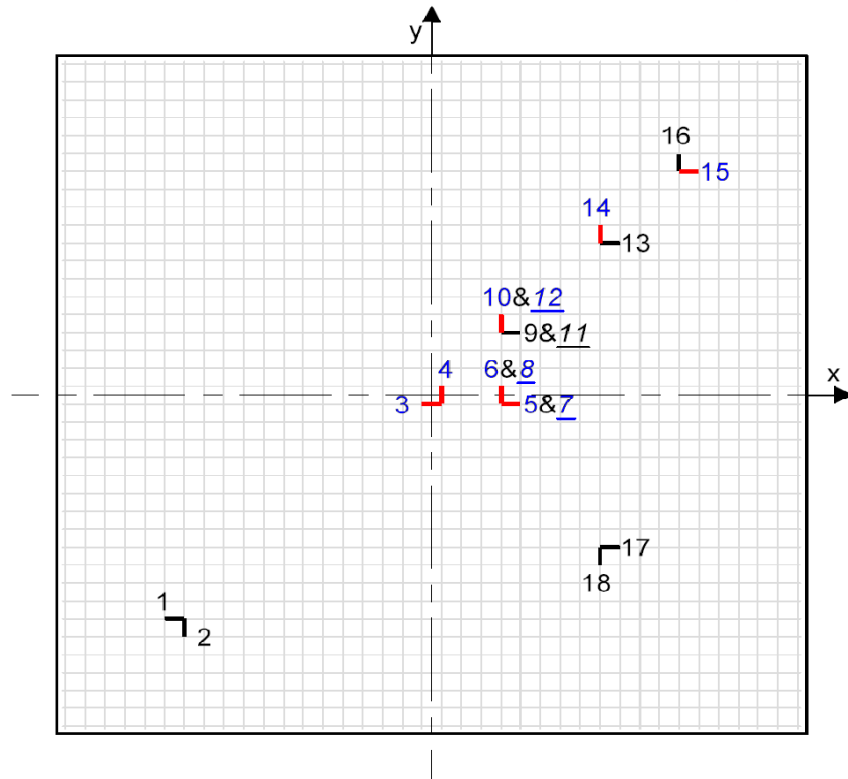


Figure A-3: Rebar strain gauge sensor locations (Vepsä, 2010a).

Table A-3: Rebar Strain Gauge Locations

Reinforcement sensors position relative to the center					
point	x (mm)	y (mm)	z(mm)	direction	position
D3	0	-27.5	-54	x	rear
D4	27.5	0	-48	y	rear
D5	220	-27.5	-54	x	rear
D6	192.5	0	-48	y	rear
D7	220	-27.5	54	x	front
D8	192.5	0	48	y	front
D10	192.5	220	-48	y	rear
D12	192.5	220	48	y	front
D14	467.5	495	-48	y	rear
D15	715	687.5	-54	x	rear
D18	467.5	-495	-48	y	rear

Displacement Results

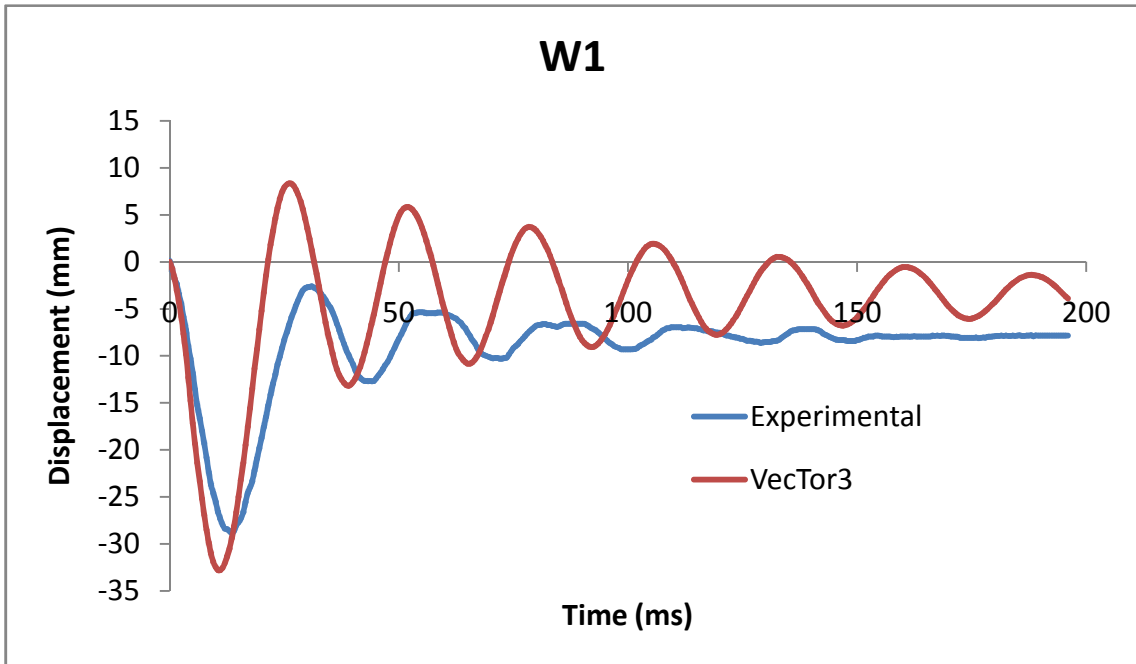


Figure A-4: Displacement results at sensor location W1 (centre of the slab).

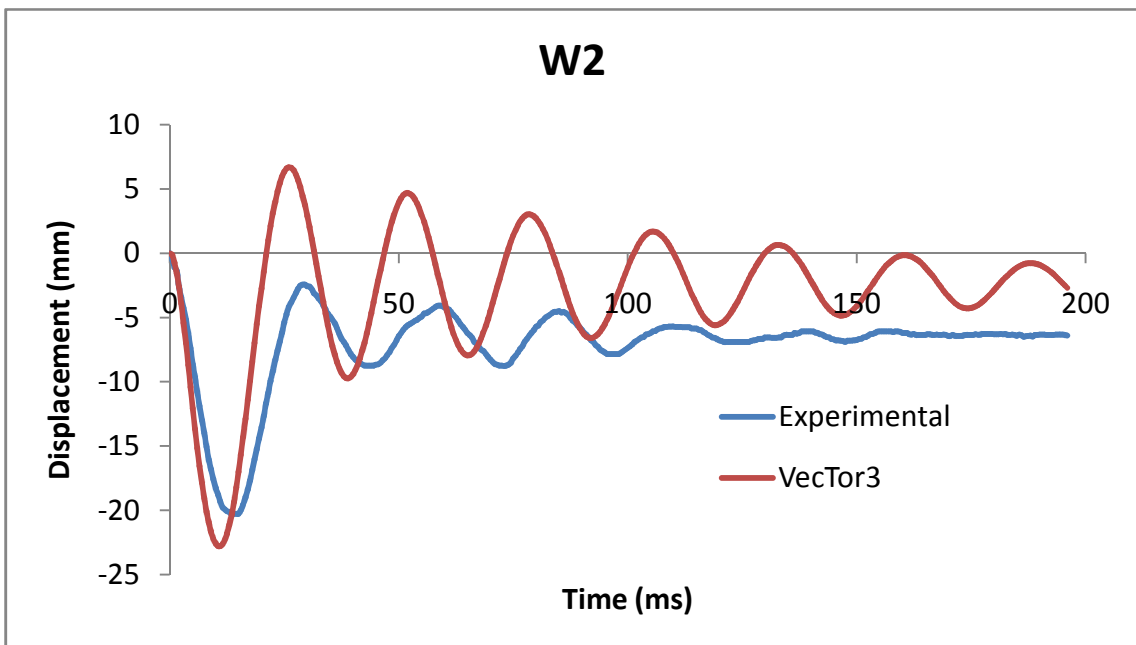


Figure A-5: Displacement results at sensor location W2.

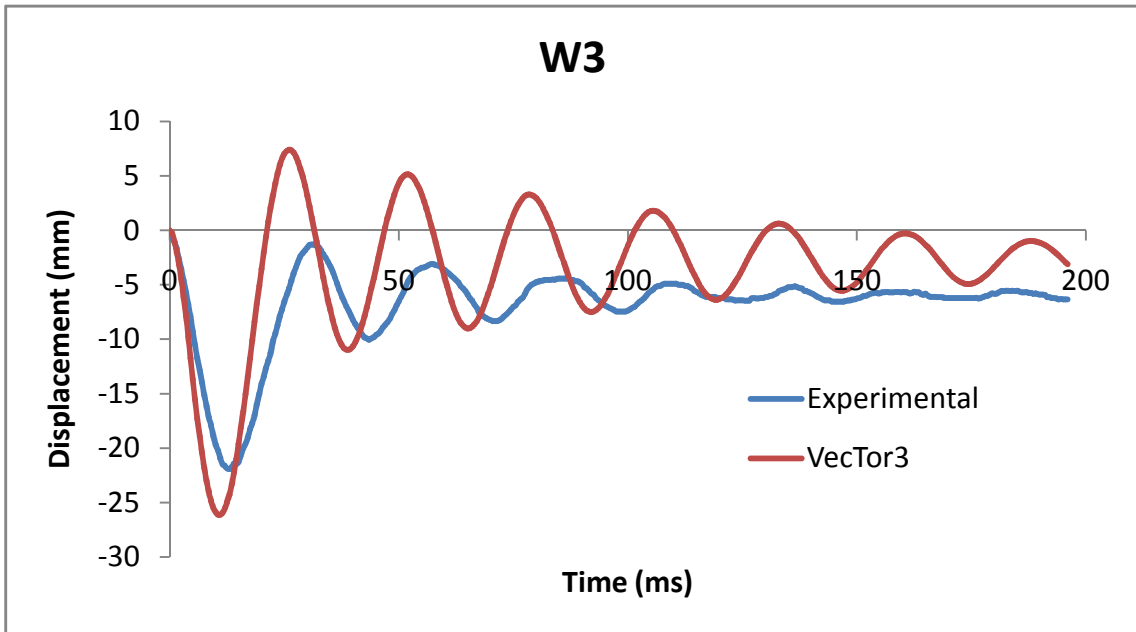


Figure A-6: Displacement results at sensor location W3.

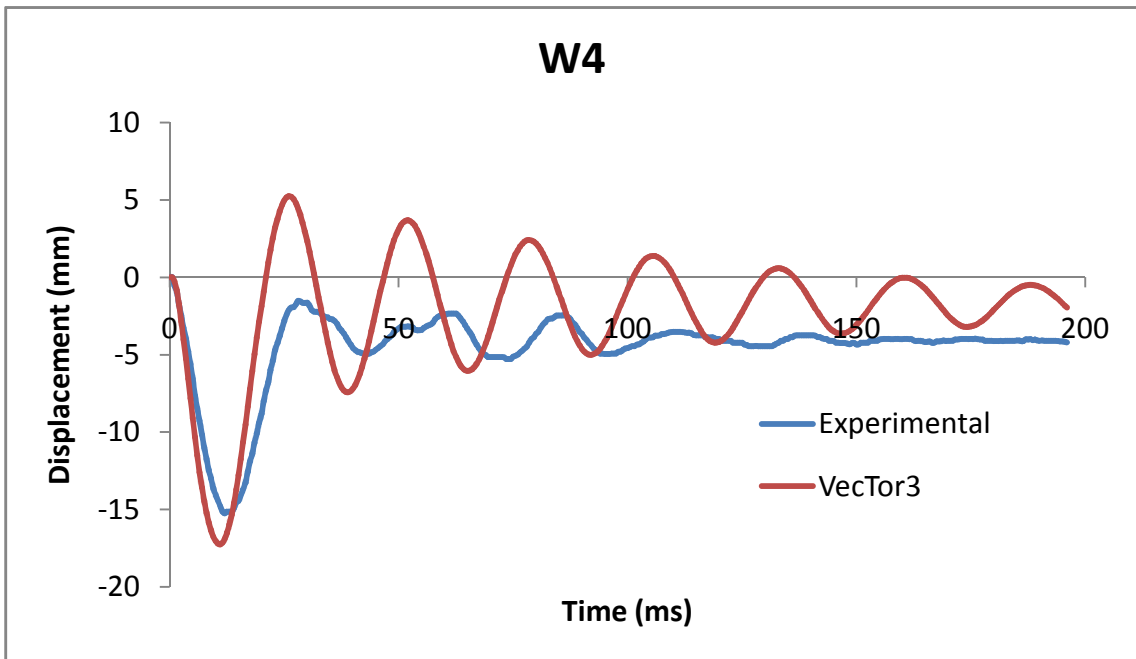


Figure A-7: Displacement results at sensor location W4.

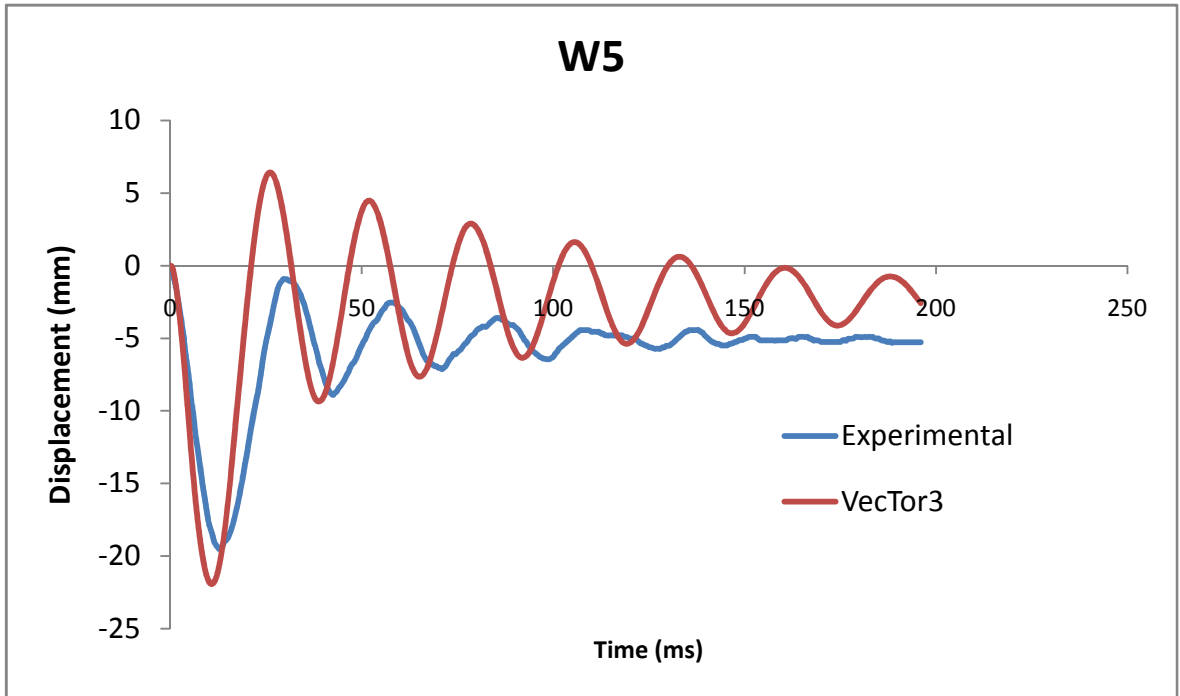


Figure A-8: Displacement results at sensor location W5.

Reinforcement Strains

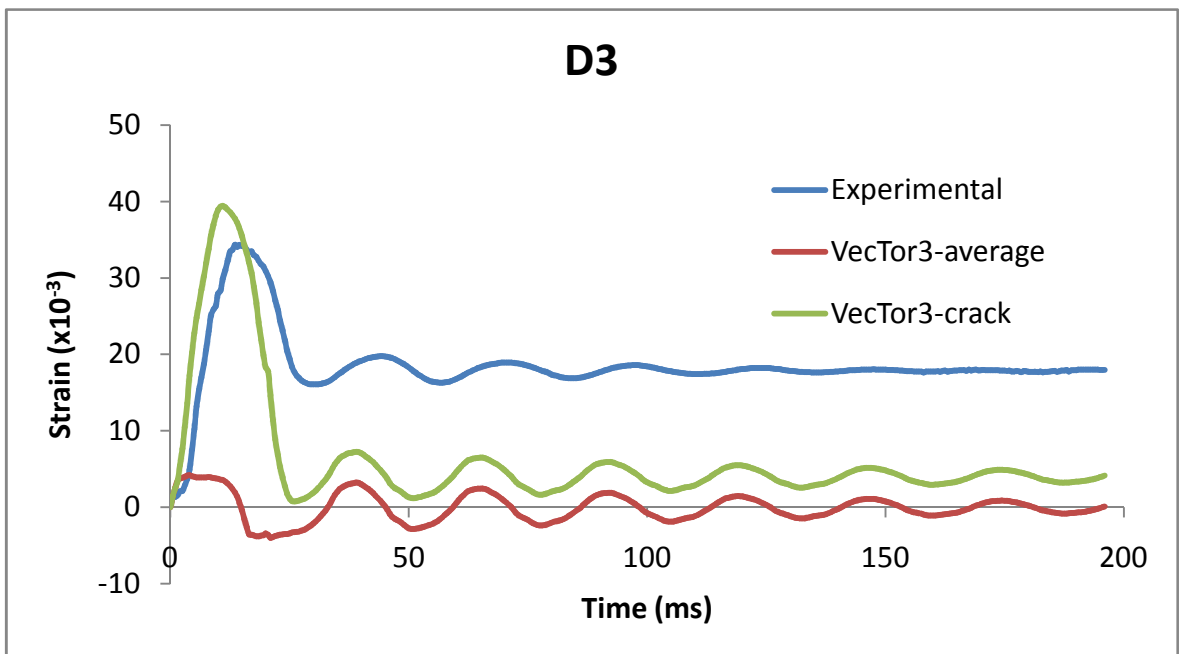


Figure A-9: Reinforcement strain D3.

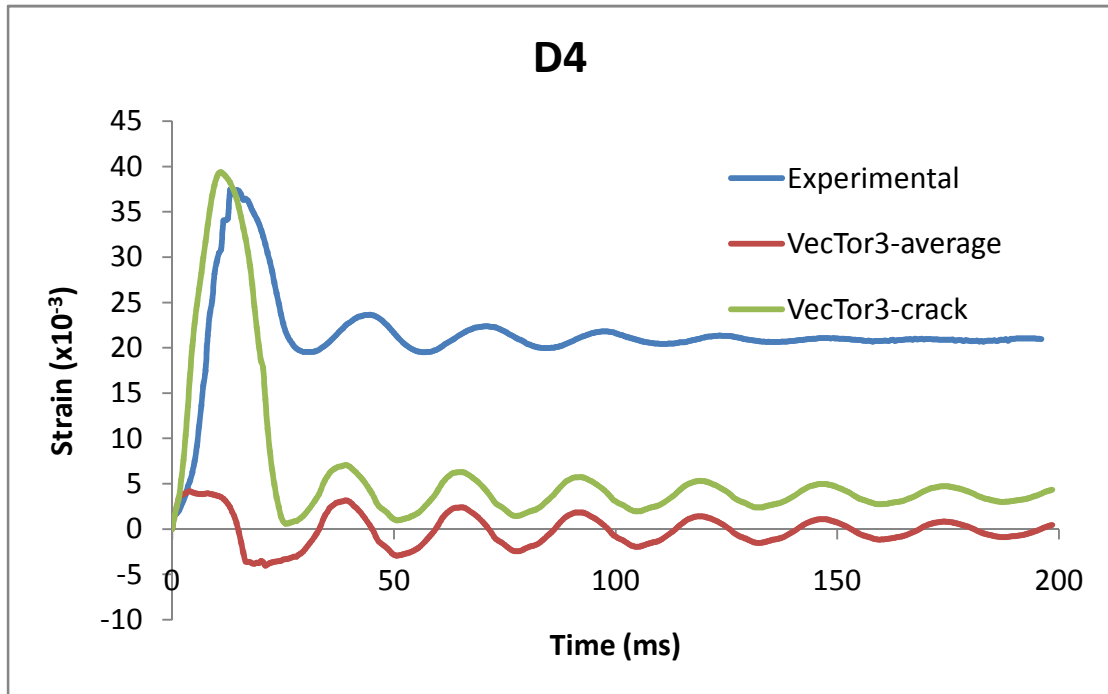


Figure A-10: Reinforcement strain D4.

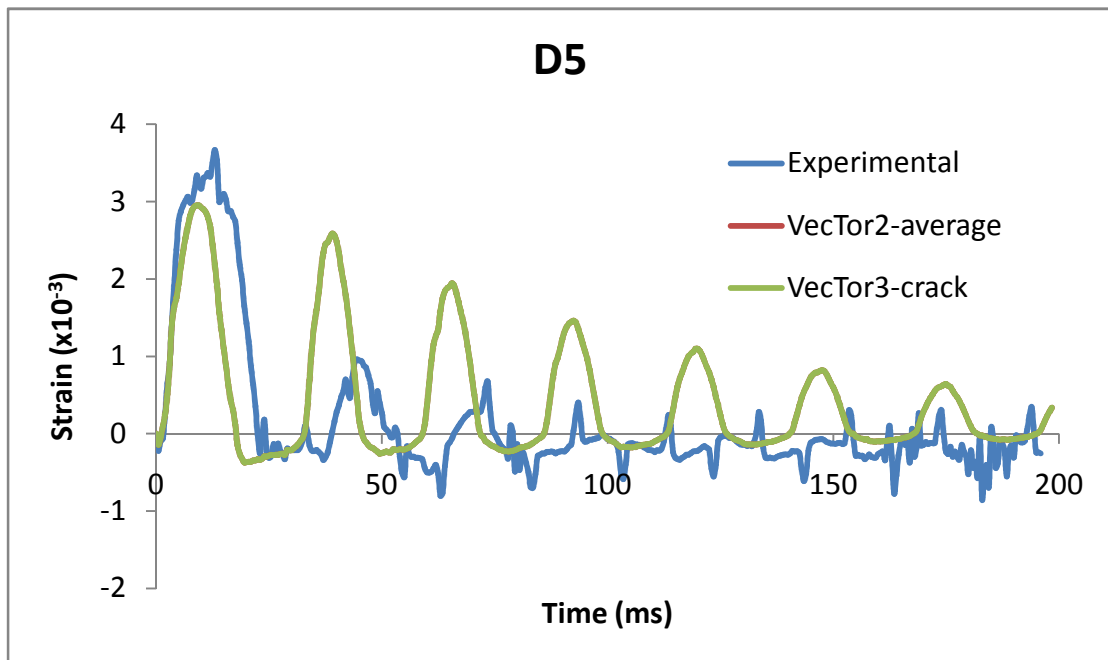


Figure A-11: Reinforcement strain D5.

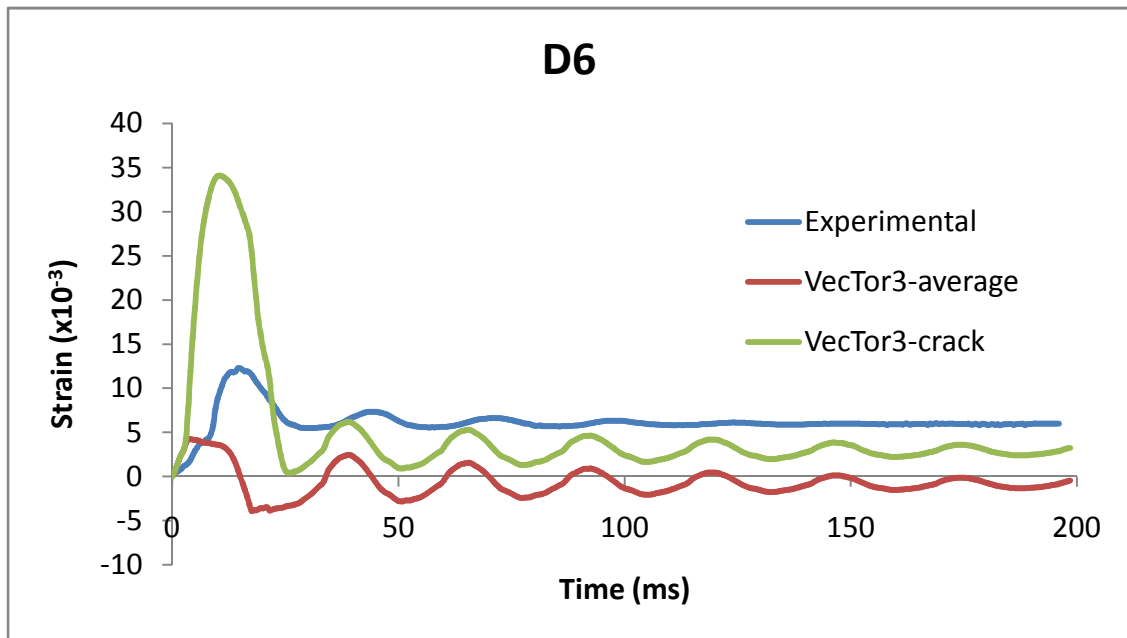


Figure A-12: Reinforcement strain D6.

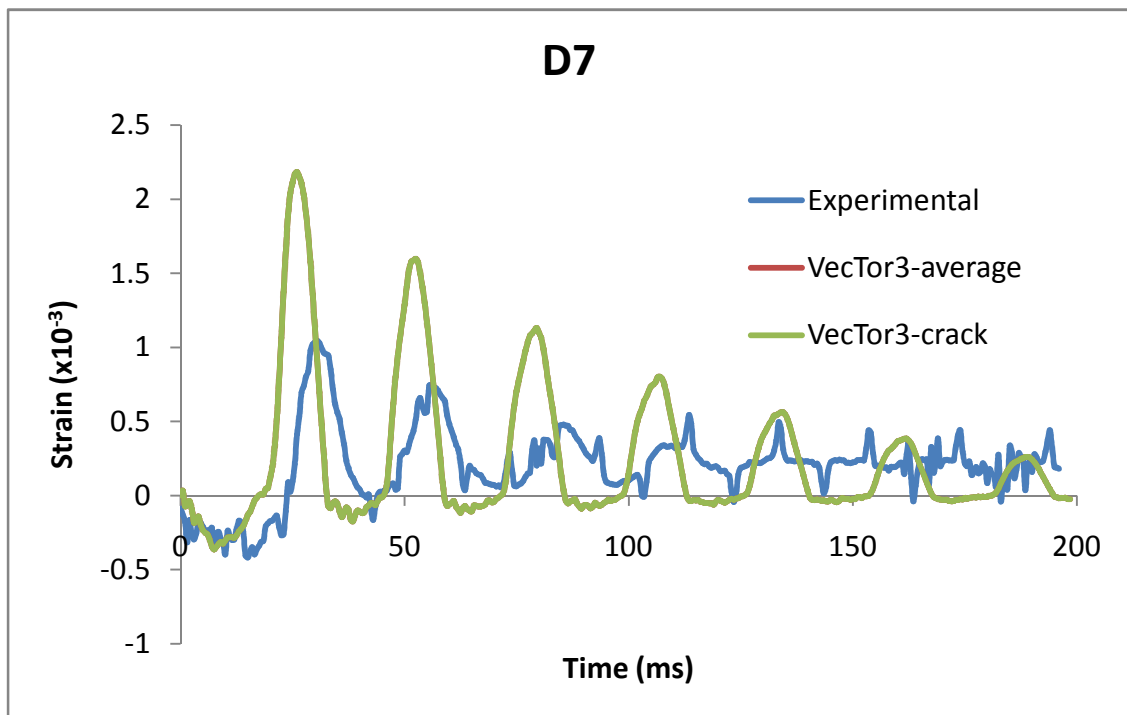


Figure A-13: Reinforcement strain D7.

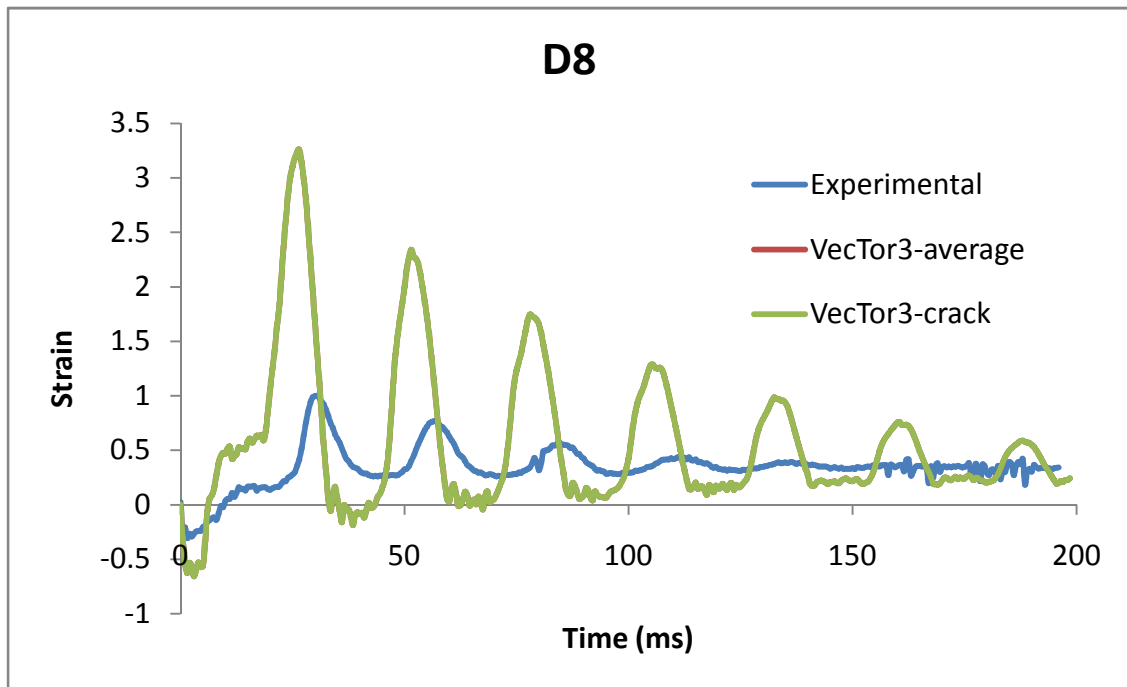


Figure A-14: Reinforcement strain D8.

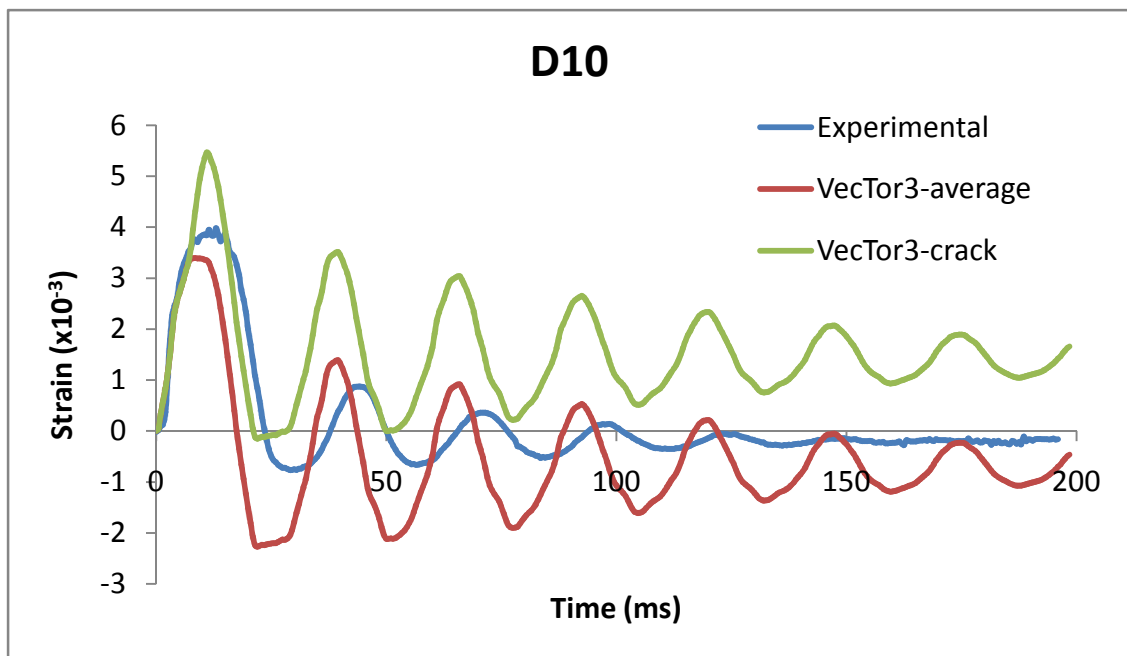


Figure A-15: Reinforcement strain D10.

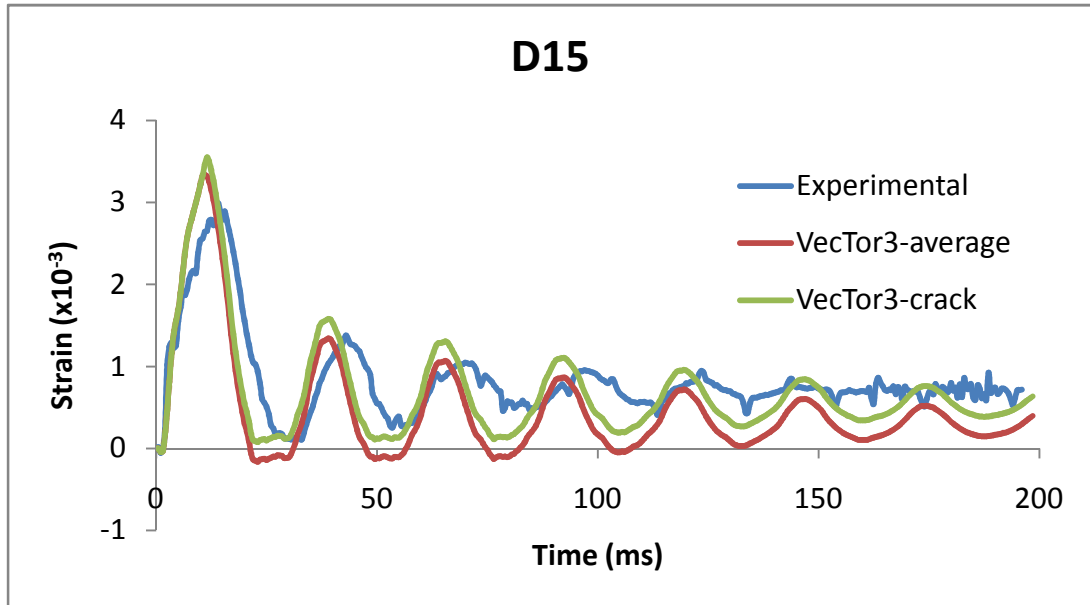


Figure A-16: Reinforcement strain D15.

Concrete Strains

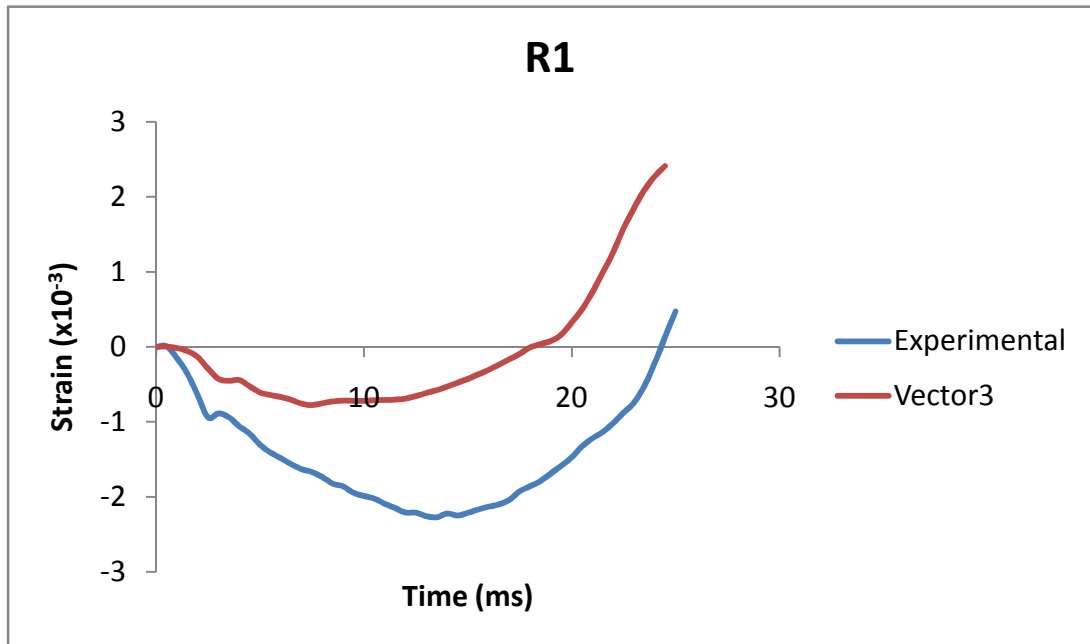


Figure A-17: Concrete strains at sensor R1.

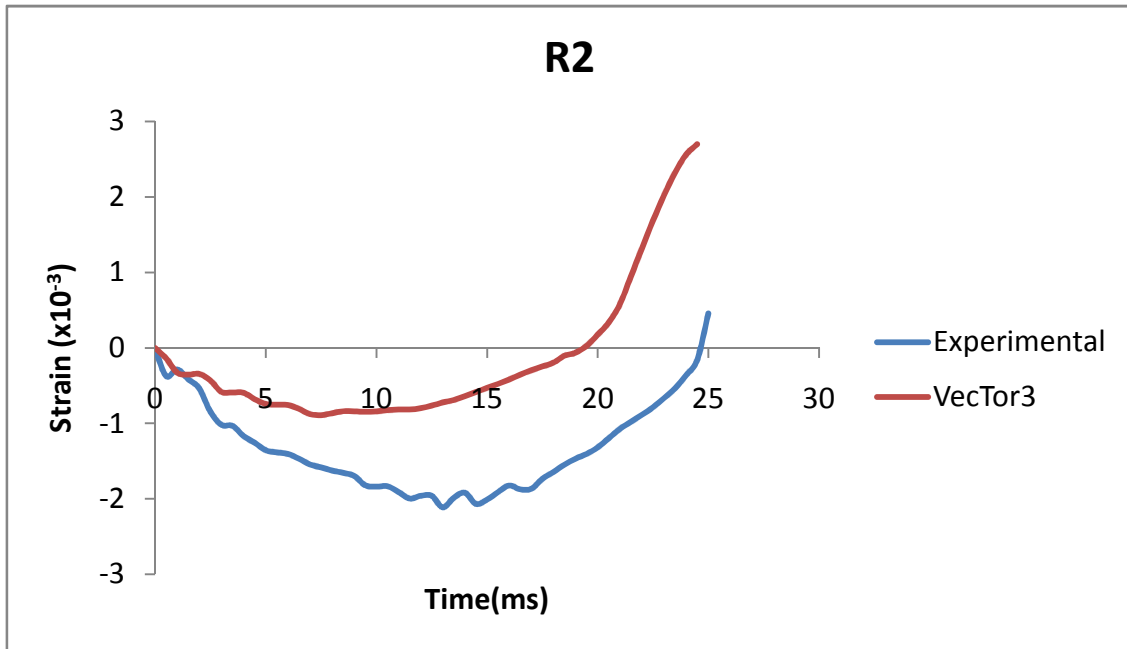


Figure A-18: Concrete strains at sensor R2 .

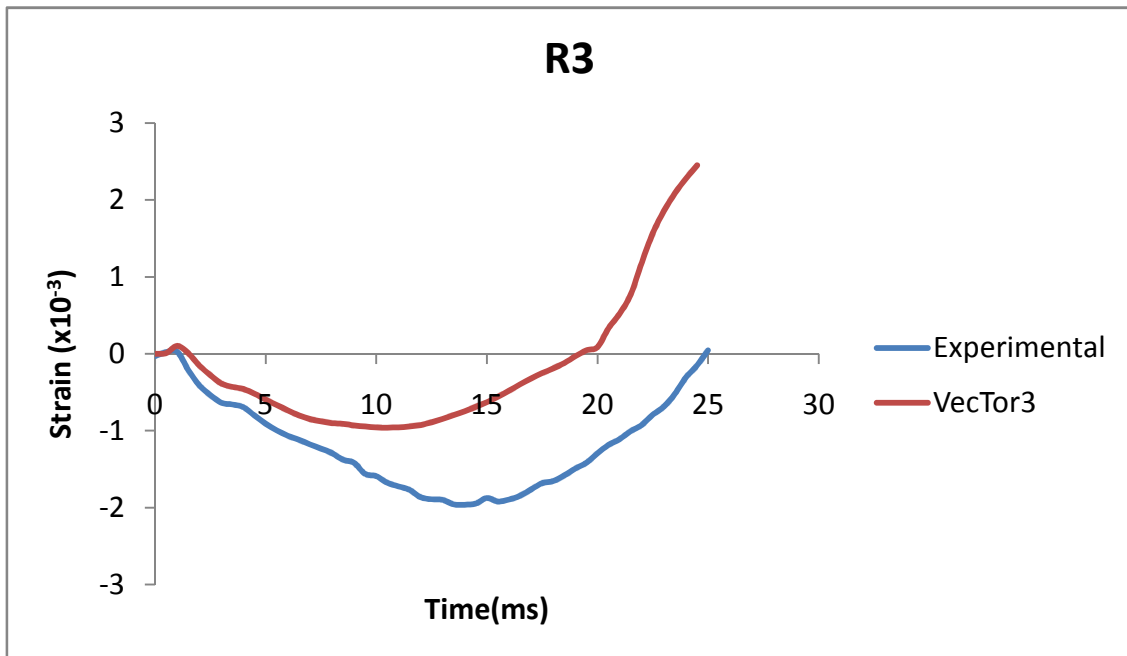


Figure A-19: Concrete strains at sensor R3.

Support Forces

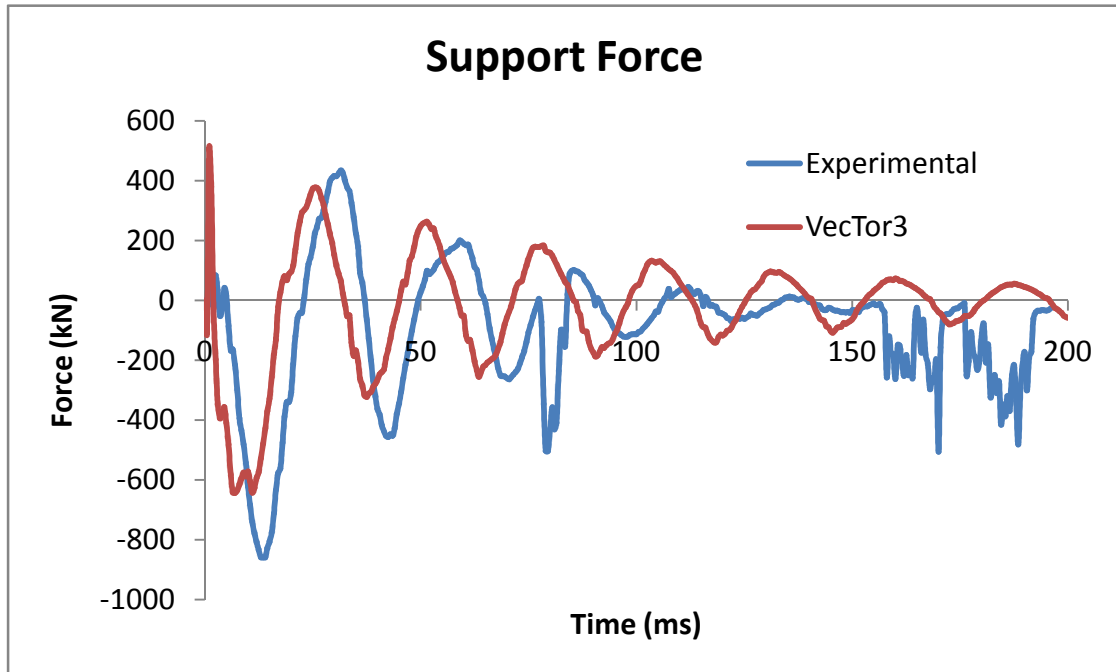


Figure A-20: Total support force.

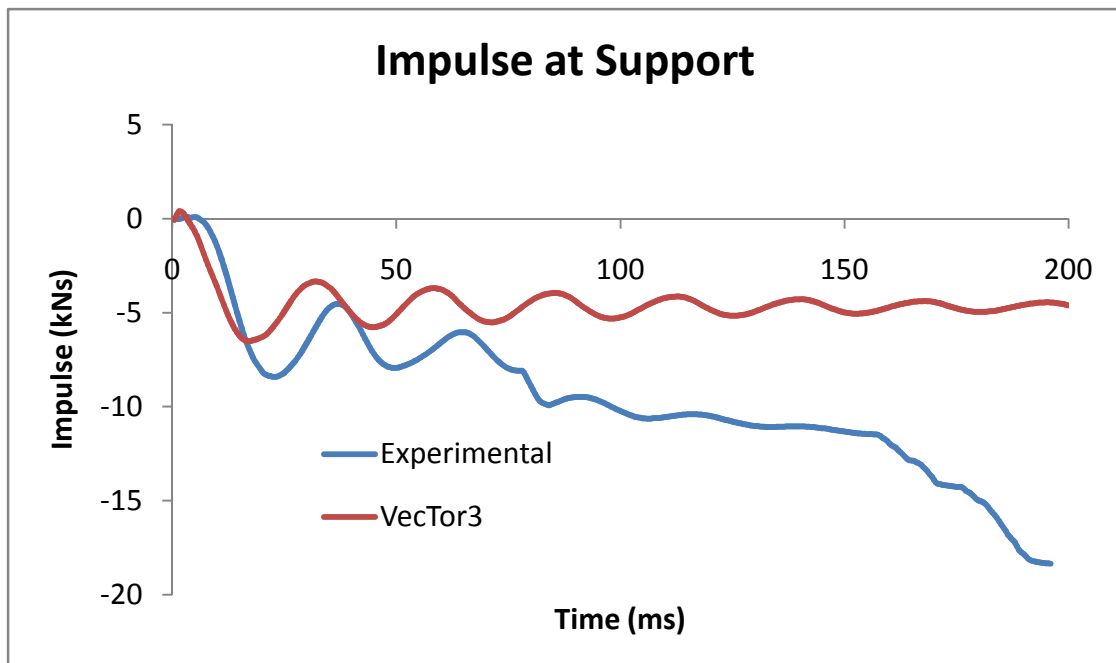


Figure A-21: Support impulse.

Appendix-B

Comparison of VecTor3 VTT_P1 Results to Experimental Results

This section compares VecTor3 results, for the base case, to the experimental results for displacements, reinforcement strains, concrete strains, and support forces. Figure B-1 and Table B-1 summarize the experimental locations of the displacement sensors. Figure B-2 and Table B-2 summarize the locations of the concrete strain sensors. Figure B-3 and Table B-3 show the locations of the reinforcement strain gauges.

Table B-1: Displacement Sensor Locations

Position relative to the center					
point	W1	W2	W3	W4	W5
x (mm)	-300	0	300	460	600
y (mm)	230	230	230	230	230
z(mm)	125	125	125	125	125
position	front	front	front	front	front

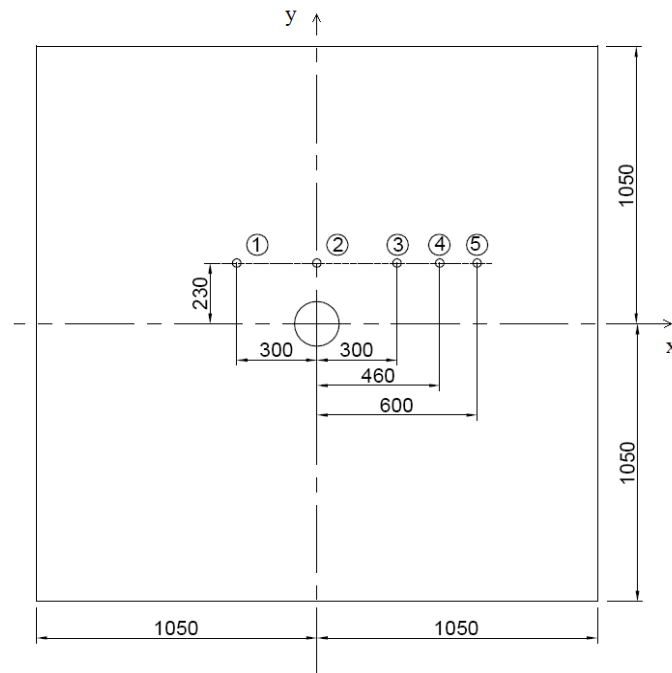


Figure B-1: Displacement sensor locations (Vepsä, 2010b).

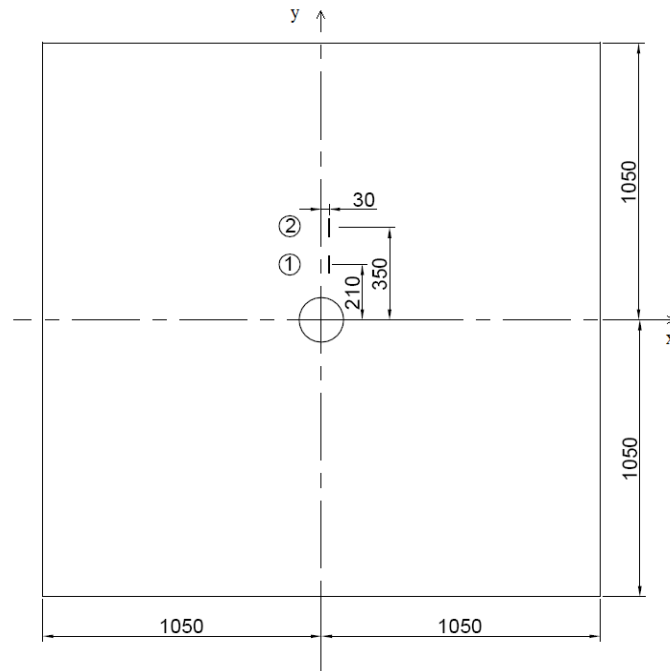


Figure B-2: Concrete strain gauge locations (Vepsä, 2010b).

Table B-2: Concrete Strain Gauge Locations

Position relative to the center		
point	1	2
x (mm)	30	30
y (mm)	210	350
z(mm)	125	125
direction	y	y
position	front	front

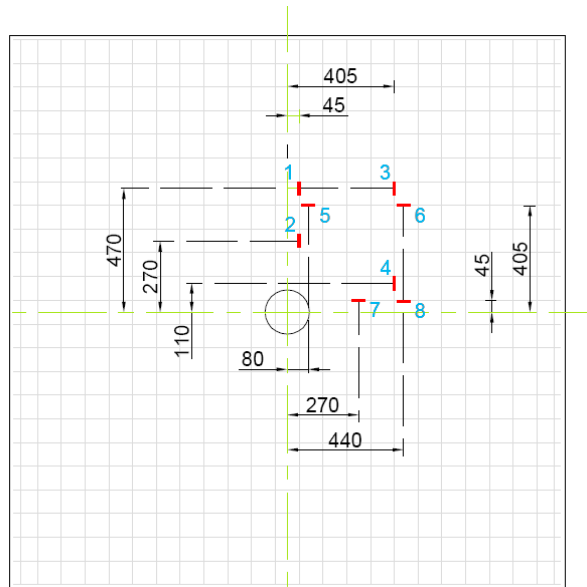


Figure B-3: Reinforcement strain gauge locations (Vepsä, 2010b).

Table B-3: Reinforcement Strain Gauge Locations

Position relative to the center					
point	x (mm)	y (mm)	z(mm)	direction	position
D1	45	470	-85	y	rear
D2	45	270	-85	y	rear
D3	405	470	-85	y	rear
D4	405	110	-85	y	rear
D5	80	405	-95	x	rear
D6	440	405	-95	x	rear
D7	270	45	-95	x	rear
D8	440	45	-95	x	rear

Displacements

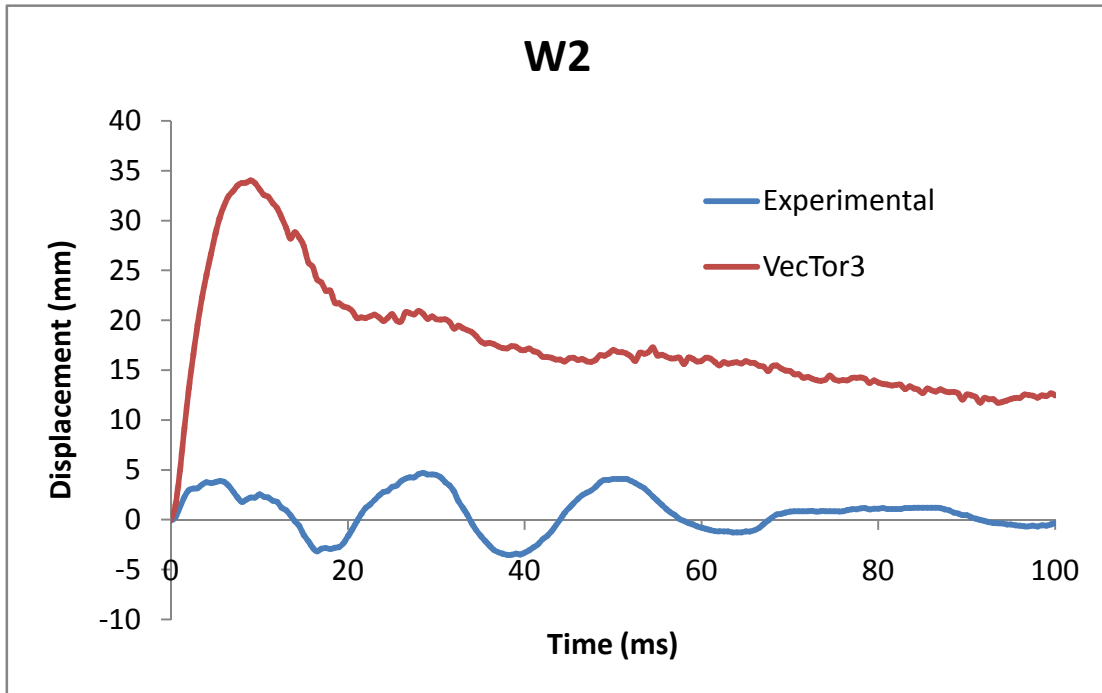


Figure B-4: Displacements at location W2.

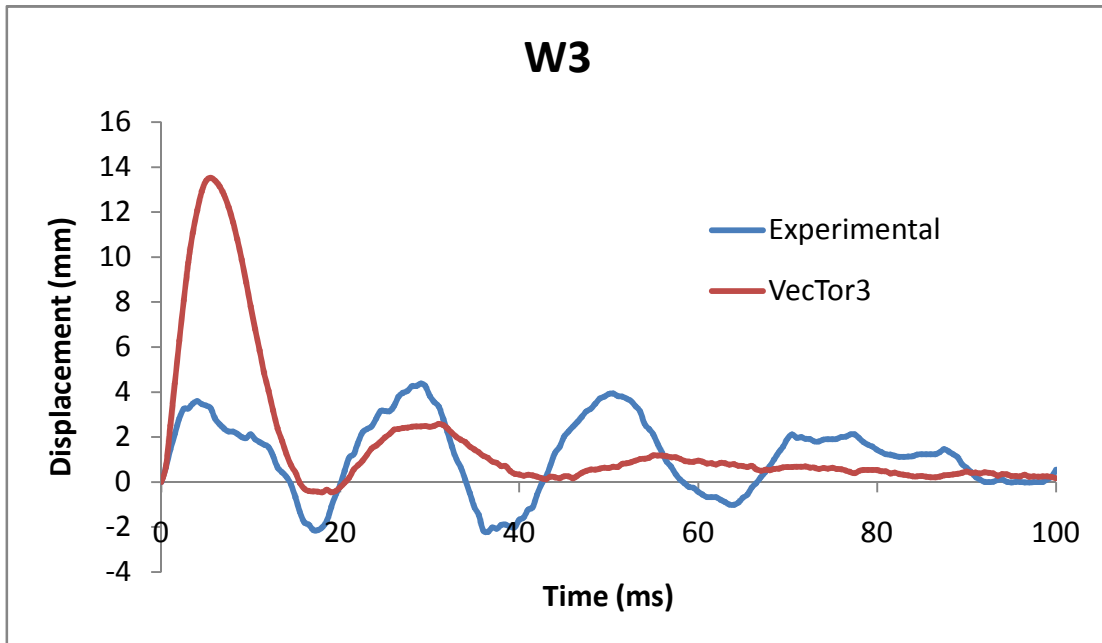


Figure B-5: Displacements at location W3.

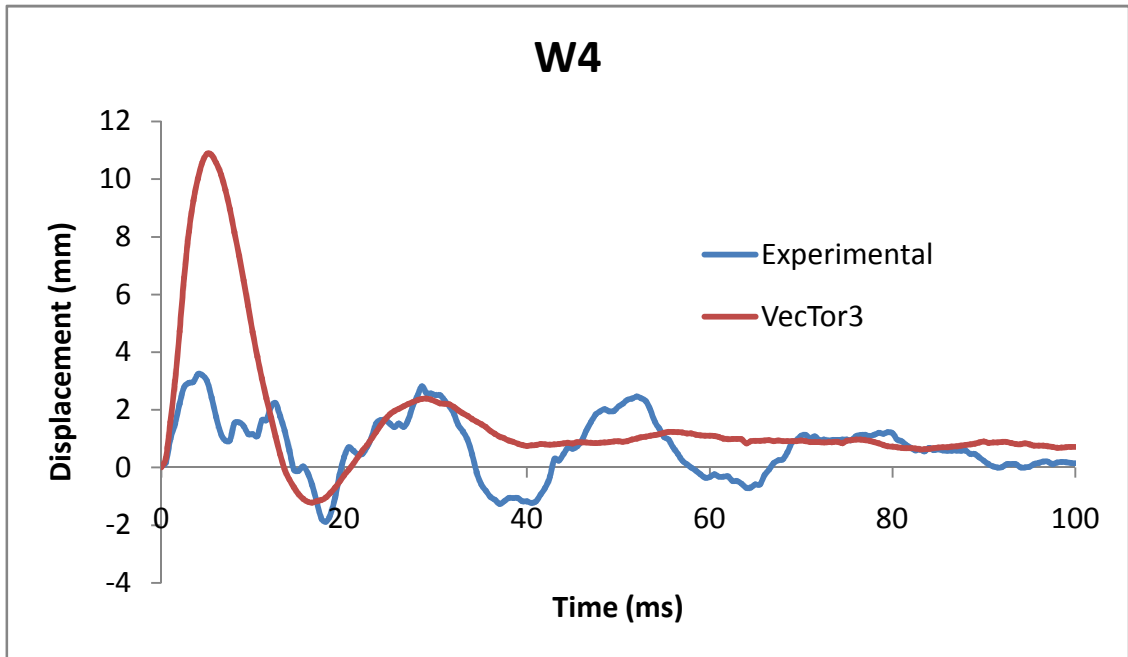


Figure B-6: Displacements at location W4.

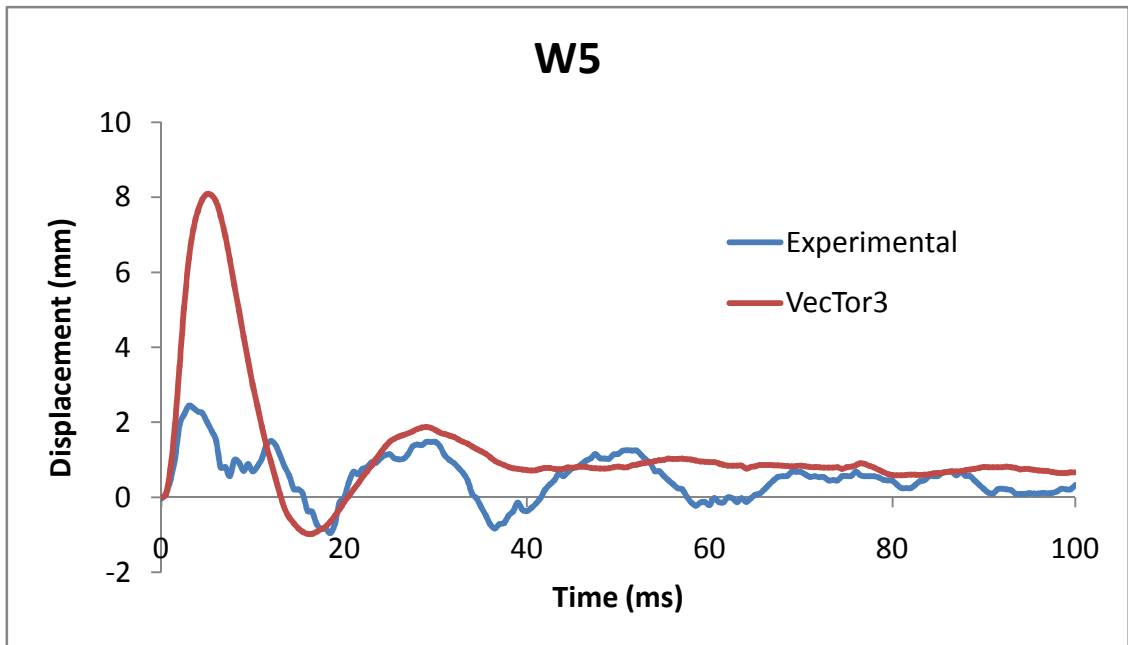


Figure B-7: Displacements at location W5.

Concrete Strains

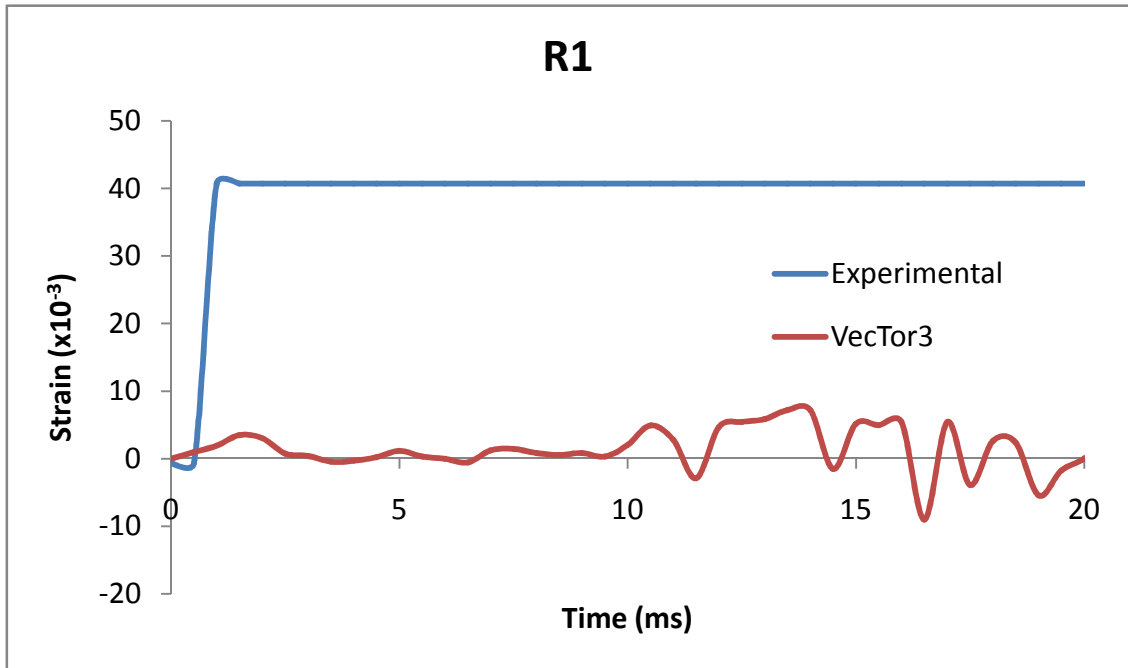


Figure B-8: Concrete strains at location R1.

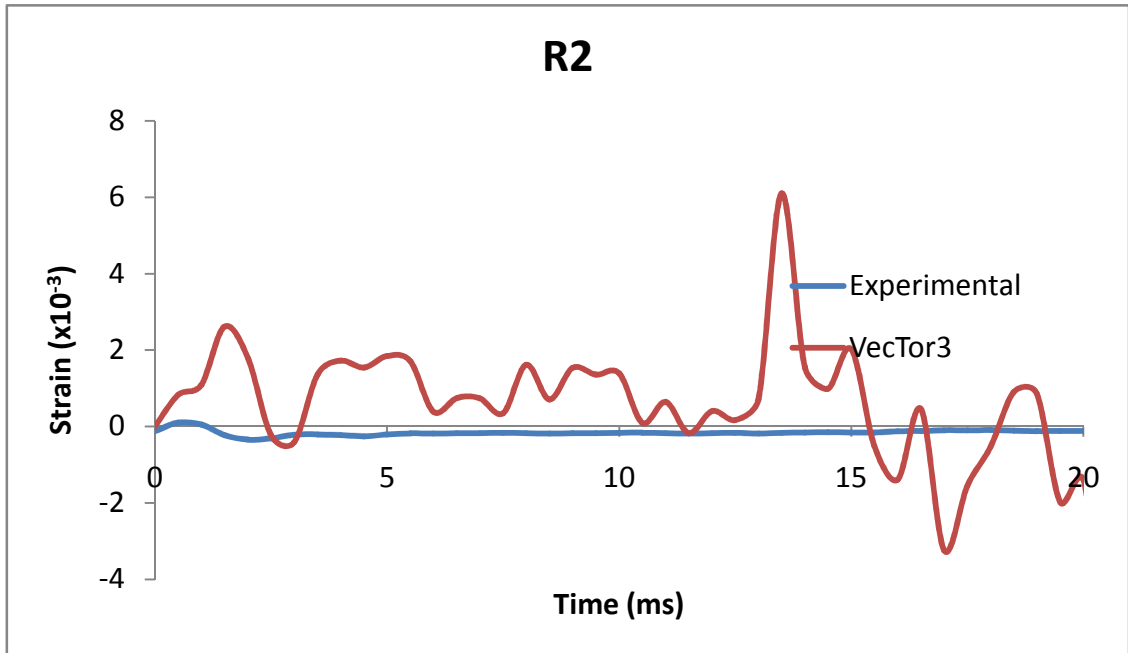


Figure B-9: Concrete strains at location R2.

Reinforcement Strains

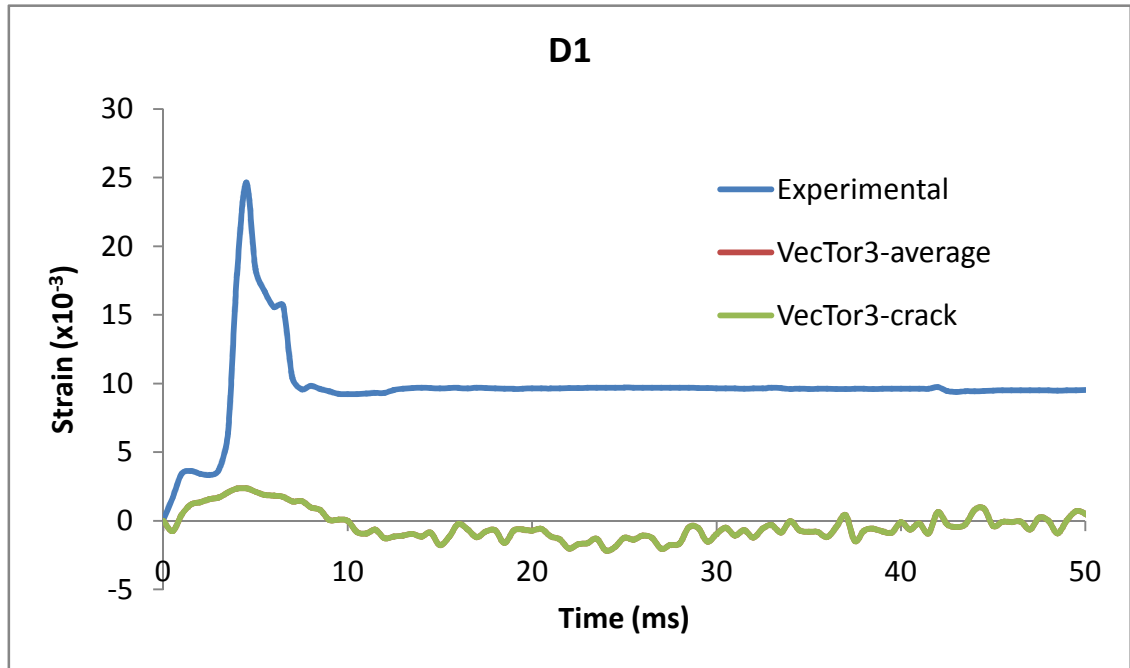


Figure B-10: Reinforcement strains at location D1.

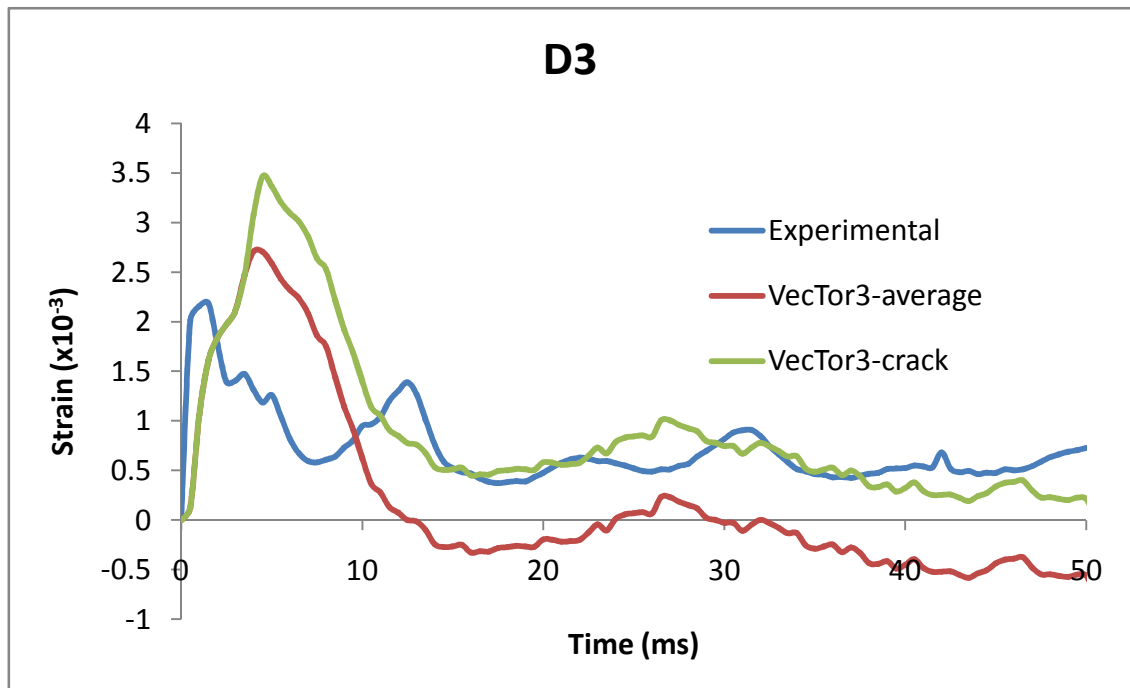


Figure B-11: Reinforcement strains at location D3.

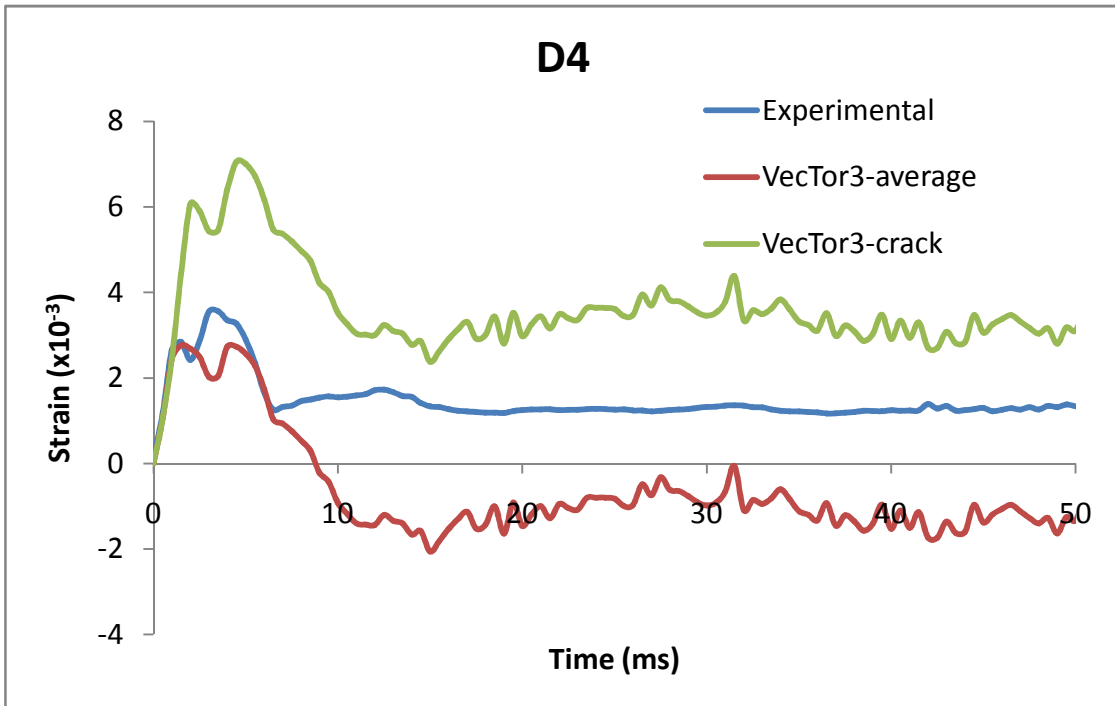


Figure B-12: Reinforcement strains at location D4.

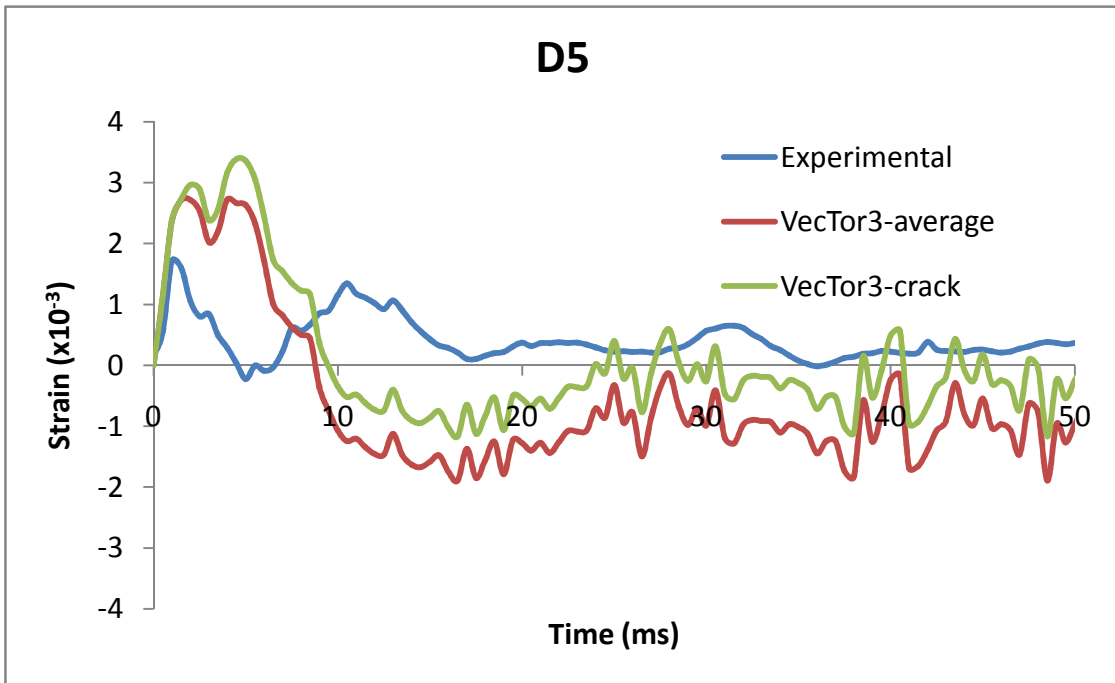


Figure B-13: Reinforcement strains at location D5.

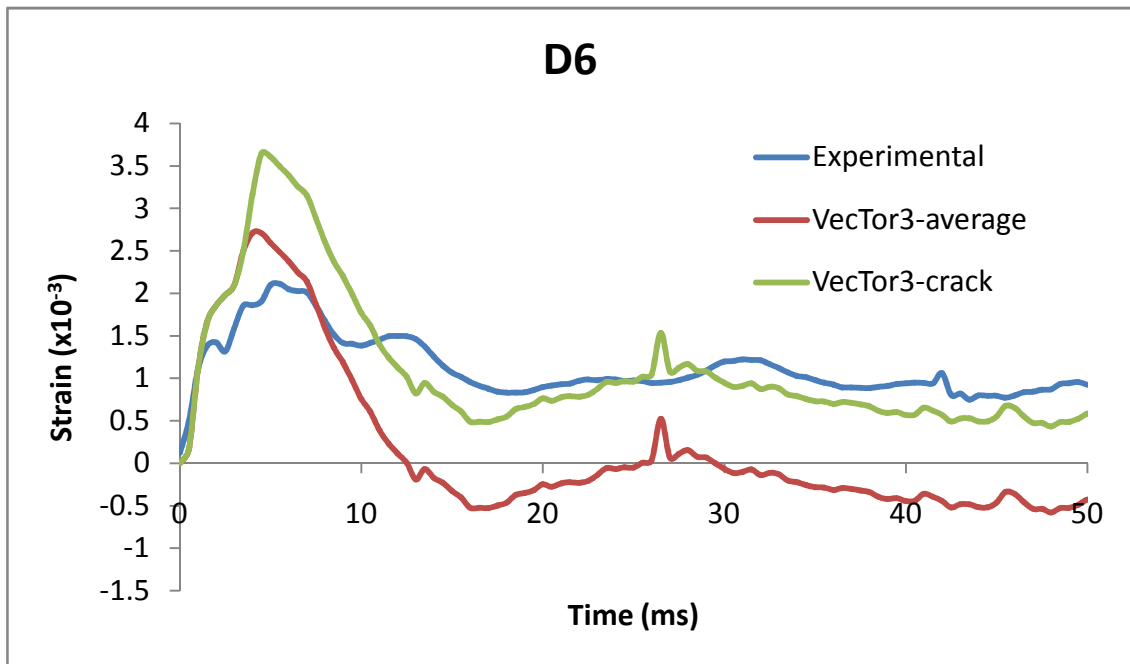


Figure B-14: Reinforcement strains at location D6.

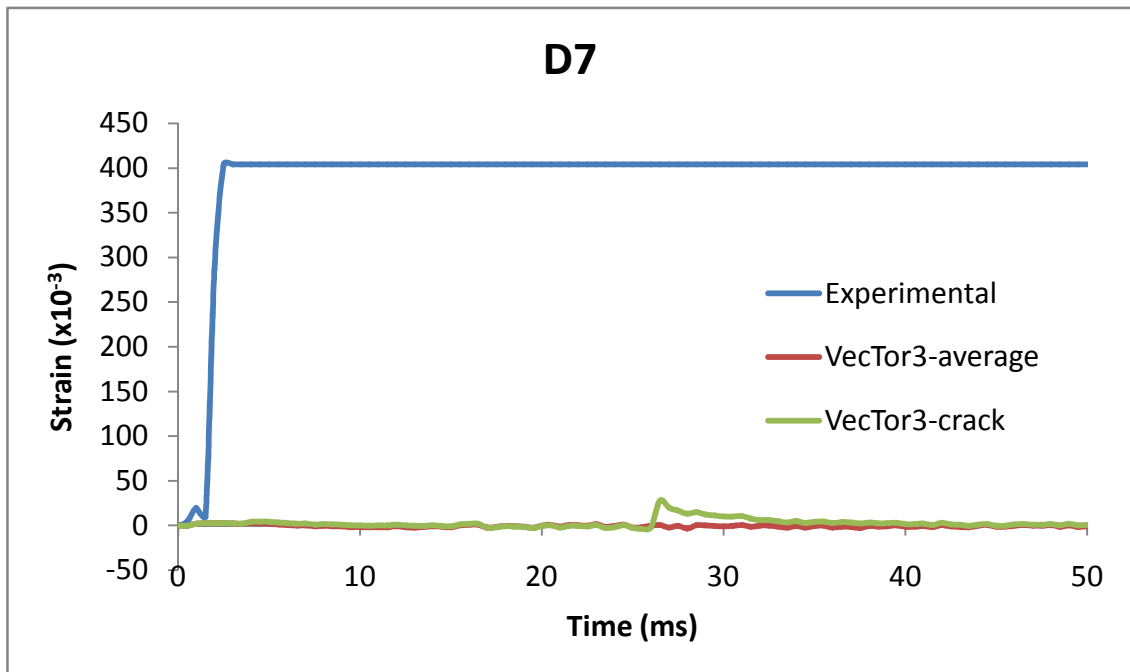


Figure B-15: Reinforcement strains at location D7.

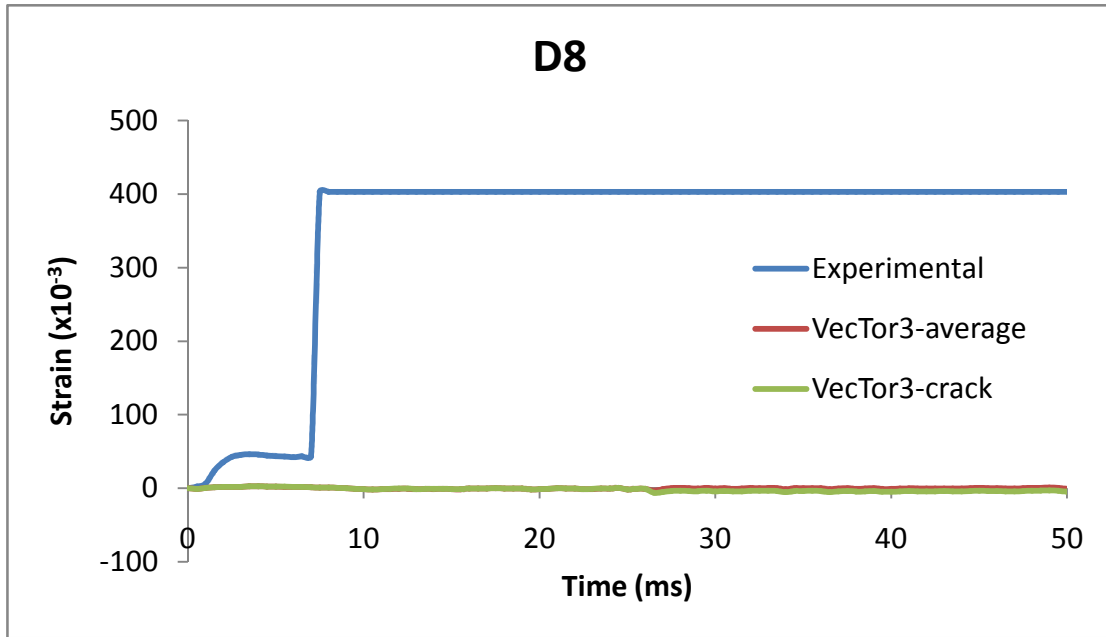


Figure B-16: Reinforcement strains at location D8.

Support Forces

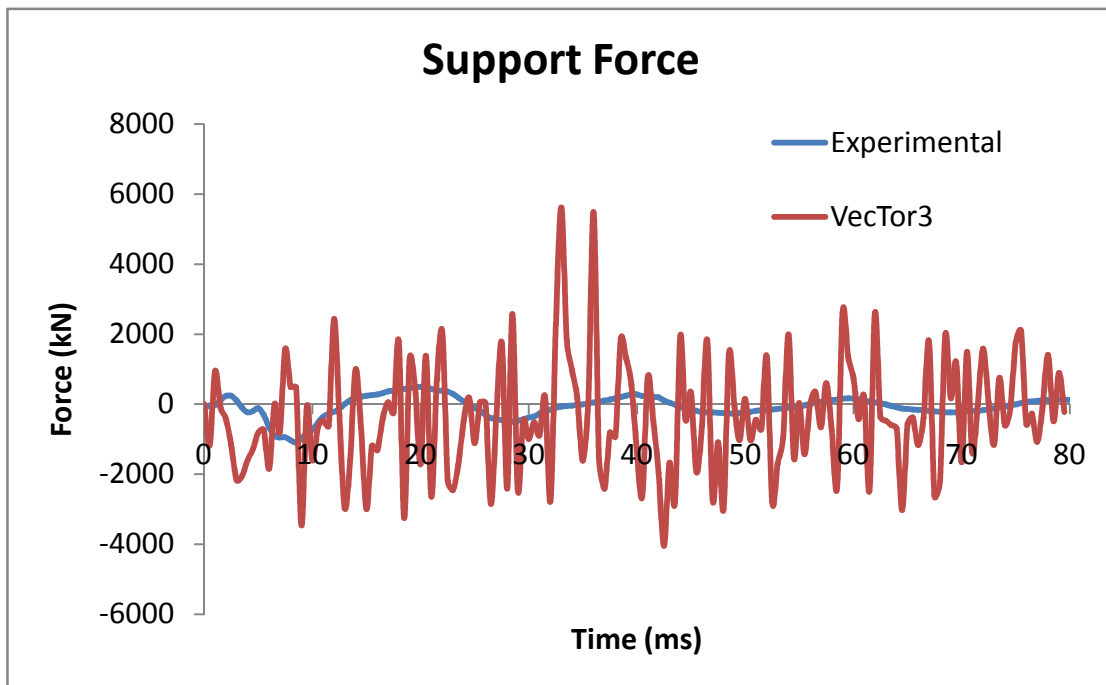


Figure B-17: Total support force.

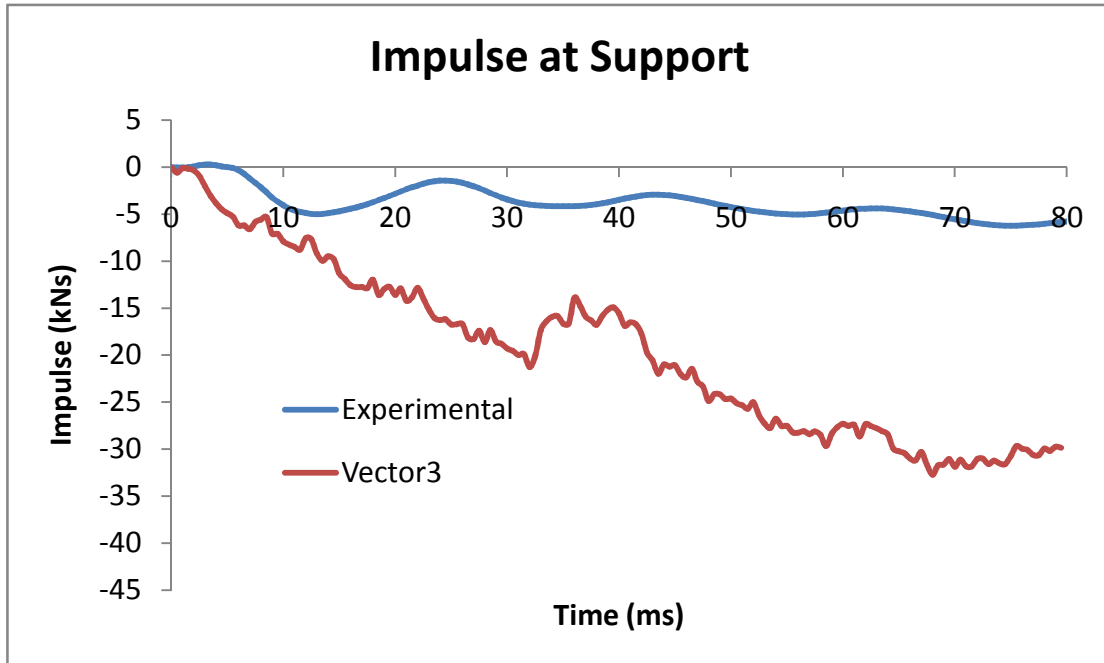


Figure B-18: Total impulse at support.